Abstract

Light transport and lasing in complex photonic structures

Seng Fatt Liew

2014

Complex photonic structures refer to composite optical materials with dielectric constant varying on length scales comparable to optical wavelengths. Light propagation in such heterogeneous composites is greatly different from homogeneous media due to scattering of light in all directions. Interference of these scattered light waves gives rise to many fascinating phenomena and it has been a fast growing research area, both for its fundamental physics and for its practical applications. In this thesis, we have investigated the optical properties of photonic structures with different degree of order, ranging from periodic to random.

The first part of this thesis consists of numerical studies of the photonic band gap (PBG) effect in structures from 1D to 3D. From these studies, we have observed that PBG effect in a 1D photonic crystal is robust against uncorrelated disorder due to preservation of long-range positional order. However, in higher dimensions, the short-range positional order alone is sufficient to form PBGs in 2D and 3D photonic amorphous structures (PASs). We have identified several parameters including dielectric filling fraction and degree of order that can be tuned to create a broad isotropic PBG. The largest PBG is produced by the dielectric networks due to local uniformity in their dielectric constant distribution. In addition, we also show that deterministic aperiodic structures (DASs) such as the golden-angle spiral and topological defect structures can support a wide PBG and their optical resonances contain unexpected features compared to those in photonic crystals.

Another growing research field based on complex photonic structures is the study

of structural color in animals and plants. Previous studies have shown that non-iridescent color can be generated from PASs via single or double scatterings. For better understanding of the coloration mechanisms, we have measured the wavelength-dependent scattering length from the biomimetic samples. Our theoretical modeling and analysis explains why single scattering of light is dominant over multiple scattering in similar biological structures and is responsible for color generation. In collaboration with evolutionary biologists, we examine how closely-related species and populations of butterflies have evolved their structural color. We have used artificial selection on a lab model butterfly to evolve violet color from an ultra-violet brown color. The same coloration mechanism is found in other blue/violet species that have evolved their color in nature, which implies the same evolution path for their nanostructure.

While the absorption of light is ubiquitous in nature and in applications, the question remains how absorption modifies the transmission in random media. Therefore, we numerically study the effects of optical absorption on the highest transmission states in a two-dimensional disordered waveguide. Our results show that strong absorption turns the highest transmission channel in random media from diffusive to ballistic-like transport.

Finally, we have demonstrated lasing mode selection in a nearly circular semiconductor microdisk laser by shaping the spatial profile of the pump beam. Despite of strong mode overlap, selective pumping suppresses the competing lasing modes by either increasing their thresholds or reducing their power slopes. As a result, we can switch both the lasing frequency and the output direction. This powerful technique can have potential application as an on-chip tunable light source.

Light transport and lasing in complex photonic structures

A Dissertation
Presented to the Faculty of the Graduate School
of
Yale University
in Candidacy for the Degree of
Doctor of Philosophy

by
Seng Fatt Liew

Dissertation Director: Professor Hui Cao

December 2014

Contents

List of Figures

Acknowledgements

Throughout my time at Yale, I have had the pleasure working with many talented people and this thesis would not have been possible without their guidance and assistance.

First of all, I want to thank my thesis advisor, Professor Hui Cao for providing direction, motivation, insight and guidance. I would also like to thank my thesis committee members Prof. Douglas Stone, Prof. Eric Dufresne and Prof. Antónia Monteiro for their valuable suggestions and advice.

Many thanks to all my fellow group members past and present. Special thank to Dr. Heeso Noh for teaching me so many knowledge in optical experiment and numerical simulation. I would also like to thank other former group members Dr. Jin-Kyu Yang, Dr. Jonathan Andreasen, Dr. Qinghai Song, Dr. Wenjie Wan and Dr. Sebastien Popoff for their assistance in various research projects. I am grateful to all the present group members Dr. Yaron Bromberg, Dr. Brandon Redding, Dr. Sebastian Knitter, Raktim Sarma, Stafford Sheehan and Wen Xiong for all the stimulating discussions.

In addition, I want to extend my thanks to all the people that I have collaborated in different research projects. I want to thank Prof. Richard Prum, Dr. Vinodkumar Saranathan, Prof. Eric Dufresne, Dr. Jason Forster, Dr. Jin-Gyu Park, Prof. Corey O'hern, Dr. Carl Schreck, Prof. Simon Mochrie, Dr. Xin Lu and Dr. Lin Yang for their collaboration in the study of structural color and photonic amorphous struc-

tures. I also appreciate Prof. Luca Dal Negro and Dr. Jacob Trevino for exposing me to the interesting golden-angle spiral lattice and their collaboration in its numerical study. I want to thank Prof. Antónia Monteiro group members, Dr. Bethany Wasik, April Dinwiddie for their effort of raising the butterflies and performing the artificial selection experiments. I also want to acknowledge the hard work of David Lilien for measuring the reflectance spectra from the butterflies. I would like to extend my gratitude to Prof. Willem Vos and Prof. Allard Mosk for their valuable inputs and collaboration in the study of light transport in absorbing disordered media. In the recent selective pumping on microdisk experiment, Dr. Li Ge had helped me a lot in the laser theory and thank Prof. Glenn Solomon for the MBE growth of GaAs wafer with embedded quantum dots. I am also grateful to Prof. Douglas Stone, Dr. Yidong Chong, Dr. Arthur Goetschy and Alex Cerjan for their teaching and collaboration in the study of light transmission and absorption in random media. I also wish to offer a big thank to Michael Power, James Agresta and Christopher Tillinghast for maintaining the fabrication facilities in clean room and Dr. Michael Rooks in YINQE. I want to thank the department secretaries, Maria Rao and Giselle DeVito for taking care of the complicated paper works for our group.

I also feel blessed for knowing so many brilliant minds in Becton, especially the students and post-docs working in the basement. Thank all of you for all the wonderful moments we spent together. Finally, I would like to thank my parents for their unflinching support throughout this challenging experience. I am very grateful for having an incredibly understanding beloved wife, without her motivation and support, I would not have been able to complete this long journey.

Chapter 1

Introduction

1.1 Complex photonic structures

Complex photonic structures refer to composite optical materials with spatial dielectric constant varying on length scales comparable to optical wavelengths. One class of the well-known photonic structures is photonic crystals (PhCs), which are characterized by periodic modulation of their spatial dielectric constant function [1–3]. Examples of PhCs in 1D, 2D and 3D are shown in Fig. 1.1. Light transport in PhCs bears a strong similarity to electron transport in crystalline solids. For example, due to the interference of waves scattered from crystal planes, there exists frequency windows that forbid light propagation [1–3]. Such a photonic band gap (PBG) is an analogue to the energy gap that exists between the conduction and valence bands of a semiconductor, where no electronic states are present. Similarly, the density of optical states vanishes within a photonic band gap, forbidding spontaneous emission, and suppressing vacuum fluctuation [4, 5]. With these properties, photonic crystals are excellent candidates to mold the flow of light in integrated photonics circuits. By artificially removing individual or a few unit cells within a PhC, its defect cavity can support optical resonances with small mode volume, spectrally localized within

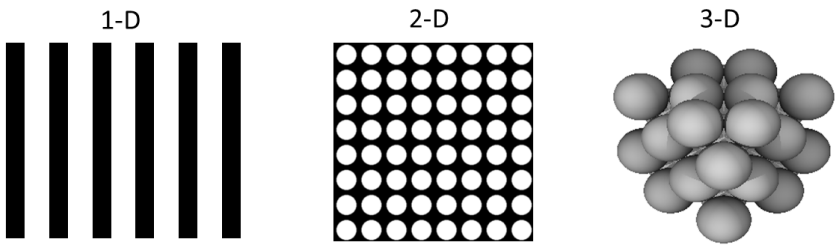

Figure 1.1: Examples of photonic crystals with periodic dielectric constant modulation in 1D, 2D and 3D. Middle panel is a square lattice PhC and the right most panel is face-centered cubic (FCC) arrangement of dielectric spheres.

the PBG with very high quality (Q) factor. This defect cavity has been used to make low-threshold lasers and enhance light-matter interaction [6]. However, due to fabrication imperfections, experimentally realized photonic crystals usually contain disorder, which affects light transport and produces unexpected features in their measured transmission/reflection spectra [7–9].

Another type of ordered structure that is devoid of spatial periodicity and generated by deterministic mathematical rules has attracted significant attention recently, due their structural complexity compared to PhCs [10–12]. They are called deterministic aperiodic structures (DASs) and are created using Thue-Morse, Rudin-Shapiro or Fibonacci sequences. The Fourier space of DASs contains spectral features that interpolate between pure-point discrete pattern in periodic crystals to a diffused pattern in random media. For example, the Fourier spectrum of a Thue-Morse structure is singular continuous. Consequently, light transport in Thue-Morse structures display unusual properties such as fractal gaps and anomalous diffusion in light transport [15–17]. Fig. 1.2(a) shows a 2D generalization of the Thue-Morse sequence with dielectric particles [13,14]. Another fascinating DAS, called Vogel's spirals, have full circular symmetry in Fourier space. Among Vogel's spirals, the golden-angle (GA) spiral displays the most intriguing structural properties, with hidden azimuthal symmetries in Fibonacci sequence [Fig. 1.2(b)]. Study of GA spirals was originally inspired by findings in nature; for example, seeds' arrangement in a sunflower head

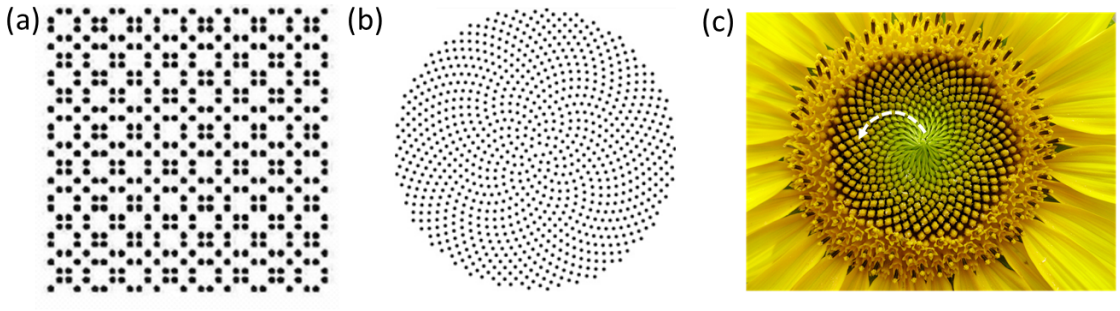

Figure 1.2: Deterministic aperiodic structures (DAS). (a, b) 2D dielectric particles arranged in the Thue-Morse sequence and Golden-angle spiral lattice. (c) Picture of a sunflower head showing spiral arms called parastichy and the seeds are arranged in spiral lattice shown in (b). Photo credit: http://www.flickr.com/photos/lucapost/694780262/.

follows this pattern [Fig. 1.2(c)] [18]. The GA spiral contains different families of spiraling arms in both clockwise and counter-clockwise directions that are called parastichy [white arrow in Fig. 1.2(c)]. Interestingly, the number of parastichy in each family belongs to the Fibonacci sequence [19]. At low-index contrast, the GA spiral supports an isotropic PBG, which is larger than the corresponding PhCs and quasi-crystals with the same filling fraction [20]. With metallic nanoparticles, plasmonic spirals generate polarization-insensitive light diffraction and planar scattering over a broad frequency range [21].

In the vast intermediate regime between ordered structures and random media, little is known about light transport in partially ordered structures. An example of a partially ordered structure that will be discussed in this thesis is a photonic amorphous structure (PAS) with only short-range order. In 2D and 3D, such structures can be generated by randomly close-packing the finite-size particles together. There exists a characteristic length scale which corresponds to the minimum center-to-center spacing between the nearest particles. The Fourier spectrum of a 2D PAS exhibits a ring pattern, which reflects the isotropic nature of the PAS, and the radius of the ring equals the dominant spatial frequency in the structure. Therefore, PASs are also optically isotropic and can be used to form complete PBGs in higher dimensions.

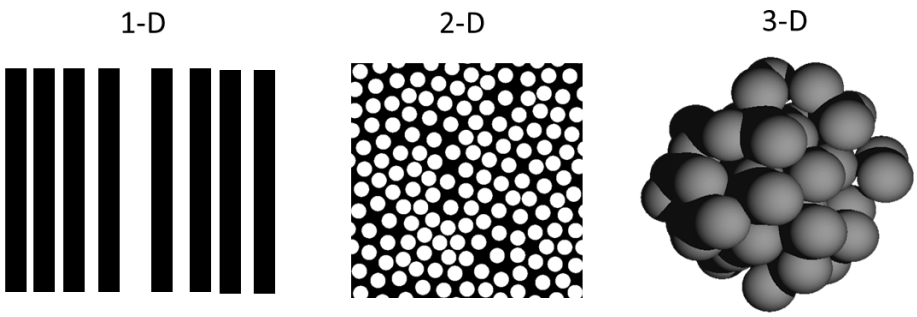

Figure 1.3: Photonic amorphous structures (PASs) in 1D, 2D and 3D. These structures only have short-range order and the dominant spatial frequency is determined by the nearest neighbor distance between particles.

Recent studies have demonstrated the formation of PBGs in two-dimensional (2D) and three-dimensional (3D) PASs with only short-range order [22–30]. At low index contrast, a PAS does not support a PBG, but it can generate angle-independent structural color through single or double scattering of light [31–35]. In fact, nature has used PAS to generate non-iridescent colors in many different animals, including birds [31, 36]. Inspired by these findings, biomimetic PASs have been fabricated by self-assembly of colloidal particles [35, 37], and have potential applications in wide-angle color displays [38–40].

Random media, with the highest level of structural complexity, are made up of a completely disordered arrangement of optical materials. Random photonic structures are most prevalent in our daily life, for example, white-paint, biological tissue, milk, fog, etc. Fourier spectra of random media display a continuous diffused pattern and contain many spectral components spanning across the optical frequency window. Consequently, random media support many degrees of freedom in time, space, polarization and optical spectrum, and they are all coupled due to multiple scattering of light. Similar to PhCs, light transport in random media also displays many interference effects that are predicted in electron transport, such as weak localization, Anderson localization, universal conductance fluctuations, open channels, and

coherent backscattering [41–44]. With the development of spatial light modulators, electromagnetic waves offer many advantages towards studying these interference effects compared to electronic systems, because using them the control of optical states is easier when compared to electronic states. Consequently, by controlling the input light state, random media can be become a versatile photonic device for use as a spectral filter, high numerical aperture lens, polarizer, etc [45–48]. Study of waves interference in random media is not only fundamentally interesting, but also has a profound impact in the fields of imaging, light harvesting, and light extraction.

In recent years, a large amount of studies on complex photonic structures has been inspired by nanostructures found in nature. With the prevalence of small-angle X-ray diffraction and electron microscopy, people have discovered that many animals, insects and plants in nature contain finely crafted nanostructures that give rise to beautiful colors [49, 50]. Inspired by these studies, biomimicry of photonic structures found in nature has become an intense area of research. However, it remains a question as to how these photonic structures have evolved over the years and whether they are related. In this thesis, we are going to investigate the coloration mechanism between closely-related butterfly species in collaboration with evolutionary biologists. In addition, we have also conducted artificial selection experiments to evolve a brown-UV colored butterfly to a violet color.

1.2 Photonic band gap

Light propagation in PhCs is highly dependent on its propagation direction with respect to different crystal planes. The interference pattern of scattered light in the far-field forms a Bragg diffraction pattern, which characterizes the underlying symmetry of the structure. Bragg diffraction of X-rays from crystalline solids is commonly

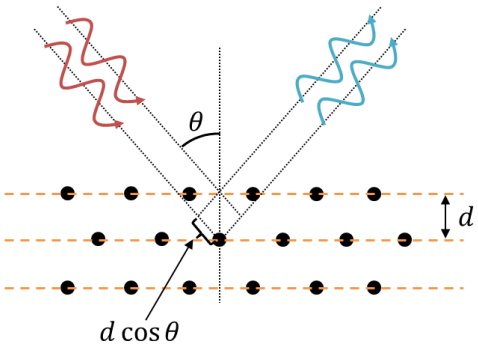

Figure 1.4: Schematic illustrating the Bragg reflection condition. When the incident angle is θ and the difference in path length between successive reflections $2d\cos(\theta)$ equals to an integer number of wavelengths λ, light reflected from a family of crystal planes with spacing d interferes constructively at the far-field.

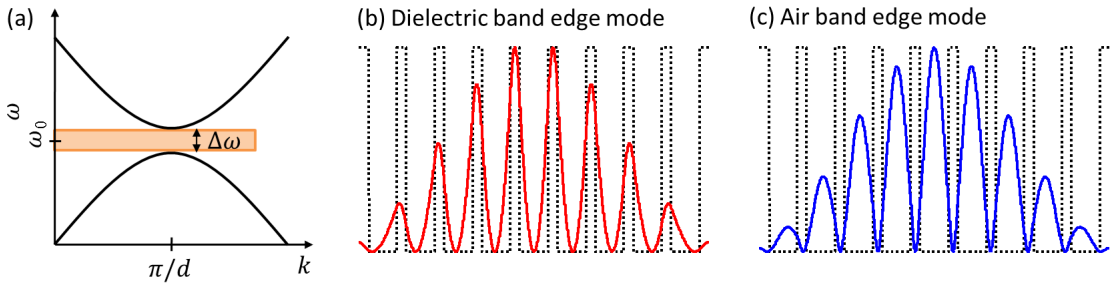

Figure 1.5: Dispersion relation and band-edge modes of a PhC. (a) Dispersion relation of a 1D PhC. The band splitting at $k = \pi/d$ creates a frequency window with width $\Delta\omega$ where no optical modes exist. (b-c) Dashed line indicates the dielectric constant profile of the 1D PhC. The solid lines correspond to the field intensity of dielectric band edge mode (b) and air band edge mode (c) respectively. The field intensity of dielectric band edge mode is concentrated in the high-index part and the air band edge mode resides in the low-index regions.

used to extract useful information such as their atomic arrangement, lattice constants, and density of defects [51]. Similarly, Bragg diffraction of optical waves from a PhC is due to interference of waves scattered from the periodic fluctuation in its refractive index. When the Bragg condition $m\lambda = 2d\cos(\theta)$ is met, the PhC acts as a perfect mirror, where d is the distance between the crystal planes. This condition is illustrated in Fig. 1.4.

The simplest PhC is a one-dimensional stack of alternating layers with different refractive indices. For certain wavelength ranges that satisfy the Bragg condition,

the reflected light from the 1D PhC interferes constructively and light propagation is forbidden. The dispersion relation that relates the frequency ω of light to its wave vector $k = 2\pi/\lambda$ is shown in Fig. 1.5(a). When the wave vector k equals to π/d, where d is the center-to-center distance between two layers with the same refractive index, the Bragg condition is met. At this wavelength, the interference of incoming light with wave vector $k = \pi/d$ and its reflected counterparts with wave vector $k = -\pi/d$ form the optical modes which resemble standing waves. There are two possible solutions for the standing wave pattern at this wave vector, one is $\cos(kx)$ and another is $\sin(kx)$. However, the field intensity of one wavefunction mostly concentrates in the high-index material and another wavefunction mainly resides within the low-index material. As these two solutions have the same wave vector but experience different average refractive indices, their frequencies must be different. This difference causes the dispersion lines to split into two branches with a frequency gap in between, which is the PBG. The mode at the low-frequency band edge concentrates in the high-index material, and it is known as the "dielectric band edge mode" [Fig. 1.5(b)]. Its counterpart at high-frequency is called the "air band edge mode" because its field intensity is localized in the low-index region [Fig. 1.5(c)]. The width of the band gap $\Delta\omega$ depends on the refractive index contrast and number of unit cells. The higher the index contrast, the larger the difference in the average refractive indices experienced by the dielectric and air band edge modes, leading to larger frequency splitting. For 2D and 3D structures, it is difficult to align band gaps in all directions due to lack of full circular or spherical symmetry in the Fourier space. As a result, complete PBGs at higher dimensionality only occur in few examples, such as the diamond structure in 3D.

Experimentally, to determine the frequency range of PBG, people often measure the transmission or reflection spectrum. Without the absorption, the transmission(reflection) spectrum will have a dip (peak) within the forbidden frequency range.

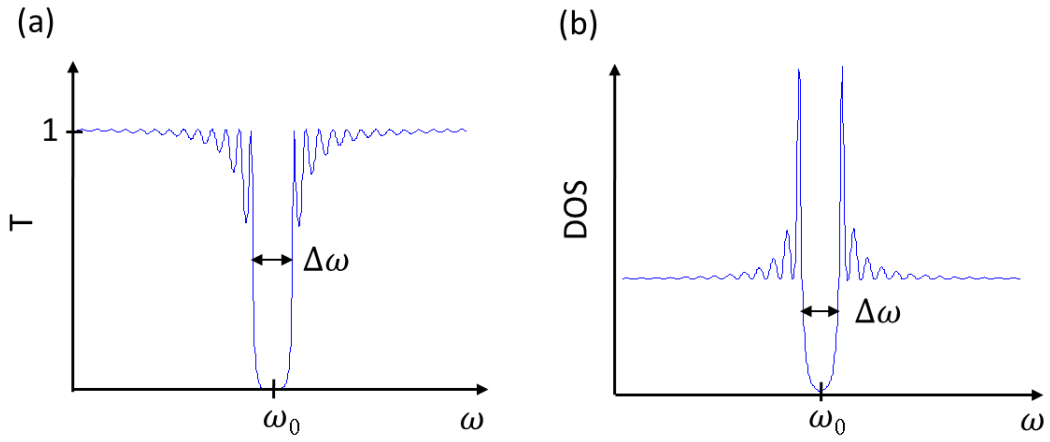

Figure 1.6: Transmission spectrum and density of optical states (DOS). (a) Transmission spectrum for a 1D PhC where the dip corresponds to the PBG. (b) Density of states for the same 1D PhC which shows the absence of optical modes within the PBG.

In 1D, a typical transmission spectrum for a PhC is shown in Fig. 1.6(a), where the transmission is zero within the PBG. At the edge of the PBG, there are several spikes with transmission equal to 1, these spikes correspond to the band edge modes. Without disorder, all the optical modes supported by the 1D PhC are spatially extended over the entire structure and thus facilitate light transmission. However, the transmission spectrum for a 2D and 3D PhC varies with the angle of incident light and is polarization dependent. Hence, polarization- and angle-resolved measurements are needed to confirm the existence of a complete PBG. Another way to tell whether there exists a complete PBG is by measuring the density of optical states (DOS). DOS of a 1D PhC is shown in Fig. 1.6(b) which shows absence of optical modes within its band gap. The DOS at any frequency includes all the optical modes irrespective of their wave vectors. As a result, a dip in DOS reflects a PBG in all directions for 2D and 3D structures. The DOS is a very important parameter to quantify the change of PBG in the presence of structural disorder, and to determine whether there is a complete PBG for partially ordered structures.

1.3 Light scattering

Defects are unavoidable in PhCs due to imperfection of the fabrication process, and it causes additional scattering of light in random directions. Hence, transmission and reflection spectra of disordered PhCs show features that are not predicted in perfect PhCs [7–9]. In addition, the interference effect of multiply scattered light from partially ordered and random media are interesting research subjects. As a result, understanding the scattering of light is crucial for the study of light transport in all complex photonic structures. Two length measures that characterize the scattering process are the scattering mean free path (l_s) and transport mean free path (l_t). The scattering mean free path, l_s, is the average distance traveled by light between two consecutive scattering events. While the transport mean free path, l_t, is the distance light travels before its propagation direction is randomized by scattering events. Usually, it takes several scatterings to totally randomize the propagation direction of incoming light and thus $l_t > l_s$. The following expression relates these two quantities together:

$$l_t = \frac{l_s}{1 - \langle \cos(\theta) \rangle} \tag{1.1}$$

where $\langle \cos(\theta) \rangle$ is the anisotropic factor, and it represents the intensity-averaged scattered light direction. $\langle \cos(\theta) \rangle = 0$ corresponds to isotropic or Rayleigh scattering, where the scatterers are much smaller than wavelength of light λ. $\langle \cos(\theta) \rangle \gg 0$ when the scatterers' size is larger than the optical wavelength, and light is mostly forward scattered. This condition is usually satisfied in the case of biological tissue where the cells are in the order of tens of micrometers. Finally, when the light is mostly backscattered, $\langle \cos(\theta) \rangle \ll 0$, and $l_t < l_s$. For example, when the light frequency is slightly higher than the first Mie resonance frequency, the scattered light will have about 180° phase difference with the incoming light. The interference between the

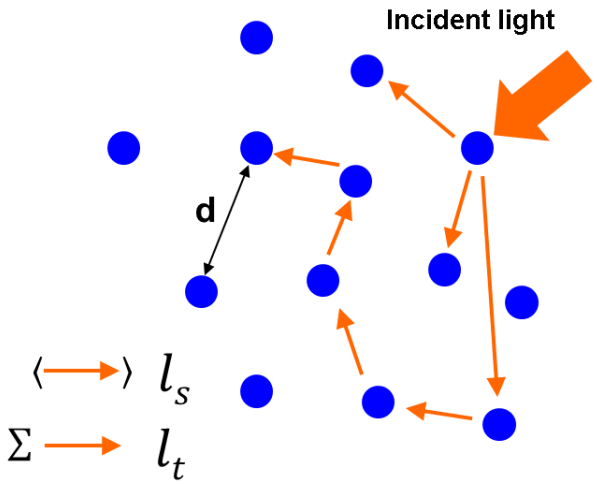

Figure 1.7: Schematic showing the scattering of the incoming light by randomly arranged scatterers. d is the average spacing between two scatterers. Each arrow represents a scattering event. For independent scattering, $d \gg \lambda$.

incident and scattered waves is constructive in the backward direction and destructive in the forward direction, leading to $\langle \cos(\theta) \rangle \ll 0$.

To estimate the magnitude of l_s and l_t, we need to know the scattering cross section of an individual particle or aggregate of particles. For low-density random aggregates [Fig. 1.7], we can estimate l_s and l_t by assuming that the scattering of light from each particle is independent from one to another. In other words, the scattered fields from all particles add up incoherently at the far-field, and there is no interaction within the near-field zone. Under this approximation, and if we assume each particle is identical, we can estimate both l_s and l_t by

$$l_s = \frac{1}{\rho\sigma} \tag{1.2}$$

$$l_t = \frac{1}{\rho\sigma_t} \tag{1.3}$$

where ρ is the particle density, $\rho \approx 1/d^n$, d is the average spacing between two particles, n is the dimensionality of the system. σ is the total scattering cross section from a single particle and σ_t is the backward scattering cross section [52]. Both σ

and σ_t are calculated using the following expressions.

$$\sigma = \int F(\Omega) d\Omega, \tag{1.4}$$

$$\sigma_t = \int F(\Omega)(1 - \cos\theta) d\Omega, \tag{1.5}$$

where $F(\Omega)$ is the differential cross section of a single particle. If the particle is a sphere, the analytical solution for $F(\Omega)$ is already derived from the Mie theory [53]. These simple estimations provide insights on the scattering strength of random media at low density. Both equation 1.4 and 1.5 assume there is no correlation in the position of the particles. Presence of positional order will modify these two equations with a correction called the structure factor [54]. The structure factor takes into account the interference of the scattered light at the far-field due to structural order. For example, in ref. [54], the anisotropy factor $\langle\cos(\theta)\rangle$ becomes negative and $l_t < l_s$ for a colloidal suspension made up of charged particles. However, with increasing particle density, the near-field interaction of the scattered fields becomes important, and this has to be taken into account for accurate estimation of l_t [55]. In chapter 4 of this thesis, we will investigate the modification of transport mean free paths by both short-range order and near-field effects in a biomimetic sample. Study of the scattering lengths in such system will not only improve our understanding of the coloration mechanism but also help us to determine the critical sample thickness for color generation.

1.4 Light transport: diffusion and localization

In non-absorbing systems, if the transport mean free path l_t is much longer than the system size L, and $l_t \gg L \gg \lambda$, the system falls in the ballistic regime. In this regime,

light mostly travels in the forward direction with few scattering events. One example is when a laser beam propagating through the atmosphere is weakly scattered by aerosol particles. However, when the system size becomes much larger than the transport mean free path ($L \gg l_t \gg \lambda$), the number of scattering events increases exponentially, light transport becomes diffusive, and the system appears turbid or opaque. The diffusion constant D of the system is connected with the transport mean free path l_t by this relation $D = \frac{1}{3} v l_t$, where v is the transport velocity of the photons. A typical characteristic time after which the diffusing photons start reaching the edge of the system can be defined as $\tau_D = L^2/D$. τ_D is usually called the diffusion time or the Thouless time [56]. The average distance a photon travels through the random system is $l_p = v/\tau_D \sim L^2/l_t$. Finally, when scattering becomes very strong such that $l_t \sim \lambda$, light may be spatially localized, as suggested in ref. [57,58]. Without absorption, this condition is the criterion for the Anderson localization transition of an electron with de Broglie wavelength λ in a disordered solid [59–61]. In this regime of strong localization, strong wave interference from different scattering events causes the renormalization of the diffusion constant to zero. The localization length ξ can be calculated from the transmission spectra of random systems of different lengths where $\xi^{-}1 = -d\langle \ln T \rangle / dL$. When $\xi > L$, the system is in the localization regime.

One of the most studied interference phenomena in disordered media is the coherent backscattering (CBS) process, which is a manifestation of the weak localization phenomenon. As a precursor to Anderson localization, the weak localization phenomenon was first studied in electronic systems, wherein it arises from the interference of electrons under multiple scattering conditions [60, 62]. Under weak localization conditions, interference of the incoming and time-reversed paths leads to the formation of energy "loops" inside the disordered media, increasing the photons' return probability, and reducing light transport in the forward direction. This process not only happens for electrons, but also for any waves propagating in disordered

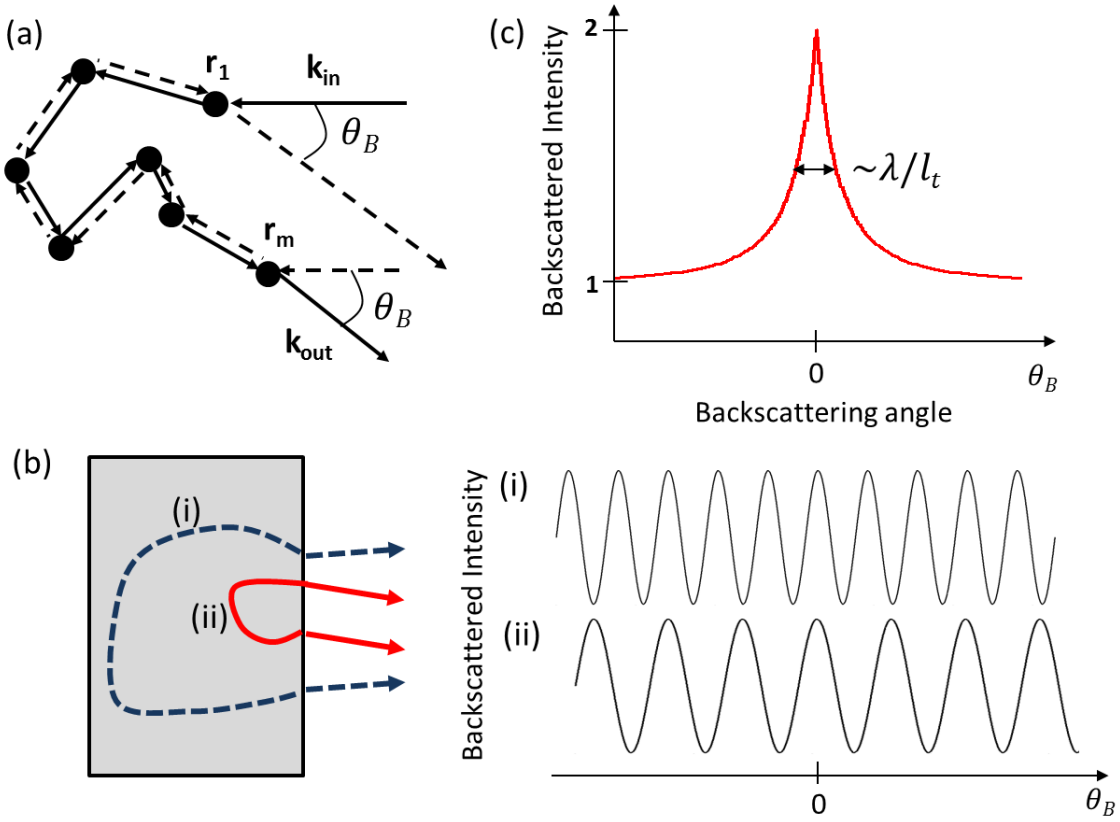

Figure 1.8: Coherent backscattering of light in random media. (a) Schematic showing that each scattering path (solid line) will have a time-reversed counterpart (dashed line) forming a pair of incomplete loops. The amount of phase shift between these two paths depends on the wavelength λ as well as spacing between the final scatterers with position at r_1 and r_m. (b) Schematic showing two possible scattering loops, each of them will generate modulation with different periodicity in their backscattered intensity. Contribution of each loop to the final coherent backscattering intensity cone depends on the scattering length l_t in the system. (c) The final coherent backscattering intensity cone after summing up all the possible scattering loops. The width of the cone is inversely proportional to the transport mean free path l_t.

media. As a result, when we measure the light reflected from a thick random media, a substantial enhancement of the intensity will be detected at angles very close to the backscattering direction. This intensity enhancement is called the coherent backscattering (CBS) cone [43, 63–66].

To understand this process, we refer to the diagram in Fig. 1.8(a), which shows two counter-propagating light paths; one is a solid line and another is a dashed line. Assuming that the spatially coherent light with wave vector k_{in} is incident onto the disordered medium, the light will be dispersed to many directions due to multiple scattering. However, note that for each scattering light path (solid line) inside the random media, there will always be another time-reversed counterpart (dashed line), forming a pair of incomplete loops. Let us consider the case where we detect the light reflected in the exact backscattering direction $\theta_B = 0$. In this case, the two counter-propagating time-reversed paths will have no phase difference and thus interfere constructively, with output intensity equal to $4I_0$, where I_0 is the input intensity. At other detection angles where $\theta_B \neq 0$, there will be a phase shift of $(k_{in}+k_{out}).(r_1\text{-}r_m)$, where r_1 and r_m are the positions of the two last scatterers on the loop and $|r_1\text{-}r_m| = l_m$. As a result, the backscattered intensity for this pair of loops will exhibit periodic modulation with periodicity dependent on the wavelength λ and l_m. The length of l_m depends on the scattering strength of the system, which infers the transport mean free path l_t. For example, as illustrated in Fig. 1.8(b), there are two scattering loops (i) and (ii) with different sizes, and their corresponding backscattered intensity is plotted on the right. If the system is highly scattering with short transport mean free path, most of the light will only penetrate little into the disordered media, and the backscattered intensity is dominated by small loops of type (ii). Consequently, after summing the contributions from all the possible loops, the final backscattered intensity cone will have a broader linewidth [Fig. 1.8(c)]. On the other hand, if the transport mean free path is long, the backscattered intensity

cone is mostly contributed contributed to by the scattering loops of type (i) and the linewidth becomes narrow. There, from the linewidth of the coherent backscattering cone, we can extract the transport mean free path. It has became a powerful technique to characterize the scattering strength of random media.

Another fascinating interference effect of electron transport in metal with disorder is the existence of highly conducting states, called "open channels" [67–70]. In the diffusive regime where $L \gg l_t$, the conductance of the system is proportional to l_t/L, which means the conductance in general is quite small. Although most of the electronic states have small conductance, it was found that there are a small amount of highly conducting states that carry most of the energy through the disordered system. Similar phenomena are observed in light transport through disordered media as well and has lately caught much attention [71–78]. In principle, these open channels enable an optimally prepared coherent input beam to transmit through a strong scattering medium with order unity efficiency. Recent developments of adaptive wavefront shaping and phase recording techniques in optics have enabled experimental studies of open channels [46,79–81]. The open channels greatly enhance light penetration into scattering media, and have a profound impact in a wide range of applications from biomedical imaging and laser surgery to photovoltaics and energy-efficient ambient lighting [46, 82, 83].

However, the effect of absorption on these open channels remains largely unexplored. Very recently, it has been shown that light absorption in strongly scattering media can be greatly enhanced or inhibited by coherent control of the input light state [84–86]. These studies show the intriguing interplay between absorption and interference of light, which can be used to control the amount of energy being deposited in the random media. In chapter 6 of this thesis, we will show how open channels for light are being modified by absorption and what their correlation is with absorption channels.

1.5 Semiconductor microdisk laser

In recent years, the wavefront shaping technique has been extended to control random lasers by designing an optimal spatial pump profile [87–90]. In fact, the concept of pump profile engineering in the field of semiconductor microcavity lasers precedes the development of spatial light modulators. Semiconductor microcavity lasers are an important light source for integrated photonic devices due to their small footprint. There are several types of microcavity lasers, including vertical-cavity surface-emitting lasers (VCSELs) with a 1D cavity formed by a pair Bragg reflectors [91]. In 2D, a photonic crystal nanocavity laser can be created by artificially removing one or more unit cells within a PhC, thus forming a defect cavity bounded by the photonic band gap effect [6]. Last but not least, microdisk lasers are one of the most promising candidates for on-chip light sources since they were demonstrated in that early 90s [92]. The main advantages of microdisk lasers are their simple geometry and low lasing threshold. In a microdisk cavity, due to high index contrast at the cavity-air boundary, light is strongly confined by total internal reflection (TIR), forming high-Q whispering-gallery modes (WGM).

For a circular microdisk cavity with radius R few times larger than the optical wavelength, its free-spectral range (FSR) is typically smaller than the gain spectrum bandwidth. Free-spectral range (FSR) is defined as the frequency spacing between two successive first radial order WGMs and can be approximated by λ/m, where m is the azimuthal number of the mode. $m \approx nkR$, where n is the refractive index of the disk and wave vector $k = 2\pi/\lambda$. With uniform pumping, as illustrated in Fig. 1.9, the WGMs can all lase simultaneously with a very small lasing threshold. Usually, due to surface roughness introduced during the fabrication process, for a large mi-

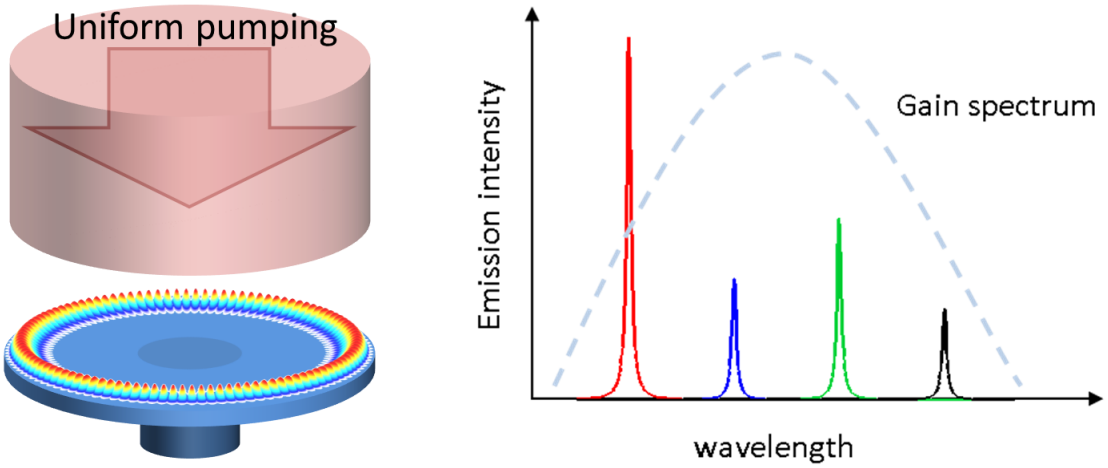

Figure 1.9: Multimode lasing from uniformly pumped microdisk laser. When a large circular microdisk with embedded gain material is pumped uniformly, most of the whispering-gallery modes covered by the gain spectrum will lase simultaneously because they all have similar Q factors and thus similar lasing thresholds.

crodisk cavity, the Q factors of the modes are restricted by scattering loss rather than tunneling loss. Hence, both their Q factors and lasing thresholds are very similar. Such a multimode lasing spectrum is typically not favorable for many applications especially as a light source for integrated photonics where single mode operation is desired. There are several ways to achieve single mode operation, for instance, by using smaller disk to increase the FSR such that there is only one mode within the gain spectrum. However, smaller disk will have lower Q factor due to increased tunneling loss and larger fabrication error.

Another efficient method to control the lasing spectrum is by engineering the pump profile to change the lasing threshold. To select a particular mode to lase, one may reduce its lasing threshold by enhancing the spatial overlap between the pump and the mode. For instance, a donut-shaped optical pump was employed to select lasing modes with desired transverse intensity profile in VCSELs and Fabry-Perot cavities [93–97]. Similarly, a ring-shaped pump profile was used to lower the lasing threshold of WGMs in circular micropillars [98] or to produce directional emission from spiral-shaped microdisk lasers [99]. The same method is applied for electrically

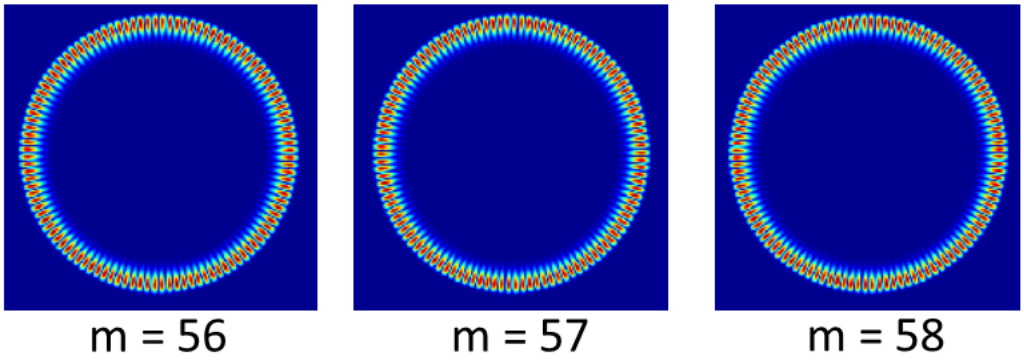

Figure 1.10: The spatial magnetic field intensity profile $|H_z(x, y)|$ of three successive first radial order WGMs. Their field profiles have strong spatial overlap at the boundary, rendering the conventional selective pumping technique unviable. In the simulation, refractive index of disk $n = 3.13$, disk radius $R = 3\mu$m and transverse electric (TE) polarization (in-plane electric field).

pumped semiconductor lasers by patterning the electrodes to match the targeted mode profiles [100–102]. Using this method, in Ref. [100], selection of lasing modes with distinct output directions in a quasi-stadium cavity was demonstrated. In addition, current injection into separate electrodes that have maximum overlap with the desired mode switches the laser's emission direction [103]. However, the pump-mode overlap technique requires *a priori* knowledge of the mode profiles and demands little spatial overlap between the targeted modes. Hence, it limits the switching capability to a few modes, and becomes practically unviable once the modes have strong spatial overlap.

In a circular microdisk cavity, the highest-Q modes have strong spatial overlap at the boundary as shown in Fig. 1.10. These three modes correspond to the first radial order WGM with orbital angular momentum equal to $m = 56$, 57 and 58 respectively. They have strong spatial overlap at the boundary and thus cannot be selectively pumped to lase separately. Nevertheless, in chapter 7 of this thesis, we will show when surface roughness is taken into account, it becomes possible to selectively cause one mode to lase by optimizing the pump profile. In addition, we will show that the emission directionality from a microdisk laser can be controlled by selecting a

different mode to lase. This selective pumping technique can potentially be extended to electric pumping and makes the microdisk laser a versatile tunable on-chip light source.

Bibliography

[1] C. Soukolis, Photonic Crystals and Light Localization in the 21st Century (Dordrecht: Kluwer Academic, 2001).

[2] J. D. Joannopoulos, S. G. Johnson, J. N. Winn and R. D. Meade, Photonic Crystals : Molding the Flow of Light (2nd Edition) (Princeton, NJ: Princeton University Press, 2008).

[3] S. Noda and T. Baba (eds), Roadmap on Photonic Crystals (New York: Kluwer Academic, 2003).

[4] E. Yablonovitch, Phys. Rev. Lett. **58**, 2059 (1987).

[5] S. John, Phys. Rev. Lett. **58**, 2486 (1987).

[6] O. Painter, R. K. Lee, A. Scherer, A. Yariv, J. D. OBrien, P. D. Dapkus and I. Kim, Science **284**, 1819 (1999).

[7] A. F. Koenderink, M. Megens, G. van Soest, W. L. Vos, and A. Lagendijk, Phys. Lett. A **268**, 104 (2000)

[8] A. F. Koenderink, and W. L. Vos, Phys. Rev. Lett. **91**, 213902 (2003)

[9] A. F. Koenderink, A. Lagendijk and W. L. Vos, Phys. Rev. Lett. **72**, 153102 (2005).

[10] E. Maciá, Rep. Prog. Phys. **69**, 397 (2006).

[11] N. Poddubny and E. L. Ivchenko, Physica E **42**, 1871 2010.

[12] L. Dal Negro and S. V. Boriskina, Las. Photon. Rev. **6**, 178 (2011).

[13] A. Barbé,and F. Von Haeseler, Int. J. Bifur. Chaos **17**, 1265 (2007).

[14] L. Dal Negro, N. N. Feng, and A. Gopinath, J. Opt. A: Pure Appl. Opt. **10**, 064013 (2008).

[15] X. Jiang, Y. Zhang, S. Feng, K. C. Huang, Y. Yi, and J. D. Joannopoulos, Appl. Phys. Lett. **86**, 201110 (2005).

[16] G. Gumbs, G. S. Dubey, A. Salman, B. S. Mahmoud, and D. Huang, Phys. Rev. B **52**, 210 (1995).

[17] F. Iglói, L. Turban, and H. Rieger, Phys. Rev. E **59**, 1465 (1999).

[18] P. Stevens, Patterns in Nature (Little, Brown and Co., New York, 1974).

[19] M. Naylor, Mathematics Magazine **75**, 163 (2002).

[20] M. E. Pollard and G. J. Parker, Opt. Lett. **34**, 2805-2807 (2009).

[21] J. Trevino, H. Cao, and L. D. Negro, Nano Lett. **11**, 2008-2016 (2010).

[22] C. Jin, X. Meng, B. Cheng, Z. Li, and D. Zhang, Phys. Rev. B **63**, 195107 (2001).

[23] H. Miyazaki, M. Hase, H.T. Miyazaki, Y. Kurokawa, and N. Shinya, Phys. Rev. B **67**, 235109 (2003).

[24] K. Edagawa, S. Kanoko, and M. Notomi, Phys. Rev. Lett. **100**, 013901 (2008).

[25] C. Rockstuhl and F. Lederer, Phys. Rev. B **79**, 132202 (2009).

[26] M. Florescu, S. Torquato, and P. Steinhardt, Proc. Nat. Acad. Sci. Am. **106**, 20658 (2009).

[27] S. Imagawa, K. Edagawa, K. Morita, T. Niino, Y. Kagawa, and M. Notomi, Phys. Rev. B **82**, 115116 (2010).

[28] M. Rechtsman, A. Szameit, F. Dreisow, M. Heinrich, R. Keil, S. Nolte, and M. Segev, Phys. Rev. Lett. **106**, 193904 (2011).

[29] J.-K. Yang, C. F. Schreck, H. Noh, S. F. Liew, M. I. Guy, C. S. O'Hern, and H. Cao, Phys. Rev. A **82**, 053838 (2010).

[30] S. F. Liew, J.-K. Yang, H. Noh, C. F. Schreck, E. R. Dufresne, C. S. O'Hern, and H. Cao, Phys. Rev. A **84**, 063818 (2011).

[31] R. O. Prum , R. H. Torres , S. Williamson , J. Dyck , Nature **396**, 28 (1998).

[32] E. R. Dufresne, H. Noh, V. Saranathan, S. G. J. Mochrie, H. Cao, and R. O. Prum, Soft Matter **5**, 1792 (2009).

[33] B. Q. Dong, X. H. Liu, T. R. Zhan, L. P. Jiang, H. W. Yin, F. Liu, and J. Zi, Opt. Express **18**, 14430 (2010).

[34] H. Noh, S. F. Liew, V. Saranathan, R. O. Prum, S. G. J. Mochrie, E. R. Dufresne, and H. Cao, Adv. Mater. **22**, 2871 **2010**.

[35] J. D. Forster, H. Noh, S. F. Liew , V. Saranathan , C. F. Schreck, L. Yang, J.-G. Park, R. O. Prum, S. G. J. Mochrie , C. S. O'Hern , H. Cao, and E. R. Dufresne, Adv. Mater. **22**, 2939–2944 (2010).

[36] V. Saranathan, et al., J. R. Soc. Interface **9**, 2563 (2012).

[37] M. H.- Ur-Rashid, A. B. Imran, T. Seki, M. Ishii, H. Nakamura, and Y. Takeoka, Chemphyschem **11**, 579 (2010).

[38] Y. Takeoka, M. Honda, T. Seki, M. Ishii, and H. Nakamura, ACS Appl. Mater. & Interfaces **1**, 982 (2009).

[39] K. Ueno, A. Inaba, Y. Sano, M. Kondoh, and M. Watanabe, Chem. Commun., 3603 (2009).

[40] I. Lee, D. Kim, J. Kal, H. Baek, D. Kwak, D. Go, E. Kim, C. Kang, J. Chung, Y. Jang, S. Ji, J. Joo, and Y. Kang, Adv. Mater. **22**, 4973 (2010).

[41] B. L. Altshuler, A. P. Lee, and R. A. Webb, Mesoscopic phenomena in solids (North Holland, Amsterdam, 1991).

[42] F. Scheffold and G. Maret, Phys. Rev. Lett. **81**, 5800 (1998).

[43] E. Akkermans and G. Montambaux, Mesoscopic Physics of Electrons and Photons (Cambridge University Press, 2007).

[44] A. Lagendijk, B. van Tiggelen, and D. S. Wiersma, Phys. Today **62**, 24 (2009).

[45] I. Freund, Physica A **168**, 49 (1990).

[46] I. M. Vellekoop, A. Lagendijk, and A. P. Mosk, Nat. Photon. **4**, 320 (2010).

[47] Y. Guan, O. Katz, E. Small, J. Zhou, and Y. Silberberg, Opt. Lett. **37**, 4663 (2012).

[48] E. Small, O. Katz, Y. Guan, and Y. Silberberg, Opt. Lett. **37**, 3429 (2012)

[49] M. D. Shawkey, N. I. Morehouse, P. and Vukusic, J. R. Soc. Interface **6**, S221-231 (2009).

[50] S. Kinoshita, S. Yoshioka, and J. Miyazaki, Rep Prog Phys **71**, 1-30 (2008).

[51] R. W. James, The Optical Principles of the Diffraction of X-rays (G. Bell & Sons, London, 1954).

[52] S. Fraden and G. Maret, Phys. Rev. Lett. **65**, 512 (1990).

[53] H. C. van de Hulst, Light Scattering by Small Particles (Dover, New York, 1981).

[54] L. F. Rojas-Ochoa, J. M. Mendez-Alcaraz, J. J. Sáenz, P. Schurtenberger, and F. Scheffold, Phys. Rev. Lett. **93**, 073903 (2004).

[55] X. T. Peng and A. D. Dinsmore, Phys. Rev. Lett. **99**, 143902 (2007).

[56] D. J. Thouless, Phys. Rev. Lett. **39**, 1167 (1977).

[57] S. John, Phys. Rev. Lett. **53**, 2169 (1984).

[58] P. W. Anderson, Philos. Mag. B **52**, 505 (1985).

[59] P. W. Anderson, Phys. Rev. **109**, 1492 (1958).

[60] E. Abrahams, P. W. Anderson, D. C. Licciardello, and T. V. Ramakrishnan, Phys. Rev. Lett. **42**, 673 (1979).

[61] A. F. Ioffe and A. R. Regel, Prog. Semicond. **4**, 237 (1960).

[62] D. E. Khmelnitskii, Physica (Amsterdam) **1268+C**, 235 (1984)

[63] Y, Kuga and A. Ishimaru, J. Opt. Soc. Am. A **8**, 831 (1984).

[64] M. P. van Albada, and A. Lagendijk, Phys. Rev. Lett. **55**, 2692 (1985)

[65] P. E. Wolf and G. Maret, Phys. Rev. Lett. **55**, 2696 (1985).

[66] E. Akkermans, P. E. Wolf, and R. Maynard, Phys. Rev. Lett. **56**, 1471 (1986).

[67] O. N. Dorokhov, Solid State Commun. **44**, 915 (1982).

[68] O. N. Dorokhov, Solid State Commun. **51**, 381 (1984).

[69] P. A. Mello, P. Pereyra, and N. Kumar, Annals of Physics **181**, 290 (1988).

[70] Y. V. Nazarov, Phys. Rev. Lett. **73**, 134 (1994).

[71] I. M. Vellekoop and A. P. Mosk, Phys. Rev. Lett. **101**, 120601 (2008).

[72] J. B. Pendry, Physics **1**, 20 (2008).

[73] W. Choi, A. P. Mosk, Q. H. Park, and W. Choi, Phys. Rev. B **83**, 134207 (2011).

[74] W. Choi, Q. H. Park, and W. Choi, Opt. Express **20**, 20721 (2012).

[75] Z. Shi and A. Z. Genack, Phys. Rev. Lett. **108**, 043901 (2012).

[76] M. Kim, Y. Choi, C. Yoon, W. Choi, J. Kim, Q. Park, and W. Choi, Nat. Photon. **6**, 581 (2012).

[77] M. Davy, Z. Shi, J. Wang, and A. Z. Genack, Opt. Express **21**, 10367 (2013).

[78] S. M. Popoff, A. Goetschy, S. F. Liew, A. D. Stone, and H. Cao, Phys. Rev. Lett. **112**, 133903 (2014).

[79] I. M. Vellekoop and A. P. Mosk, Opt. Lett. **32**, 2309 (2007).

[80] Z. Yaqoob, D. Psaltis, M. S. Feld, and C. Yang, Nat. Photon. **2**, 110 (2008).

[81] S. M. Popoff, G. Lerosey, R. Carminati, M. Fink, A. C. Boccara, and S. Gigan, Phys. Rev. Lett. **104**, 100601 (2010).

[82] S. Popoff, G. Lerosey, M. Fink, A. C. Boccara, and S. Gigan , Nat. Commun. **1**, 81 (2010).

[83] W. L. Vos, T. W. Tukker, A. P. Mosk, A. Lagendijk, and W. L. IJzerman, Appl. Opt. **52**, 2602 (2013).

[84] Y. D. Chong, L. Ge, H. Cao, and A. D. Stone, Phys. Rev. Lett. **105**, 053901 (2010).

[85] W. Wan, Y. D. Chong, L. Ge, H. Noh, A. D. Stone, and H. Cao, Science **331**, 889 (2011).

[86] Y. D. Chong and A. D. Stone, Phys. Rev. Lett. **107**, 163901 (2011).

[87] M. Leonetti and C. Lpez, Appl. Phys. Lett. **102**, 071105 (2013).

[88] N. Bachelard, J. Andreasen, S. Gigan, and P. Sebbah, Phys. Rev. Lett. **109**, 033903 (2012).

[89] N. Bachelard, S. Gigan, X. Noblin, and P. Sebbah, Nat. Phys. Advance online publication, doi:10.1038/nphys2939 (2014).

[90] T. Hisch, M. Liertzer, D. Pogany, F. Mintert, and S. Rotter, Phys. Rev. Lett. **111**, 023902 (2013).

[91] K. Iga, IEEE J. of Selected Topics in Quan. Elec. **6**, 1201 (2000).

[92] S. L. McCall, A. F. J. Levi, R. E. Slusher, S. J. Pearton, and R. A. Logan, Appl. Phys. Lett. **60**, 289 (1992).

[93] S. F. Pereira, M. B. Willemsen, M. P. van Exter, and J. P. Woerdman, Appl. Phys. Lett. **73**, 2239 (1998).

[94] Y. F. Chen and Y. P. Lan, J. Opt. B **3**, 146 (2001)

[95] Y. F. Chen, Y. P. Lan, and S. C. Wang, Appl. Phys. B **72**, 167 (2001).

[96] J.-F. Bisson, A. Shirakawa, Y. Sato, Y. Senatsky, and K.-I. Ueda, Opt. Rev. **11**, 353 (2004).

[97] D. Naidoo, T. Godin, M. Fromager, E. Cagniot, N. Passilly, A. Forbes, and K. At-Ameur, Opt. Commun. **284**, 5475 (2011).

[98] N. B. Rex, R. K. Chang, and L. J. Guido, IEEE Photon. Technol. Lett. **13**, 1 (2001).

[99] G. D. Chern, H. E. Tureci, A. D. Stone, R. K. Chang, M. Kneissl, and N. M. Johnson, Appl. Phys. Lett. **83**, 1710 (2003).

[100] T. Fukushima, T. Harayama, P. Davis, P. O. Vaccaro, T. Nishimura, and T. Aida, Opt. Lett. **27**, 1430 (2002).

[101] M. Kneissl, M. Teepe, N. Miyashita, N. M. Johnson, G. D. Chern, and R. K. Chang, Appl. Phys. Lett. **84**, 2485 (2004).

[102] S. Shinohara, T. Harayama, T. Fukushima, M. Hentschel, T. Sasaki, and E. E. Narimanov, Phys. Rev. Lett. **104**, 163902 (2010).

[103] T. Fukushima and T. Harayama, IEEE J. Sel. Top. Quantum Electron. **10**, 1039 (2004).

Chapter 2

Effect of correlated and uncorrelated disorder on 1D photonic structures

2.1 Introduction

[1] Since its invention twenty years ago [2, 3], photonic crystal has attracted much attention for the promise of full control of light propagation and localization [4–6]. Rapid developments in nanotechnology have made the fabrication of photonic crystals operating at optical frequency possible. However, structural disorder that is introduced unintentionally during the fabrication process limits the widespread application of photonic crystal [7]. The performance of two-dimensional (2D) photonic crystal waveguides for slow light application is degraded by scattering loss from the fabrication disorder [8–10]. The omnidirectional photonic band gap (PBG), which allows ultimate control of spontaneous emission of atoms, is fragile to the non-uniformity in three-dimensional (3D) inverted opal structures [11, 12]. Hence, a thorough under-

1. This chapter is primarily based on the work published in ref. [1].

standing of the effects of structural disorder is essential to improve photonic crystal devices.

Recently, there have been many experimental and theoretical studies on how disorder influences light propagation and localization in one-dimensional (1D) [13–16], 2D [17–19] and 3D photonic crystals [20–26]. The types of disorder depend on the fabrication processes. The "top-down" approach including lithography and etching has been widely used in fabrication of 2D photonic crystals. The typical disorder is random variation in size and shape of building blocks, and the randomness is usually uncorrelated. The "bottom-up" approach such as self-assembly introduces randomness in both position and size of building blocks. The positions of neighboring building blocks are often correlated in the closely-packed structures. Most theoretical studies on disorder in photonic crystals are focused on uncorrelated disorder. Recently it has been shown that correlation of disorder may result in strong anomalies of light localization [27–30]. The difference between correlated and uncorrelated disorder is not well understood, except in metallic photonic crystal slabs [31].

In this chapter, we introduce both correlated randomness and uncorrelated randomness in position and size of building blocks, and study how they modify light transmission, localization length, density of photonic states, and decay rate of resonant modes in 1D dielectric photonic crystals. The results highlight the different effects that correlated disorder and uncorrelated disorder have on photonic crystals. The photonic band gaps are more robust against uncorrelated disorder due to preservation of long-range structural order. The dips in the spectra of transmission and density of photonic states that correspond to PBGs become narrower in the presence of uncorrelated disorder, but wider in the case of correlated disorder. Correlation of disorder enhances light localization near the band edges, while uncorrelated disorder causes a divergence of localization length near the gap edges. The resonant modes near the pass band center experience the strongest fluctuation of decay rates in the

presence of uncorrelated disorder. In contrast, the correlated disorder induces a larger fluctuation of decay rates for the band gap modes than the pass band modes.

2.2 Correlation of disorder

Our structures consist of N dielectric layers separated by air gaps. In the absence of disorder, the period of 1D photonic crystal is a. The position of the m-th dielectric layer is $x_m = ma$. The thickness of each dielectric layer is d. Randomness is introduced to either position or thickness of dielectric layers. In the case of position disorder, the position of each dielectric layer is perturbed while its thickness remains constant. If every dielectric layer is shifted randomly from its position in the periodic system, the positions of neighboring dielectric layers are uncorrelated [Fig. 2.1(a)]. The position of the m-th dielectric layer is $x_m = ma + \delta x_m$, where δx_m is a random number distributed uniformly between $-\Delta a$ and Δa, and Δ represents the degree of disorder. Alternatively, the positions of neighboring dielectric layers can be correlated by introducing randomness to their spacings [Fig. 2.1(b)]. Namely, $x_m = x_{m-1} + a + \delta x_m$. Thus x_m includes all position variations of the preceding layers, $x_m = ma + \sum_{j=1}^{m} \delta x_j$.

In the case of size disorder, the thickness of dielectric layers is varied, while their positions do not change. If the thickness of each dielectric layer is varied independently from d, the size disorder is uncorrelated [Fig. 2.1(c)]. The thickness of m^{th} dielectric layer is given by $d_m = d + \delta d_m$, where δd_m is a random number distributed uniformly between $-\Delta d$ and Δd. The size disorder becomes correlated if the thickness of the m-th dielectric layer is fluctuated around that of the $m-1$-th layer, $d_m = d_{m-1} + \delta d_m = d + \sum_{j=1}^{m} \delta d_j$ [Fig. 2.1(d)].

For structural characterization of the disordered photonic crystals, we computed

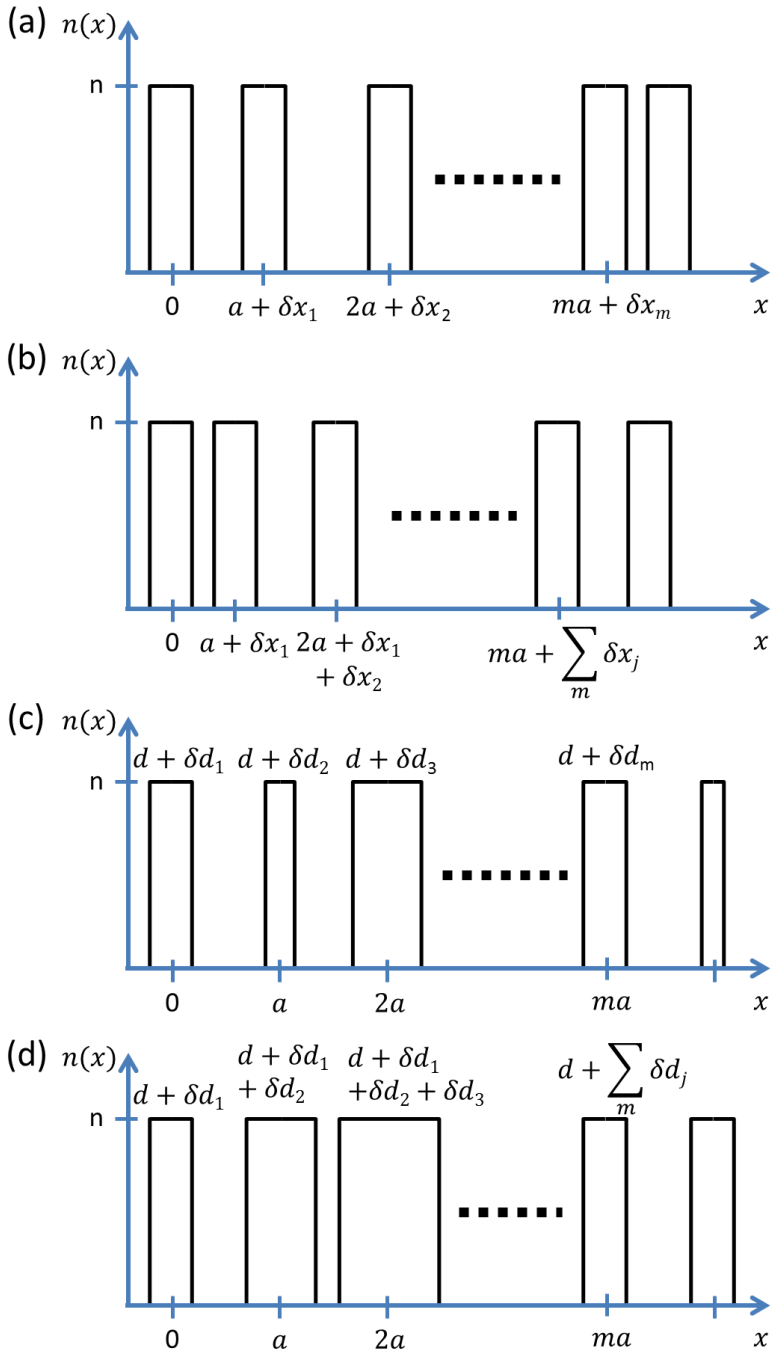

Figure 2.1: 1D photonic structure with (a) uncorrelated and (b) correlated position disorder. (c,d) Structure with (c) uncorrelated and (d) correlated size disorder.

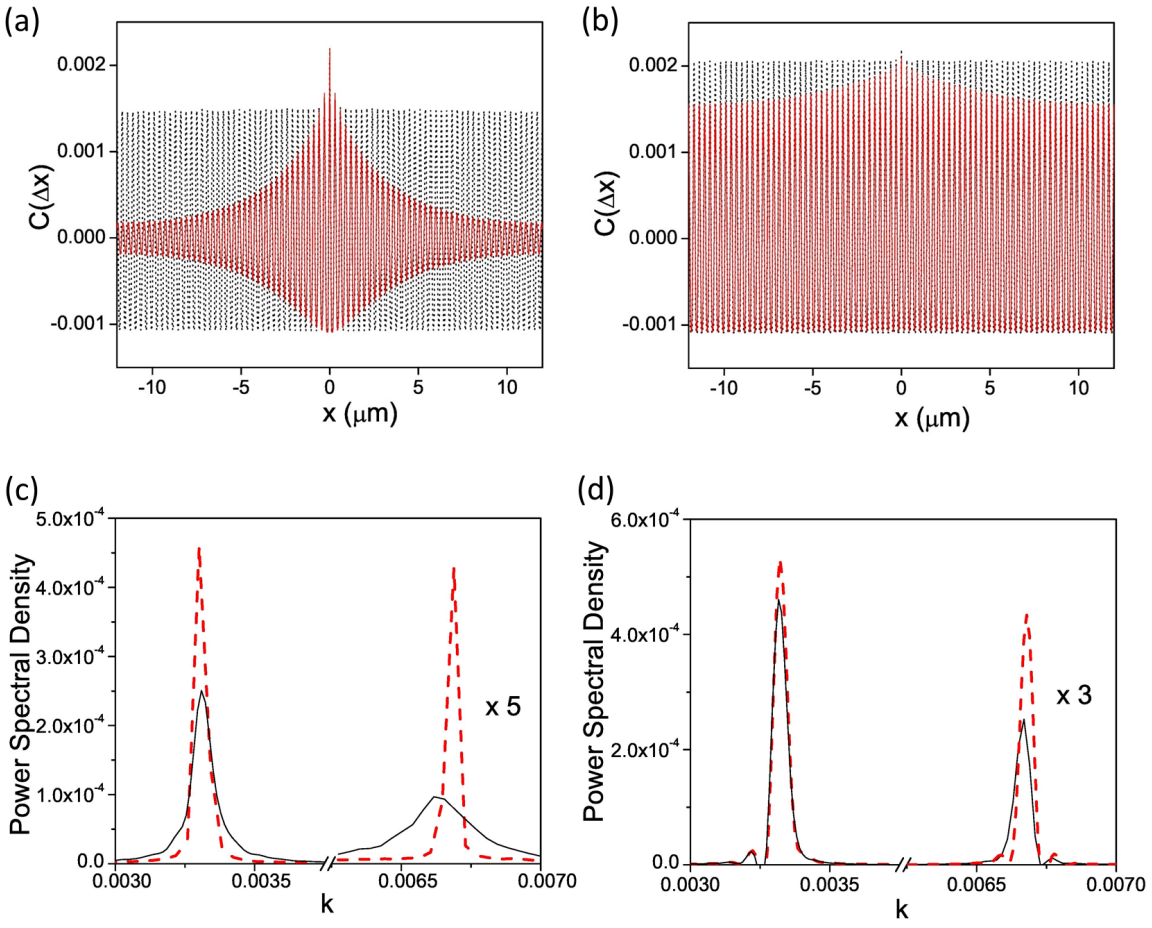

Figure 2.2: Spatial correlation functions $C(\Delta x)$ and Fourier spectrum for 1D photonic crystals with position disorder (a),(c) or size disorder (b),(d). The solid curves represent correlated disorder, the dashed curves uncorrelated disorder. The degree of disorder $\Delta = 0.1$. Note that the second peaks in spatial Fourier spectra are magnified.

correlation functions and spatial Fourier spectra. The spatial correlation function is $C(\Delta x) \equiv \langle \delta n(x) \delta n(x + \Delta x) \rangle$, where $\delta n(x) = n(x)/\bar{n} - 1$, $n(x)$ is the refractive index at position x, and $\bar{n}$ is the average refractive index for one configuration, and $\langle ... \rangle$ represents averaging over many configurations with the same degree of disorder Δ. Fig. 2.2(a) and (b) show the correlation functions for position disorder and size disorder. In the case of uncorrelated disorder, $C(\Delta x)$ is independent of Δx as long as $\Delta x \neq 0$. Hence, the structure has a long-range order. With increasing disorder Δ, the value of $C(\Delta x)$ decreases, indicating the structural correlation is reduced by disorder. In the case of correlated disorder, $C(\Delta x)$ decays with increasing distance Δx. Thus the structural correlation or order is short-ranged. For the same value of Δ, the structural correlation in the presence of size disorder is larger than that of position disorder. This suggests the position disorder reduces structural correlation more dramatically.

Fourier transform of $n(x)$ gives the spatial Fourier spectrum[Fig. 2.2(c) and (d)]. The peaks in Fourier spectra correspond to the spatial periods of structures. The peak height reflects the strength of spatial periodicity, and the peak width is inversely proportional to the dimension of ordered regions. In the case of uncorrelated disorder, we find the Fourier peak height decreases as Δ increases while the peak width remains nearly constant. This behavior reflects long-range order of the structure. In the case of correlated disorder, the peak height decreases more quickly and the peak width increases with Δ. The peak broadening indicates the ordered regions shrink in size, and the structural order becomes short-ranged.

2.3 Transmission and localization length

We used the transfer matrix method to calculate the transmission spectra of 1D disordered photonic crystals. The parameters in the numerical simulations are $n = 1.05$, $N = 81$, $a = 300$nm, and $d = 100$nm. Scattering is weak due to small refractive index contrast. For each type of disorder, the transmission spectra are obtained by averaging over $10^3 - 10^4$ configurations with the same degree of disorder. We focus on the transmission dip that corresponds to the fundamental PBG, and investigate how disorder changes the gap width and depth. D is the depth of transmission dip normalized to that in the absence of disorder [inset of Fig. 2.3(a)], and W the full width at half minimum (FWHM) of the transmission dip normalized to that without disorder [inset of Fig. 2.3(b)].

With the introduction of disorder, the transmission dip becomes shallower. For both position disorder and size disorder, the reduction of D is larger if the disorder is correlated. Figure 2.3(a) shows that the correlated disorder causes a rapid drop of D even when $\Delta < 0.3$. However, once Δ exceeds 0.3, the falling of D slows down. The uncorrelated disorder leads to a different behavior, D decreases slowly at smaller Δ then faster at larger Δ.

Figure 2.3(b) shows that the gap width W evolves in the opposite way between the correlated disorder and uncorrelated disorder. For both position and size disorder, the correlated disorder makes the gap wider, while the uncorrelated disorder makes it narrower. The position disorder causes a larger change of W than the size disorder for the same Δ. We attribute the larger effect of position disorder to the relatively small refractive index contrast in our structures. For larger n, the trend may be different [11].

We also calculated the variation of transmission T with structure length L. In the case of correlated disorder, T decreases with increasing L both inside and outside the PBG. Figure 2.4(a) shows the transmission spectra for various lengths L of struc-

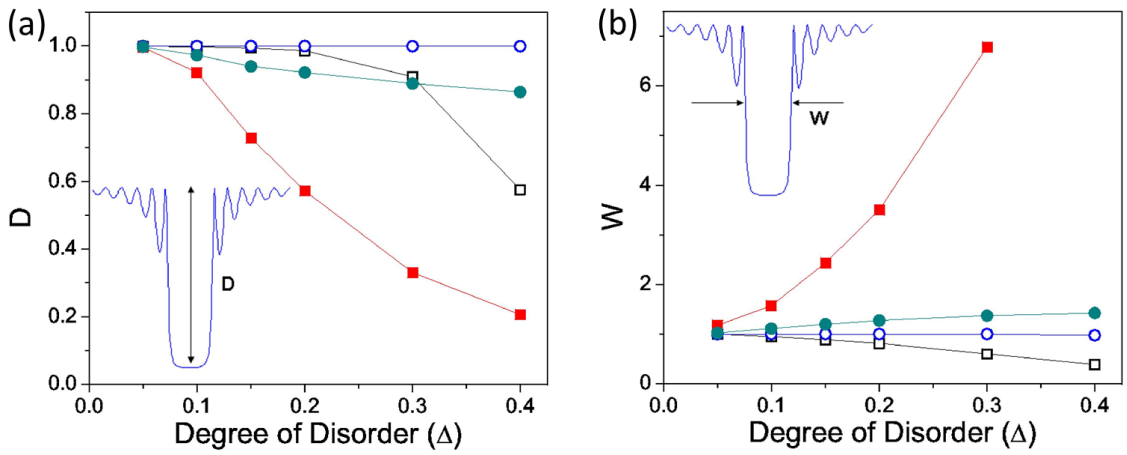

Figure 2.3: Depth D (a) and width W (b) of the transmission dip as a function of degree of disorder Δ. Squares and circles represent position disorder and size disorder, respectively. Solid symbols are for correlated disorder and open symbols for uncorrelated disorder.

tures with a fixed degree of correlated position disorder, $\Delta = 0.3$. The frequency ω is normalized to the center frequency ω_0 of the fundamental PBG. From the decay of T with L, we obtained the localization length, $\xi = -L/\langle \ln T \rangle$ [32]. Figure 2.5(a) is a plot of ξ versus ω/ω_0 for several values of Δ. The vertical lines mark the edges of the fundamental PBG. With increasing disorder, ξ increases inside the gap and decreases in the pass bands. Near the band edges, ξ first decreases then increases with Δ. Therefore, correlated disorder weakens the interference effect that suppresses light transmission in the gap of a periodic structure, leading to an increase of transmission. In the pass bands, the effect of disorder is opposite, it enhances light localization and reduces transmission. Near the band edge, a small degree of disorder improves localization but large disorder suppresses it.

The dependence of T on L is quite different in the case of uncorrelated disorder. Figure 2.4(b) is a log-linear plot of T versus ω/ω_0 for different lengths L of structures with a fixed degree of uncorrelated position disorder $\Delta = 0.3$. Unlike the case of correlated disorder where the shape of transmission spectra remains qualitatively the

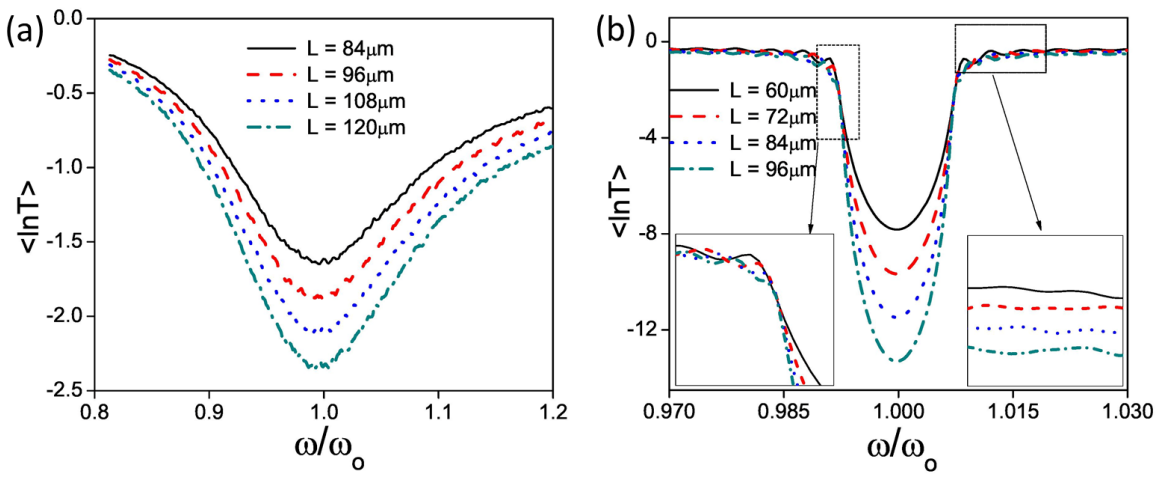

Figure 2.4: $\ln T$ versus ω/ω_0 for several lengths L of structures with a fixed degree of position disorder $\Delta = 0.3$. The randomness is correlated in (a) and uncorrelated in (b).

[htbp]

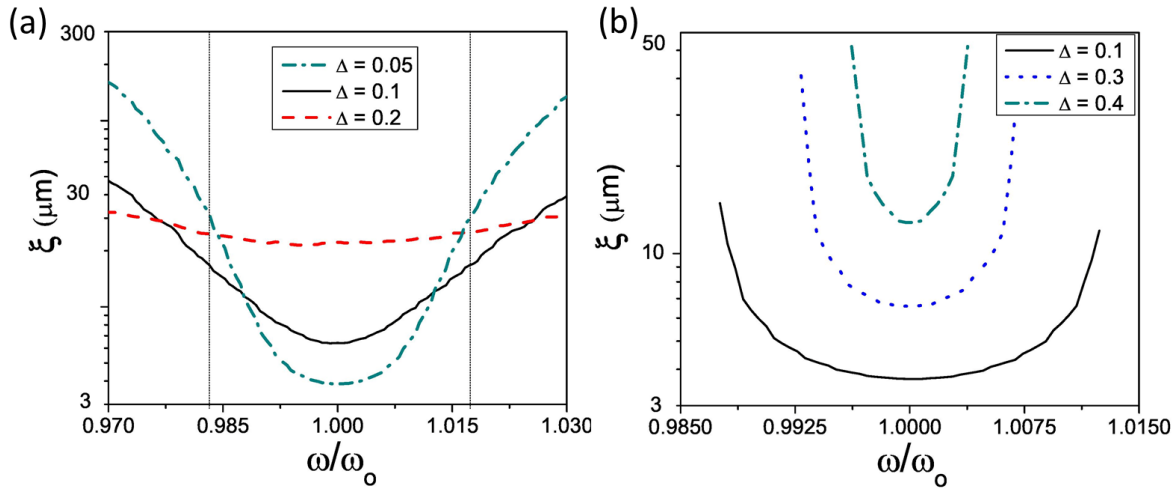

Figure 2.5: Localization length ξ as a function of normalized frequency ω/ω_0. The position disorder is correlated in (a) and uncorrelated in (b).

same with increasing L, the uncorrelated disorder modifies the shape of transmission spectra. The edges of transmission dip become much sharper at larger L. In the presence of long-range order, the interference effect becomes stronger in the larger system, making the transmission dip steeper. Near the gap center T decreases quickly with increasing L. The decrement slows down as the frequency moves away from the gap center. Close to the edges of PBG the transmission curves for different L cross [left inset of Fig. 2.4(b)]. Around the crossing points, T changes little with L. Beyond the crossing points, T oscillates with frequency. Farther away from the crossing points, the oscillation dies out, and T again decreases with increasing L [right inset of Fig. 2.4(b)]. The crossing points move towards the gap center with increasing Δ. Figure 2.5(b) shows the localization length ξ within the PBG. ξ increases with Δ, similar to the case of correlated disorder. The major difference is that ξ rises rapidly as ω moves towards the gap edges and diverges at the crossing points. This result reflects the underlying long-range order.

2.4 Density of Photonic States

Next, we studied the effects of disorder on the density of photonic states $\rho(\omega)$. We follow the definition for density of states in a 1D finite-length structure in reference [33] and obtain $\rho(\omega)$ from the complex transmission coefficient $t = \sqrt{T}\exp(i\phi)$ [33, 34]. The effective wavevector is $k_{eff} = \phi/L$, where ϕ is the total phase accumulated by the light propagates through the structure and L is the total length of the finite structure. It gives $\rho(\omega) = dk_{eff}/d\omega$. $\rho(\omega)$ is normalized by the density of states (DOS) for a homogeneous medium with an effective group velocity $v^{eff} = c[f/n + (1-f)]$, where f is the filling fraction of the dielectric material with refractive index n [33].

In a periodic structure, the DOS is depleted within the PBG, and peaked near

the band edges. Disorder creates defect states inside the gap. $\rho(\omega)$ is obtained by ensemble average over $10^3 - 10^4$ configures with the same type and degree of disorder. Figure 2.6(a) shows the normalized $\rho(\omega)$ for various degree of uncorrelated position disorder. ω is normalized to ω_0. With increasing Δ, the depletion of DOS inside the PBG is diminished. Outside the PBG, the high peaks of DOS at the band edges are reduced, and at large disorder the normalized $\rho(\omega)$ approaches unity. Since $\rho(\omega)$ never reaches below one outside the PBG, the DOS dip gets narrower at larger Δ. The correlated disorder has more dramatic effect on DOS. As shown in Fig. 2.6(b), the DOS gap is quickly filled by defect states, and the large peaks at the band edges diminish rapidly while being broadened. At certain Δ, the normalized $\rho(\omega)$ is reduced to below unity outside the PBG, resulting in a broadening of the DOS gap. Eventually at large disorder, the DOS dip disappears and the normalized $\rho(\omega)$ becomes unity at all frequencies.

Figure 2.7(a) plots the normalized DOS at the frequency ω_1 of the PBG center

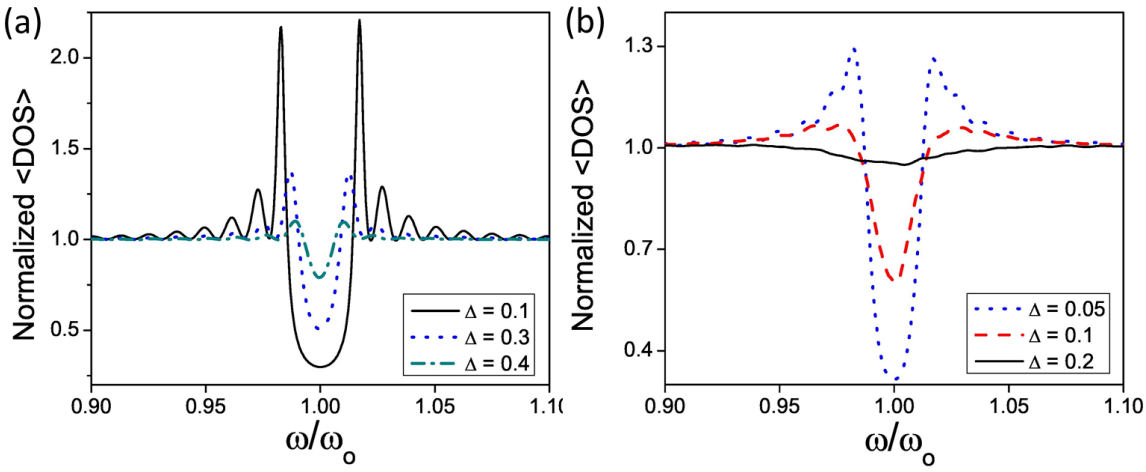

Figure 2.6: Normalized density of States (DOS) $\rho(\omega)$ versus ω/ω_0 in 1D structures with various degree Δ of uncorrelated position disorder (a) and correlated position disorder (b).

and the frequency ω_2 of the largest DOS peak at the band edge versus the degree of position disorder. The correlated disorder causes a much faster rise of $\rho(\omega_1)$ with Δ.

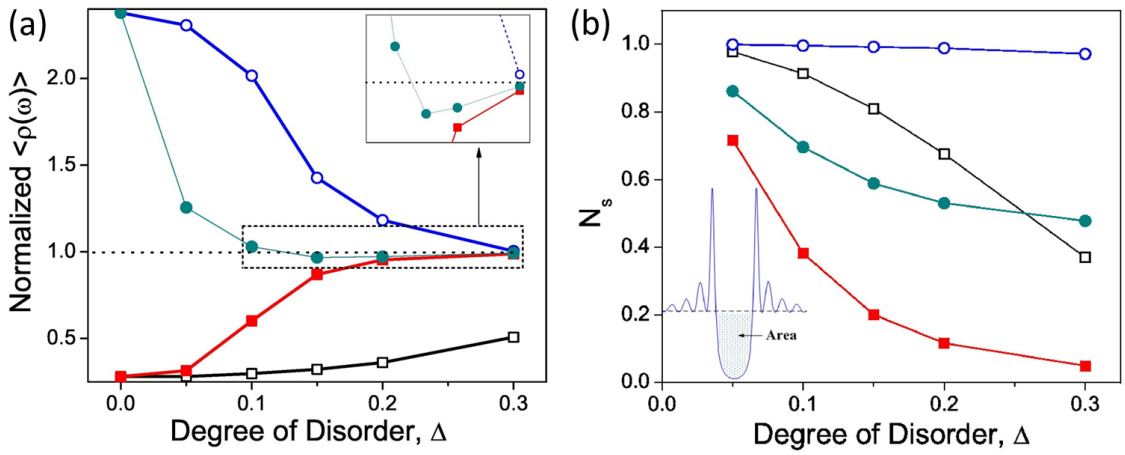

Figure 2.7: (a) Normalized $\rho(\omega)$ as a function of degree Δ of correlated position disorder (solid symbols) and uncorrelated position disorder (open symbols) at the frequency ω_1 of the PBG center (squares) and the frequency ω_2 of the largest DOS peak at the band edge (circles). (b) Total number of depleted states N_s as a function of Δ (symbols notation is the same with Figure 2).

$\rho(\omega_2)$ first decreases then increases with Δ for the correlated disorder, while it decreases monotonically with increasing Δ in the case of uncorrelated disorder. Similar behaviors are observed for the size disorder.

For a quantitative description of depletion of photonic states, we computed the area of DOS dip [inset of Fig. 2.7(b)] to obtain the total number of depleted states N_s. Figure 2.7(b) is a plot of N_s, normalized by its value in the absence of disorder, as a function of Δ. With increasing disorder, more defect states appear in the gap and N_s is reduced. For both correlated position and size disorder, N_s decreases first rapidly with increasing Δ, then gradually at large Δ. The trend is opposite for uncorrelated position and size disorder. N_s decreases slowly at smaller Δ. Once Δ exceeds a critical value, N_s drops quickly. Hence, the PBG is more robust against small uncorrelated disorder. This is attributed to the preservation of long-range order.

2.5 Decay rates of resonant modes

Finally we investigated the modification of resonant modes by disorder. γ is the imaginary part of eigenfrequency that is calculated with the outgoing boundary condition [35]. In a finite-sized periodic structure, the modes at the band edges have the lowest decay rates. γ increases as the frequency moves towards the pass band center. Structural disorder perturbs both the frequency and decay rate of resonant modes. Their values fluctuate from one configuration to another. We ensemble-averaged the decay rates of modes within a small frequency window, $\Delta\omega_n = (\omega_{n+1}+\omega_n)/2-(\omega_n+\omega_{n-1})/2$, centered at each mode of frequency ω_n in the periodic structure. Every data point in Fig. 2.8(a) and (b) represents the decay rate $\bar{\gamma}$ averaged over $10^3 - 10^4$ configurations with the same degree of position disorder. In the pass bands the modes with frequencies around the band center have reduced $\bar{\gamma}$ with increasing Δ, while the modes near the band edges have higher $\bar{\gamma}$ at larger disorder. The defect modes appear inside the PBG, and they have lower $\bar{\gamma}$ than the modes outside the gap. At large disorder, the decay rate is nearly constant for all modes as the PBG disappears. The trends are similar for correlated disorder and uncorrelated disorder, though the latter modifies the decay rates more than the former. Similar results are obtained for the size disorder.

To quantify the decay rate fluctuation, we computed the variance of γ, $var(\gamma) = \langle(\gamma/\bar{\gamma} - 1)^2\rangle$, where $\langle ...\rangle$ represents the ensemble average over modes within the small frequency window $\Delta\omega_n$. Figure 2.9(a) and (b) show the variance of decay rates for correlated and uncorrelated position disorder.

In the case of uncorrelated disorder, the modes close to the pass band centers have large $var(\gamma)$. To explain the large fluctuation of decay rates, we plot in Fig. 2.10(a) the frequency and decay rate of all modes in 50 configurations with the same degree of uncorrelated position disorder $\Delta = 0.1$. It is evident that deep in the pass bands there are some very leaky modes, leading to large fluctuation of γ.

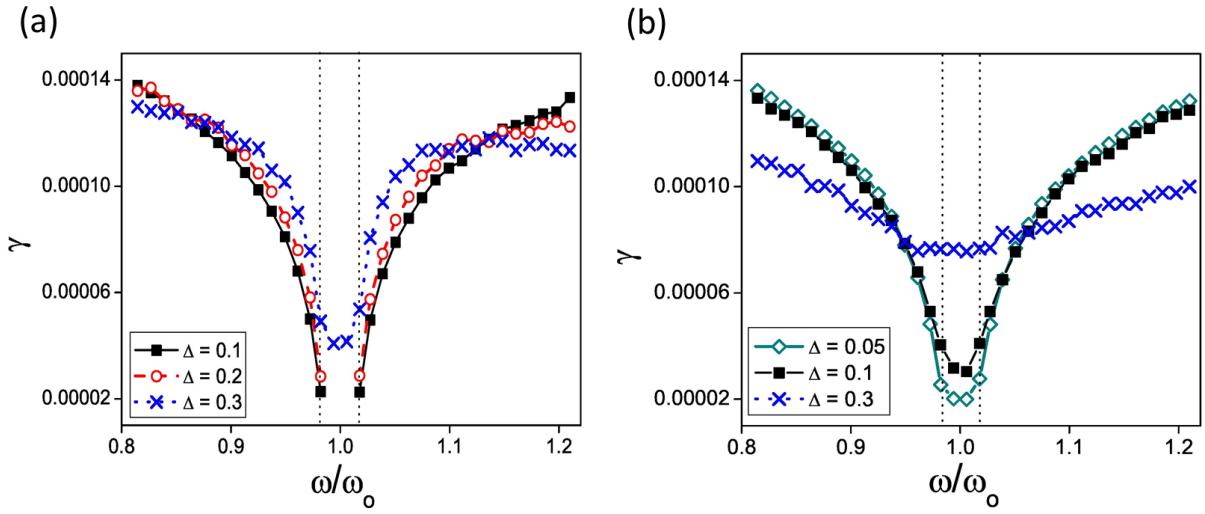

Figure 2.8: (a) Average decay rate of resonant modes in 1D structure with different degree Δ of uncorrelated position disorder (a) and correlated position disorder (b).

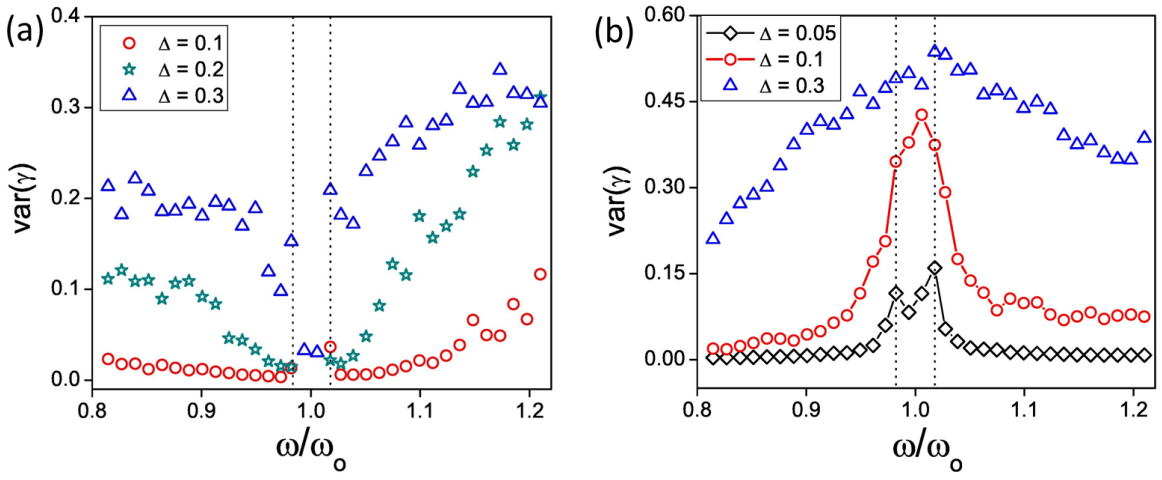

Figure 2.9: (a) Variance of decay rate of resonant modes in 1D structure with different degree Δ of uncorrelated position disorder (a) and correlated position disorder (b).

Figure 2.10(b) shows the spatial distribution of electric field intensity for one of such leaky modes. The mode is concentrated near one boundary of the system, leading to significant leakage of light from the boundary. It resembles the doorway state in an open cavity [36]. Hence, the decay rates of the majority of modes near the pass band center are reduced by disorder, resulting in an decrease of $\bar{\gamma}$. However, a few of them acquires extremely large decay rates, leading to an increase of $var(\gamma)$. Such "doorway states" are mostly likely to be formed at frequency close to the pass band center where the interference effect resulting from the structural periodicity is the weakest. As the frequency moves away from the pass band center, the interference effect becomes stronger due to the existence of long-range order. It is more difficult for the "doorway states" to be formed by uncorrelated disorder, causing a decrease of $var(\gamma)$. Near the band edges $var(\gamma)$ rises again, indicating the band edge modes are very sensitive to disorder. This is because the band edge modes are formed via strong interference of multiply reflected light, and a small perturbation of structure can induce a large modification.

In the systems with correlated disorder, the very leaky modes can also be found

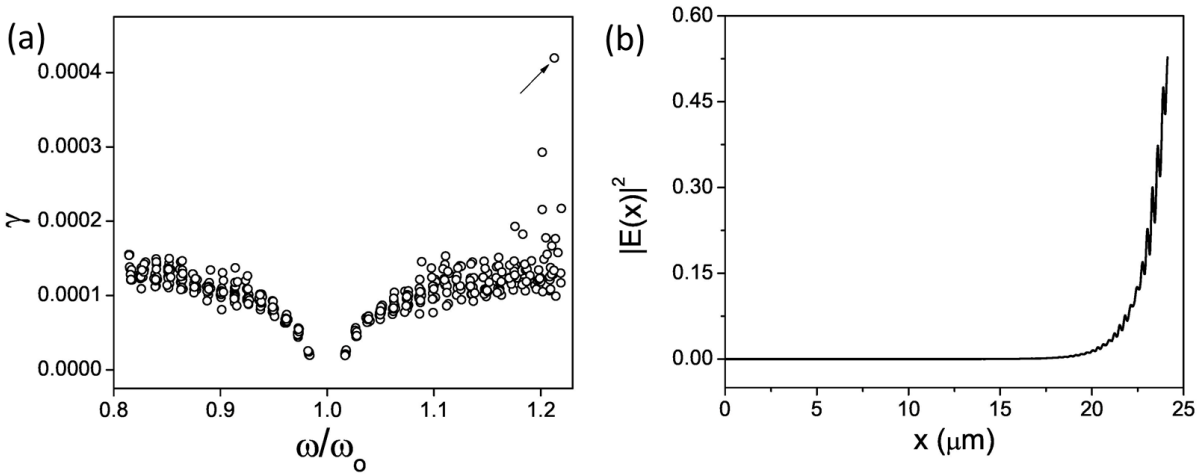

Figure 2.10: (a) Normalized frequency ω/ω_0 and decay rate γ of all modes in 50 configurations with the same degree of uncorrelated position disorder $\Delta = 0.1$. (b) Spatial distribution of electric field intensity for one leaky mode marked by an arrow in (a).

near the pass band centers, leading to similar values of $var(\gamma)$ as the case of uncorrelated disorder. However, $var(\gamma)$ does not decrease as the frequency moves towards the band edges. This is attributed to the lack of long-range order which is necessary to suppress the formation of very leaky modes. Near the band edges, $var(\gamma)$ increases and exhibits double peaks for small Δ. With increasing disorder, the double peaks move towards the gap center, and merge to a single peak at certain Δ. This behavior is consistent with the result in [15], and is related to the breakdown of single parameter scaling. Therefore, the correlated disorder causes larger fluctuation of γ for the band gap modes than the pass band modes, while the opposite is true for the uncorrelated disorder.

2.6 Conclusion

We introduce both correlated and uncorrelated randomness in position and thickness of dielectric layers in 1D periodic structures, investigate their effects on light transmission, localization length, density of photonic states, and decay rate of resonant modes. The systems with uncorrelated disorder maintain the long-range order, while the ones with correlated disorder have only short-range order. Our simulation results illustrate the differences between correlated disorder and uncorrelated disorder.

The correlated disorder diminishes the transmission dips that correspond to PBGs more quickly than the uncorrelated disorder. The robustness of PBGs against uncorrelated disorder is attributed to the preservation of long-range order of the structures. Another difference is that the uncorrelated disorder makes the transmission dips narrower while the uncorrelated disorder makes them wider than those in the perfectly ordered systems.

As the degree of structural disorder Δ increases, the localization length ξ increases

inside the PBG and decreases outside the PBG. Unlike the case of correlated disorder, ξ diverges near the gap edges in the case of uncorrelated disorder. This divergence is attributed to edge sharpening of the transmission dips by increasing system length.

Like the dips in the transmission spectra, the dips in the photonic density of states are narrowed by uncorrelated disorder and widened by correlated disorder. The total number N_s of depleted photonic states within a PBG falls rapidly at small degree Δ of correlated disorder, then slowly at large Δ. The trend is just opposite for the uncorrelated disorder, the drop of N_2 is gradual at small Δ, then accelerates at larger Δ.

The structural disorder not only produces defect states inside the PBG, but also reduces the decay rate of resonant modes in the pass bands. In the presence of uncorrelated disorder, the variance of decay rates is the highest near the pass band center due to the formation of very leaky modes. In contrast, the correlated disorder causes a larger fluctuation of decay rates for the band gap modes than the pass band modes.

We think that the general conclusions presented in this chapter can be extended to higher dimensions. However, cautions must be exerted because in 2D and 3D connected network structure can be formed which does not exist in 1D. It has been shown that a connected network can be more robust against disorder than a disconnected structure [37]. Therefore, further studies on 3D disordered structures consist of both cermet and network topologies are shown in the following chapter.

Bibliography

[1] S. F. Liew and H. Cao, J. Opt. **12**, 024011 (2010)

[2] E. Yablonovitch, Phys. Rev. Lett. **58**, 2059 (1987)

[3] S. John, Phys. Rev. Lett. **58**, 2486 (1987)

[4] C. Soukolis, Photonic Crystals and Light Localization in the 21st Century (Dordrecht: Kluwer Academic, 2001)

[5] J. D. Joannopoulos, S. G. Johnson, J. N. Winn and R. D. Meade, Photonic Crystals : Molding the Flow of Light (2nd Edition) (Princeton, NJ: Princeton University Press, 2008)

[6] S. Noda and T. Baba (eds), Roadmap on Photonic Crystals (New York: Kluwer Academic, 2003)

[7] A. F. Koenderink, A. Lagendijk and W. L. Vos, Phys. Rev. Lett. **72**, 153102 (2005)

[8] S. Hughes , L. Ramunno, J. F. Young and J. E. Sipe, Phys. Rev. Lett. **94**, 033903 (2005)

[9] L. O' Faolain, T. P. White, D. O' Brien, X. Yuan , M. D. Settle and T. F. Krauss, Opt. Express **15**, 13129 (2007)

[10] R. J. P. Engelen, D. Mori, T. Baba and L. Kuipers, Phys. Rev. Lett. **101**, 103901 (2008)

[11] Z. Y. Li, X. D. Zhang, and Z. Q. Zhang, Phys. Rev. B **61**, 15738 (2000)

[12] A. V. Lavrinenko, W. Wohlleben and R. J. Leyrer, Opt. Express **17**, 747 (2009)

[13] A. R. McGrun, K. T. Christensen and F. M. Mueller, Phys. Rev. B **47**, 13120 (1993)

[14] V. D. Freilikher, B. A. Liansky and I. V. Yurkevich, Phys. Rev. E **51**, 6301 (1995)

[15] L. I. Deych ,D. Zaslavsky and A. A. Lisyansky, Phys. Rev. Lett. **81**, 5390 (1998)

[16] S. H. Chang, H. Cao and S. T. Ho, IEEE Journal of Quantum Electronics **39**, 9197 (2003)

[17] A. A. Asatryan, P. A. Robinson, L. C. Botten, R. C. McPhedran, N. A. Nicorovici and C. M. Sterke, Phys. Rev. E **62**, 5711 (2000)

[18] W. R. Frei and H. T. Johnson, Phys. Rev. B **70**, 165116 (2004)

[19] M. A. Kaliteevski, D. M. Beggs, S. Brand, R. A. Abram, and V. V. Nikolaev, Phys. Rev. E **73**, 056616 (2006)

[20] Y. A. Vlasov, Kaliteevski M A, and V. V. Nikolaev, Phys. Rev. B **60**, 1555 (1999)

[21] V. N. Astratov V N, A. M. Adawi, S. Fricker, M. S. Skolnick, D. M. Whittaker, and P. N. Pusey, Phys. Rev. B **66**, 165215 (2002)

[22] R. Rengarajan, D. Mittleman, C. Rich, and V. Colvin, Phys. Rev. E **71**, 016615 (2005)

[23] A. Rodriguez, M. Ibanescu, J. D. Joannopoulos, and S. G. Johnson, Opt. Lett. **30**, 3192 (2005)

[24] E. Palacios-Lidon, B. H. Juarez, E. Castillo-Martinez, and C. Lopez, J. Appl. Phys. **97**, 063502 (2005)

[25] L. Braginsky and V. Shklover, Phys. Rev. B **73**, 085107 (2006)

[26] L. A. Dorado, R. A. Depine, G. Lozano, and H. Miguez, Phys. Rev. B **76**, 245103 (2007)

[27] F. A. B. F. de Moura and M. L. Lyra, Phys. Rev. Lett. **81**, 3735 (1998)

[28] H. Cheraghchi, S. M. Fazeli, and K. Esfarjani, Phys. Rev. B **72**, 174207 (2005)

[29] M. Titov and H. Schomerus, Phys. Rev. Lett. **95**, 126602 (2005)

[30] U. Kuhl, F. M. Izrailev, and A. A. Krokhin, Phys. Rev. Lett. **100**, 126402 (2008)

[31] D. Nau, A. Schonhardt, C. Bauer, A. Christ, T. Zentgraf, J. Kuhl, M. W. Klein, and H. Giessen, Phys. Rev. Lett. **98**, 133902 (2007)

[32] S. A. Gredeskul and Y. S. Kivshar, Phys. Rep. **216**, 1 (1992)

[33] J. M. Bendickson, J. P. Dowling, and M. Scalora, Phys. Rev. E **53**, 4107 (1996)

[34] C. Barnes, W. C. Tan, and J. B. Pendry, J. Phys. Condens. Matter **3**, 5297 (1991)

[35] X. H. Wu, J. Andreasen, H. Cao, and A. Yamilov, J. Opt. Soc. Am. B **24**, A26 (2007)

[36] J. Okolowicz, M. Ploszajczak and I. Rotter, Physics Reports **374**, 271 (2003)

[37] M. M. Sigalas, C. M. Soukolis, C. T. Chan, R. Biswas, and K. M. Ho, Phys. Rev. B **59**, 12767 (1999)

Chapter 3

2D & 3D complex photonic structures

3.1 Photonic Band Gaps in 3D Network Structures with Short-range Order

3.1.1 Introduction

[1] A photonic band gap (PBG) describes a frequency range within which light propagation is prohibited due to depletion of optical states. The most known structures having PBGs are photonic crystals (PhCs) with periodic modulations of dielectric constant [2]. Since PhCs are anisotropic, PBGs vary with directions. To have a complete PBG, the gaps in all directions must overlap in frequency. This condition is difficult to achieve for many PhCs, for example, simple cubic lattices. It is therefore easier to produce complete PBGs in more isotropic structures, e.g. photonic quasicrystals that possess higher rotational symmetry (but no translational symmetry) [3, 4]. Photonic amorphous structures (PAS) are most isotropic, due to the

1. Chapter 3.1 is primarily based on the work published in ref. [1].

absence of long-range translational or rotational order. Recent studies demonstrate that PBGs can be formed in two-dimensional (2D) and three-dimensional (3D) PAS with short-range order [5–11]. However, the exact physical mechanism or condition for the PBG formation in PAS is not well understood. An improved fundamental understanding of PBG formation would allow researchers to design photonic amorphous materials with optimized and tunable PBGs.

In addition to geometric order, structural topology plays an important role in forming a PBG. For the composite dielectric materials consisting of two components with different refractive indices, there are two cases regarding the topology of the high-index component. (i) Cermet topology: the high-index material consists of isolated inclusions, each of which is completely surrounded by the low-index material. (ii) Network topology: the high-index material is connected and forms a continuous network running through the whole composite. Previous studies of periodic structures have indicated that the cermet topology is more favorable for the PBG formation of a scalar wave, while the network topology for a vector field [12]. Such conclusions also apply to PAS. For example, in 2D PAS, PBGs for the transverse magnetic (TM) polarization (electric field out of plane) are easily obtained with isolated islands of high-index materials, because the electric field has same polarization direction everywhere and can be regarded as a scalar wave. For the transverse electric (TE) polarization (electric field in plane), the electric field has varying polarization direction and behaves like a vector field, thus it is easier to produce PBGs in connected dielectric networks [13]. It has been proposed that a hybrid structure with a mixture of both topologies can possess a full PBG for both TE and TM polarizations [9].

It is much more difficult to form complete PBGs in 3D structures. Substantial reductions in the density of optical states (DOS) have been demonstrated in PAS composed of randomly packed dielectric spheres of uniform size [8], as a result of evanescent coupling of the Mie resonances of individual spheres. Dielectric net-

work structures, for example, the photonic amorphous diamond (PAD), exhibit much stronger depletion of the DOS [7, 10]. It was conjectured that the tetrahedral bonding configuration in the PAD plays an important role in the formation of isotropic PBG. However, the PAD is constructed from a "continuous-random-network" (CRN) originally developed for modeling of amorphous Si or Ge [14], thus it is difficult to separate the relative contributions of tetrahedral bonding and local geometric order to the PBG formation. Identifying the key parameters that determine when a PBG will form in PAS is important not only for developing novel photonic glasses [15], but also for understanding color generation in nature [16]. Both cermet and network topologies have been found in color-producing PAS of many animal species [17, 18]. It is also conjectured that pseudo PBGs may be formed and responsible for non-iridescent coloration of many PAS [19].

In this chapter, we present a detailed numerical study of the DOS and PBGs in 3D PAS. We vary the topology, short-range geometric order, refractive index contrast, and filling fraction to maximize the depletion of DOS and the strength of PBG in the absence of long-range structural order. This study allows us to identify the essential elements for the formation of PBGs in PAS. In Sec. 3.1.2, we describe the methods used to generate PAS numerically and analyze their structural and topological properties. The calculated DOS for both cermet and network topologies are presented in Sec. 3.1.3, together with interpretations of the results. In Sec. 3.1.4, we explore dielectric networks with different degrees of structural order to maximize the reduction in the DOS.

3.1.2 Structure generation and characterization

Spheres packings

We first study dielectric composites with the cermet topology—high-index dielectric spheres embedded within a low-index host material (air). We employ a two-stage numerical protocol to generate 'just-touching', jammed sphere packings in a cubic simulation cell with varying positional order [20,21]. First, liquid states of monodisperse spheres are cooled at fixed packing fraction $\phi = 0.60$ from an initial high temperature T_0 to zero temperature at different rates. In the second step, each zero-temperature configuration is compressed in steps of $\Delta\phi = 10^{-3}$ followed by minimization of the total energy until a static packing with infinitesimal particle overlaps is obtained. By varying the cooling rate, we are able to create static packings with a range of positional order and packing fractions from random close packing at $\phi = 0.64$ to the face centered cubic (FCC) structure at $\phi = 0.74$. In general, the slowly cooled samples can be compressed to higher packing fractions. Figure 3.1 (a) shows a cluster of 50 spheres from the interior of a jammed sphere packing containing 1000 spheres at $\phi = 0.64$. For comparison, we generate completely disordered configurations by placing spheres randomly in the cubic box with no overlaps at $\phi = 0.35$.

Dielectric network

We also generate structures with network topologies, where the high-index dielectric material forms the continuous network, using two methods. For the first method, we invert the cermet structure of jammed dielectric spheres in air. The inverse structure consists of low-index (air) spherical inclusions in a continuous high-index dielectric network. By adjusting the radius R of the spheres (but fixing their positions), we can vary the air fraction γ in the inverse structure. An inverse structure with $\gamma = 0.8$

is shown in Fig. 3.1 (b). At this γ, adjacent air spheres begin to overlap and the dielectric material exhibits an irregular topology.

The second method, which is based on an algorithm described in Ref. [9, 22], produces more uniform network topologies than those from the first method. In this method, a 3D Delaunay tessellation is performed on the sphere centers from the cermet structures in Sec. 3.1.2. Each tetrahedron of the tessellation has four facets shared with four neighbors. We then calculate the center of mass of each tetrahedron, and connect the centers of mass of nearest neighbors by a dielectric rod. This creates a tetrahedrally connected dielectric network, where each junction (vertex) has four dielectric bonds. All dielectric rods have same radius W, but different lengths d. By changing W, we can vary the air fraction γ. A tetrahedral network with $\gamma = 0.8$ is shown in Fig.3.1 (c).

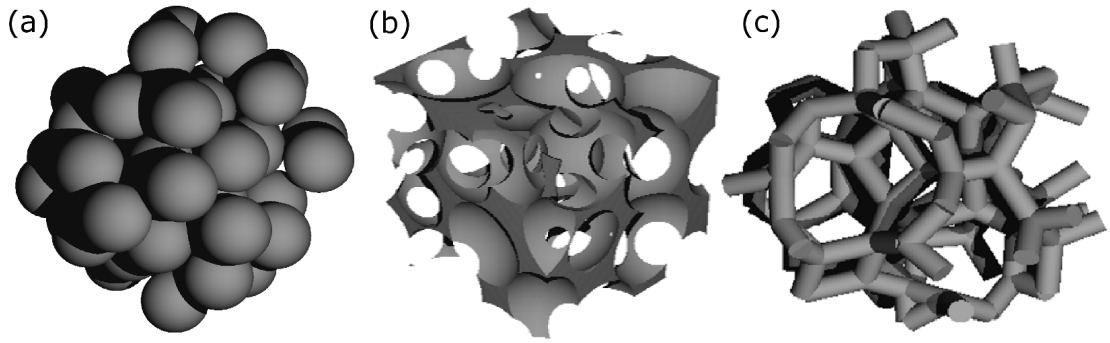

Figure 3.1: Three examples of photonic amorphous structures: (a) jammed packing of dielectric spheres at $\phi = 0.64$, (b) inverse structure of (a) with air fraction $\gamma = 0.8$, and (c) tetrahedral network of dielectric rods with $\gamma = 0.8$ obtained from the Delaunay tessellation of (a).

Structural characterization

We now calculate the density autocorrelation function and spatial Fourier spectra of the cermet and network structures described above. Since the dielectric spheres embedded in air and the corresponding inverted structure possess identical geometrical properties, we focus only on the air spheres and tetrahedral network structures

below.

As shown in the inset to Fig. 3.2 (a), the 3D spatial Fourier transform of the tetrahedral network structures displays concentric spherical shells without discrete Bragg peaks, which reflects structural isotropy and a lack of long-range order. The radii of the shells provides the characteristic spatial modulation frequencies of the structures. Similar results are obtained for the tetrahedral networks generated from the jammed sphere packings. The angle-averaged power spectra for both sphere and network structures are plotted in Fig. 3.2 (a). The main peak represents the dominant spatial frequency, and its width is inversely proportional to the average size of ordered domains [23]. The sphere and network structures have similar peak widths, and thus comparable domain sizes.

We also calculated the real-space density autocorrelation function $C(\Delta r)$ aver-

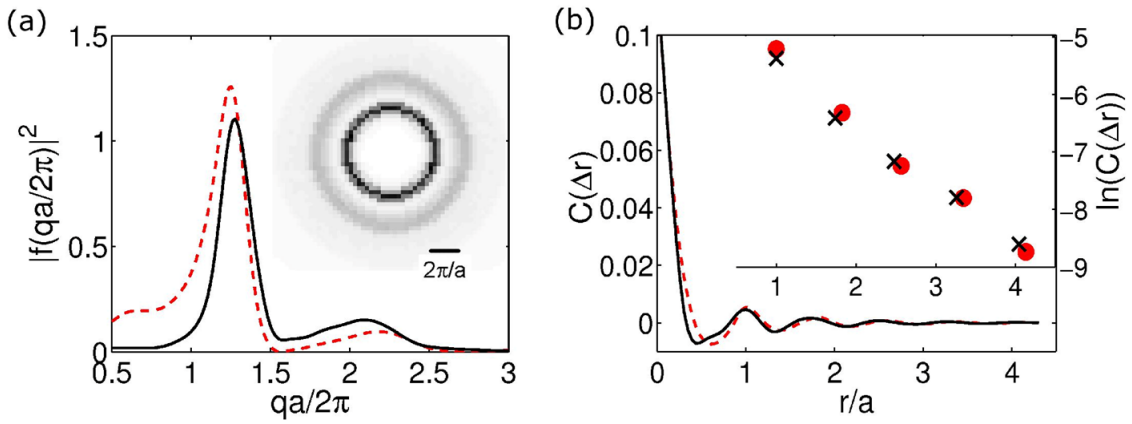

Figure 3.2: Structural characterization of photonic amorphous structures. (a) Angle-averaged power spectra of the spatially Fourier transformed density for jammed sphere packings (dashed line) and tetrahedral networks (solid line) versus $qa/2\pi$, where q is the spatial frequency and a is the mean spacing between spheres. The inset shows a cross-section of the 3D power spectrum for the tetrahedral network. (b) Angle-averaged density autocorrelation for the sphere packing and network structures. The inset shows the amplitudes of the oscillatory peaks of $C(\Delta r)$ for sphere packings (circles) and tetrahedral networks (crosses).

aged over all angles for the sphere and network structures [23]. As shown in Fig. 3.2 (b), both structures display highly damped oscillations of $C(\Delta r)$. The first peak away

from $\Delta r = 0$ is located at the average spacing a between nearest neighbors. We find that the amplitudes of the oscillatory peaks decay exponentially [inset to Fig. 3.2 (b)] with a decay length (excluding the first peak) $\xi_r \approx 0.9a$ for the sphere packings and $1.1a$ for the tetrahedral networks. Hence, there are weak spatial correlations and short-range order in these PAS.

3.1.3 DOS of PAS with cermet and network topologies

In this section, we describe calculations of the DOS for jammed dielectric spheres in air, the inverse structure, and the tetrahedral networks of dielectric rods using the order-N method [24]. We choose a cubic supercell with size $8.7a$ containing 1000 spheres and refractive indices $n = 3.6$ and 1 for the high- and low-index materials, respectively. We find that the optimal air fraction that yields the largest reduction of the DOS is $\gamma = 0.75$ for the dielectric sphere packings and 0.80 for both the inverse structure and tetrahedral network. The DOS was ensemble-averaged over five distinct configurations at the optimal γ for each topology, and then normalized by the DOS of a "homogeneous" medium with the same γ. The latter structure is generated by placing cubic dielectric voxels (with lateral dimension $0.043a$, which is much smaller than the wavelength of light λ) randomly in the supercell.

As shown in Fig. 3.3, the maximal DOS reduction occurs in the tetrahedral network structure, which is two orders of magnitude larger than that for the dielectric spheres and inverse structures. For the tetrahedral networks, the PBG is formed at normalized frequency $d/\lambda \approx 0.22$, where d is the average length of dielectric rods and $d/a = 0.39$. The width of the PBG normalized by the gap center frequency is $\sim 5.5\%$. The modest reduction in the DOS at $a/\lambda \approx 0.41$ for the dielectric spheres stems from Mie resonances of individual spheres [8]. The uniformity of the dielectric spheres allows the coupling of their Mie resonances, which of the lowest order for

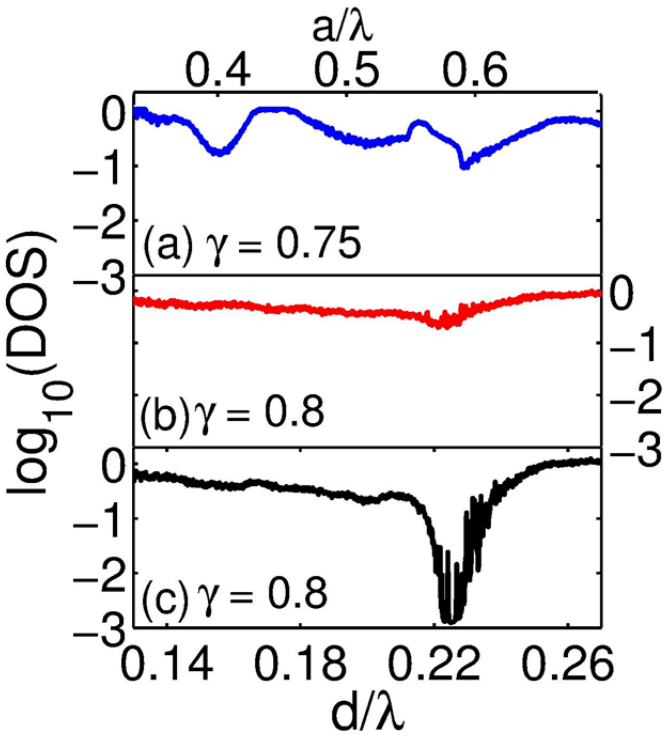

Figure 3.3: DOS for (a) jammed dielectric spheres in air with $\gamma = 0.75$, (b) inverted structures with $\gamma = 0.8$, and (c) tetrahedral networks with $\gamma = 0.8$. The wavelength λ is normalized by the mean spacing between spheres a (average bond length d) on the top (bottom) scale.

isolated dielectric spheres in air occurs at $a/\lambda \approx 0.41$. In contrast, the air sphere structures have only a small reduction of the DOS in the frequency range where the tetrahedral networks show a pronounced PBG, despite the fact that both structures have dielectric network topology and similar degree of spatial correlation. It is clear that the dramatic difference in the DOS cannot be explained by the small differences in spatial correlations.

Our studies of jammed dielectric sphere packings show that uniformity in the size of dielectric spheres leads to strong coupling of Mie resonances that result in a depletion of the DOS. In the inverse structure of air spheres, the basic scattering unit is the dielectric filling between air spheres. For the tetrahedral network structure, the basic scattering unit is centered at each junction where four dielectric rods meet. Note that in the network topology, the adjacent scattering units are connected, in contrast with the cermet topology. To compare the uniformity of local scattering units in dielectric networks, we calculate the average refractive index near the center of each unit. For the tetrahedral network structure, we calculate the mean refractive index $\bar{n}$ within a sphere of radius r whose center coincides with the center of each junction. We then compute the average $\langle \bar{n}(r) \rangle$ and its variance $V(r)$ over all junctions. For the air spheres, the dielectric junction center is set at the center of refractive index distribution within each tetrahedron obtained from the 3D Delaunay tessellation of the sphere centers. Similarly, we calculate the mean refractive index $\bar{n}$ around each junction center, $\langle \bar{n}(r) \rangle$, and $V(r)$ averaged over all junctions.

In Fig. 3.4 (a) we show that on average the tetrahedral network and air spheres structure have similar distributions of the mean refractive index $\langle \bar{n}(r) \rangle$ around each dielectric junction. In addition, the average refractive index for both networks approaches the same value at large r since the air fraction γ is the same for both structures. However, the variance $V(r)$ of $\bar{n}$ for the two network structures shows marked differences for all r as shown in Fig. 3.4 (b). The tetrahedral network possesses much

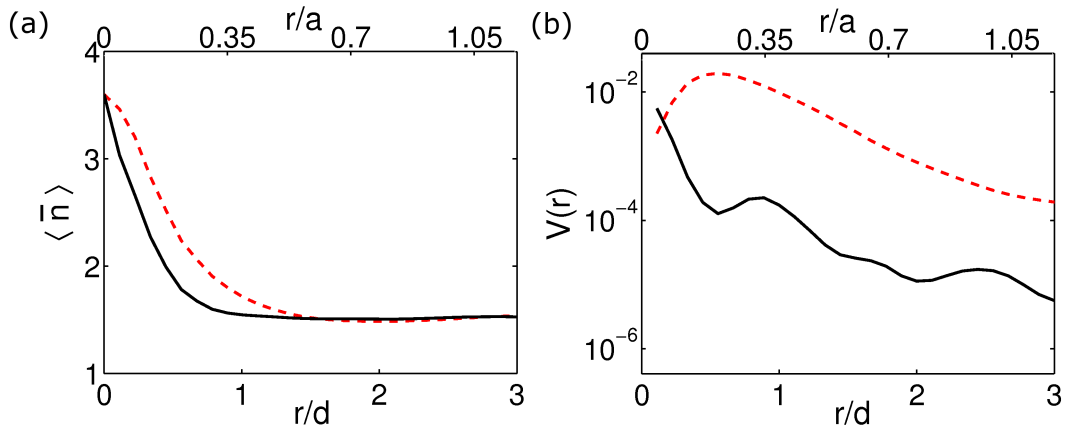

Figure 3.4: Uniformity of the local scattering environment for the dielectric networks of tetrahedral bonding (solid line) and air spheres (dashed line). (a) Mean index of refraction $\langle \bar{n}(r) \rangle$ and (b) variance $V(r)$ within a distance r from the dielectric junction center. r is normalized by the mean spacing of spheres a (average bond length d) on the top (bottom) scales.

smaller fluctuations in $\bar{n}$ from one junction to another. Thus, the scattering units are much more uniform for the tetrahedral network than those in the air spheres. The uniformity of local refractive index distribution ensures similar scattering characteristic of individual dielectric junctions and facilitates their coupling which leads to a dramatic depletion of the DOS.

The formation of a PBG in the tetrahedral network structure also depends on the air fraction γ and the refractive index of the dielectric material n. In Fig. 3.5 (a), we show the variation of the PBG for different values of γ while keeping n at 3.6. Reducing the air fraction below 0.8 leads to a decrease in the PBG. A reduction in γ increases the average refractive index of the structure, thus reducing the ratio of the index difference $(n-1)$ to the average refractive index. It leads to a decrease of the overall scattering strength, and a weakening of the PBG. In contrast, if γ is increased to above 0.8, there is an insufficient amount of high-index material to scatter light. Thus, there exists an optimal air fraction γ at which the scattering strength is maximal and the PBG is the largest. The optimal value of γ varies with the refractive index contrast. As shown in Fig. 3.5 (b), as n decreases, the maximal DOS reduction

shifts to smaller γ value. In addition, the DOS dip becomes shallower, reflecting the PBG effect is weaker at lower refractive index contrast. While the depth of DOS reduction changes slightly when n varies from 3.6 to 3.2, it drops by nearly two orders of magnitude with a further reduction of n from 3.2 to 2.8. This threshold behavior indicates there is a cut-off value of n for the PBG formation in the tetrahedral network structure.

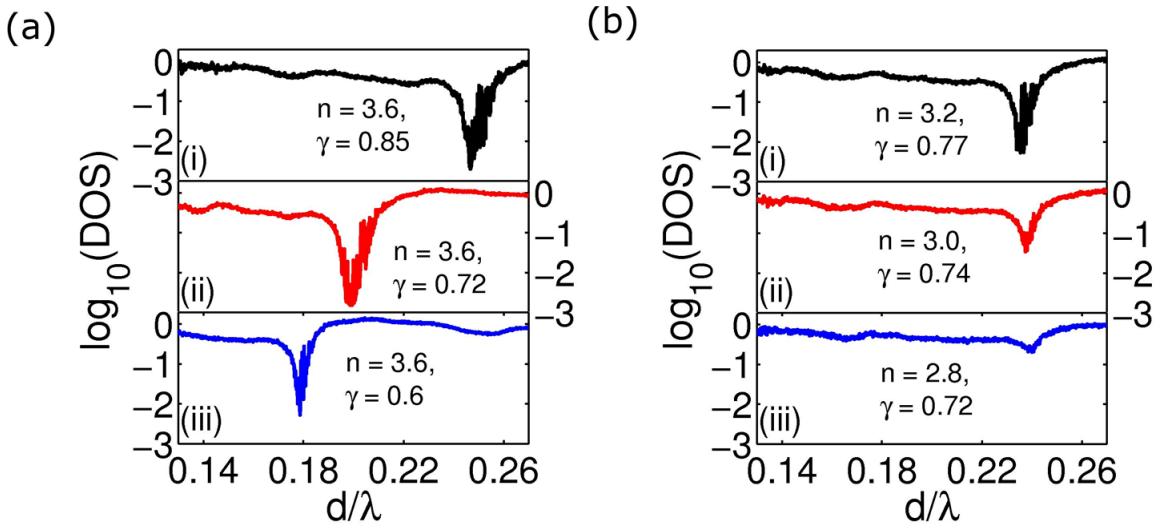

Figure 3.5: DOS of tetrahedral networks for different values of the air fraction γ and refractive index n. (a) $n = 3.6$, (i)$\gamma = 0.85$, (ii)$\gamma = 0.72$, and (iii) $\gamma = 0.6$. (b) (i) $n = 3.2$, $\gamma = 0.77$, (ii)$n = 3.0$, $\gamma = 0.74$ and (iii) $n = 2.8$, $\gamma = 0.72$.

3.1.4 Effect of short-range order

In addition to the factors studied above, short-range positional order and tetrahedral bond order play important roles in the formation of PBGs in PAS. In this section, we focus on the dielectric network of tetrahedral bonding, which yields the largest PBGs, and vary the amount of positional and tetrahedral bond order. In particular, we tune the positional order of the original sphere packings from which the tetrahedral networks are formed. The degree of positional order increases with the volume fraction

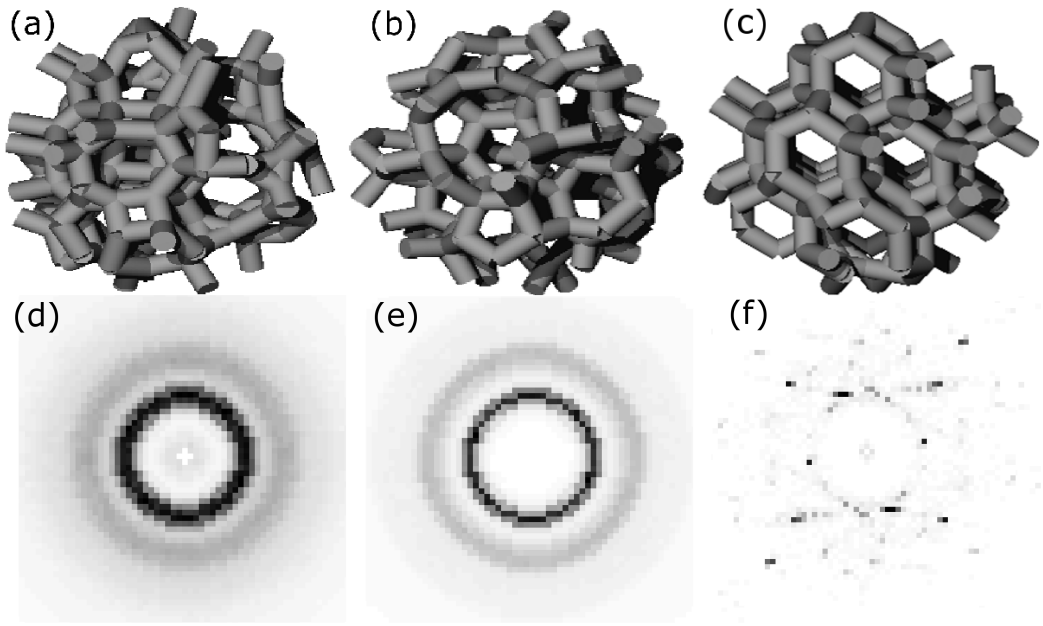

Figure 3.6: Tetrahedral dielectric networks generated from sphere packings with packing fraction (a) $\phi = 0.35$, (b) 0.64, and (c) 0.69. 2D cross-sections of the 3D spatial Fourier spectra of the corresponding tetrahedral networks are shown in (d), (e), and (f).

of spheres ϕ, which varies from 0.35 to 0.69. We label the tetrahedral networks (Fig. 3.6 (a)-(c)) generated from the sphere packings at $\phi = 0.35$, 0.64, and 0.69 as A, B, and C. 2D cross-sections of the 3D spatial Fourier spectra for these structures are presented in Fig. 3.6 (d)-(f). The power spectra of networks A and B consist of concentric shells, but the shell width is notably larger for A. Thus both A and B are isotropic structures, but B possesses more positional order than A. In contrast to A and B, network C features discrete diffraction peaks in the Fourier spectrum, and the structure is no longer isotropic.

In Fig. 3.7, we compare the DOS of the tetrahedral networks A, B, and C, with the refractive index of the dielectric rods set to $n = 3.6$. By adjusting the dielectric rod radius W, we find that the optimal air fraction for all three structures is $\gamma = 0.8$. As expected, network A, with the least positional order, possesses the smallest depletion in the DOS. However, network C with the strongest degree of positional order has

a smaller DOS depletion than network B. This result contrasts with recent findings for 2D PAS with air cylinders embedded in dielectric materials that show increasing positional order leads to stronger DOS depletion [23]. To understand these results, we must also compare the uniformity of the local refractive index distribution and the structural topology of the three network structures at fixed radius W of the dielectric rods. We find that networks B and C have comparable fluctuations in $\bar{n}$ over all the junctions. Thus, local uniformity does not explain the difference in the depletion of the DOS for networks B and C.

To investigate the effects of local topology on the depletion of the DOS, we

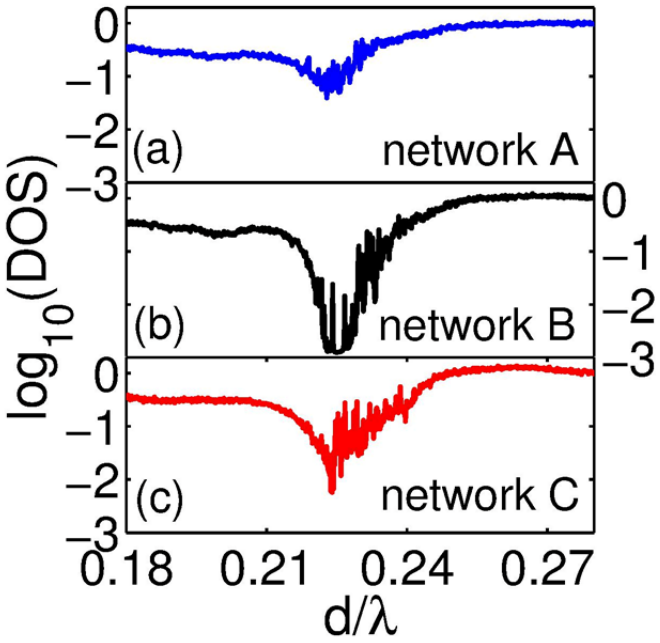

Figure 3.7: The DOS for three tetrahedral dielectric networks (a) A, (b) B, and (c) C with positional order increasing from A to C.

compute the tetrahedral order parameter [9, 10]

$$\zeta = 1 - \frac{3}{8}\sum_{j=1}^{3}\sum_{k=j+1}^{4}\left(\cos\psi_{jk} + \frac{1}{3}\right)^2, \tag{3.1}$$

where ψ_{jk} is the angle between two dielectric rods joined at a junction in the tetrahedral network [25]. For a periodic diamond network, $\psi_{jk} = 109.5°$, $\cos(\psi_{jk}) = -1/3$ for all j and k, and thus $\zeta = 1$ at each junction. If the dielectric rods are randomly orientated, $\langle\zeta\rangle = 0$. In Fig. 3.8, we plot the distributions of ψ_{jk} and ζ for the A, B, and C networks, and provide the mean values ($\bar{\psi}_{jk}$ or $\bar{\zeta}$), and standard deviations s_ψ and s_ζ.

Network A possesses the widest distributions for both ψ_{jk} and ζ, which indicates

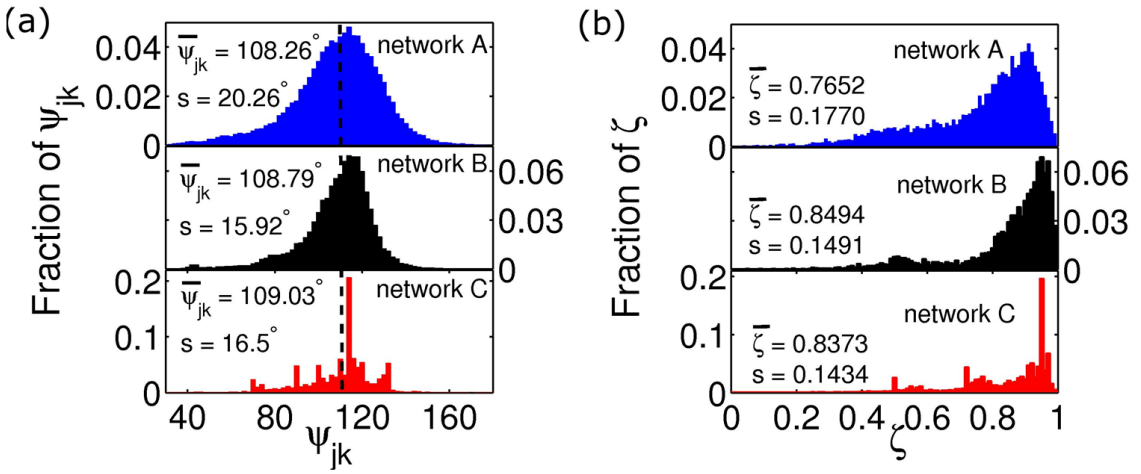

Figure 3.8: (Characterization of the local topology for networks A, B and C. (a) The distribution of angles ψ_{jk} between dielectric rods j and k at each tetrahedral junction. The vertical dashed line indicates the angle for the periodic diamond structure, $\psi_{jk} = 109.5°$. (b) Distribution of the tetrahedral order parameters ζ at each junction. The average $\bar{\psi}_{jk}$ and $\bar{\zeta}$ and standard deviations s_ψ and s_ζ are also provided.

that the local topology varies significantly from one junction to another and the bond angles within each junction are not uniform. The distributions of ψ_{jk} and ζ are narrower for network B, and are peaked at $\psi_{jk} = 114°$ and $\zeta = 0.95$, which indicates that most of the junctions have a similar topology to that in a diamond lattice. In contrast, network C displays multi-modal distributions for ψ_{jk} and ζ. For example, the ζ distribution possesses peaks at $\zeta = 0.95$, 0.72, and 0.5. The first peak reveals that there are many junctions with strong tetrahedral order, while the second and third peaks reflect the existence of many "defect" junctions with low ζ. Such defect

junctions are likely located at domain boundaries, and introduce irregularity in the local configuration of scattering units. Figures 3.7 and 3.8 show that photonic amorphous networks with strong tetrahedral order and few defect junctions have broad PBGs.

3.2 Localized photonic band edge modes and orbital angular momenta of light in a golden-angle spiral

3.2.1 Introduction

[2] Golden-angle spirals have been discovered in the arrangements of seeds, leaves, and stalks in sunflowers, pine cones, artichokes, celery, daisies, and many other plants [27]. Such patterns give the most even distributions of seeds in the sunflower heads, with no seeds clumping. Mathematically the golden-angle spiral is a form of Fermat's spiral representing the densest packing of identical circles within a circular region. Those circles form many spiral arms, or parastichies, in clockwise (CW) and counter-clockwise (CCW) directions. The numbers of parastichies are consecutive numbers in the Fibonacci series, the ratio of which approximates the golden ratio [28]. Inspired by nature, optical properties of spiral structures have been explored in recent years. For instances, photonic crystal fibers (PCF) with air holes arranged in the golden-angle spiral pattern exhibit large birefringence with tunable dispersion [29]. Nanoplasmonic spirals generate polarization-insensitive light diffraction and planar scattering over a broad frequency range [30].

Another fascinating feature of the golden-angle spiral structure is its ability to create an isotropic photonic bandgap (PBG), which inhibits light propagation in all directions [31]. In fact the 1D analogue of dielectric layers stacked in Fibonacci sequence have been explored earlier and shown to possess multiple photonic bandgaps [35, 36]. Of course, the most well-known structures that produce PBGs are photonic crystals [32], but their structural anisotropy leads to spectral mismatch of gaps in different directions. To have complete PBGs, more isotropic structures, e.g. photonic

2. Chapter 3.2 is primarily based on the work published in ref. [26].

quasicrystals with higher rotational symmetries, are preferred [33, 34]. However, the photonic quasicrystals still have discrete Fourier spectra and are not fully isotropic. The golden-angle spiral has better isotropy because its Fourier space is diffuse and circularly symmetric [30]. It has been predicted [31] that a 2D golden-angle spiral array of dielectric cylinders in air, even with low refractive index contrast, can create a broad omnidirectional PBG for transverse magnetic (TM) polarization. The gap width exceeds that in a six-fold lattice or a 12-fold fractal tiling. One advantage over the photonic amorphous structure which can also produce an isotropic PBG is that the golden-angle spiral structure is deterministic and has predictable and reproducible properties. The absence of sample to sample variations is critical to many applications.

Although it is now known that the golden-angle spiral can produce an omnidirectional PBG, little is known on the nature of its photonic band edge modes. In photonic crystals, the photonic band edge modes have low group velocities and high quality factors, thus useful to slow light devices and lasers. The band edge modes are spatially extended in the photonic crystals, but can be critically localized in the photonic quasicrystals which lacks translational symmetry [33, 34, 37]. The golden-angle spiral does not have discrete translational or rotational symmetries, and its band edge modes are distinct from those in photonic crystals and quasicrystals. Recent studies demonstrated that spiral structures can transfer net orbital angular momentum to the scattered optical waves [30]. Hence, the unique structural characteristic of the golden-angle spiral may impose unique and novel features on the photonic band edge modes.

In this paper, we present a systematic study on the photonic band edge modes in 2D golden-angle spiral arrays of air holes in dielectric host media. The PBG exists for the transverse electric (TE) polarization, and multiple classes of band edge modes are identified. Each class is localized in a specific region of the structure, due to spa-

tial inhomogeneity in the distribution of neighboring air holes. We discover that the photonic band edge modes possess discrete angular momenta that correspond to the Fibonacci numbers, which are associated with the parastichies in the spiral structure. The close relationship between the structural properties and characteristics of the photonic band edge modes is unveiled using the Fourier Bessel spatial analysis. The unique properties of the photonic band edge modes in the golden-angle spiral may lead to applications in light emitting devices and optical sensors.

3.2.2 Structural analysis of the golden-angle spiral

The golden-angle spiral, also called the Vogel's spiral, was first proposed by Vogel to simulate the seeds distribution in a sunflower head [38]. The location of each seed or circle is specified by a simple generation rule and expressed in the polar coordinate (r, θ) as

$$r = b\sqrt{q}\,, \tag{3.1}$$

$$\theta = q\alpha\,, \tag{3.2}$$

where $q = 0, 1, 2, \ldots$ is an integer, b is a constant scaling factor, $\alpha = 360^\circ/\phi^2 \approx 137.508^\circ$ is an irrational number known as the "golden angle", $\phi = [1 + 5^{1/2}]/2 = 1.6180339\ldots$ is the golden ratio. The value of ϕ is approached by the ratio of two consecutive numbers in the Fibonacci series $(1, 2, 3, 5, 8, 13, 21, 34, 55, 89, 144, \ldots)$. With this generation rule, the qth circle is rotated azimuthally by the angle α from the location of the $(q-1)$th one, and also pushed radially away from the origin by a distance $\Delta r = b\left(\sqrt{q} - \sqrt{q-1}\right)$.

Figure 3.9(a) shows a golden-angle spiral that consists of $N = 1000$ circles. Visually there are multiple families of spiral arms formed by the circles. Within each

family, the spiral arms, also called parastichies, are regularly spaced. Some of the families have parastichies all twisting in the CW direction, and the others in the CCW direction. The families are all intertwined. The number of parastichies in every family is a Fibonacci number [28].

The 2D spatial Fourier spectrum of the golden-angle spiral is shown in Fig.

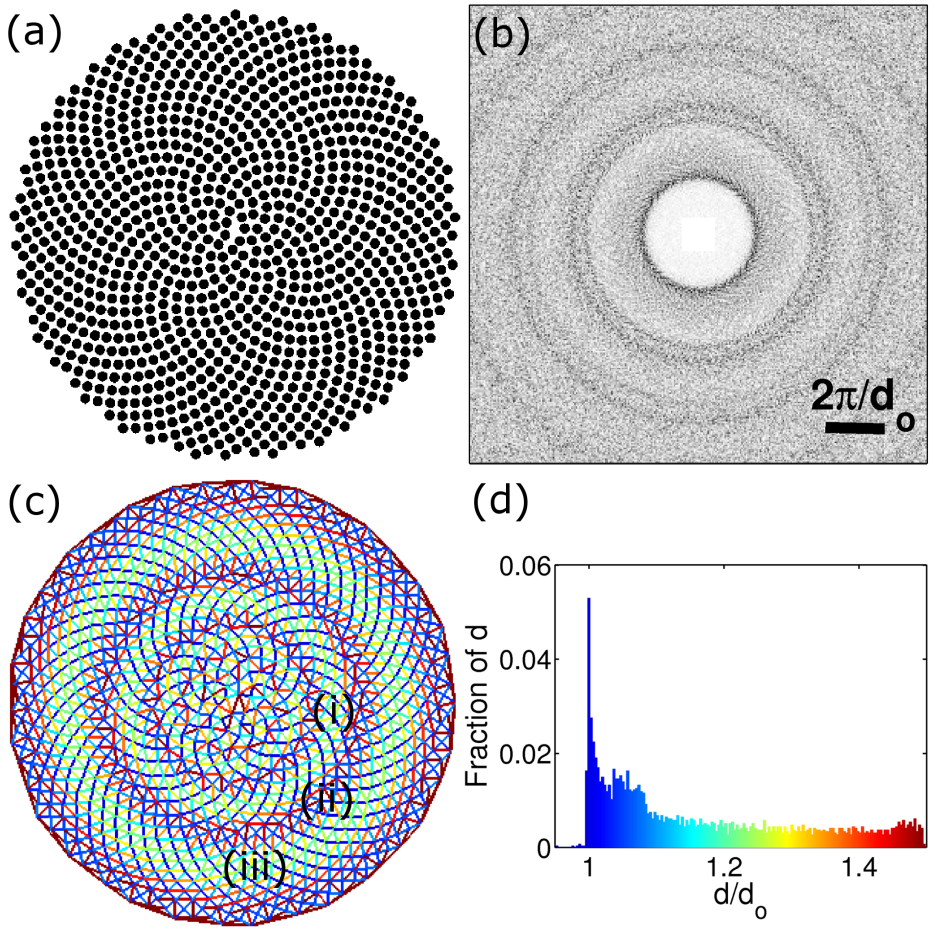

Figure 3.9: (a) Golden-angle spiral array consisting of 1000 circles. (b) Spatial Fourier spectrum of the spiral structure in (a). (c) Delaunay triangulation of (a). The line segments that connect neighboring circles are color-coded by their lengths d. (d) Statistical distribution of the distance between neighboring particles d normalized to the most probable value d_o. The colors are consistent to those in (c).

3.9(b). It has a continuous background, on top of which are discrete concentric rings. The isotropy of the Fourier space reflects the structural isotropy. The diffuse background in the Fourier space indicates the golden-angle spiral is not a quasicrystal,

but has many more spatial frequency components [30]. The radii of discrete rings correspond to the dominant spatial frequencies of the structure. We extract the distance between neighboring particles d by performing the Delaunay triangulation on the spiral array. In Fig. 3.9(c), each line segment connects two neighboring circles, and its length d is color coded. The statistical distribution of d in Fig. 3.9(d) is broad and non-Gaussian. d is normalized by d_0, the most probable value of d where the distribution is peaked. d_0 scales linearly with b, as shown in [30]. The broad distribution of d is consistent with the rich Fourier spectrum. The brightest ring in the Fourier space, which is also the smallest, has a radius close to $2\pi/d_o$. The non-uniform color distribution in Fig. 3.9(c) reveals the spatial variation of neighboring particles spacing in the spiral structure. This special type of spatial inhomogeneity is a distinctive feature of the golden-angle spiral, and it has a significant impact on its optical resonances as will be shown later.

In order to better understand the structural complexity of the golden-angle spiral, we perform a Fourier Bessel spatial analysis. The Fourier Bessel transform decomposes the density function associated with the spiral structure in a series of Bessel functions.

$$f(m, k_r) = \frac{1}{2\pi} \int_0^{\infty} \int_0^{2\pi} r \, dr \, d\theta \, \rho(r, \theta) \, J_m(k_r r) \, e^{im\theta} \,, \tag{3.3}$$

where the density function $\rho(r, \theta)$ is shown in Fig. 3.9(a), the azimuthal number m is an integer, and k_r represents a spatial frequency in the radial direction. The 2D plot of $|f(m, k_r)|^2$ shown in Fig. 3.10(a) illustrates that there are multiple and well-defined azimuthal components m in the golden-angle spiral. After integrating over the radial frequency k_r, we obtain $F(m) = \int |f(m, k_r)|^2 k_r dk_r$ which is plotted in Fig. 3.10(b). The frequency range of integration is $[\pi/d_o, 3\pi/d_o]$, centered around the dominant spatial frequency $2\pi/d_o$. We notice interestingly the dominant m values

are 5,8,13,21,34,55,89, which are Fibonacci numbers and represent the number of parastichies in each family. Later we will demonstrate that the parastichies encode discrete angular momenta, quantized in the Fibonacci numbers, onto the optical resonances.

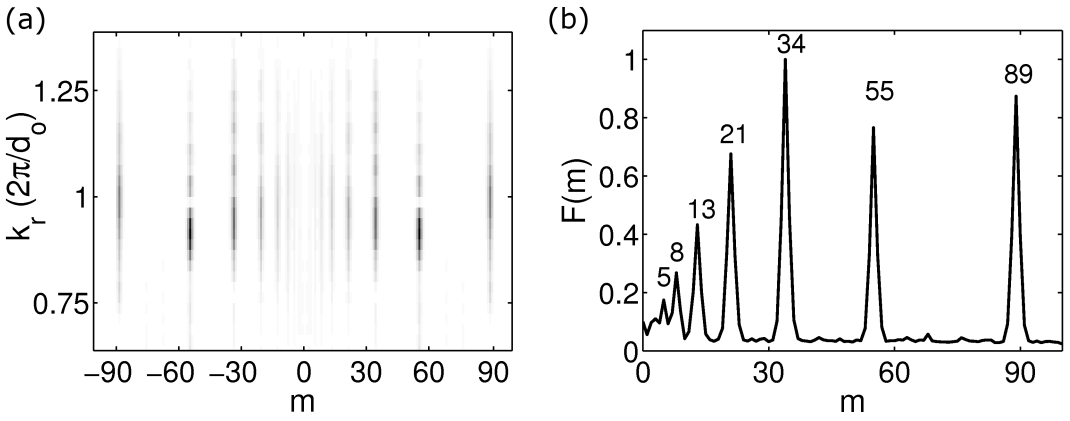

Figure 3.10: Fourier Bessel Transform (FBT) of the golden-angle spiral structure in Fig. 3.9(a) gives $|f(m,k)|^2$ (a) and $F(m)$ (b).

3.2.3 Photonic bandgap and band edge modes

We investigate now the optical properties of a golden-angle spiral that consists of $N = 1000$ air cylinders in a dielectric medium with refractive index $n = 2.65$. This structure, inverse of that in Ref. [31], facilitates the formation of PBG for the TE polarized light with (E_r, E_θ, H_z). We calculate the local density of optical states (LDOS) at the center of the spiral structure, $g(\mathbf{r},\omega) = (2\omega/\pi c^2) Im[G(\mathbf{r},\mathbf{r},\omega)]$, where $G(\mathbf{r},\mathbf{r'},\omega)$ is the Green's function for the propagation of H_z from point $\mathbf{r}$ to $\mathbf{r'}$. The numerical calculation is implemented with a commercial program COMSOL (version 3.5) [39]. Since the golden-angle spiral has a finite dimension, light may leak through the outer boundary. In our simulation, the spiral structure is surrounded by a perfectly matched layer that absorbs the escaped light. From the calculated LDOS in Fig. 3.11, we clearly see a PBG, and its width is about 11% of the gap center fre-

quency.

There are two peaks inside the gap at $d_o/\lambda = 0.323$ and 0.331. They represent

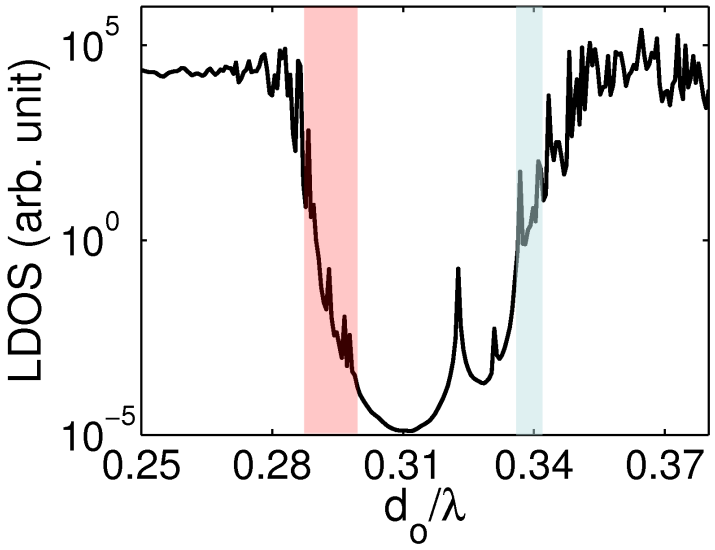

Figure 3.11: LDOS calculated at the center of the golden-angle spiral array as a function of the normalized frequency d_o/λ. The regions at the lower and upper band edge where the band edge modes exist are highlighted.

defect modes localized at the center of the spiral array where a small dielectric region free of air holes acts as a structural defect. At both edges of the gap, there are many more peaks which correspond to the band edge modes. Those on the higher (lower) frequency edge of the gap are denoted as upper (lower) band edge modes. Due to light leakage through the open boundary of the spiral structure, the band edge modes have complex frequencies, and the imaginary parts of the frequencies represent the leakage rates. We calculate the complex frequencies $\omega = \omega_r + i\omega_i$ and spatial field distributions of the band edge modes using the eigensolver of COMSOL. The quality factor $Q = \omega_r/2\omega_i$ is obtained for every mode. From their frequencies and field patterns, we identify several classes of the band edge modes. Within each class the modes have similar field patterns and display monotonic variation of Q. Two classes of the lower band edge modes are labeled in a plot of Q vs. $d_o/\lambda = \omega_r d_o/2\pi c$ in Fig. 3.12(a), another two classes of the upper band edge modes in Fig. 3.12(b). Within

each class, the modes are ordered numerically following their spectral distances from the edge of the PBG. As the modes in each class move further away from the PBG, the frequency spacing of adjacent modes increases and the Q decreases.

The spatial distributions of the magnetic field (H_z) for the first three modes in

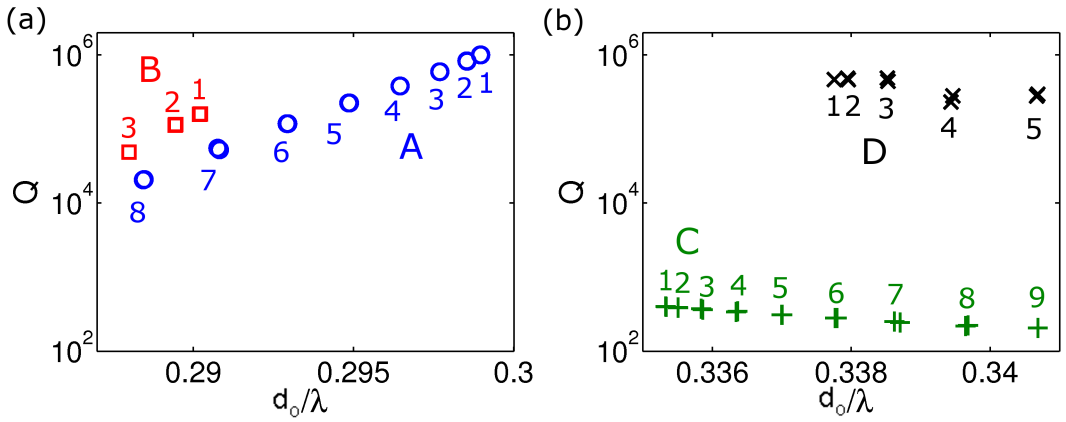

Figure 3.12: Quality factors of the lower band edge modes (a) and upper band edge modes (b) versus the normalized frequency d_o/λ.

classes A, B, C and D are presented in Figs. 3.13-3.16. Every mode is accompanied by a degenerate mode, e.g., A1 and A1' have the same frequency and complementary spatial profile. The lower band edge modes have magnetic (electric) field mostly concentrated in the air (dielectric) part of the structure, while the upper band edge modes are just the opposite. This behavior is similar to that of a photonic crystal, but there are also remarkable differences. The band edge modes in the golden-angle spiral are spatially localized, each class of modes is confined within a ring of different radius. As long as the ring is notably smaller than the system size, the modes are insensitive to the boundary, as for the localized states. For example, mode D1 remains unchanged when the air cylinders near the boundary are removed [D1" in Fig. 3.16].

A careful inspection of the mode profiles reveals that the class A modes have the magnetic field maxima along the parastichies that are formed by the air cylinders and twist in the CCW direction, while class B follow a different family of parastichies that twist in the CW direction. These local standing wave pattern behaviors indicate

light is confined in the direction perpendicular to the parastichies via Bragg scattering from the air holes. Since the orientation of parastichies changes with the polar angle, these standing waves rotate azimuthally and wrap around to form a circular pattern. Similarly, the magnetic field maxima of class C modes stay along the dielectric parastichies that are formed in between the air cylinders and twist in the CCW direction, and class D on a different family of dielectric parastichies twisting in the CW direction. Bragg scattering from the dielectric parastichies leads to the confinement of light in a ring. The envelop functions of the band edge modes exhibit clear modulations in the azimuthal direction. The number of nodes (zero points) is an odd integer for the modes in class A, B, C, but an even integer for D. This feature, as will be explained later, is related to the number of parastichies on which the modes are located.

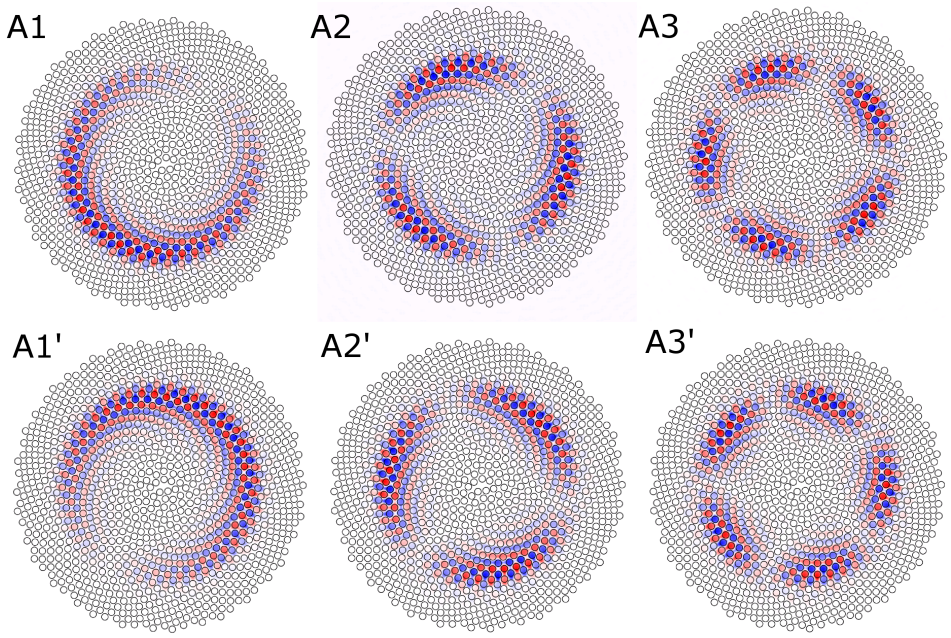

Figure 3.13: Spatial distributions of magnetic field H_z for the first three pairs of band edge modes of class A. The modes are localized within a ring of radius $\sim 12d_o$.

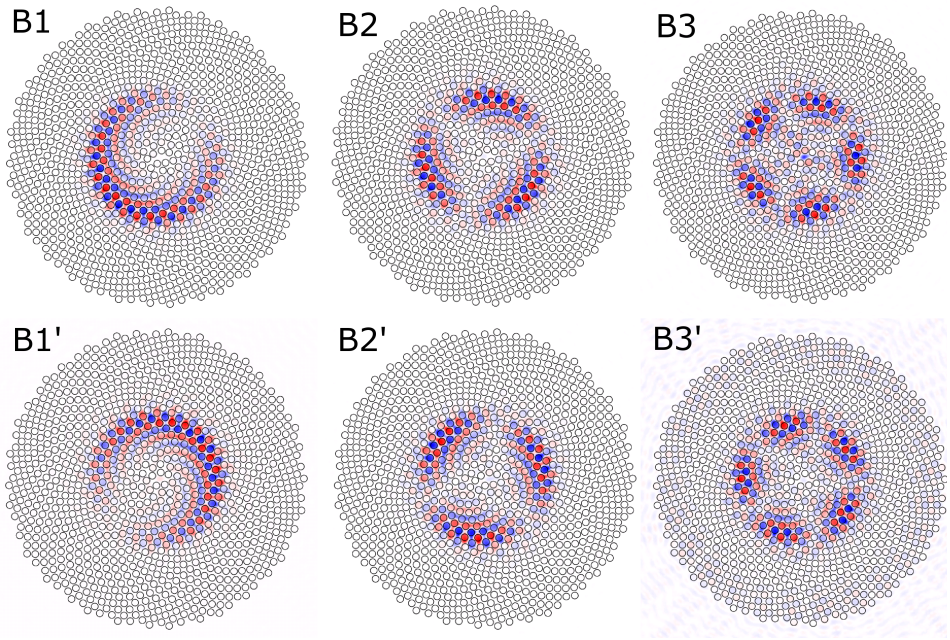

Figure 3.14: Spatial distributions of magnetic field H_z for the first three pairs of band edge modes of class B. The modes are localized within a ring of radius $\sim 7d_o$, close to the center of spiral than the modes of class A.

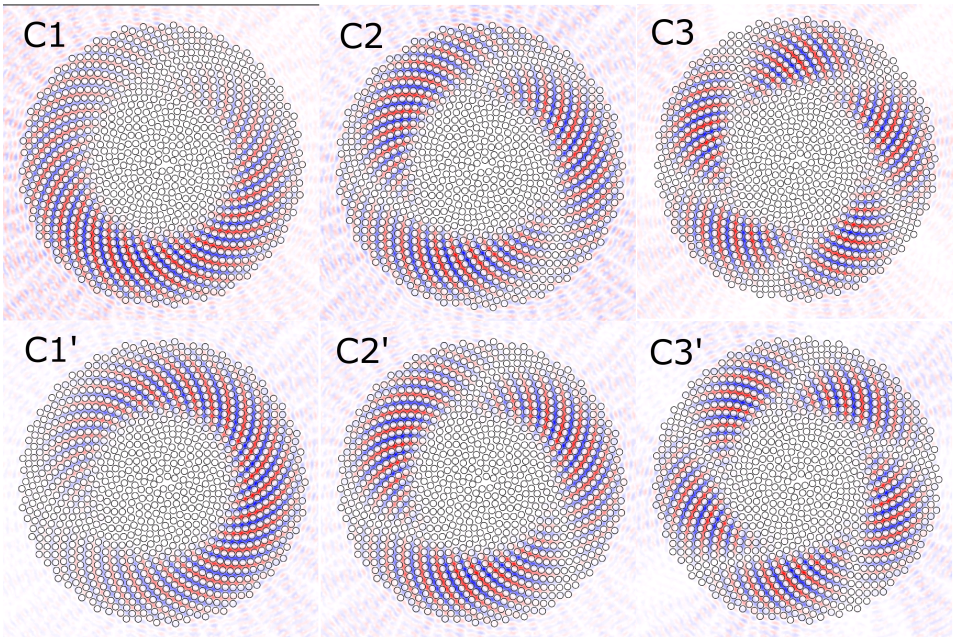

Figure 3.15: Spatial distributions of magnetic field H_z for the first three pairs of band edge modes of class C. The modes are located near the boundary of the spiral and have stronger light leakage through the boundary.

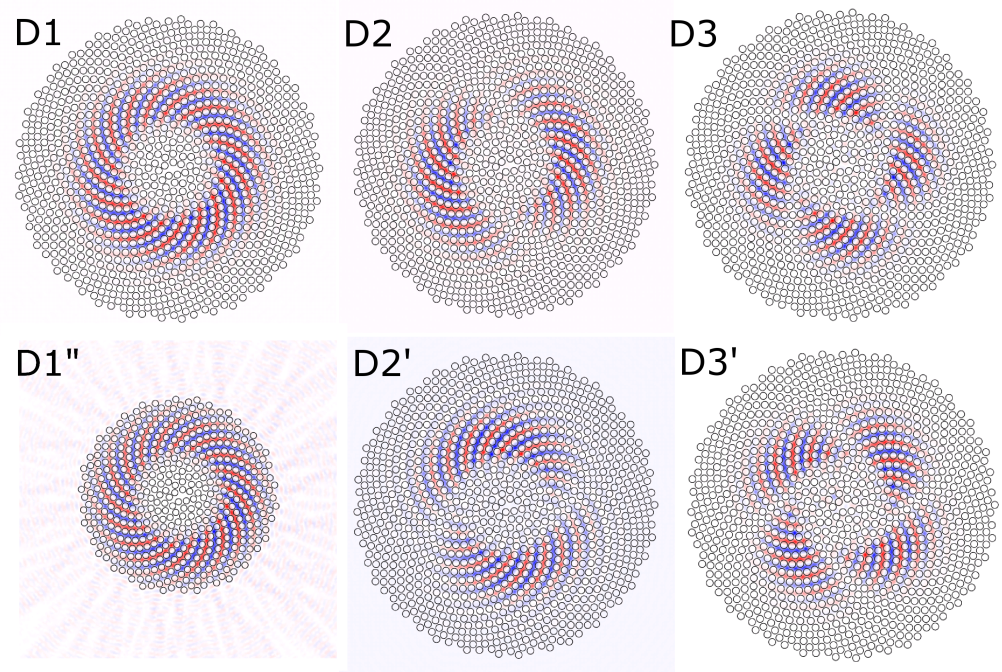

Figure 3.16: Spatial distributions of magnetic field H_z for the first three pairs of band edge modes of class D. The modes are localized closer to the center of the spiral and have small light leakage through the outer boundary. Mode D1" has the same field distribution as D1 after the air cylinders in the outer layer of the spiral are removed. The light leakage increases since the mode is closer to the boundary now. The insensitivity of mode D1 to the change at the boundary confirms it is a localized mode.

3.2.4 Spatial inhomogeneity and localization

In this section, we will demonstrate that the spatial localization of photonic band edge modes in the golden-angle spiral structure results from inhomogeneous distribution of spacing between neighboring particles d. From the colors of line segments connecting neighboring circles in Fig. 3.9(c), we see alternating rings of green color [(i) and (iii) in Fig. 3.9(c), $1.1d_0 < d < 1.3d_0$] and blue-reddish color [(ii) in Fig. 3.9 (c), $d_0 < d < 1.1d_0$ (blue) and $1.3d_0 < d < 1.5d_0$ (red)]. Different classes of band edge modes are localized in the rings of distinct colors. For example, by overlaying the region that contains 90% energy of modes in class A on the color map of d in Fig. 3.9(c), we find these modes are confined in region (ii), which is sandwiched by regions (i) and (iii) of different color. The distribution of d in region (ii) is distinct from that in (i) or (iii), leading to a change of PBG. We compute the LDOS in regions (i), (ii) and (iii) by removing air cylinders outside that region. As highlighted in Fig. 3.17(b), the frequency range of class A modes is inside the PBG of region (i) and (iii) but outside the PBG of region (ii). Consequently, light within this frequency range is allowed to propagate in region (ii) but not in (i) or (iii). Hence, regions (i) and (iii) act like barriers that confine class A modes in region (ii).

Next we consider the upper band edge modes, e.g. class C modes that concentrate in region (iii). The LDOS in region (ii) exhibits little difference from that in (iii) within the frequency range of class C modes. Thus region (ii) does not act like a barrier to confine modes in (iii). However, in region (iii) the distances between some air cylinders match the wavelengths of class C modes, thus providing distributed feedback for the formation of class C modes. Consequently, the class C modes stay mostly in region (ii), even though there is no barrier at the boundary of this region. It is similar to the formation of resonances in the conventional distributed feedback structures. Thanks to its broad distribution of spacing between neighboring particles d, the golden-angle spiral can support numerous modes at different frequencies. The

spatial inhomogeneity of d leads to mode confinement in different parts of the structure.

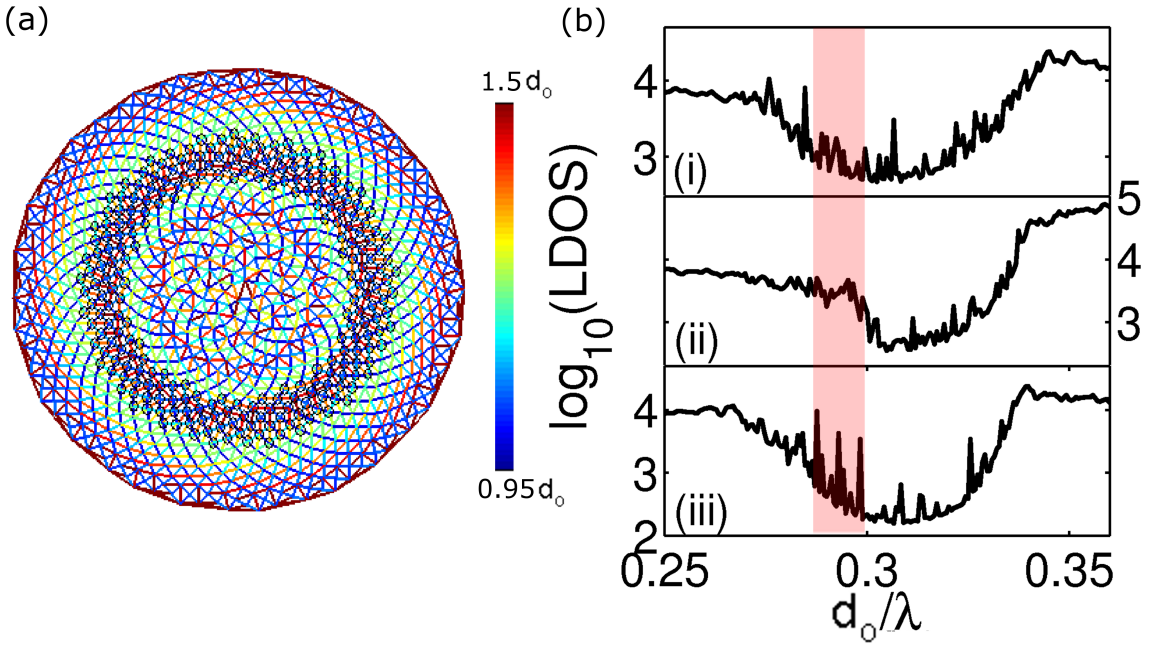

Figure 3.17: (a) Overlay of the region where class A modes are localized on the color map of the neighboring particles distance of air cylinders revealing class A modes stay mostly inside a ring labeled (ii) and sandwiched between two other rings (i) and (iii). (b) LDOS in the regions (i), (ii) and (iii).

3.2.5 Discrete angular momentum

As mentioned earlier, the standing wave patterns of the photonic band edge modes are formed by distributed feedback from the parastichies that spiral out. One example is presented in Fig. 3.18 (a), where the dashed arrows denote two families of parastichies along which the field maxima of mode A1 follow. The magnetic field H_z oscillates between the positive maxima on one parastichy and the negative maxima on the next one of the same family. We perform the FBT on the field distribution by replacing $\rho(r,\theta)$ in Eq. (3) with $H_z(r,\theta)$. To compare with the FBT of the structure $[\rho(r,\theta) > 0]$, we set $m' = 2m$ and $k'_r = 2k_r$ for the field FBT, which is equivalent to

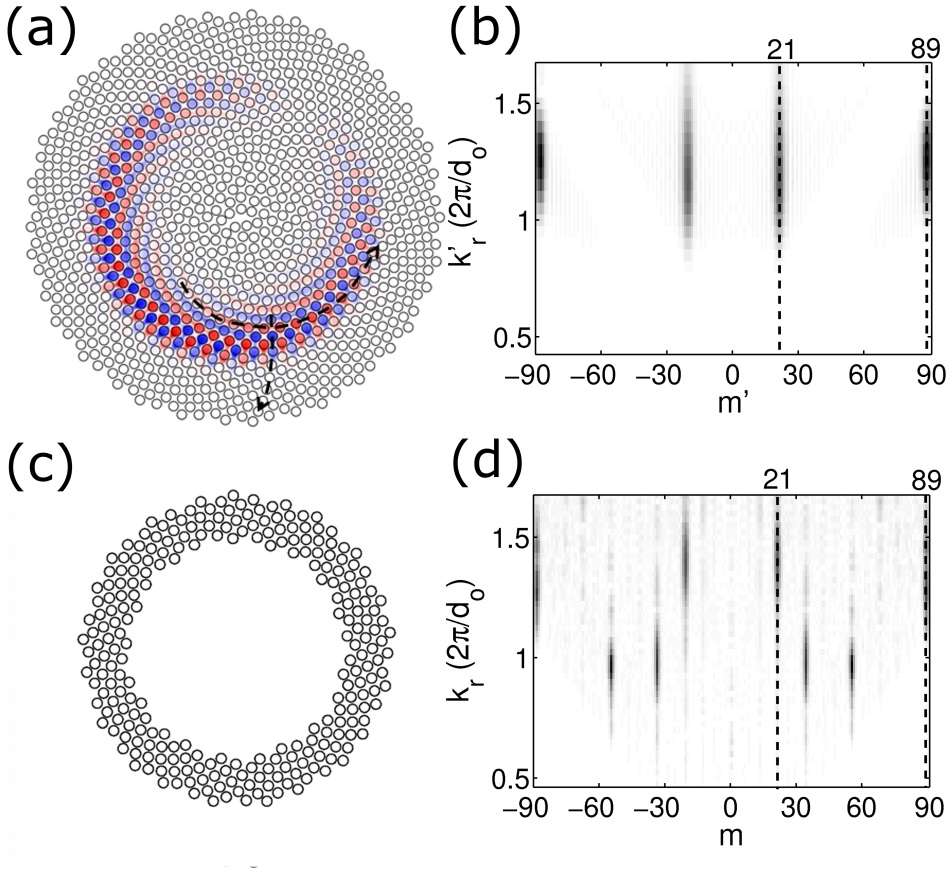

Figure 3.18: (a) Magnetic field distribution of mode A1 revealing the field maxima follow a family of 21 parastichies twisting in the CCW direction and another family of 89 parastichies in the CW direction (both are marked by the dashed arrows). (b) FBT of the field distribution in (a) gives $F(m', k_r')$. (c) Region of the spiral array that contains 90% energy of mode A1 is shown after removing the air cylinders outside. (d) FBT of the structure in (c) gives $F(m, k_r)$ of the local region where mode A1 stays.

considering the FBT of the field intensity distribution.

As shown in Fig. 3.18 (b), mode A1 has discrete angular momenta $m' = 21$ and $m' = 89$, both are Fibonacci numbers. To find their origin, we perform FBT of the structure in the region where mode A1 is localized [Fig. 3.18(c)]. The result is presented in Fig. 3.18(d), and show indeed $m = 21$ and $m = 89$ components with radial frequency k_r similar to that in the field profile of mode A1. While there are also $m = 34$ and $m = 55$ components in the structure, they are at lower k_r, thus corresponding to modes at lower frequencies and further away from the band edge. Hence, these analysis show that the angular momenta of the band edge modes are imparted by the underlying structure, more specifically, the parastichies in the golden-angle spiral. Similar analysis of mode B1 reveals that it supports angular momenta $m = 13$ and $m = 55$. They are also Fibonacci numbers, but smaller than those of mode A1, because mode B1 is localized in a smaller ring that has less number of parastichies.

Moving to the upper band edge, Figure 3.19(a) shows that mode D1 is located along the parastichies twisting in the CW direction (marked by the dashed arrow). FBT of the mode profile gives a single dominant angular momentum component at $m' = 34$. FBT of the corresponding region where D1 locates also reveals that there is a $m = 34$ component at the similar value of k_r. Other m components in the structure have higher k_r, thus corresponding to higher-frequency modes farther away from the band edge. Similar analysis of mode C1 reveals that it has angular momentum $m' = 55$, and the underlying structure contains a family of 55 parastichies.

With a better understanding of the connections between the mode profiles and the underlying structures, we can now explain why the numbers of nodes in the envelope functions are either odd or even for all modes belonging to one class. Note that the number of parastichies that correspond to mode A1, B1 or C1 is an odd number, but that for D1 is an even number. A1, B1 or C1 has one node in the envelop function, while D1 has none. As mentioned previously, the field maxima alternate between

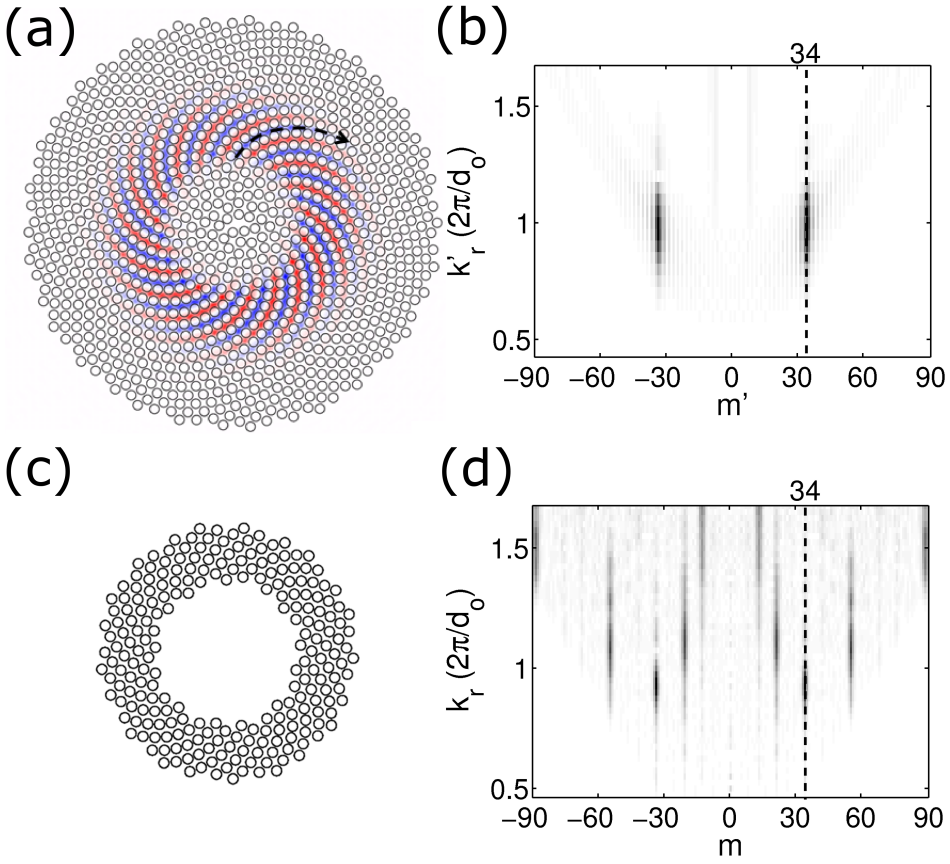

Figure 3.19: (a) Magnetic field distribution of mode D1 revealing the field maxima follow a family of 34 parastichies twisting in the CW direction(marked by the dashed arrow). (b) FBT of the field distribution in (a) gives $F(m', k_r')$. (c) Region of the spiral array that contains 90% energy of mode D1 is shown after removing the air cylinders outside. (d) FBT of the structure in (c) gives $F(m, k_r)$ of the local region where mode D1 stays.

the positive on one parastichy and the negative on the next. After wrapping around one turn (360°) and returning to the original parastichy, the field maxima must coincide with the one at the original parastichy. This is possible when there are an even number of parastichies, e.g. for mode D1. For mode A1, B1, or C1, the number of parastichies is an odd number, thus the field maxima would change sign after one turn. Since the field maxima of different sign cannot coincide spatially, there must be a radial shift, e. g., the positive maxima of the returning field shift away from the negative maxima of the original field along the parastichy, and there is a field node in between them. After a second round trip, there must be another nodal point. All these nodal points of the field form a node for the envelop function.

For the higher-order modes in every class of A-D, the number of nodes in the

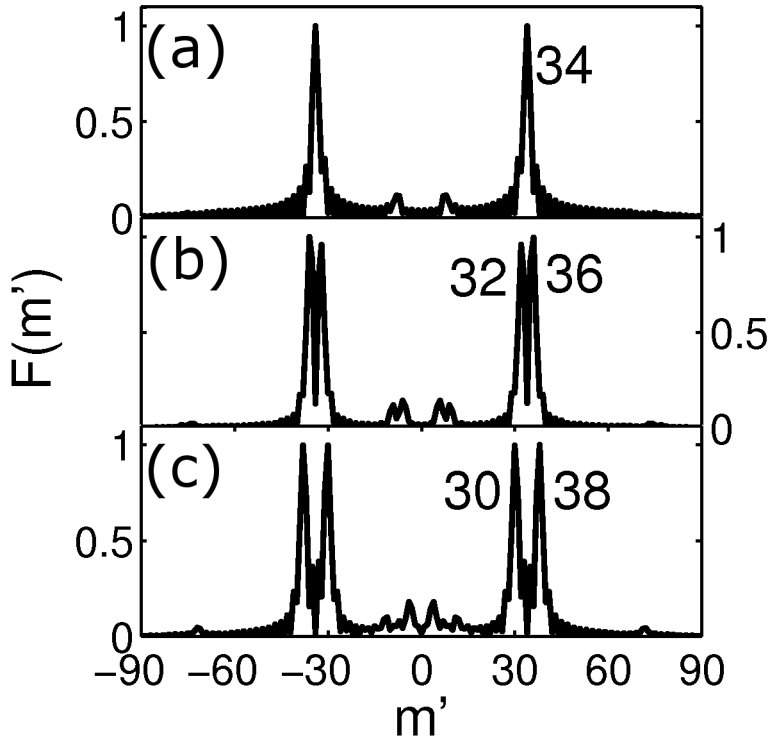

Figure 3.20: $F(m')$ from the FBT of the field profiles of mode D1 (a), D2 (b), and D3 (c) illustrating the splitting of the peak due to azimuthal modulations of the envelop functions of D2 and D3.

envelop function increases in a step of two, thus remain as an odd number for A-C and an even number for D. The addition of an even number of radial shift of field maxima adds a multiple of 2π to the phase of the returning field, and does not affect the constructive interference at the starting point. We perform FBT on the field distributions of the higher-order modes, and find the additional nodes in the envelope function causes a splitting of the peaks in $F(m')$. For example, mode D1 has only a single peak at $m = 34$ [Fig. 3.20(a)], while D2 has two peaks at $m = 32$ and $m = 36$ [Fig. 3.20(b)]. The change in m, $\Delta m = 2$, is equal to the number of nodes in the envelope function. For D3 mode [Fig. 3.20(c)], $\Delta m = 4$ due to four nodes in the envelop function. Such splitting is observed in all higher-order modes of classes A, B and C. The azimuthal modulation of the envelop function introduces additional angular momenta to the band edge modes.

3.2.6 Conclusion

In summary, we have studied numerically the photonic bandgap and band edge modes in the golden-angle spiral array of air cylinders in dielectric media. Despite the absence of long-range translational and rotational order, there exists a significant PBG for the TE polarized light. The upper and lower band edge modes can be categorized into different classes based on the field patterns. Due to spatial inhomogeneity in the distances of neighboring air holes, the band edge modes are localized within the rings of different radii via Bragg scattering from the parastichies in the spiral structure, and wrapped around azimuthally to form circular patterns which carry the well-defined angular momenta. The band edge modes have discrete angular momenta that originate from different families of the parastichies whose numbers correspond to the Fibonacci numbers. The unique structural characteristic of the golden-angle spiral impose special features on the band edge modes that are absent in the photonic

crystals and quasicrystals. These modes may lead to unusual properties of light transport in the spiral structure, and also produce laser emission with well-defined angular momenta when optical gain is added.

3.3 Optical resonances in topological defect structures

3.3.1 Introduction

Topological defects in liquid crystals have attracted a lot of attention recently for efficient generation of optical vortices [40–42]. By spin-to-orbital momentum coupling, an incoming circularly polarized beam is converted to a vortex beam after transmitting through a liquid crystal thin film with topological defects. However, the liquid crystal molecules are much smaller than optical wavelengths, thus light cannot be trapped at the topological defect. The questions are whether photonic structures with topological defects can support optical resonances and if so how they are different from those in photonic crystals (PhCs). To address these questions, we perform a numerical study on topological defect structures with wavelength-scale anisotropic scattering units. These structures do not possess any translational symmetry as each scattering unit is rotated as a function of their center position. Recent studies show that the flow of optical energy can be molded to form optical vortices in plasmonic nanostructures [43, 44]. In this work, we demonstrate another scheme of generating vortex-like energy flow by strategically tuning the form factors across the sample. We have observed extended optical resonances which exhibit circular flux flow around the singular point in the topological defect structure. In addition, we artificially remove some scattering units at the center of the structure to generate defect states with high Q factor. High Q localized modes with broken chiral symmetry are formed within the defect cavity. Such chiral cavities may be useful to enhance or suppress light interaction with chiral materials.

3.3.2 Topological defect structure

In our simulation, we adopted the elliptical shape scattering units which emulate the elongated liquid crystal molecules. As shown in Fig. 3.21(a), we arrange the air ellipses with aspect ratio of 1.4 periodically on a square lattice in a dielectric background with refractive index $n = 2.83$. The air area fraction is 28%. We define the crystal orientation parallel to the major axis of ellipses as X_1 and the orthogonal one as X_2. In Fig. 3.21(b), we compare the transverse electric (TE) photonic band structures between the square lattices consist of air ellipses (solid line) and circles (dashed line). Due to anisotropy of the scattering unit, degeneracy of optical resonances at the $\Gamma - X_1$ and $\Gamma - X_2$ crystal orientation is lifted for the square lattice tiled with elliptical air holes. Comparing to circular air holes, the dielectric region between two adjacent ellipses decreases in X_1 direction, causing the reduction of the effective index. The opposite happens in the X_2 direction where the effect index increases. As a result, the frequency of the optical resonances at X_1 direction increases and vice versa for resonances at X_2 direction.

A photonic topological defect structure is then generated by rotating each ellipses on the lattice to different directions. The orientation of each ellipses on the lattice is determined by a simple rule, $\phi = k\theta + c$, where ϕ is the angle between the major-axis of an ellipse with the horizontal x-axis, θ represents the polar angle of the center position of the ellipse, k is the disclination strength and c is a constant. Fig. 3.21(c) shows a topological defect structure with $k = 1$ and $c = \pi/4$ which resembles a matter vortex. The orientation of an ellipse ϕ at the center of the structure is undefined and thus it is a singular point. At each four corners of this topological defect structure, all the ellipses are aligned in same direction but they are rotated from one corner to another by 90 degrees. As a result, this structure is aperiodic and does not possess any mirror symmetries, i.e. the chiral symmetry is broken. The spatial Fourier transform of the topological defect structure (Fig. 3.21(e)) possesses

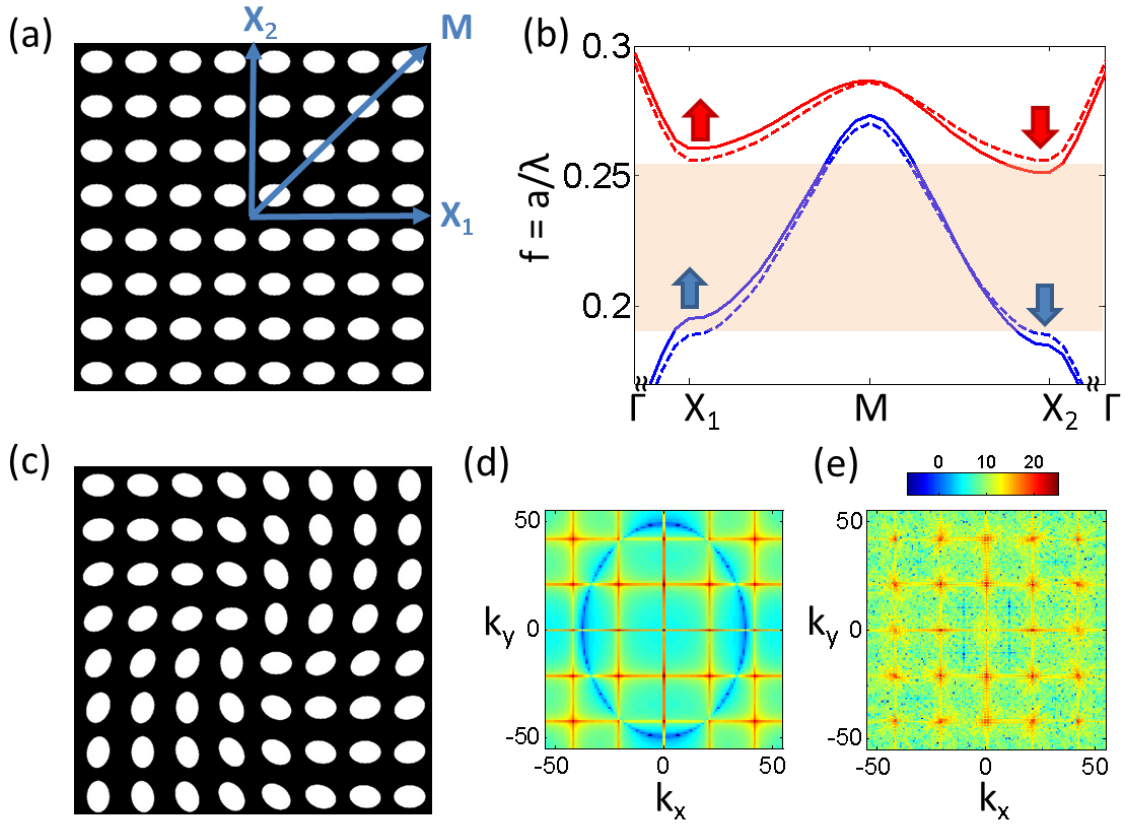

Figure 3.21: Square lattice PhC and topological defect structure. (a) PhC with elliptical shape unit cells. The three crystal orientations are indicated. (b) Photonic band structures for transverse electric polarization in square lattice with circular shape scattering units (dashed line) and elliptical shape scatteiring units. (c) Topological defect structure with $k = 1$ and $c = \pi/4$. (d,e) Spatial Fourier spectra of the square lattice in (a) and (c). Elliptical shape form factor is observed in the Fourier spectra for (a).

the same dominant Bragg peaks as in a square lattice PhC (Fig. 3.21(d)). However, due to constantly rotating ellipses, the elliptical shape form factor curve (blue color line in Fig. 3.21(d)) which exists in the Fourier spectrum of a PhC is smeared out in the Fourier spectrum of the topological defect structure.

3.3.3 Optical resonances at major crystal orientations

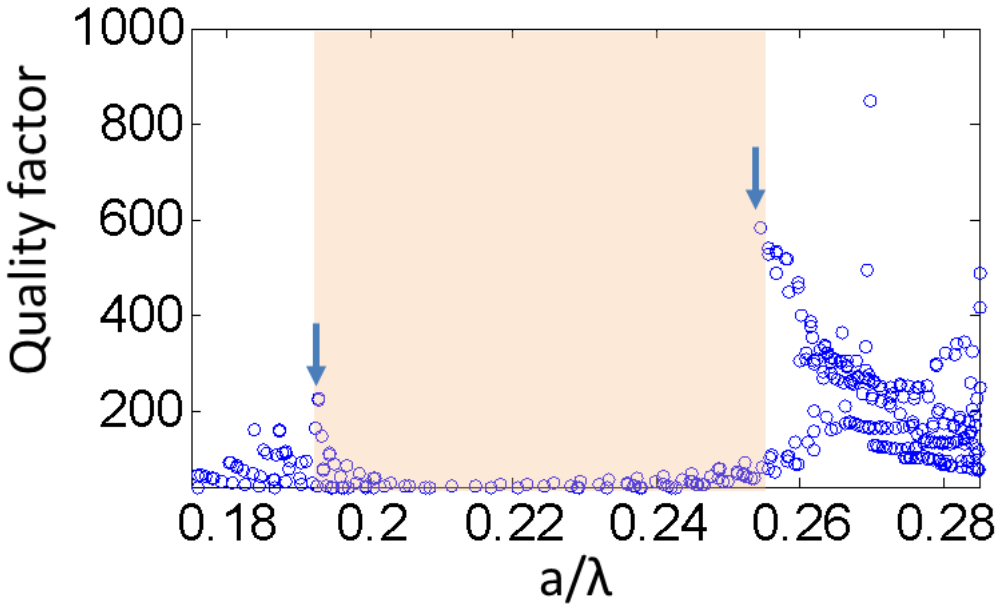

Figure 3.22: Modes' quality factor distribution in a photonic topological defect structure. The shaded area corresponds to the partial band gap in the $Gamma - X$ direction for a PhC with circular air holes. The topological defect structure preserves the partial band gap effect where the density of modes is lower within the shaded frequency range. The high-Q modes at the boundary of the shaded region correspond to the modified band-edge modes.

Since the topological defect structure is aperiodic, we limit our numerical simulation to a structure composed of N = 1024 elliptical air holes. Aspect ratio of the ellipses is fixed at 1.4. In the numerical simulation, the structure is surrounded by dielectric medium and terminated by perfectly matched layers to absorb light leaked out from the structure. We consider transverse electric (TE) polarization, with only

(Ex, Ey, Hz) field components. For an open system, one can define quasi-normal mode. These are eigenfunctions of the Maxwell equations with complex frequency that satisfy the boundary conditions of the outgoing wave. They describe states that have stationary normalized spatial profiles and amplitudes decaying in time due to radiative losses. We used the finite element method (COMSOL) to compute the complex eigenfrequency ($\omega = \omega_r + i\omega_i$) of the modes and their spatial fields distribution. In Fig. 3.22, we show the mode's quality factor ($2\omega_i/\omega_r$) distribution for the topological defect structures. Even though the structure lacks translational symmetry, the mode quality factor distribution remains very similar to the PhC, and the photonic band gap effect is preserved.

Therefore, we expect that the quasi-normal modes in the topological defect structure evolve from the ones in PhC, and their spectral frequencies are close. Here, we focus on the quasi-normal modes with highest frequency a/λ along certain crystal direction which are usually termed as "band edge modes" in PhC. For each direction, there are two band edge modes, one has field intensity localized in the air regions, which is called air band edge mode and the opposite one is called dielectric band edge mode. Fig. 3.23(a) and (b) show the spatial distribution of magnetic field $H_z(x, y)$ for the dielectric band edge mode at $\Gamma - X_1$ and air band edge mode at $\Gamma - X_2$ in a PhC with elliptical shape unit cells. The band edge modes are formed via Bragg reflection from the dielectric-air ellipses layers in the $\Gamma - X_1$ and $\Gamma - X_2$ directions. The quality factor of these two modes are higher than their counterparts in each direction. This is because from the photonic band calculation in Fig. 3.21(b), the frequencies of mode (a) and (b) shift towards the center of the partial photonic band gap. On the other hand, the frequencies of their counterparts shift away from the partial photonic band gap center and into the pass band. As a result, mode (a) and (b) have better confinement with higher Q factors.

In Fig. 3.23(c) and (d), we plot the corresponding quasi-normal modes found in

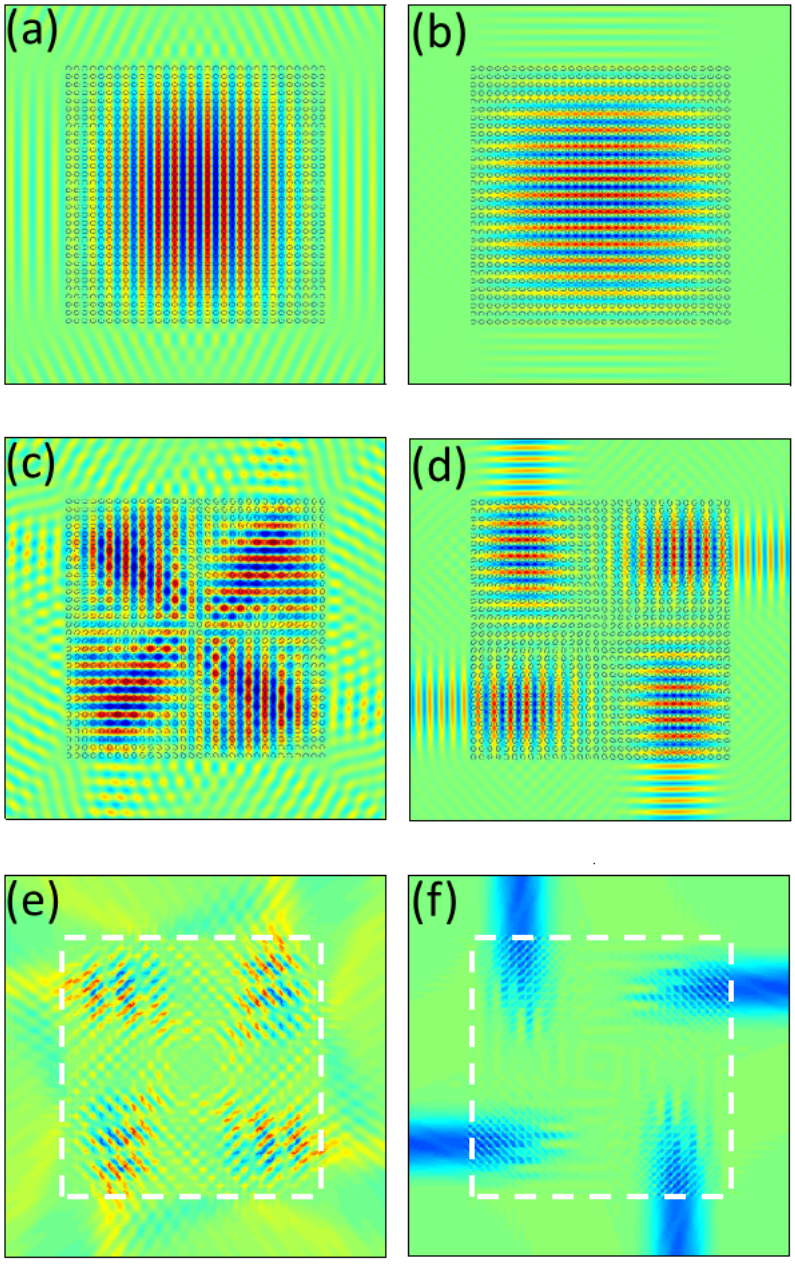

Figure 3.23: Quasi-normal modes in topological defect structure at $\Gamma - X_1$ and $\Gamma - X_2$ directions. Spatial magnetic field distribution $real H_z(x, y)$ of the band edge modes in a PhC (a,b) and topological defect structure (c,d). (a,c) correpond to dielectric band edge modes in $\Gamma - X_1$ direction and (b,d) are air band edge modes in $\Gamma - X_2$ direction. (e,f) Spatial distribution of the angular momentum density $J_z(x, y)$ for modes (c) and (d).

the topological defect structures with very similar frequency and local spatial field distribution to the modes shown in Fig. 3.23(a) and (b). Vortex-like arrangement of elliptical air holes (Fig. 3.21(c)) creates local crystalline regions at four corners of the topological defect structure which resemble the PhC in Fig. 3.21(a). The ellipses located approximately at around 45° and 225° have major-axis parallel to the y-axis, and at 135° and 315°, they become parallel to the x-axis. This alternating arrangement of ellipses rotation enables the formation of modes which support the PhC-like spatial field distribution within each crystalline regions. As a result, the mode pattern consists of four separated regions with same spatial field distribution but rotated 90° going from one corner to the next. Note that close to the center of the structure, the orientations of the ellipses change more drastically from one to another than those at the corners, so the field intensity diminishes going into the center. The field amplitude at the center of the structure becomes zero which resemble the singular point in a vortex field. As the field of the mode extends to the edge of the structure, the radiative decay rate is high and thus the Q of the modes becomes lower than their counterparts in a PhC.

From the spatially rotated field pattern of the modes, one might expect the mode exhibits vortex-like energy flow. To investigate such phenomena, we compute the spatial distribution of the angular momentum density $J_z = r \times p_\theta$, where r is the radial distance to the center of structure, p_θ is the azimuthal component of the time-averaged Poynting vector $\vec{S}(x,y) = \frac{1}{2}\mathrm{Re}[\vec{E}(x,y) \times \vec{H}^*(x,y)]$ divided by square of free space velocity of light. p_θ is positive if the azimuthal energy flow is counterclockwise (CCW) and negative for clockwise (CW). The angular momentum density J_z is an analogue to the mechanical torque. Fig. 3.23(e) and (f) show the spatial distribution of $J_z(x,y)$ for mode (c) and (d) respectively. For mode (c), the dominant angular momentum density is in counterclockwise (CCW) direction where the spatially averaged $\langle J_z(x,y)\rangle_{x,y} = 0.36$. On the other hand, mode (d) contains mostly clockwise

(CW) components with $\langle J_z(x,y)\rangle_{x,y}$ = - 0.96. As a result, these topological defect resonances can potentially be used to exert a net torque on nanoparticles in an optical tweezer setup.

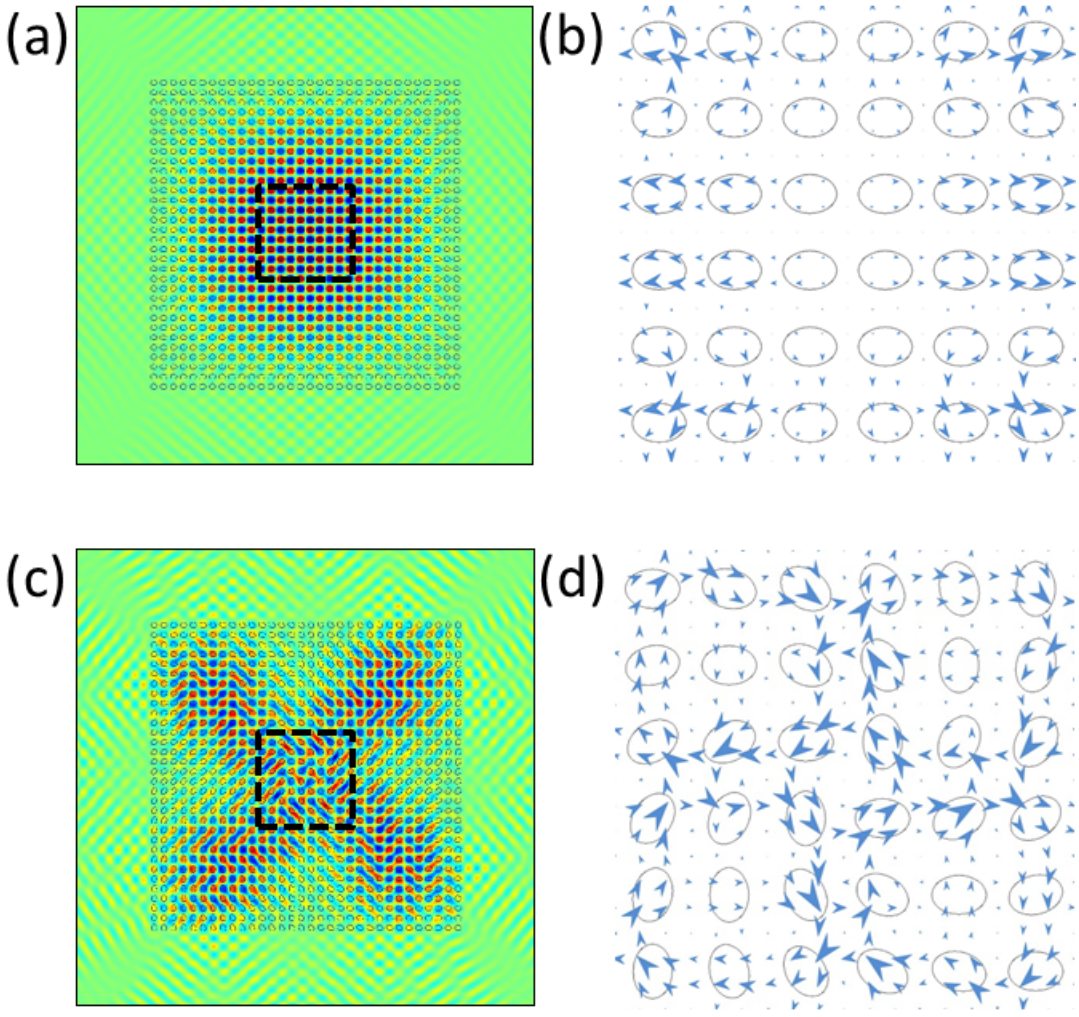

Figure 3.24: Dielectric band edge modes at $\Gamma - M$ crystal orientation. (a,c) Spatial magnetic field distribution $real H_z(x,y)$ of the modes for a PhC and topological defect structure. (c,d) Arrows plot of the Poynting vectors within boxed regions of the field profiles in (a) and (c). The topological defect resonance shows circular energy flow in the counter-clockwise direction which is absence in the PhC.

At another major crystal orientation $\Gamma - M$, the light fields contain spatial frequency in 45° direction. As a result, the field profile of a PhC dielectric band edge mode resembles the conventional "checkerboard" pattern [Fig. 3.24(a)]. To visualize

the energy flow, we generate a spatial arrows plot for the Poynting vectors. For the mode in a PhC, the energy only flow outwards from the center of the structure with growing amplitude due to the complex eigenfrequencies [Fig. 3.24(b)]. On the other hand, the field profile of the corresponding topological defect resonance is distorted by the continuously rotating elliptical shape particles and resembles a "cross" sign [Fig. 3.24(c)]. Furthermore, from Fig. 3.24(d), we observe circular flow of energy in the counter-clockwise direction close to the center of the structure.

3.3.4 Defect states in topological defect structures

We have observed that by introducing topological defect in a square lattice of ellipses, the flux can be molded to exhibit circular flow. However, all the spatially extended band edge modes have very low Q because light can leak out from the structure easily at the boundary. To trap light within the topological defect structure, we artificially removed 16 ellipses from the center and form a defect cavity [Fig. 3.25(a)]. In Fig. 3.25(b), there exists several high-Q modes within the partial band gap in the $\Gamma - X$ direction. In particular, there exist a defect mode (c) with Q about one order of magnitude higher than the rest of the modes.

For this mode (c), we compute its spatial distribution of Poynting vectors in Fig. 3.26(a) and its spatial distribution of angular momentum denstiy J_z in Fig. 3.26(b). This high-Q defect mode exhibits net energy flow in the counter-clockwise direction and possess net orbital angular momenta to form an optical vortex. To understand why this happen, we need to consider the boundary of the defect region which contains continuously rotating ellipses. As result, the chiral symmetry of the defect cavity is broken and this breaks the balance of scattering for CCW and CW waves. For this high-Q defect mode, the CW wave experience more scattering loss compared to the CCW wave and thus the net energy flow in the CCW direction. To confirm that this

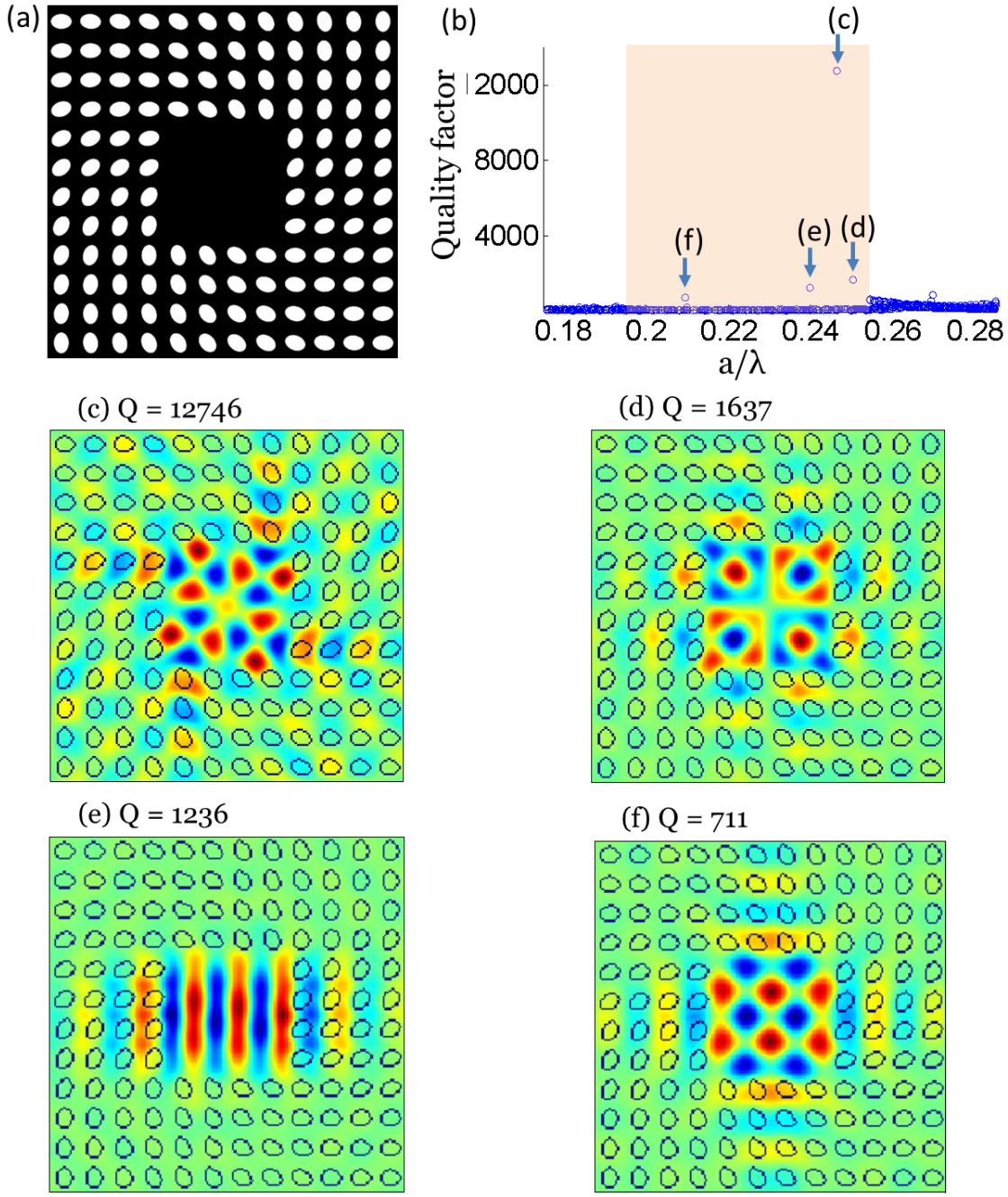

Figure 3.25: Defect states in topological defect structure. (a) A defect cavity is created by artificially removing 16 ellipses at the center of the structure. (b) Quality factors for several defect states are highlighted and their spatial field profiles are shown in (c-f).

is the underlying mechanism, we compute another defect state within a topological defect structure with the paramter c flipped to -1. As shown in Fig. 3.26(c), all the ellipses are rotated 90° from those in Fig. 3.26(a). Consequently, we observe that both the energy flow and net orbital angular momenta are dominated by the CW component, which is opposite to the previous one seen in Fig. 3.26(a) and (b). From these observations, we can conclude that due to the breaking of chiral symmetry at the boundary of the defect cavity, the high-Q mode contain net orbital angular momenta and thus form an optical vortex.

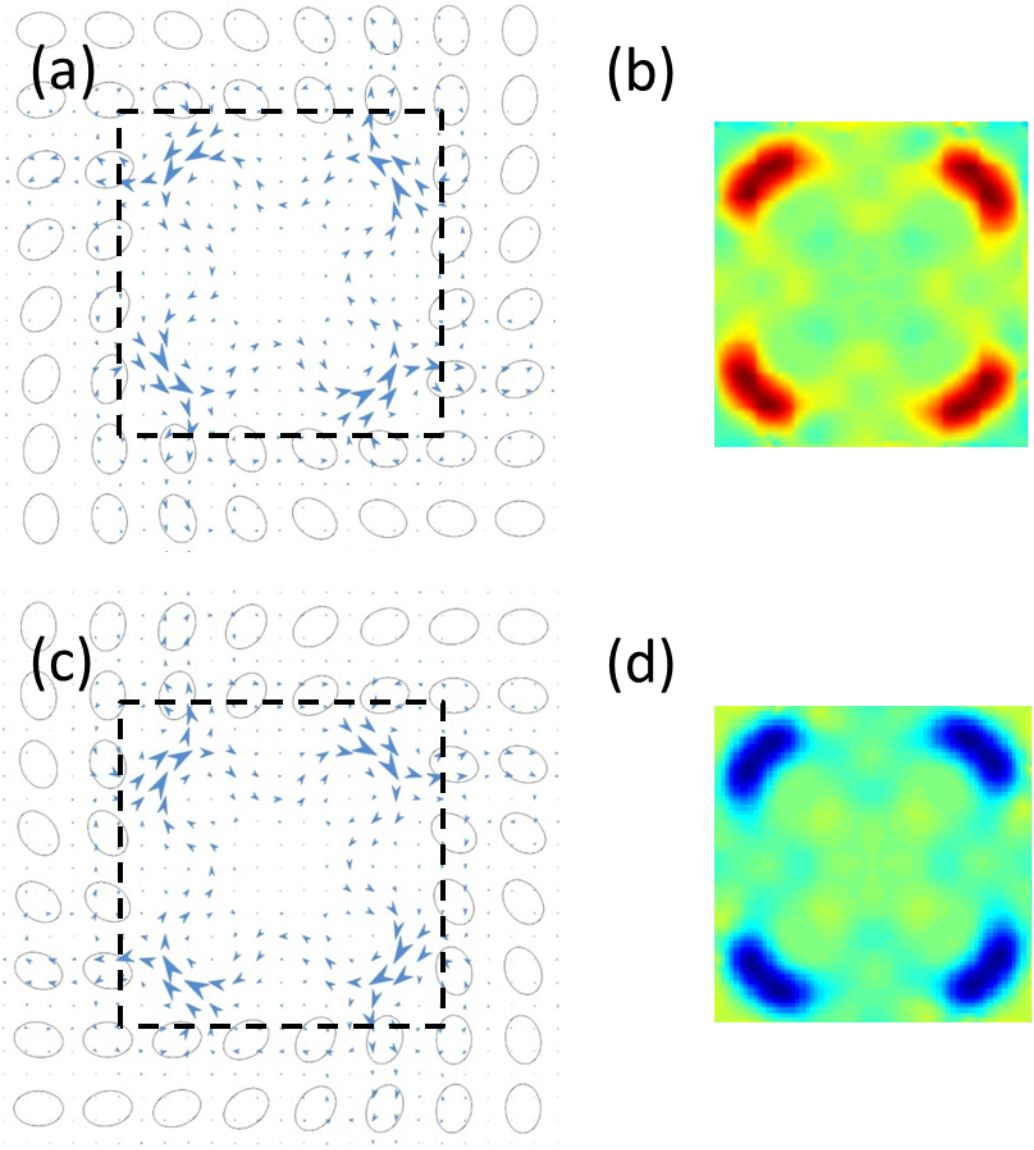

Figure 3.26: Optical vortices generation in a defect cavity with broken chiral symmetry. (a) Arrows plot of the Poynting vectors within the defect cavity showing a net flow of flux in the counter-clockwise direction. (b) Spatial distribution of the angular momentum density J_z within the boxed region of the mode in (a), showing it mainly has net orbital angular momenta in the counter-clockwise direction and thus it forms an optical vortex. (c) This structure contains the opposite "charge" compared to (a). Consequently, the net energy flow also flips to become clockwise. (d) The optical vortex now have net orbital angular momenta in the clockwise direction.

Bibliography

[1] S. F. Liew, J.-K. Yang, H. Noh, C. F. Schreck, E. R. Dufresne, C. S. O'Hern, and H. Cao, Phys. Rev. A **84**, 063818 (2011).

[2] J.D. Joannopoulos, S. Johnson, J. Winn, and R. Meade, Photonic Crystals: Molding the Flow of Light (Princeton University Press, Princeton, NJ, 2008).

[3] D. Levine and P.J. Steinhardt, Phys. Rev. Lett. **53**, 2477 (1984).

[4] Y.S. Chan, C.T. Chan, and Z.Y. Liu, Phys. Rev. Lett. **80**, 956 (1998).

[5] C. Jin, X. Meng, B. Cheng, Z. Li, and D. Zhang, Phys. Rev. B **63**, 195107 (2001).

[6] H. Miyazaki, M. Hase, H.T. Miyazaki, Y. Kurokawa, and N. Shinya, Phys. Rev. B **67**, 235109 (2003).

[7] K. Edagawa, S. Kanoko, and M. Notomi, Phys. Rev. Lett. **100**, 013901 (2008).

[8] C. Rockstuhl and F. Lederer, Phys. Rev. B **79**, 132202 (2009).

[9] M. Florescu, S. Torquato, and P. Steinhardt, Proc. Nat. Acad. Sci. Am. **106**, 20658 (2009).

[10] S. Imagawa, K. Edagawa, K. Morita, T. Niino, Y. Kagawa, and M. Notomi, Phys. Rev. B **82**, 115116 (2010).

[11] M. Rechtsman, A. Szameit, F. Dreisow, M. Heinrich, R. Keil, S. Nolte, and M. Segev, Phys. Rev. Lett. **106**, 193904 (2011).

[12] E.N. Economou and M.M. Sigalas, Phys. Rev. B **48**, 13434 (1993).

[13] R.D. Meade, A.M. Rappe, K.D. Brommer, and J.D. Joannopoulos, J. Opt. Soc. Am. B **10**, 328-332 (1993)

[14] G.T. Barkema and N. Mousseau, Phys. Rev. B **62**, 4985 (2000).

[15] P.D. García, R. Sapienza, C. López, Adv. Mater. **22**, 12 (2010).

[16] R.O. Prum, Bird Coloration(Harvard University Press, Cambridge, MA, 2006), Vol. 1, pp. 295-353.

[17] E. R. Dufresne, H. Noh, V. Saranathan, S. G. J.Mochrie, H. Cao, and R. O. Prum, Soft Matter **5**, 1792 (2009).

[18] H. Noh, S. F. Liew, V. Saranathan, S. G. J. Mochrie, R. O. Prum, E. R. Dufresne, and H. Cao, Adv. Mater. **22**, 2871 (2010).

[19] B.Q. Dong, X.H. Liu, T.R. Zhan, L.P. Jiang, H.W. Yin, F. Liu, and J. Zi, Opt. Express **18**, 14430 (2010).

[20] G.-J. Gao, J. Blawzdziewicz, and C.S. O'Hern, Phys. Rev. E **74**, 061304 (2006).

[21] C.S. O'Hern, L.E. Silbert, A.J. Liu, and S.R. Nagel, Phys. Rev. E **68**, 011306 (2003).

[22] O. Sigmund and K. Hougaard, Phys. Rev. Lett. **100**, 153904 (2008).

[23] J.-K. Yang, C. F. Schreck, H. Noh, S. F. Liew, M. I. Guy, Corey S. O'Hern, and H. Cao, Phys. Rev. A **82**, 053838 (2010).

[24] C. T. Chan, Q. L. Yu, and K. M. Ho, Phys. Rev. B **51**, 16635 (1995).

[25] P.-L. Chau and A.J. Hardwick, Mol. Phys. 93, 511 (1998).

[26] S. F. Liew, H. Noh, J. Trevino, L. Dal Negro, and H. Cao, Opt. Express **19**, 23631 (2011).

[27] P. Stevens, *Patterns in Nature* (Little, Brown and Co., New York, 1974).

[28] M. Naylor "Golden, $\sqrt{2}$, and π Flowers : A Spiral Story," Mathematics Magazine **75**, 163 (2002).

[29] A. Agrawal, N. Kejalakshmy, J. Chen, B. M. A. Rahman, and K. T. V. Grattan, "golden-angle spiral photonic crystal fiber : polarization and dispersion properties," Opt. Lett. **22**, 2716-2718 (2008).

[30] J. Trevino, H. Cao, and L. D. Negro, "Circularly Symmetric Light Scattering from Nanoplasmonic Spirals," Nano Lett. **11**, 2008-2016 (2010).

[31] M. E. Pollard and G. J. Parker, "Low-contrast bandgaps of a planar parabolic spiral lattice," Opt. Lett. **34**, 2805-2807 (2009).

[32] J. D. Joannopoulos, S. G. Johnson, J. N. Winn, and R. D. Meade, *Photonic Crystals: Molding the Flow of Light*, 2nd ed. (Princeton U. Press, Princeton, 2008).

[33] Y. S. Chan, C. T. Chan, and Z. Y. Liu, "Photonic Band Gaps in Two Dimensional Photonic Quasicrystals," Phys. Rev. Lett. **80**, 956 (1998).

[34] M. Florescu, S. Torquato, and P. J. Steinhardt, "Complete band gaps in two-dimensional photonic quasicrystals," Phys. Rev. B **80**, 155112 (2009).

[35] D. Lusk, I. Abdulhalim, F. Placido, "Omnidirectional reflection from Fibonacci quasi-periodic one-dimensional photonic crystal," Opt Commun **198**, 273 (2001).

[36] W. Steurer and D. Sutter-Widmer, "Photonic and phononic quasicrystals," J. Phys. D: Appl. Phys. **40**, R229 (2007).

[37] L. Dal Negro, C. J. Oton, Z. Gaburro, L. Pavesi, P. Johnson, A. Lagendijk, R. Righini, M. Colocci, and D. S. Wiersma, "Light transport through the band-edge states of Fibonacci quasicrystals," Phys. Rev. Lett. **90**, 055501 (2003).

[38] H. Vogel, "A better way to construct the sunflower head," Mathematical Biosciences **44**, 179 (1979).

[39] http://www.comsol.com

[40] R. Barboza, U. Bortolozzo, G. Assanto, E. Vidal-Henriquez, M. G. Clerc, and S. Residori, Phys. Rev. Lett. **109**, 143901 (2012).

[41] E. Brasselet, Phys. Rev. Lett. **108**, 087801 (2012).

[42] C. Loussert, U. Delabre, and E. Brasselet, Physical Review Letters **111**, 037802 (2013).

[43] S. V. Boriskina and B. M. Reinhard, Opt. Express **19**, 22305 (2011).

[44] S. V. Boriskina and B. M. Reinhard, Nanoscale **4**, 76 (2012).

Chapter 4

Short-range Order and Near-Field Effects on Optical Scattering and Structural Coloration

4.1 Introduction

[1] Structural color, which has been widely employed in nature, originates from light scattering by nanostructures with spatial variation in the refractive index on the scale of optical wavelengths. The most studied examples are periodic structures that produce iridescent color via Bragg scattering [2, 3]. In recent years, there is a growing interest in the previously unappreciated class of quasi-ordered structures that can generate non-iridescent color [4–8]. Such structures have only short-range order and are isotropic, making color invariant with viewing angle in natural lighting conditions. Biomimetic samples have been fabricated by self-assembly of colloidal particles [8, 9], and have potential applications in wide-angle color displays [10–12].

We recently studied the mechanism of coloration of quasi-ordered nanostructures

1. This chapter is primarily based on the work published in ref. [1].

in feather barbs of many bird species [5]. Single scattering of light [7], with contributions from double scattering [13, 14], is shown to determine the color. The angular dispersion and polarization characteristic of the major/secondary peak in the scattering spectra agree well to the predictions of single/double scattering. Local structural correlation leads to strong backward scattering of light within a narrow frequency range, which is selected by the characteristic length scale of the structure. A puzzle left from our previous study is why only low-order scattering events are observed from those structures even though simple estimations of scattering length would predict strong multiple scattering. As an example, Fig. 4.1 shows part of a cross-sectional transmission electron micrograph (TEM) of the feather barb of *Cotinga maynana* (a blue green bird). The nanostructured layer underneath the cortex is about 10 μm thick, and consists of random close-packed [15,16] spherical air cavities in a β-keratin matrix. The transport mean free path l_t of light in this structure, assuming independent scattering approximation, is significantly smaller than the thickness of the nanostructured layer. Thus, one might expect that multiple scattering to dominate over single scattering and remove wavelength dependence in the reflection spectrum. However, such structures create vivid colors in reflection as shown in Ref. [5]. The dominant peak in the optical scattering spectrum coincides with the X-ray scattering peak, confirming the former is from single scattering of light [7].

To resolve this puzzle, we have directly measured the transport mean free path l_t in biomimetic samples, which are made of random close-packed dielectric spheres in air [Fig. 4.2]. The reason we use biomimetic samples instead of biological samples is that the nanostructured layers in the latter [Fig. 4.1] are too thin for the coherent backscattering (CBS) experiment which we perform to extract l_t [17]. We find an order of magnitude difference between the measured value of l_t and the estimated one over a broad frequency range. Our theoretical analysis reveals that short-range order and near-field effects reduce the overall (angle-integrated) scattering strength and in-

crease l_t dramatically. Thus, in the biological samples which have similar scattering strength as the biomimetic samples, the transport mean free path is comparable to the thickness of nanostructured layer. Consequently, single scattering is much stronger than multiple scattering, and dominates coloration.

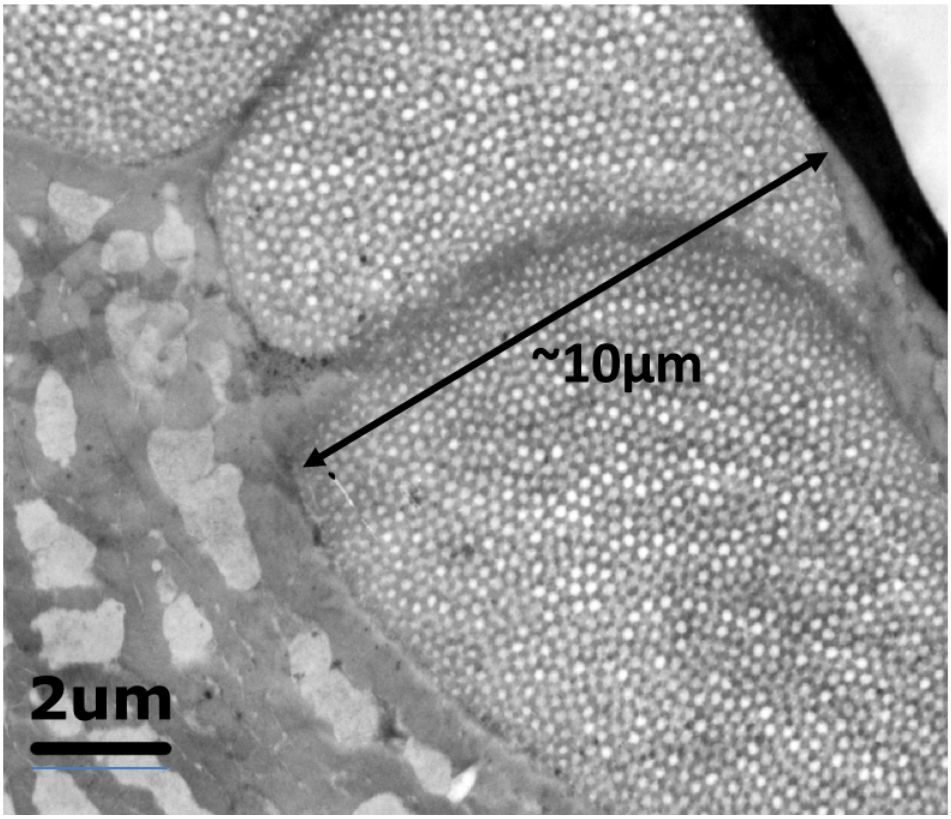

Figure 4.1: Transmission electron micrograph (TEM) showing the amorphous photonic structure (right part) in a feather barb of *Cotinga maynana* that produces blue color. Uniform spherical air cavities (white) are closely packed in β-keratin (grey). The structure is isotropic and has only short-range order.

4.2 Measurement of transport mean free path

To avoid polycrystalline structures that can be easily formed with monodisperse spheres, we fabricate the biomimetic samples by self-assembly of bi-disperse spheres of

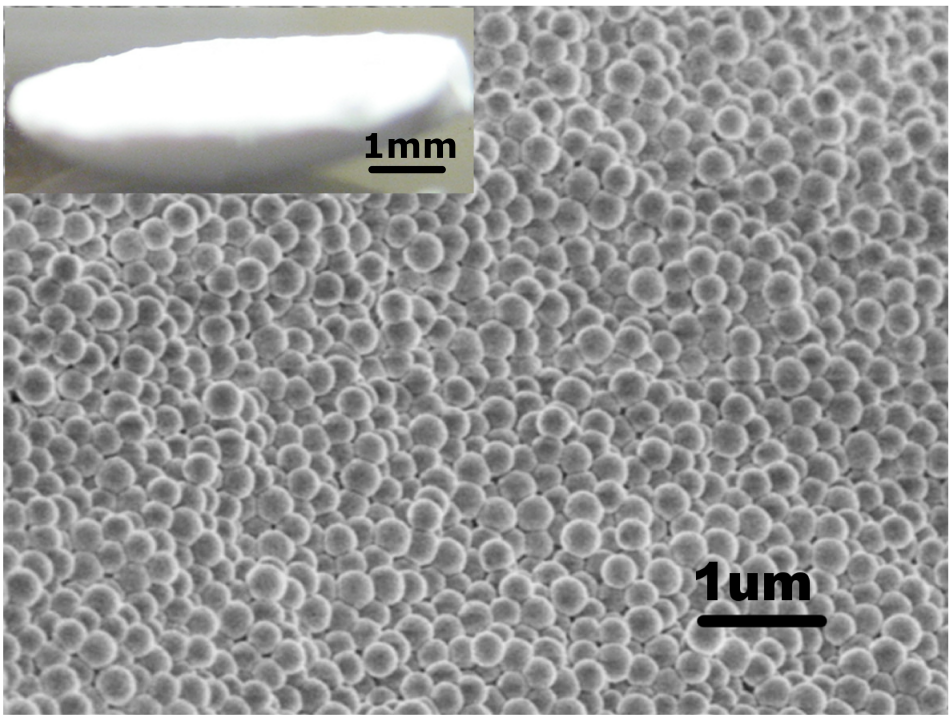

Figure 4.2: Scanning electron micrograph (SEM) of our biomimetic sample made of random close-packed polystyrene spheres of two sizes. Inset is a photo image of the entire sample.

polystyrene [18]. Fabrication of the samples were performed in Prof. Eric Dufresne's lab in Yale by Dr. Jason Forster. First, the monodisperse spheres are synthesized using a surfactant-free polymerization technique [8, 19]. The sphere size can be varied by changing the methanol concentration. Then, equal volumes of monodisperse suspensions with polydispersity of 2% are mixed to make a bi-disperse suspension. An approximate 0.5 mL droplet of this bi-disperse suspension is pipetted into a 5 cm diameter petri dish containing 5 mL of Fluorinert FC-70. The suspension droplet is almost completely surrounded by Fluorinert, allowing slow evaporation of water. After all the water has evaporated from the suspension, the sample is removed from Fluorinert, and placed on a Kimwipe to allow any residual Fluorinert to drain from the sample. The final sample has a dome shape [inset of Fig. 4.2]. The maximum thickness at the center is about 1 mm, much larger than the thickness of nanostructured layers in bird feather barbs [Fig. 4.1].

Figure 4.2 is a scanning electron micrograph (SEM) taken from the interior surface of a cracked sample. It shows the polystyrene spheres are random close-packed. This structure is the inverse of that with air spheres in the bird feather [Fig. 4.1]. It also resembles the color-producing structures made of dielectric spheres in some species of beetles [6]. We have performed small-angle X-ray scattering (SAXS) measurement on the sample for quantitative structural characterization. The SAXS data yield a diffused ring pattern as shown in the inset of Fig. 4.3(a), indicating the structure is isotropic. Azimuthal-averaged SAXS intensity (black solid curve) in Fig. 4.3(a) reveals that our structure has a dominant spatial frequency $q_o = 0.03$ nm^{-1}. The corresponding spatial periodicity is $a = 2\pi/q_o = 210$ nm. The form factor of monodisperse spheres causes regular oscillation of SAXS intensity at large q value, where the structure factor diminishes. Since our sample has bi-disperse spheres, there are two oscillations with slightly different periods. Their beating can be clearly seen in Fig. 4.3(b) (black solid curve). By fitting the oscillation and beating of the SAXS intensity with the analytical expression of form factors [red dashed line in Fig. 4.3(b)], the diameters of two spheres are found to be 223 nm and 265 nm respectively.

To characterize the scattering properties of our biomimetic samples, we have performed coherent backscattering (CBS) experiment to obtain the transport mean free path l_t as a function of wavelength λ. A supercontinuum light source is used to cover a broad range of λ from 520 nm to 700 nm. Beyond this range, several lasers with operation wavelengths of 406 nm, 445 nm, and 473 nm are used to probe scattering at shorter λ. Supercontinuum light is generated in a photonic crystal fiber by femtosecond pulses from a mode-locked Ti:Sapphire laser (pulse width $\sim$ 200 fs, repetition rate 76 MHz). The output beam is dispersed by a diffraction grating, and a slit picks light at certain wavelength (with a bandwidth of 5 nm). The filtered light is collimated and incident on the sample after passing through a linear polarizer. The illumination spot on the sample surface is about 2 mm in diameter. The sample is

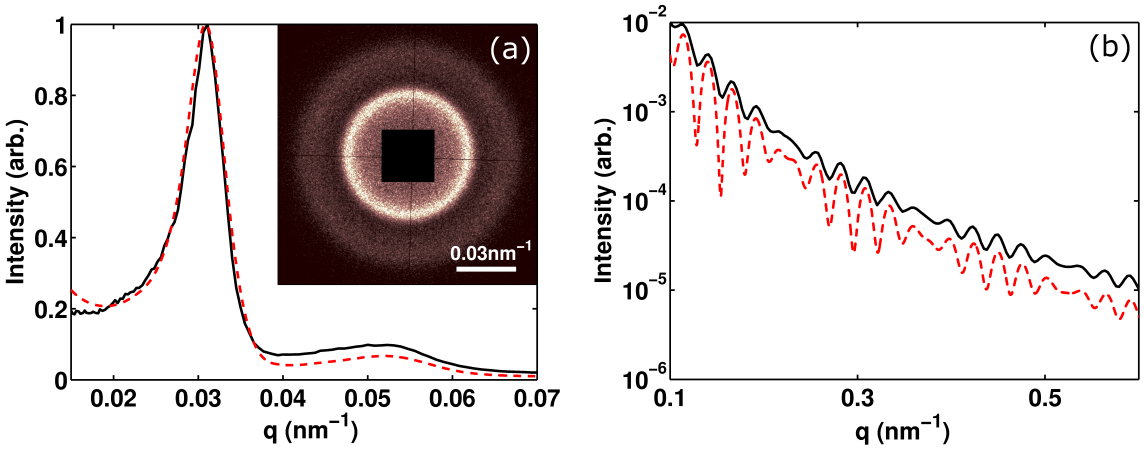

Figure 4.3: Small Angle X-ray Scattering (SAXS) measurement of the biomimetic sample. (a) SAXS pattern (inset) showing an isotropic ring pattern. The azimuthal-averaged SAXS intensity (black solid line in main panel) reveals the existence of a dominant spatial frequency in the structure. The red-dashed curve is obtained from the power Fourier spectrum of a computer-simulated structure shown in Fig.4.6(a). (b) Log-linear plot of SAXS intensity (black solid line) at high q value featuring the oscillation and beating, caused by the form factors of bi-disperse spheres. Red dashed curve is from the calculation with form factors of two spheres with diameters 265 nm and 223 nm. The red dashed curve is shifted vertically for better comparison.

tilted in such a way that the surface reflection of the incident beam deviates from the backscattering direction.

The scattered light with polarization parallel to the incident one is detected by a photomultiplier tube. An optical chopper and a lock-in amplifier are used to enhance the signal to noise ratio. The scattered light intensity I_s is measured as a function of angle θ_B from the backscattering direction. The sample is rotated during the measurement to smear out the speckle pattern. Figure 4.4 shows the measured $I_s(\theta_B)$ at $\lambda = 473$ nm, 580 nm and 660 nm. As λ increases, the CBS cone becomes narrower, indicating l_t is longer. The measured $I_s(\theta_B)$ is fitted by the analytical expression of CBS intensity [17], taking into account the finite angular resolution $\delta\theta$ of the experimental apparatus. By replacing the scattering sample with a highly-reflective mirror, we determine $\delta\theta \simeq 0.6$ mrad. Fitting parameters for $I_s(\theta_B)$ are the enhancement factor, the constant background from single scattering, and the transport mean free path

l_t. By repeating the CBS measurement at many wavelengths, we obtain l_t as a function of λ (black squares in Fig. 4.5]. The fitting error for all data points are below 5%.

4.3 Theoretical analysis

To interpret the experimental data, we estimate $l_t = (\rho\sigma_t)^{-1}$ from the transport cross section σ_t [20],

$$\sigma_t = \frac{\pi}{k^2}\int_0^\pi B(\theta)\sin\theta(1-\cos\theta)d\theta, \tag{4.1}$$

where

$$B(\theta) = xF_{11}(\theta)S_{11}(\theta) + (1-x)F_{22}(\theta)S_{22}(\theta) + 2\sqrt{x(1-x)}F_{12}(\theta)S_{12}(\theta). \tag{4.2}$$

The partial structure factors for the bi-disperse system are

$$S_{11}(q) = \frac{1}{\sqrt{N_1N_1}}\langle\sum_{n,m} e^{i\mathbf{q}\cdot(\mathbf{r}_n^{(1)}-\mathbf{r}_m^{(1)})}\rangle - \sqrt{N_1N_1}\delta(q), \tag{4.3}$$

$$S_{22}(q) = \frac{1}{\sqrt{N_2N_2}}\langle\sum_{n,m} e^{i\mathbf{q}\cdot(\mathbf{r}_n^{(2)}-\mathbf{r}_m^{(2)})}\rangle - \sqrt{N_2N_2}\delta(q), \tag{4.4}$$

$$S_{12}(q) = \frac{1}{\sqrt{N_1N_2}}\langle\sum_{n,m} e^{i\mathbf{q}\cdot(\mathbf{r}_n^{(1)}-\mathbf{r}_m^{(2)})}\rangle - \sqrt{N_1N_2}\delta(q). \tag{4.5}$$

The binary form factors are $F_{11} = f_{s,1}f_{s,1}^* + f_{p,1}f_{p,1}^*$, $F_{22} = f_{s,2}f_{s,2}^* + f_{p,2}f_{p,2}^*$, and $F_{12} = Re[f_{s,1}f_{s,2}^* + f_{p,1}f_{p,2}^*]$ [21–23]. Particles with diameter 265 nm are labeled as 1, and 223 nm as 2. N_1 and N_2 denote the numbers of larger and smaller particles respectively. $x = N_1/(N_1+N_2)$ is the fraction of larger particles in the mixture, which is 0.4 in our sample. f_s and f_p are the scattering amplitudes of two orthogonal polarizations from a spherical particle, which can be calculated by Mie scattering

theory [24]. $k = 2\pi n_{eff}/\lambda_o$ is the scattering wave vector, where n_{eff} is the effective refractive index of the scattering medium. $q = 2k\sin(\theta/2)$ is the spatial frequency, where θ is the scattering angle ranging from 0° in the forward direction to 180° in the backward direction. The particle density is $\rho = \phi/[xv_1 + (1-x)v_2]$, where v_1 and v_2 are the volumes of particles with diameter 265 nm and 223 nm respectively.

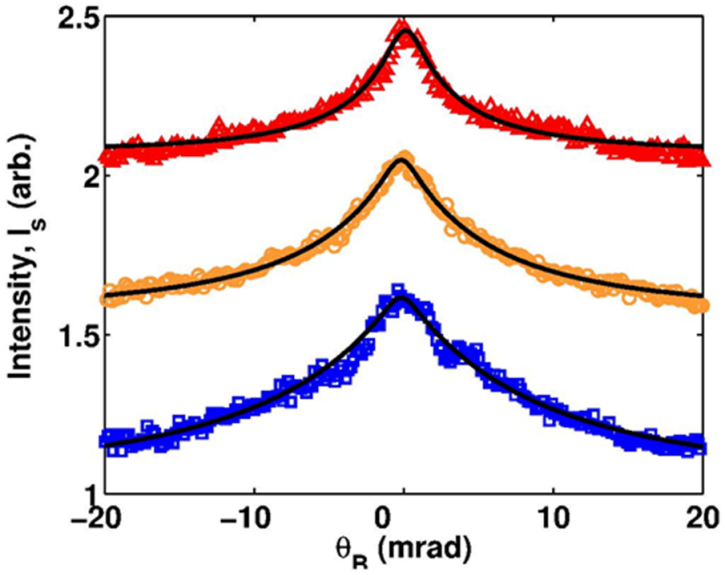

Figure 4.4: Coherent backscattering (CBS) measurement (a) CBS intensity I_s vs. scattering angle θ_B, measured at $\lambda = 660$ nm (red triangle), 580 nm (orange circle) and 473 nm (blue square). $\theta_B = 0$ in the backscattering direction. Black solid lines represent the fitted curves.

We start with a simple estimation of l_t in our sample with two assumptions. First, we assume independent scattering of light by individual particles. Secondly, we ignore the short-range order by assuming the particles are randomly located without any correlation, namely, $S_{11} = 1$, $S_{22} = 1$, and $S_{12} = 0$. The dielectric spheres have the refractive index of $n = 1.58$, and the filling fraction of $\phi = 64\%$ [25]. The form factors are calculated from optical scattering of individual dielectric spheres in air. The computed value of l_t is plotted by the green dash-dotted line in Fig. 4.5.

Next, we take into account local correlation of particle position in the random

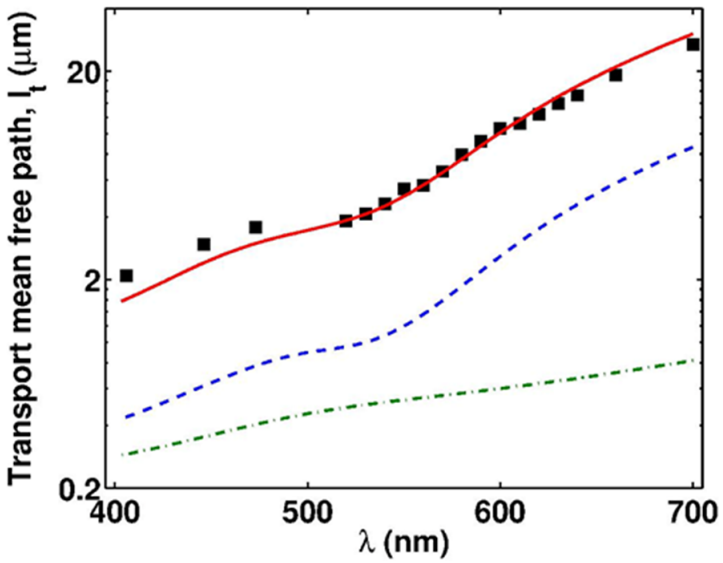

Figure 4.5: Measured (black square) and estimated (lines) transport mean free path l_t vs. wavelength λ. Green dash-dots curve represents l_t estimated without short-range order and near-field effects, blue dashed line is with short-range order but no near-field effects, and red solid curve is with both.

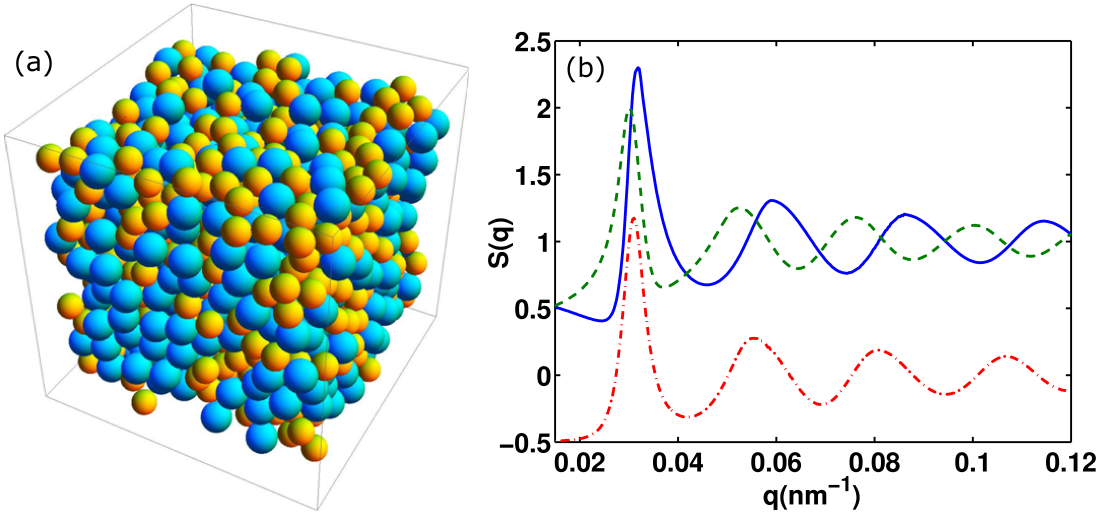

Figure 4.6: (a) Computer-simulated structure of random close-packed spheres of diameters 265 nm (blue) and 223 nm (yellow). (b) Partial structure factors computed for the structure in (a). Blue solid curve is S_{11}, green dashed curve S_{22}, and red dash-dots curve S_{12}.

close-packed structure by including the structure factors of the bi-disperse system in the estimation of l_t. However, it is very difficult, if not impossible, to accurately extract all partial structure factors S_{11}, S_{22}, and S_{12} from the SAXS data. Alternatively, they are obtained from a computer-simulated random close-packed system of 1000 bi-disperse spheres of diameters equal to the experimental values [Fig. 4.6(a)] using the methods described in Ref. [26]. The filling fraction is 64% [25]. The partial structure factors are calculated from the center positions of all spheres and plotted in Fig. 4.6(b). Power Fourier spectrum, computed by Fourier transform of this structure, matches well the azimuthal-averaged SAXS intensity in Fig. 4.3(a). This agreement confirms that our sample has a filling fraction of 64%, because with identical sphere sizes and number ratio x of bi-disperse spheres, the dominant spatial frequency would coincide only if the filling fraction is the same. The estimated l_t is plotted by the blue dashed line in Fig. 4.5. Its value is increased from the previous estimation as a result of short-range order. This result is a little surprising, as structural correlation is often thought to enhance light scattering, at least, at certain wavelength. Short-range structural order introduces the phase correlation of light scattered by adjacent particles, leading to constructive interference in certain direction and destructive interference in other directions. To be more concrete, let us consider light with an incident wave vector $\mathbf{k}_i$ being scattered to a wave vector $\mathbf{k}_o$. The scattering is elastic, $|\mathbf{k}_i| = |\mathbf{k}_o| = k$. The difference between $\mathbf{k}_i$ and $\mathbf{k}_o$ is provided by the spatial vector $\mathbf{q}$ of the structure, $\mathbf{k}_o - \mathbf{k}_i = \mathbf{q}$. For example, in the backward scattering direction, $\mathbf{k}_o = -\mathbf{k}_i$, thus $2k = q$. The dominant spatial frequency q_o of the random close-packed system causes the strongest backward scattering at $k = q_o/2$. Consequently, l_t exhibits a shallow "dip" at the corresponding $\lambda \approx 550$ nm [blue dashed line in Fig. 4.5] [27]. More generally, for any $k > q_o/2$, short-range structural order introduces a phase correlation of light scattered by adjacent particles. They constructively interfere in specific directions, enhancing the scattered light intensity. However, in all other

directions they interfere destructively, suppressing light scattering. The suppression of scattering intensity occurs in many more directions than the enhancement. Hence, the total (angle-integrated) scattering strength reduces and l_t increases. It has been shown in Ref. [28] that short-range order reduces scattering and is responsible for the transparency of cornea to visible light. However, in Ref. [28], the characteristic length scale of the nanostructure is about an order of magnitude smaller than the optical wavelength, while in our case they are comparable.

In the above two estimations of l_t, we calculate the form factors by assuming the particles are situated in a background of air. However, in a random close-packed system, particles are in contact with each other, and the scattering cross section of a particle is affected by the presence of nearby particles [29]. The near-field coupling of the adjacent particles modifies the form factor of an "average" particle. Such near-field effects have been reported in the study of white pigmentation using TiO_2 particles [30] and it is called optical crowding. Scattering of solar electromagnetic radiation by dust particles in the atmosphere or on the surface of celestial bodies are also affected by the near-field effects [31]. To take into account the near-field effects in our random close-packed sample, the form factors of particles are computed by assuming each particle is effectively surrounded by a homogeneous dielectric background of refractive index n_b. The value of n_b is obtained by averaging the actual refractive index surrounding a particle with a weighting factor from an exponentially-decaying evanescent field. Namely,

$$n_b = \frac{\int_0^\infty n(r) e^{-\alpha r/\lambda_o} r^2 dr}{\int_0^\infty e^{-\alpha r/\lambda_o} r^2 dr} \tag{4.6}$$

where r is the distance from a particle's surface, $n(r)$ is the ensemble-averaged refractive index based on on the sphere packings described above, and α is a fitting parameter that we expect to depend on the refractive indices of the particles and the

surrounding medium as well as the local particle packing geometry. We can calculate l_t for any value of α using the modified form factors with background refractive index n_b from Eq.(4.6). The least square fitting between the measured and estimated values of l_t for all probed wavelengths gives $\alpha = 14.1 \pm 3.2$. The relative standard error is $\approx 9\%$. With larger/smaller α value, the magnitude of l_t decreases/increases, but the shape of the curve remain constant. The final estimated l_t which includes the short-range order and near-field effects is plotted by red solid line in Fig. 4.5, and in good agreement with the experimental values at all measured wavelengths. This result indicates that short-range order and near-field effects reduce the scattering strength by one order of magnitude in random close-packed structures.

4.4 Discussion and Conclusion

Although the transport mean free path has been well studied in disordered photonic crystals with long-range order [32–35], there have been only a few studies on amorphous photonic structures with short-range order. It has been shown in colloidal liquids, local order induces a local minimum of the transport mean free path [27]. Since the particles are not closely packed, the near-field effect is negligible. In Ref. [29], l_t is shown to increase at high filling fraction of a random close-packed random film of monodisperse dielectric spheres. This result is explained by accounting for evanescent wave coupling of contacting spheres. The modification of near-field scattering environment is included in the form factors of isolated scatterers in an effective dielectric background. The background refractive index is obtained after setting a coupling length that scales linearly with λ. Following this method, we calculate n_b as a function of wavelength and plot (with blue dashed line) in Fig. 4.7(a). Its value displays a sharp rise at $\lambda \sim 200$ nm. Within the wavelength range of our study, its value

is nearly invariant with λ. The l_t calculated with this background index is roughly 3 times larger than the measured values for our samples (not shown). For comparison, we plot (with black solid line) in Fig. 4.7(a) the value of n_b obtained from Eq.(4.6) with $\alpha = 14.1$. It has a much more gradual increase with λ. The background index n_b is notably lower within the wavelength range of our measurement. The good agreement between the estimated l_t with this n_b and the measured values over a broad wavelength range clearly shows that our proposed model works better to incorporate the near-field effects in a random close-packed scattering environment. The asymptotic behavior of n_b can be understood as follows. At longer wavelength, the near-field of a particle would extend farther away, coupling to more particles and probe the global environment. Thus the background refractive index approaches that of a homogenized medium which is $n_h = 1.39$ in our case. In the short-wavelength limit, the particle would only be able to sense its immediate environment and n_b approaches the refractive index of air. As an example, we plot in Fig. 4.7(b) the scattering efficiency Q_{sca} of a dielectric sphere in different backgrounds. Q_{sca} is defined as the ratio of the total scattering cross section over the geometrical cross section of a sphere. The sphere diameter is 244 nm and the refractive index is 1.58. Q_{sca} calculated with background n_b from Eq. (4.6) approaches that of scattering in air at short wavelength, and that in homogenized medium of n_h at long wavelength.

Assuming the same α value, we have estimated $l_t \approx 5\mu$m at $\lambda = 540$ nm the center wavelength of the major reflection peak for the nanostructures of bird feather barb as shown in Fig. 4.1. Thus, l_t is comparable to the total thickness of the scattering nanostructures, and single scattering is dominant over multiple scattering to produce color. However, the nanostructures of bird feather barb (air cavities embedded in β-keratin) are inverse of the biomimetic structures (dielectric spheres in air), and the value of α is likely to be different. We expect the α value determined here is not

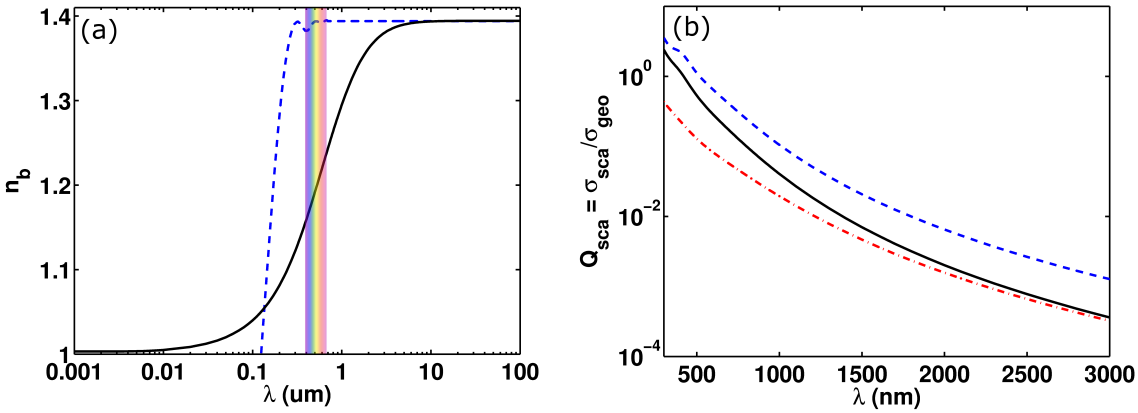

Figure 4.7: (a) Near-field effects on form factors can be included in an effective background refractive index n_b, whose value is calculated from Eq.(4.6). It approaches the refractive index of air at short wavelength, and that of a homogenized medium at long-wavelength. The wavelength range of our CBS measurement is highlighted with color. For comparison, the value of n_b obtained from Ref. [29] is plotted with blue dashed line. (b) Calculated scattering efficiency Q_{sca} of a dielectric sphere in different backgrounds. The sphere has a diameter 244 nm and a refractive index of 1.58. $Q_{sca} = \sigma_{sca}/\sigma_{geo}$ is the ratio of the scattering cross section σ_{sca} to the geometical cross section σ_{geo}. The refractive index of the background is equal to n_b from Eq.(4.6) (black solid line), $n_h = 1.39$ of the homogenized medium (blue dashed line), and that of air 1 (red dash-dotted line).

universal, since it depends on the properties of the scatterer and its surrounding. It is sensitive to the parameters such as ratio of refractive index of scatterer with its background, size of scatterer and maybe the packing geometry. Hence, further study of light scattering by systematic tuning of the above mentioned parameters has the potential of fully characterizing α, and providing physical insight to dependent scattering.

In summary, we have measured the transport mean free path l_t with coherent backscattering in amorphous photonic structures over a broad wavelength range. Such structures are made of random close-packed dielectric spheres of two sizes, and have only short-range order. The measured l_t is significantly larger than the estimated value based on the assumptions of independent scattering and the absence of structural order. With particles in close contact with one another, we must consider the phase correlation of scattered light and local scattering environment. Short-range order accounts for the interference of light scattered from particles located in close proximity. Near-field effects originate from the evanescent wave coupling of adjacent particles and leads to reduced refractive index contrast between particles and surrounding. Both increase the transport mean free path. Since many color-producing biological nanostructures consist of random close-packed dielectric or air spheres, we expect both effects exist. They increase l_t and make it comparable to the total size of the nanostructure. Consequently, single scattering becomes dominant over multiple scattering, and is responsible for structural coloration.

Bibliography

[1] S. F. Liew, J. Forster, H. Noh, C. F. Schreck, V. Saranathan, X. Lu, L. Yang, R. O. Prum, C. S. OHern, E. R. Dufresne, and H. Cao, Opt. Express **19**, 8208 (2011).

[2] P. Vukusic and J. R. Sambles, "Photonic structures in biology," Nature **424**, 852–855 (2003).

[3] S. Kinoshita, S. Yoshioka, and J. Miyazaki, "Physics of structural colors," Rep. Prog. Phys. **71**, 076401 (2008).

[4] R. O. Prum, R. H. Torres, S. Williamson, and J. Dyck, "Coherent light scattering by blue bird feather barbs," Nature (London) **396**, 28–29 (1998).

[5] E. R. Dufresne, H. Noh, V. Saranathan, S. G. J. Mochrie, H. Cao, and R. O. Prum, "Self-assembly of amorphous biophotonic nanostructures by phase separation," Soft Matter **5**, 1792–1795 (2009).

[6] B. Q. Dong, X. H. Liu, T. R. Zhan, L. P. Jiang, H. W. Yin, F. Liu, and J. Zi, "Structural coloration and photonic pseudogap in natural random close-packing photonic structures," Opt. Express **18**, 14430–14438 (2010).

[7] H. Noh, S. F. Liew, V. Saranathan, R. O. Prum, S. G. J. Mochrie, E. R. Dufresne, and H. Cao, "How non-iridescent colors are generated by quasi-ordered structures of bird feathers," Adv. Mater. **22**, 2871–2880 (2010).

[8] J. D. Forster, H. Noh, S. F. Liew , V. Saranathan , C. F. Schreck, L. Yang, J.-G. Park, R. O. Prum, S. G. J. Mochrie , C. S. O'Hern , H. Cao, and E. R. Dufresne, "Biomimetic isotropic nanostructures for structural coloration," Adv. Mater. **22**, 2939–2944 (2010).

[9] M. H.- Ur-Rashid, A. B. Imran, T. Seki, M. Ishii, H. Nakamura, and Y. Takeoka, "Angle-independent structural color in colloidal amorphous arrays," Chemphyschem **11**, 579–583 (2010).

[10] Y. Takeoka, M. Honda, T. Seki, M. Ishii, and H. Nakamura, "Structural colored liquid membrane without angle dependence," ACS Appl. Mater. & Interfaces **1**, 982–986 (2009).

[11] K. Ueno, A. Inaba, Y. Sano, M. Kondoh, and M. Watanabe, "A soft glassy colloidal array in ionic liquid, which exhibits homogenous, non-brilliant and angle-independent structural colors," Chem. Commun., 3603–3605 (2009).

[12] I. Lee, D. Kim, J. Kal, H. Baek, D. Kwak, D. Go, E. Kim, C. Kang, J. Chung, Y. Jang, S. Ji, J. Joo, and Y. Kang, "Quasi-amorphous colloidal structures for electrically tunable full-color photonic pixels with angle-independency," Advanced Materials **22**, 4973–4977 (2010).

[13] H. Noh, S. F. Liew, V. Saranathan, R. O. Prum, S. G. J. Mochrie, E. R. Dufresne, and H. Cao, "Double Scattering of light from biophotonic nanostructures with short-Range Order," Optics Express, **18**, 11942–11948 (2010).

[14] H. Noh, S. F. Liew, V. Saranathan, R. O. Prum, S. G. J. Mochrie, E. R. Dufresne, and H. Cao, "Contribution of double scattering to structural coloration in quasi-ordered nanostructures of bird feathers," Phys. Rev. E, **81**, 051923 (2010).

[15] S. Torquato, T. M. Truskett, and P. G. Debenedetti, "Is Random Close Packing of Spheres Well Defined?,"Phys. Rev. Lett. **84**, 2064–2067 (2000).

[16] J. G. Berryman, "Random close packing of hard spheres and disks," Phys. Rev. A **27**, 1053–1061 (1983).

[17] E. Akkermans and G. Montambaux, *Mesoscopic Physics of Electrons and Photons* (Cambridge University Press, 2007).

[18] C. F. Schreck and C. S. O'Hern, "Computational methods to study jammed systems", in Experimental and Computational Techniques in Soft Condensed Matter Physics, ed. by J. S. Olafsen, (Cambridge University Press, New York, 2010).

[19] Y. Chonde and I. M. Krieger, "Emulsion polymerization of styrene with ionic comonomer in the presence of methanol," Journal of Applied Polymer Science, **26**, 1819–1827 (1981).

[20] S. Fraden and G. Maret, "Multiple light scattering from concentrated, interacting suspensions," Phys. Rev. Lett. **65**, 512–515 (1990).

[21] L. Blum and G. J. Stell, "Scattering function for polydisperse fluids of hard or permeable spheres,"J. Chem. Phys. **71**, 42–46 (1979).

[22] W. L. Griffith, R. Triolo, and A. L. Compere, "Analytical scattering function of a polydisperse Percus-Yevick fluid with Schulz -(Γ-) distributed diameters," Phys. Rev. A **35**, 2200–2206 (1987).

[23] Y. Huang, Z. Sun, and E. M. Sevick-Muraca, "Assessment of electrostatic interactions in dense colloidal suspensions with multiply scattered light," Langmuir **18**, 2048–2053 (2002).

[24] H. C. van de Hulst, *Light Scattering by Small Particles* (Dover, New York, 1981).

[25] C. S. O'Hern, L. E. Silbert, A. J. Liu, and S. R. Nagel, "Jamming at zero temperature and zero applied stress: The epitome of disorder," Phys. Rev. E **68**, 011306 (2003).

[26] G.-J. Gao, J. Blawzdziewicz, and C. S. O'Hern, "Frequency distribution of mechanically stable disk packings," Phys. Rev. E **74**, 061304 (2006).

[27] L. F. Rojas-Ochoa, J. M. Mendez-Alcaraz, J. J. Sáenz, P. Schurtenberger, and F. Scheffold, "Photonic properties of strongly correlated colloidal liquids," Phys. Rev. Lett. **93**, 073903 (2004).

[28] R. W. Hart and R. A. Farrell, "Light scattering in the cornea," J. Opt. Soc. Am. **59**, 766–773 (1969).

[29] X. T. Peng and A. D. Dinsmore, "Light propagation in strongly scattering, random colloidal films: the role of the packing geometry," Phys. Rev. Lett. **99**, 143902 (2007).

[30] L. E. McNeil, R. H. French, "Multiple scattering from rutile TiO2 particles," Acta Mater. **48**, 4571–4576 (2000).

[31] E. V. Petrova, V.P. Tishkovets, and K. Jockers, "Interaction of particles in the near field and opposition effects in regolith-like surfaces," Solar System Research **43**, 100–115 (2009).

[32] A. F. Koenderink, M. Megens, G. van Soest, W. L. Vos and A. Lagendijk, "Enhanced backscattering from photonic crystals," Phys. Lett. A **268**, 104–111 (2000).

[33] J. Huang, N. Eradat, M. E. Raikh, and Z. V. Vardeny, "Anomalous coherent backscattering of light from optical photonic crystals," Phys. Rev. Lett. **86**, 4815–4818 (2001).

[34] A. F. Koenderink, A. Lagendijk, and W. L. Vos, "Optical extinction due to intrinsic structural variations of photonic crystals," Phys. Rev. B **72**, 153102 (2005).

[35] P. D. García, R. Sapienza, L. S. Froufe-Pérez, and C. López, "Strong dispersive effects in the light-scattering mean free path in photonic gaps," Phys. Rev. B **79**, 241109 (2009).

Chapter 5

Evolution of structural color on butterfly wings

5.1 Introduction

[1] Organisms produce colors in two basic ways: by synthesizing pigments that selectively absorb light of certain spectral bands and, thus, only light outside the absorption bands is backscattered (chemical color), or by developing nano-morphologies that enhance reflection of light of certain wavelengths by interference (physical color or structural color). Structural colors play major roles in natural and sexual selection in many species [2], and have a broad range of applications in color display, paint, cosmetics, and textile industries [3]. Structural color surveys across widely divergent species have revealed a large diversity of color-producing mechanisms [4–10]. However, there has been a lack of systematic study and comparison of how different colors from closely-related species or within populations of a single species evolve, even though their colors can vary dramatically. By examining how these species/populations evolve different colors, it is possible to identify the minimal amount of morphologi-

1. This chapter is primarily based on the work published in ref. [1].

cal change that results in significant color variation. Furthermore, this research may serve as an inspiration for future application of similar evolutionary principles to the design of photonic devices for color tuning, light trapping or beam steering [3, 11–21]. From an evolutionary biology point of view, we are curious to examine how structural colors respond to selection pressure, and whether there is sufficient standing genetic variation in natural populations to allow rapid evolution of novel colors. The butterflies were raised in the insectory of Prof. Antonia Monteiro's lab in Yale and the artificial selection experiment was carried out in her lab. Here we focus on determining the morphological changes and the physical mechanisms that cause the evolution of violet structural color in populations of a single species, and also across different species within a single genus of butterflies.

We focus on the genus Bicyclus (Lepidoptera: Nymphalidae), composed of more than 80 species that predominantly exhibit brown color along with marginal eyespots. Some Bicyclus species, however, have independently evolved transverse bands of bright violet/blue structural color on the dorsal surface of the forewings (black asterisks in Fig. 5.1(a)) [22, 23]. One species, Bicyclus anynana, has become a model species amenable to laboratory rearing, and multiple aspects of its marginal eyespots (size, relative width of the color rings, shape) have been altered by artificial selection [24–28]. However, change of color (hue), either pigmentary or structural, via artificial selection has not been reported. B. anynana does not exhibit bright violet coloration on its wings and therefore provides an excellent opportunity to investigate whether there is genetic potential to produce violet color upon directed selection. We investigated this potential by performing an artificial selection experiment in B. anynana that targeted the color of the specific dorsal wing region that evolved violet/blue coloration in other members of the genus [Fig. 5.1(b-g)].

B. anynana, like other butterflies, has two types of scales (cover and ground) which alternate each other within a row, with cover scales partially covering the

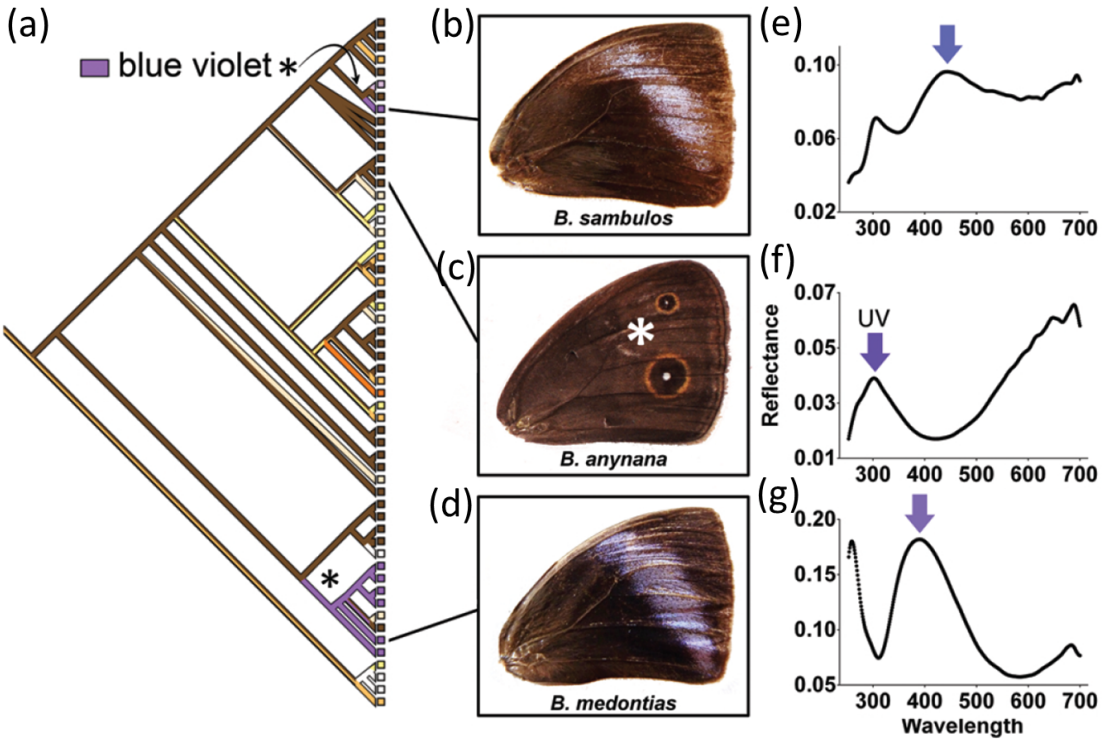

Figure 5.1: (a) A phylogenetic estimate of Bicyclus butterfly relationships (modified from [33]) illustrating the evolution of color in the genus. The black asterisks mark two clades that evolved violet/blue color independently, represented here by B. sambulos and B. medontias. (b-d) Dorsal wing images of B. sambulos, B. anynana (region used for artificial selection marked by white asterisk), and B. medontias. (e-g) Graphs of reflectance spectra of the blue/violet wing band showing reflectance peaks in the 400-450 nm range and in the brown-colored homologous region in B. anynana with a UV reflectance peak centered at 300 nm (colored arrows).

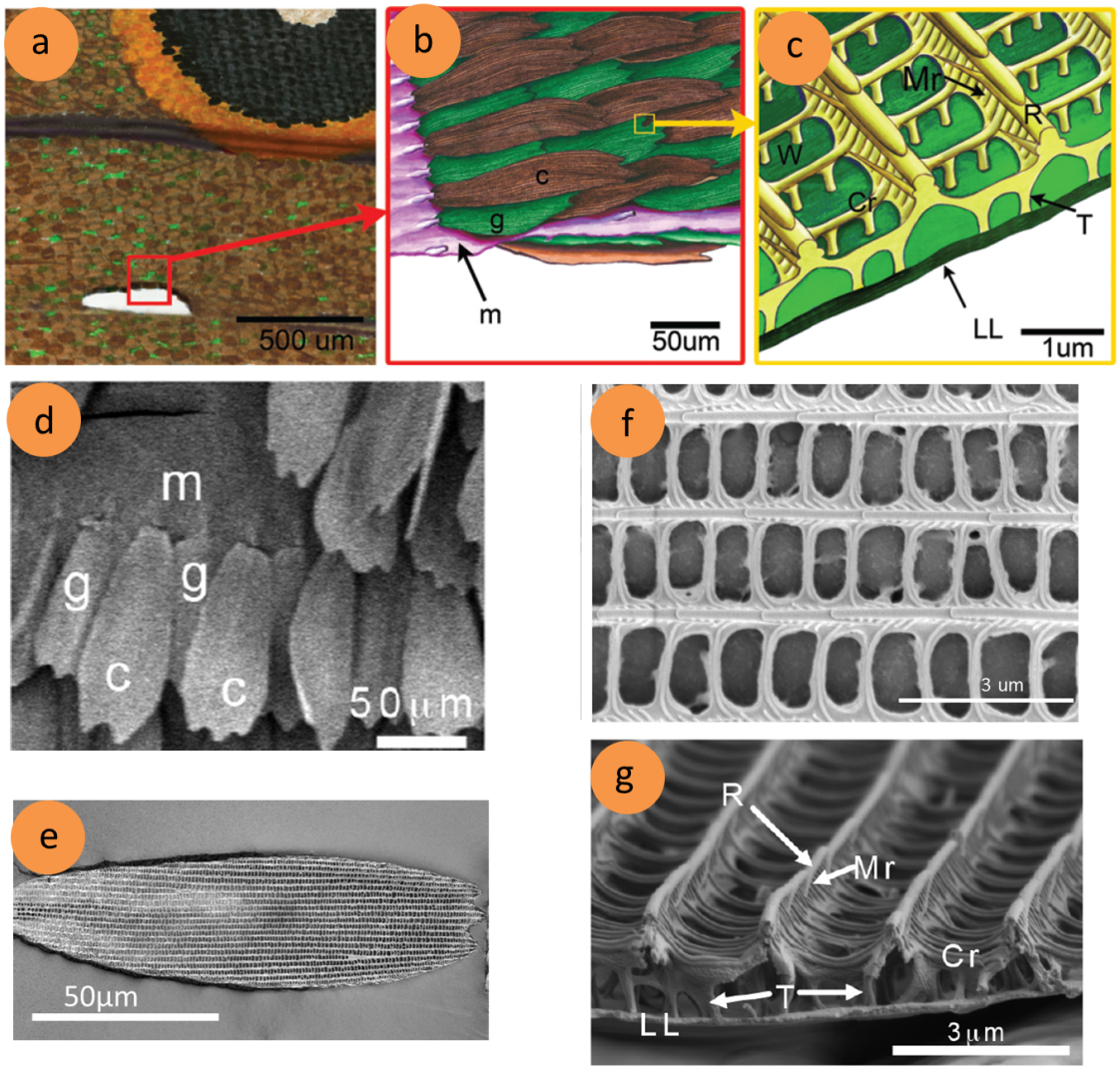

Figure 5.2: (a) Three-dimensional illustration of the wing and scales in the selected wing area of B. anynana. (b) Magnified view of the ripped region in (a) showing how cover (c; brown) and ground (g; green) scales are attached to the wing membrane (m, pink), and alternate each other along rows. Scales on the other (ventral) side of the wing membrane are also visible. (c) Cross-sectional view of a single scale, showing the trabeculae (T) connecting the lower lamina (LL) to the upper lamina that includes ridges (R), microribs (Mr), and crossribs (Cr). Windows (W) are the spaces between the ridges and crossribs. Both cover and ground scales have the same basic morphology. Panels H-J are illustrations by Katerina Evangelou. (d-g) Scanning electron microscope (SEM) images of B. anynana brown wing scales. (d) Section of the wing where the scales in the top left corner have been removed and the wing membrane (m) is visible. Attached to the membrane are the cover (c) and ground (g) scales, which alternate each other along rows. (e) A cover scale showing its fine sculpting on the abwing surface. (f,g) Top-view and tilt-view of a B. anynana wild-type cover scale.

ground scales, and where both scales attach to a wing membrane [Fig. 5.2(a,b,d)] [29]. Both cover and ground scales contain a lower lamina with a continuous smooth surface below a region composed of longitudinal ridges and crossribs, collectively referred to as the upper lamina, and connected to the lower lamina via pillars called trabeculae [Fig. 5.2(c,e,f,g)] [7]. Previous studies on butterflies showed that structural color can be produced by the interference of light reflected from the overlapping lamella that build the longitudinal ridges, from microribs protruding from the sides of the longitudinal ridges, or from the lower lamina which can vary in thickness and patterning [30, 31] [see Fig. 5.2(c)]. However, it is not clear how the violet/blue color is produced in members of the two Bicyclus clades that separately evolved this color, whether B. anynana can be made to evolve the same violet/blue color via artificial selection, and whether it will generate the color in the same way as the other species. To answer these questions, we have conducted detailed optical characterization and structural analysis of butterfly wing scales from three separate species and artificially evolved populations of Bicyclus to illustrate how color is generated and how it has evolved.

5.2 Artificial selection for violet scale color in B. anynana

Optical reflectance spectra of the violet/blue colored bands on the dorsal forewings of two representative species from the two clades that independently evolved violet/blue color, B. sambulos and B. medontias, exhibit peaks in the wavelength range of 400-450 nm [Fig. 5.1(e,g)]. The reflectance spectrum from the same wing region in B. anynana does not show any peak in the violet/blue wavelength range (380-495 nm), but it does show a peak in the ultraviolet (UV) at the wavelength of 300 nm [Fig.

5.1(f)]. The aim of our artificial selection experiment was to shift this UV peak to the violet/blue range of the spectrum.

5.2.1 Experimental animals

B. anynana were reared at 27°C, 80% humidity in Prof. Monteiro's lab, as previously described [32]. Upon eclosion, virgin male and female adults were isolated from one another to ensure virginity and kept in cooler conditions (17°C) until all animals of that generation emerged and were measured. Selected adults were mated with each other, subsequently preserved in glassine envelopes, and stored at -20°C. SEM and reflection microspectrophotometry analyses were done with females of B. anynana and male specimens of two other species: B. sambulos, collected in 9/2012 from the Lake Kivu region of the eastern Democratic Republic of Congo, and B. medontias, collected from the Ebogo region of Cameroon, both generously provided by Steve Collins. A multi-locus phylogenetic estimate of Bicyclus relationships was constructed and modified from previous Bicyclus studies to illustrate the relationship between B. anynana, B. sambulos, and B. medontias [33]. Briefly, this estimate is the consensus of trees drawn from a posterior distribution populated by a Metropolis-coupled Markov chain Monte Carlo exploration of tree likelihood space [34].

5.2.2 Selection procedure

We artificially selected the most extreme B. anynana individuals of each sex by measuring their reflectance spectra from a region of the dorsal forewing associated with violet/blue color in other Bicyclus species (white asterisk in Fig. 5.1(c), approximately 1 mm in diameter). Individuals displaying reflectance peaks nearest to 400 nm were bred with each other, and this procedure was repeated six times during eight

consecutive generations. Due to low adult numbers, all individuals in generations 4 and 7 were allowed to reproduce and did not undergo selection. This procedure led to the gradual increase of reflectance peak wavelength for the selected population. In the parental generation (generation 1), the average wavelength of the reflectance peak for the targeted dorsal region was 311 nm for males and 341nm for females. By generation 8, the peaks shifted to 362 nm and 385 nm in males and females, respectively [Fig. 5.3(a)]. Selected individuals exhibited significantly increased reflectance in the wavelength range of 400-500 nm.

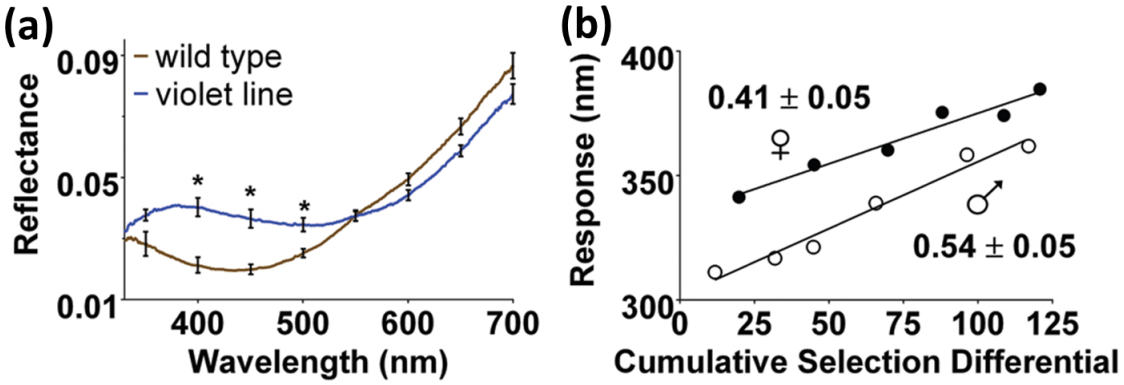

Figure 5.3: (a) Representative reflectance spectra of wild-type (wt) and violet-line (violet) females. (b) Response to selection plotted against a cumulative measure of the selection pressure applied to each generation, and realized heritability (h2) estimates for reflectance peak wavelength in B. anynana females (closed circles) and males (open circles) over 6 generations of selection.

5.2.3 Realized heritability

The proportion of the variation in reflectance peak wavelength that is due to additive genetic variation in our lab population is called the realized heritability (h2) [35]. This measure of heritability was estimated from two quantities: the response to selection and the cumulative selection differential. The response to selection (Y axis in

Fig. 5.3(b)) tracks the change in mean reflectance peak wavelength for all individuals in a generation over the course of the selection experiment. The cumulative selection differential (X axis in Fig. 5.3(b)) is a cumulative measure of the selection pressure applied in each generation. The selection pressure applied in a particular generation is estimated by subtracting the mean reflectance peak wavelength of all the individuals in a generation from the mean reflectance peak wavelength of the selected individuals in that generation. In Fig. 5.3(b), the response of one generation is plotted against the cumulative selection differential of the previous generations. From a linear fit of the data, we obtained the slope, which is the realized heritability (h2). Graphs for realized heritability and reflectance data were constructed using GraphPad Prism (v. 6.00; GraphPad Software, La Jolla, CA).

The realized heritabilities, h2, are 0.41 (41%) in females and 0.54 (54%) in males) [Fig. 5.3(b)], which explains the rapid response to selection. This measure of heritability was estimated from the selection pressure applied and the response to selection (reflectance peak wavelength shift). In summary, our artificial selection experiment demonstrated that B. anynana lab populations have significant additive genetic variation controlling reflectance peak wavelength that allowed the rapid evolution of a novel scale color.

5.3 Changes to ground scales led to B. anynana violet color evolution

5.3.1 Scale optical imaging and microspectrophotometry

To determine how the violet color evolved, we performed optical measurements on the wings of females from generation 8, whose dorsal reflectance peak was closest to 400

nm [Fig. 5.3(a)]. All scale images were taken on a Nikon Optiphot 66 microscope in reflection or transmission mode using BD Plan 5X to 40X lenses and a moticam 2500 USB camera at maximum (5mp) resolution. The reflectance spectra were taken using an Ocean Optics HR2000+ spectrometer, either attached to the Nikon microscope for the visible spectra or, for the ultraviolet, using a home-built microscope including an Oriel Instruments 66902 Xenon Arc Lamp and a Nikon TU Plan Fluor Epi 50x objective lens (numerical aperture = 0.8). Measurements performed on the wing were taken from three scales and/or wing areas from each of 5 different individuals, and measurements for individual scales (taken against a black background of carbon-coated glass) represent 3 scales in each of 3 different individuals. Reflectance spectrum for each sample/scale was measured in triplicate and then averaged. Analysis of Variance (ANOVAs) to test for significant differences in mean reflectance between wild-type or violet scales were calculated for a variety of reflectance points along the spectrum using JMP statistical software package (v.10, SAS Institute Inc., Cary, NC).

Comparisons of optical images of wild-type (wt) and violet-line (violet) B. anynana female wings revealed patches of violet color in the violet-line individuals, from regions where cover scales were missing and ground scales were fully exposed, suggesting the violet color is produced by the ground scales [Fig. 5.4(a)]. Indeed, high-magnification images of single ground scales from violet-line females showed an intense violet reflection when compared to wild-type scales[Fig. 5.4(b)]. In order to investigate in a quantitative manner which scale types were primarily contributing to the violet color, we measured reflectance spectra from individual cover scales (while attached to the wing) from both wild-type and violet-line females, then from ground scales (after removing some cover scales), and finally from the wing membrane (with both cover and ground scales removed).

We found no significant changes in violet reflectance of cover scales or wing membranes between wild-type and violet-line individuals [Fig. 5.4(c)]. However, ground

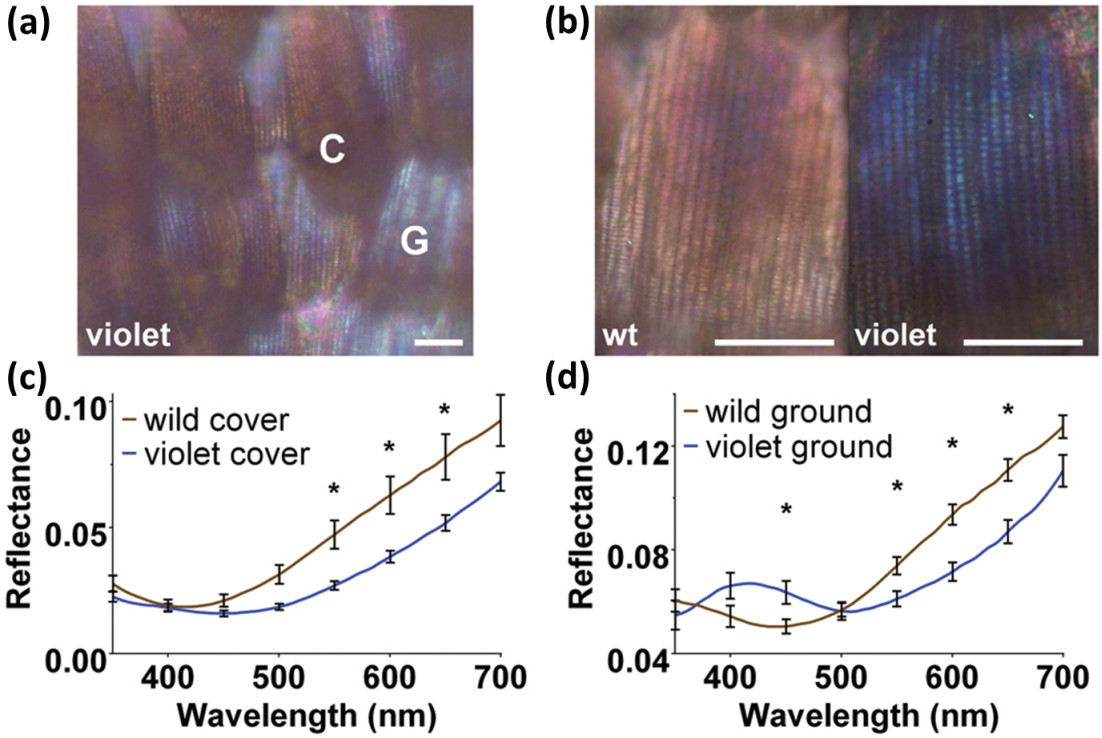

Figure 5.4: (a) Image of violet cover (C) and ground (G) scales with violet hue visible only in ground scales. (b) Images of wild-type (left) and violet (right) ground scales (generation 8) in the selected wing region. (c) Mean reflectance spectra (of 5 wild-type and 5 violet females) for cover scales and (d) for ground scales on the wing with cover scales removed. In all graphs, error bars represent standard error of the mean and asterisks represent statistically significant differences in reflectance. Scales bars in C and D = 20 μm. Note the reflectance from ground scales with cover scales removed (d) peaked at a slightly longer wavelength than the reflectance taken directly from an intact violet-line wing Fig. 5.3(a), due to the inclusion of both ground scales and cover scales (averaged over a relatively large area) in Fig. 5.3(a).

scales in violet-line females exhibited a significant increase in reflectance between 400 nm and 450 nm, compared to wild-type ground scales [Fig. 5.4(d)]. We conclude that changes to the ground scales in B. anynana are primarily responsible for violet color evolution in this artificial selection experiment.

To pinpoint where the violet color was produced, we isolated single cover and ground scales and measured reflectance spectra from both the abwing and adwing scale surfaces (those facing away and facing towards the wing membrane, respectively). Our results confirmed that violet-line ground scales exhibited more visible violet color (matching the reflectance spectra) relative to wild-type ground scales [Fig. 5.5(a,b)]. Both surfaces, but especially the adwing surface of these scales, had significantly higher reflectance in the violet range of the spectrum (380-450 nm) than the corresponding surface of wild-type ground scales. The higher reflectance from the adwing surface of the violet-line ground scales indicates the violet color originates from the lower lamina of the scale. The adwing of cover scales also showed a significant increase in reflectance at the violet wavelength (450 nm), but the abwing reflectance barely changed [Fig. 5.5(c,d)]. Therefore, both ground and cover scales evolved violet color, which is produced in the lower lamina of the scales, but ground scales changed more dramatically.

To explore whether changes in scale pigmentation contributed to scale color evolution, and to understand the difference in reflectance from the adwing and abwing surfaces, we measured light transmission through isolated cover and ground scales, and obtained the absorbance spectra $\log_{10}[T'(\lambda)]$, where $T'(\lambda)$ represents the measured transmittance of scales immersed in refractive index matching fluid. The violet-line ground scales exhibit significantly higher transmission or lower absorption compared to their wild-type counterparts [Fig. 5.6(a, b)]. Variation in transmission is due to light absorption by pigments observed in the mass of the scales. The reduced absorp-

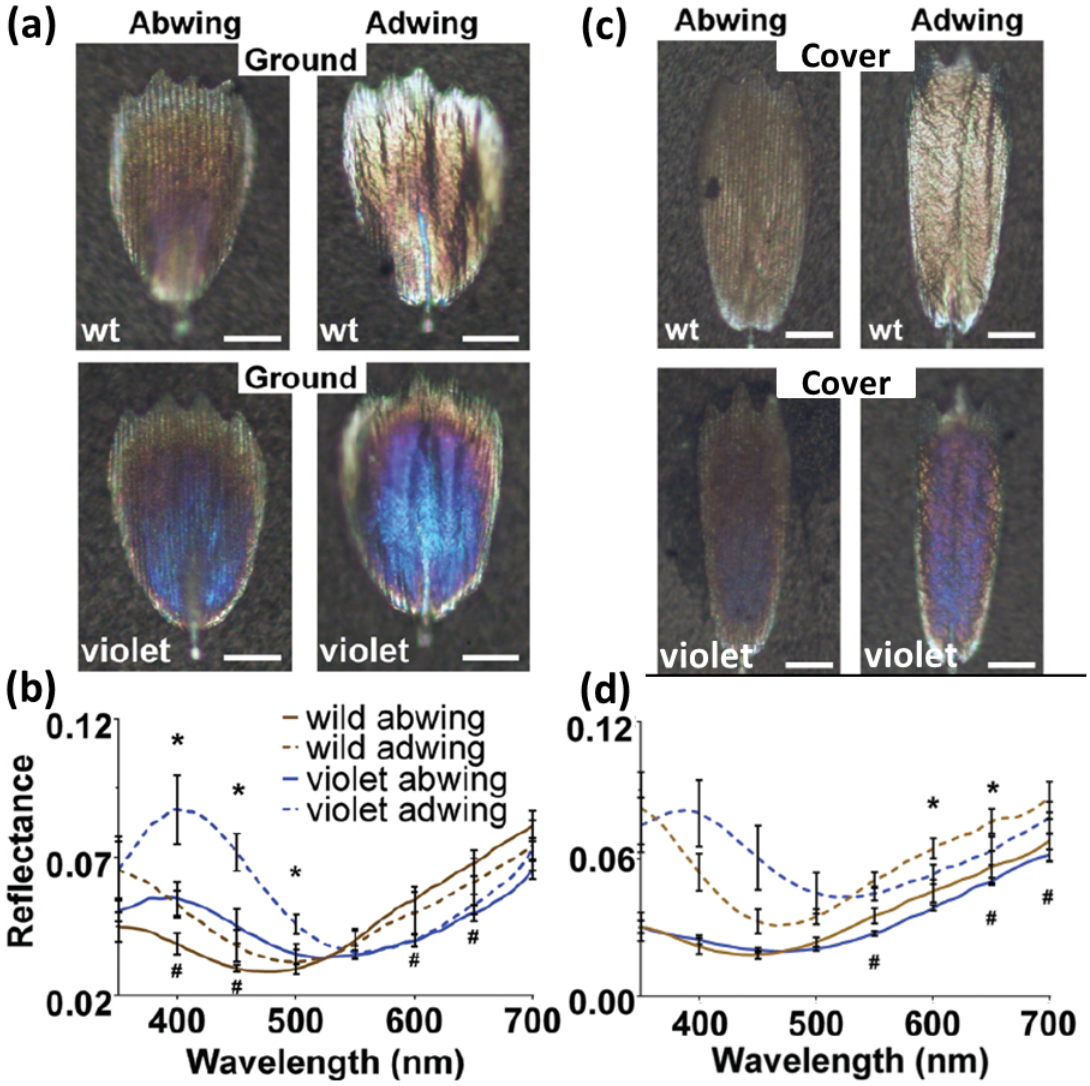

Figure 5.5: (a, c) Images of abwing (left column) and adwing (right column) surfaces of individual ground/cover scales from wild-type (top row) and violet-line (bottom row) females. (b, d) Reflectance spectra of individual ground/cover scales from wild-type (wild) and violet-line (violet) individuals. Scale bar is 20 μm. In (b, d), error bars represent standard error of the mean and statistically significant differences in reflectance are indicated with asterisks ($\star$) for the adwing surfaces of scales or pound symbols (#) for abwing scale surfaces.

tion in the violet-line scales increases light reflection from the lower lamina of these scales. In addition, the ridges and crossribs were the less transmissive areas across all scale types and we notice that these structures appear to have evolved a thinner appearance in violet line versus wt scales [Fig. 5.7]. These changes in morphology on the upper surface of the scale will have contributed to the lower absorption of the violet-line scales. Differences in reflectance measured from adwing and abwing surfaces can be attributed to additional absorption and scattering of light by the ridges and cross-ribs that are only present in the upper lamina [Fig. 5.6(a)] [31]. Hence, the appearance of the violet color resulted from a combination of enhanced reflection and reduced absorption by the violet-line ground scales.

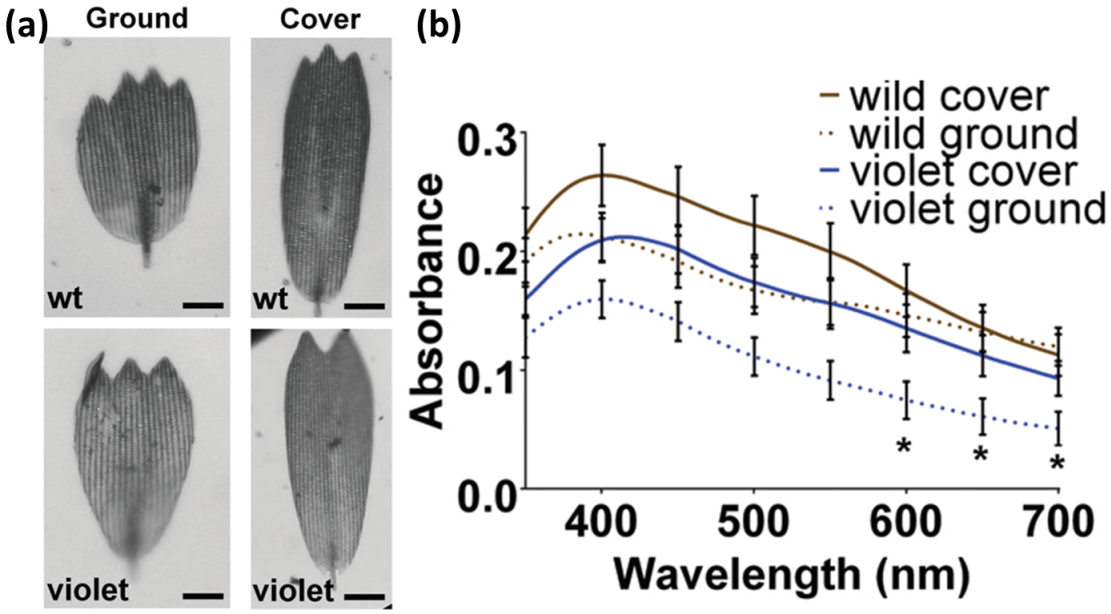

Figure 5.6: (a) Transmission images for B. anynana wild-type (top row) and violet (bottom row) cover scales (right column) and ground scales (left column). (b) Absorbance measurements for individual scales. Scale bars = 20 μm.

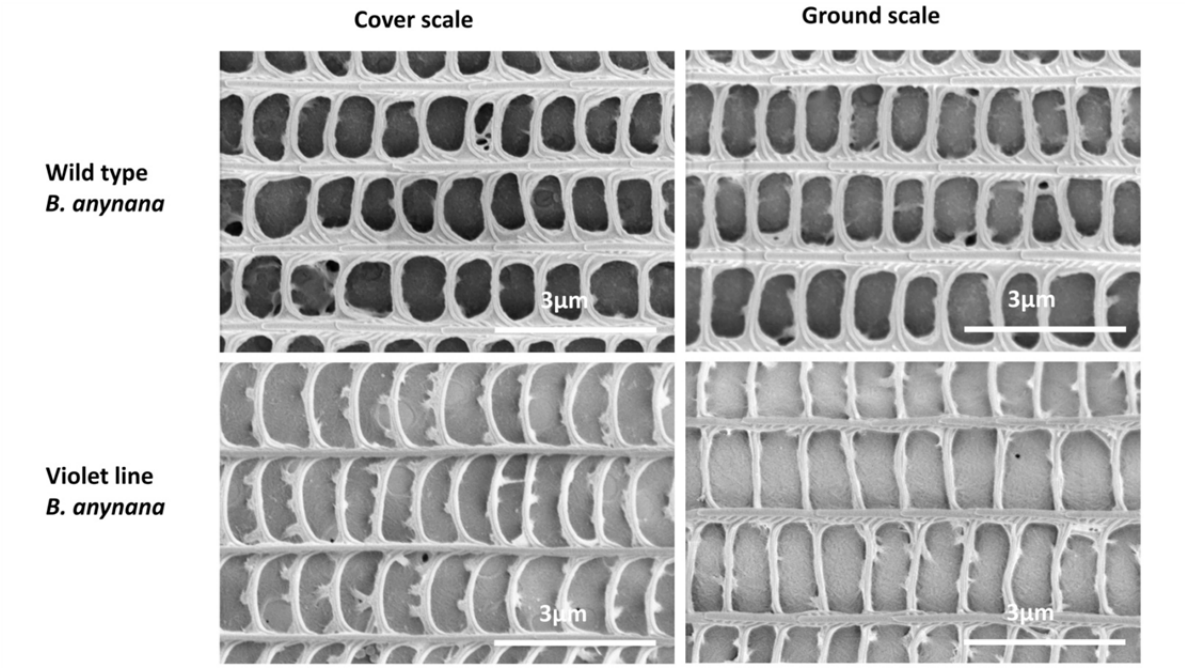

Figure 5.7: SEMs of cover and ground scales of Bicyclus species. Top-view SEM images of cover (left column) and ground (right column) scales of wild-type and violet-line B. anynana. The scale structures are similar, and the lower lamina is clearly visible through the windows of the upper lamina.

5.4 Structural analysis of violet scales

5.4.1 Scanning electron microscopy (SEM)

To discover the mechanism that produces the violet color in selected B. anynana, we collected scanning electron microscope (SEM) images of the scales nanomorphologies. Butterfly wings were first soaked in a mixture of water and alcohol, then dipped into liquid nitrogen for approximately 5 minutes to ensure thorough freezing. Following freezing, the wings were removed from liquid nitrogen and immediately sectioned in the region of the color band using a microtome blade [36]. After complete evaporation of the remaining liquid at room temperature, the wing fragment was pressed gently against a conductive carbon tape to transfer the scales onto the tape, which was then attached to the sample mount. The samples were first imaged with an optical microscope to identify the scale type and the color-producing regions on the scales,

then they were coated with a layer of 10nm gold to increase sample conductivity. To obtain cross-sectional SEM images of the scales, the samples were mounted on a rotation stage. All SEM images were taken using a SU-70 UHR Schottky (Analytical) FE-SEM (Hitachi High Technologies America, Inc.) at 2kV accelerating voltage and 28A probe current.

Although cover scales are more elongated than ground scales, their nanomorphologies are similar, i.e., both have a typical ridge-lamellar structure similar to previously described nymphalid wing scales [Fig. 5.2(c)] [29, 30]. Note also that the lower lamina is clearly visible through the windows in the upper lamina [Fig. 5.7] A direct comparison of optical and SEM images of the same cross-sectioned scales allowed us to measure the thickness of the lower lamina from the color-producing region of cover and ground scales [Fig. 5.8(a,b)]. Using measurements from multiple scales we obtained an estimate of the average lamina thickness for each scale type [Fig. 5.8(c)]. While unselected B. anynana cover and ground scale lower laminae have almost the same thickness (120 nm), both became thicker through artificial selection. Thickness of cover scale lamina increased from 126 ± 13 nm (95% CI) to 144 ± 5 nm (F = 2.8, p = 0.142), while that of ground scales increased significantly from 120 ± 23 nm in wild-type to 176 ± 10 nm in the violet-line individuals (F = 21.8, p ¡ 0.01).

5.4.2 Numerical simulations of reflectance spectra from lower lamina

To investigate whether the increases in lower lamina thickness were responsible for the spectral shifts in reflectance peaks (i.e., in scale color), we numerically calculated the reflectance spectra for the lower lamina by modeling it as a dielectric thin-film. Lamina thickness was set to the measured values for each scale type, and the refractive

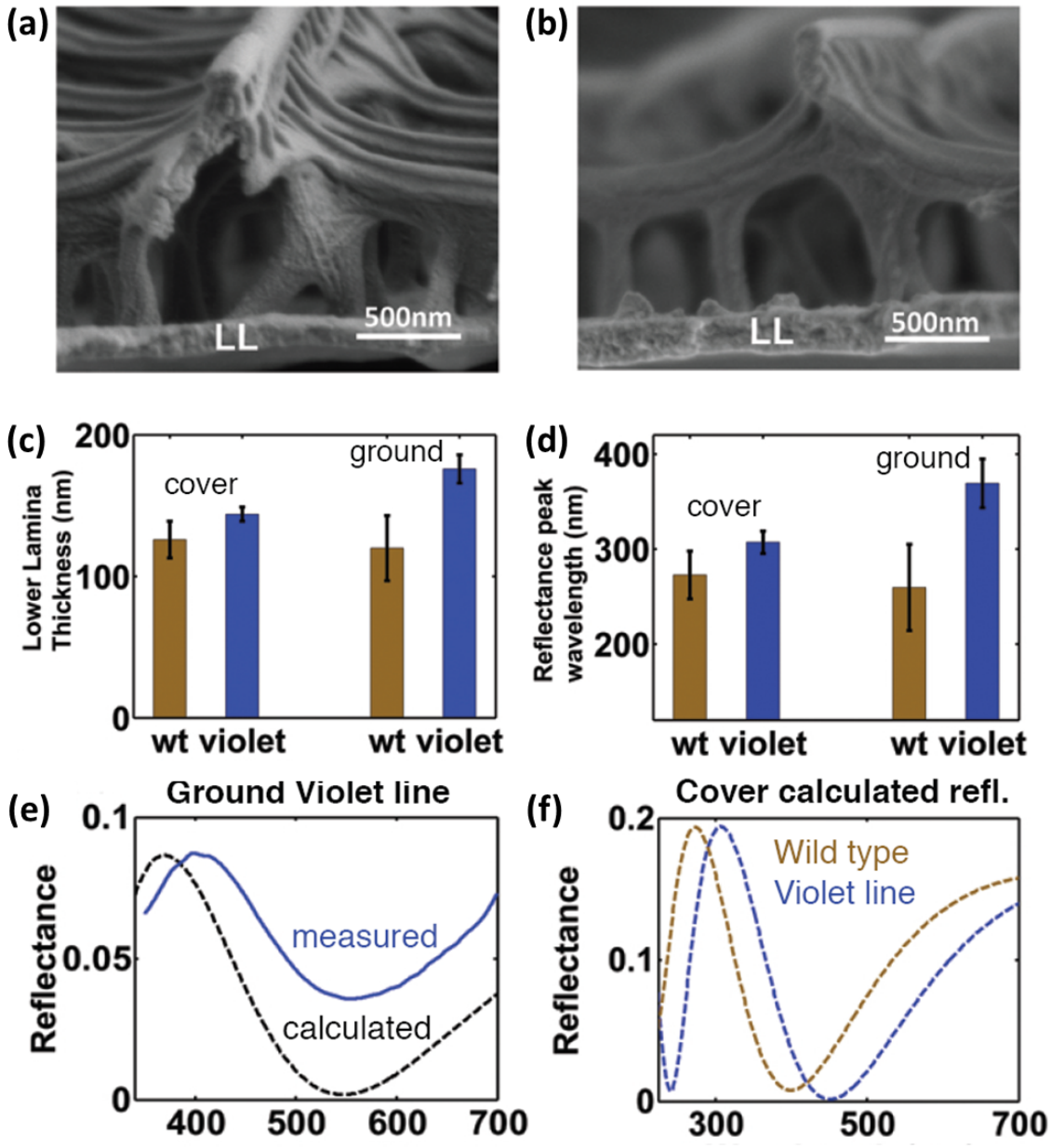

Figure 5.8: (a, b) Magnified cross-sectional SEM images of lower lamina (LL) in a wild-type cover scale (a) and a violet-line ground scale (b). (c) Mean lower lamina thickness measured from the cross-sectional SEM images of cover and ground scales of wild-type and violet-line B. anynana. The error bar represents 95% confidence intervals for the means. (d) Calculated reflectance peak wavelengths of lower lamina using the individually measured thickness values of cover and ground scales of wild-type and violet-line B. anynana. (e) Comparison of the calculated (dashed line) and measured (solid line) reflectance spectra of the violet-line ground scales. Because our calculations did not include absorption caused by pigments in the thin-film, the magnitude of the calculated reflectance peak is higher than that observed. Peak magnitudes were normalized by lowering the magnitude of the calculated reflectance peak to match the magnitude of the measured peak. (f) Calculated reflectance spectra for the cover scales of wild-type (brown dashed line) and violet-line (purple dashed line) B. anynana.

index and its variation with wavelength were set according to previous measurements of non-pigmented butterfly wing scale chitin [37]. We also took into account the range of incident angle of the light and the variation in thickness of the lower lamina. However we did not include lamina absorption due to pigments in the calculation, since it is not known how much of the measured absorbance occurred in the lower versus upper lamina. In the violet-line ground scales, the measured and calculated reflectance spectra exhibited similar modulation with wavelength, which is a clear spectral signature that confirms the reflectance peak is produced by thin-film interference [Fig. 5.8(e)]. The calculated peak wavelength (374 nm), however, is slightly lower than the average measured peak wavelength (405 nm) [Fig. 5.8(e)]. Similar results were obtained for the wild-type ground scales. In sum, the calculated spectral shift from wild-type to violet-line ground scales is close to the measured shift, but the calculated reflectance peaks have a shorter wavelength [Fig. 5.8(d)]. For the cover scales, the calculated shift in reflectance peaks was from 273 nm (wild-type) to 310 nm (violet-line) [Fig. 5.8(f)]. These calculated reflectance peak wavelengths were also slightly lower than the measured values [300 nm in Fig. 5.1(f)]. The peak remained in the UV range due to the smaller increment of lower lamina thickness in cover scales compared to that in ground scales. Simultaneously, the calculated reflectance at longer wavelengths (500 nm 700 nm) was reduced [Fig. 5.8(f)], in agreement with results in Fig. 5.4(c). Consequently, the violet-line cover scales appeared dark violet as compared to the wild-type cover scales [Fig. 5.5(d)].

We attribute the discrepancies in simulated and measured reflectance peak wavelength described above to a modification of the refractive index of lower lamina induced by pigments within it, which was not included in our calculation. The measured absorbance spectra of our various scale types [Fig. 5.6(b)] do not exactly match the melanin absorbance spectrum [31,38,39], indicating that brown scales in B. anynana either do not contain melanin or, more likely, contain additional pigments besides

melanin. Since the type and amount of pigments that exist in the lower lamina of scales are not known, it is impossible for us to correctly estimate the change of refractive index value due to pigmentation. However, the shape of the measured reflectance spectra as well as the direction of the observed spectral shifts of the reflectance peak, from UV to violet, indicate that the observed color change in ground scales is caused by the increase in thickness of the lower lamina of these scales.

5.5 Natural evolution of violet/blue color within the Bicyclus genus

After demonstrating that B. anynana can readily produce violet colored scales, we investigated how the other members of the Bicyclus genus naturally evolved their violet/blue colors. The Bicyclus genus is composed of over 80 species [22, 23], and violet/blue color has evolved twice independently in two separate lineages [black asterisks in Fig. 5.1(a)]. To identify the primary sources of violet/blue color on the dorsal wing bands of these species, we isolated cover and ground scales from representative species from each lineage, B. sambulos, B. medontias [Fig. 5.1(b,d)], and examined their reflectance and transmittance spectra.

In B. sambulos, optical reflectance images of isolated cover and ground scales revealed that the violet/blue color was predominantly coming from the cover scales [Fig. 5.9(a)]. Reflectance measurements showed enhanced light reflection in the wavelength range of 400-500 nm from both sides of the cover scale, while ground scales had no peak in this wavelength range [Fig. 5.9(b)]. Absorbance measurements [Fig. 5.9(c)] and transmission images [Fig. 5.9(d)] show that cover scales from the violet/blue dorsal band region had the lowest absorbance, followed by ground scales in the same

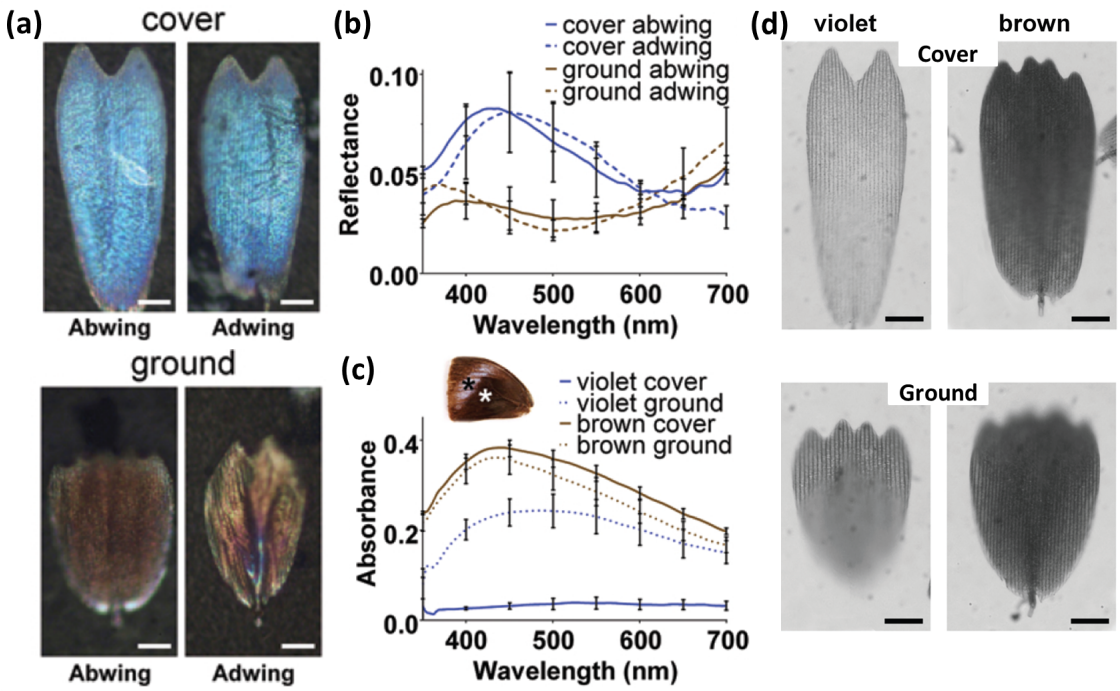

Figure 5.9: B. sambulos: (a) Images of abwing and adwing surfaces of individual cover (top) and ground (bottom) scales from B. sambulos. (b) Reflectance spectra of individual cover and ground scales. (c) Absorbance measurements for B. sambulos scales from blue region (denoted by black asterisk in inset) and brown region of the dorsal wing (white asterisk in inset). (d) Transmission images of B. sambulos cover scales (top) and ground scales (bottom), left column is from the blue region and right column is from the brown region. Scale bars = 20 μm.

region, compared to the cover and ground scales in the adjacent brown region. Since the cover scales in the violet/blue wing band region of B. sambulos were much less pigmented than those of B. anynana, the difference in reflectance measured from both abwing and adwing surfaces is much smaller. SEM images of B. sambulos cover and ground scales [Fig. 5.10] revealed similar nanomorphologies to the scales of B. anynana. From the cross-sectional SEM images, we measured the lower lamina thickness of cover scales to be 204 ± 13 nm. These measurements produce a calculated reflectance spectrum with a peak at 428 ± 26 nm, which agrees well to the measured reflectance peak at 450 nm [Fig. 5.9(b)]. These results confirm that the violet/blue color is produced via thin-film interference in the lower lamina of cover scales. In summary, the violet/blue color of B. sambulos is primarily produced by cover scales and not by ground scales, as we observed in B. anynana, but the mechanism of color production is the same in both species.

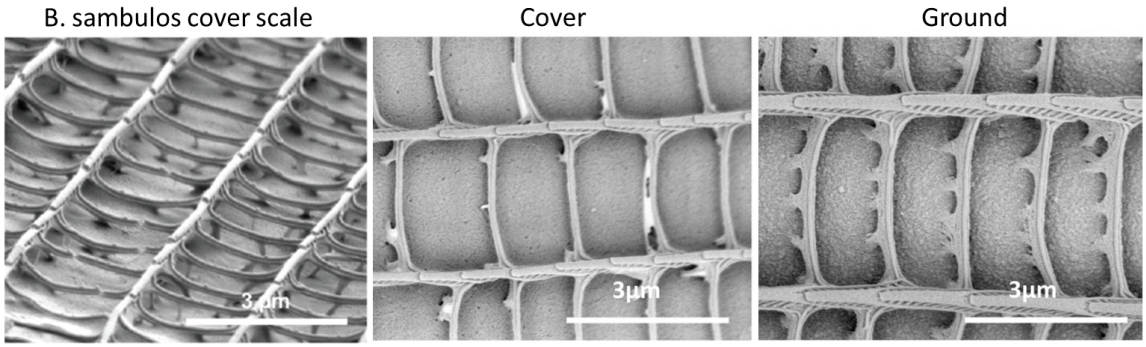

Figure 5.10: SEM images for B. sambulos cover scale in tilt-view (left) and top-view (middle), ground scale in top-view (right). The scale structure is very similar to the one of B. anynana shown in Fig. 5.7.

In B. medontias, the violet color was visible from both sides of cover and ground scales [Fig. 5.11(a)]. The scales' optical reflectance data [Fig. 5.11(b)] was similar to the reflectance of B. sambulos cover scales, except for a slight shift in the wavelengths of the reflectance peaks. The scales' absorbance data[Fig. 5.11(c)] were also similar

to those of B. sambulos, where the violet scales had lower absorption relative to the adjacent brown scales. SEM images of the violet scales [Fig. 5.12] showed similar scale nanomorphologies to the scales of both B. anynana and B. sambulos, suggesting the violet color is produced by the same mechanism. Further confirmation of thin-film interference was observed in a cover scale of B. medontias, part of which adhered to the substrate, which led to the disappearance of the violet color [Fig. 5.12(b)]. Color produced by thin-film interference relies on the interference of light reflected from the top and bottom surfaces of a thin film, such as the lower lamina of a scale. When one side of the scale lamina is attached to the closely index-matched substrate, light reflection from that interface is greatly reduced, thus the thin-film interference diminishes, and color disappears as observed in that preparation.

5.6 Discussion

Here we document the first artificial selection study on structural color in butterflies and show that structural violet color can evolve in a short period of time (6 generations) in a lab-reared butterfly population. We also show that violet/blue structural color has evolved independently within a genus and that the descendant species are using the same mechanism for color generation (thin-film interference) but in different scale types: ground scales in B. anynana, cover scales in B. sambulos, and both scale types in B. medontias. Violet structural color in B. anynana evolved via changes in cuticular properties (i.e. thickness) of the lower lamina of individual wing scales, concurrently with a decrease in absorption in the same scales.

Structural color is more often produced by cover scales because they overlay

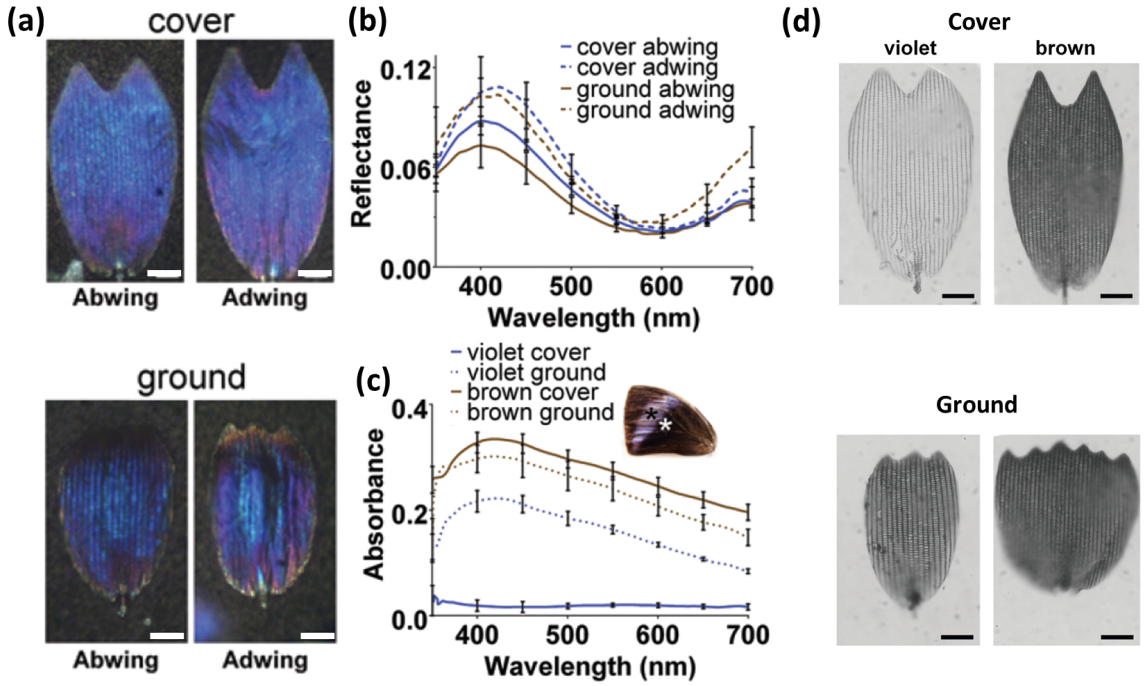

Figure 5.11: B. medontias: (a) Images of abwing and adwing surfaces of individual cover (top) and ground (bottom) scales from B. medontias. (b) Reflectance spectra of individual cover and ground scales. (c) Absorbance measurements for B. medontias scales from blue region (denoted by black asterisk in inset) and brown region of the dorsal wing (white asterisk in inset). (d) Transmission images of B. medontias cover scales (top) and ground scales (bottom), left column is from the blue region and right column is from the brown region. Scale bars = 20 μm.

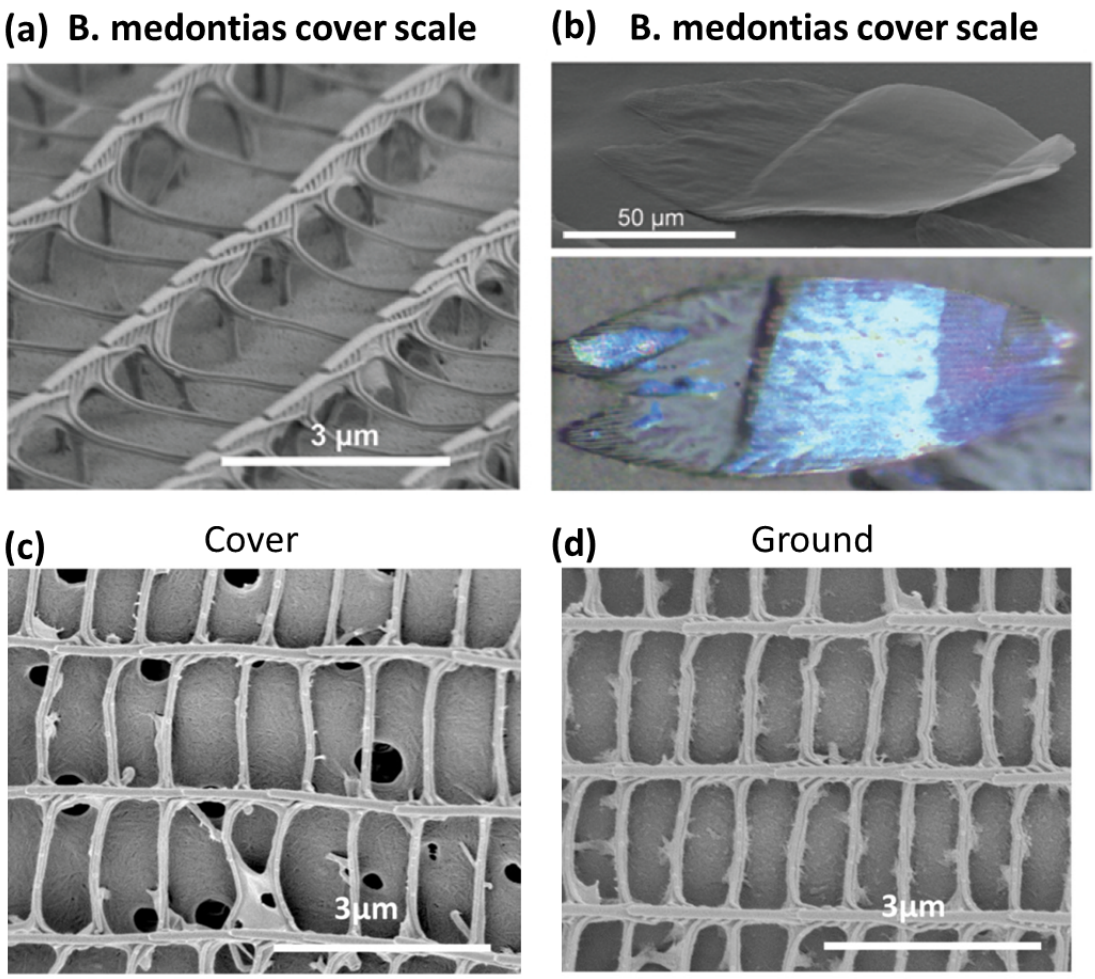

Figure 5.12: (a)SEM image of a B. medontias cover scale in tilt-view. (b) SEM (top) and optical image (bottom) showing part of a B. medontias scale (with adwing surface facing up) adhering to the substrate leading to the disappearance of color produced by thin-film interference. (c,d) Top-view SEM images for cover and ground scales of B. mendontias showing similar nanostructure with B. anynana.

ground scales and are more exposed to incident light [7]. Thus, the evolution of violet color in B. anynana ground scales is unexpected, and we speculate it may be a result of the artificial selection procedure. The relatively high density cages where we kept the animals, before they were measured and selected, as well as the handling during measurement, may have led to partial loss of some cover scales, preferentially exposing the ground scales to selection, and leading to their more extensive modification. This unexpected result, compared to the natural evolution of blue color in the other species of Bicyclus, revealed that both cover and ground scales in B. anynana have the remarkable potential to be independently modified through the process of selection.

Our results, in conjunction with other recent studies [40], suggest that structural colors can evolve rapidly and ultimately play pivotal roles in butterfly fitness and diversity. For instance, structurally colored wing patterns in butterflies have been proposed to function as species recognition signals, as sexually dimorphic signals involved in female mate choice, and as signals that are predictive of nuptial gift size [40–43]. Furthermore, the evolution of these colors in only certain species of a genus, as we have documented here for Bicyclus, may depend less on the availability of genetic variation in natural populations for producing these colors and more on natural or sexual selection favoring specific colors. While we know of no comparable artificial selection study on pigmentary color in butterflies, previous research on pigmentary color evolution in birds revealed that shifts to new diets and/or gains/losses of enzymatic steps in biochemical pathways were required to modify the color due to pigments acquired through diet [44, 45]. In contrast, structural colors, as exemplified here, can evolve simply via quantitative variation in the amount of cuticular secretions produced by individual cells, without modification of any additional material property. This may lead to a faster rate of evolution of structural colors in nature, as compared to pigmentary colors, and should be examined in future.

Finally, by identifying a process, artificial selection, that can readily lead to structural color evolution in butterflies, our study lays the ground for future research on the genetics of structural colors, e.g. by crossing selected lines within a species, followed by linkage mapping. In addition, the artificial selection used in this study may inspire future applications of similar evolutionary principles to the design of reconfigurable photonic materials and devices.

Bibliography

[1] B. R. Wasik*, S. F. Liew*, D. Lilien*, A. J. Dinwiddie, H. Noh, H. Cao, and A. Monteiro, PNAS, DOI:10.1073/pnas.1402770111 (2014).

[2] M. D. Shawkey, N. I. Morehouse, P. and Vukusic, "A protean palette: colour materials and mixing in birds and butterflies," J R Soc Interface **6**, S221-231 (2009).

[3] S. Kinoshita, S. Yoshioka, and J. Miyazaki, "Physics of structural colors," Rep Prog Phys **71**, 1-30 (2008).

[4] C. M. Eliason, P. P. Bitton, and M. D. Shawkey, "How hollow melanosomes affect iridescent colour production in birds," Proc Biol Sci **280**, 20131505 (2013).

[5] L. D'Alba, et al., "Colour-producing -keratin nanofibres in blue penguin (Eudyptula minor) feathers," Biol Lett **7**, 543-546 (2011).

[6] V. Saranathan, et al., "Structure and optical function of amorphous photonic nanostructures from avian feather barbs: a comparative small angle X-ray scattering (SAXS) analysis of 230 bird species," J R Soc Interface **9**, 2563-2580 (2012).

[7] H. Ghiradella, "Structure and development of iridescent lepidopteran scales - The papilionidae as a showcase family," Ann Entomol Soc Am **78**, 252-264 (1985).

[8] S. Wickham, M. C. Large, L. Poladian L, and L. S. Jermiin, "Exaggeration and suppression of iridescence: the evolution of two-dimensional butterfly structural colours," J R Soc Interface **3**, 99-108 (2006).

[9] A. E. Seago, P. Brady, J. P. Vigneron, and T. D. Schultz, "Gold bugs and beyond: a review of iridescence and structural colour mechanisms in beetles (Coleoptera)," J R Soc Interface **6**, S165-184 (2009).

[10] P. Vukusic and J. R. Sambles, "Photonic structures in biology," Nature **424**, 852-855 (2003).

[11] D. P. Gaillot, et al., "Composite organic-inorganic butterfly scales: production of photonic structures with atomic layer deposition," Phys Rev E Stat Nonlin Soft Matter Phys **78**, 031922 (2008).

[12] Chung K, et al., "Flexible, angle-independent, structural color reflectors inspired by morpho butterfly wings," Adv Mater **24**, 2375-2379 (2012).

[13] F. Song, H. Su, J. Chen, D. Zhang, and W. Moon, "Bioinspired ultraviolet reflective photonic structures derived from butterfly wings (Euploea)," Applied Physics Letters **99**, 163705-163703 (2011).

[14] J. W. Galusha, M. R. Jorgensen, and M. H. Bartl, "Diamond-structured titania photonic-bandgap crystals from biological templates," Adv Mater **22**, 107-110 (2010).

[15] M. Crne, et al., "Biomimicry of optical microstructures of Papilio palinurus," Europhys Lett **93**, 14001 (2011).

[16] M. Harun-Ur-Rashid M, et al., "Angle-independent structural color in colloidal amorphous arrays," Chemphyschem **11**, 579-583 (2010).

[17] K. Watanabe, et al., "Optical measurement and fabrication from a Morpho-butterfly-scale quasistructure by focused ion beam chemical vapor deposition," J. Vac. Sci. Technol. B **23**, 570-574 (2005).

[18] I. Lee, et al., "Quasi-amorphous colloidal structures for electrically tunable full-color photonic pixels with angle-independency," Adv Mater **22**, 4973-4977 (2010).

[19] Y. Takeoka, M. Honda, T. Seki, M. Ishii, and H. Nakamura, "Structural colored liquid membrane without angle dependence," ACS Appl Mater Interfaces **1**, 982-986 (2009).

[20] N. Kumano, et al., "Multicolor polymer-dispersed liquid crystal," Adv Mater **23**, 884-888 (2011).

[21] N. Kumano, T. Seki, M. Ishii, H. Nakamura, and Y. Takeoka "Tunable angle-independent structural color from a phase-separated porous gel," Angew Chem Int Ed Engl **50**, 4012-4015 (2011) .

[22] M. Condamin, "Monographie du genre Bicyclus: Lepidoptera Satyridae," Thesis (IFAN, Paris, Dakar, 1973).

[23] A. Monteiro and N. E. Pierce, "Phylogeny of Bicyclus (Lepidoptera: Nymphalidae) inferred from COI, COII, and EF-1alpha gene sequences," Mol Phylogenet Evol **18**, 264-281 (2001).

[24] A. Monteiro, P. Brakefield, and V. French, "The evolutionary genetics and developmental basis of wing pattern variation in the butterfly Bicyclus anynana," Evolution **48**, 1147-1157 (1994).

[25] A. Monteiro, P. Brakefield, and V. French, "Butterfly eyespots: The genetics and development of the color rings," Evolution **51**, 1207-1216 (1997).

[26] A. Monteiro, P. M. Brakefield, and V. French, "The genetics and development of an eyespot pattern in the butterfly Bicyclus anynana: response to selection for eyespot shape," Genetics **146**, 287-294 (1997).

[27] P. Beldade, P. M. Brakefield, and A. D. Long, "Contribution of Distal-less to quantitative variation in butterfly eyespots," Nature **415**, 315-318 (2002).

[28] C. E. Allen, P. Beldade, B. J. Zwaan, and P. M. Brakefield, "Differences in the selection response of serially repeated color pattern characters: standing variation, development, and evolution," BMC Evol Biol **8**, 1-13 (2008).

[29] H. F. Nijhout, "The Development and Evolution of Butterfly Wing Patterns," (Smithsonian Institution Press, Washington, D.C., 1991) pp.1-297.

[30] H. Ghiradella, "Structure of iridescent lepidopteran scales - variations on several themes," Ann Entomol Soc Am **77**, 637-645 (1984).

[31] D. G. Stavenga, H. L. Leertouwer, and B. D. Wilts, "Colouration principles of nymphaline butterflies - thin films, melanin, ommochromes and wing scale stacking," J Exp Biol. **217**, 2171-80 (2014).

[32] E. L. Westerman, A. Hodgins-Davis, A. Dinwiddie, and A. Monteiro, "Biased learning affects mate choice in a butterfly," Proc Natl Acad Sci USA **109**, 10948-10953 (2012).

[33] J. C. Oliver and A. Monteiro, "On the origins of sexual dimorphism in butterflies," Proc Biol Sci **278**, 1981-1988 (2011).

[34] F. Ronquist and J. P. Huelsenbeck, "MrBayes 3: Bayesian phylogenetic inference under mixed models," Bioinformatics **19**, 1572-1574 (2003).

[35] D. S. Falconer, "Introduction to Quantitative Genetics" (Longman Wiley, Burnt Mill, Harlow, Essex, England New York, 1989) 3rd Ed, pp. xii-438.

[36] J. J. Bozzola and L. D. Russell, "Electron Microscopy: Principles and Techniques for Biologists" (Jones and Bartlett, Boston, 1999) 2nd Ed, pp. xxiii-670.

[37] H. L. Leertouwer, B. D. Wilts, and D. G. Stavengam "Refractive index and dispersion of butterfly chitin and bird keratin measured by polarizing interference microscopy," Opt Express **19**, 24061-24066 (2011).

[38] D. G. Stavenga, H. L. Leertouwer, T. Hariyama, H. A. De Raedt, and B. D. Wilts, "Sexual dichromatism of the damselfly Calopteryx japonica caused by a melanin-chitin multilayer in the male wing veins," PLOS One **7**, e49743 (2012).

[39] D. G. Stavenga, H. L. Leertouwer, and B. D. Wilts, "Quantifying the refractive index dispersion of a pigmented biological tissue using Jamin-Lebedeff interference microscopy," Light Sci Appl **2**, e100 (2013).

[40] P. K. Rajyaguru, K. V. Pegram, A. C. Kingston, and R. L. Rutowski, "Male wing color properties predict the size of nuptial gifts given during mating in the Pipevine Swallowtail butterfly (Battus philenor)," Naturwissenschaften **100**, 507-513 (2013).

[41] R. L. Rutowski, J. M. Macedonia, D. J. Kemp, and L. Taylor-Taft, "Diversity in structural ultraviolet coloration among female sulphur butterflies (Coliadinae, Pieridae)," Arthropod Struct Dev **36**, 280-290 (2007).

[42] Z. Bálint, K. Kertész, G. Piszter, Z. Vértesy, and L. P. Biró, "The well-tuned blues: the role of structural colours as optical signals in the species recognition of a local butterfly fauna (Lepidoptera: Lycaenidae: Polyommatinae)," J R Soc Interface **9**, 1745-1756 (2012).

[43] K. A. Robertson and A. Monteiro, "Female Bicyclus anynana butterflies choose males on the basis of their dorsal UV-reflective eyespot pupils," Proc Biol Sci **272**, 1541-1546 (2005).

[44] K. J. McGraw, G. E. Hill, R. Stradi, and R. S. Parker, "The influence of carotenoid acquisition and utilization on the maintenance of species-typical plumage pigmentation in male American goldfinches (Carduelis tristis) and northern cardinals (Cardinalis cardinalis)," Physiol Biochem Zool **74**, 843-852 (2001).

[45] R. O. Prum, A. M. LaFountain, J. Berro, M. C. Stoddard, and H. A. Frank, "Molecular diversity, metabolic transformation, and evolution of carotenoid feather pigments in cotingas (Aves: Cotingidae)," J Comp Physiol B **182**, 1095-1116 (2012).

Chapter 6

Effect of absorption on light transport in disordered waveguides

6.1 Introduction

[1] In mesoscopic transport, wave interference plays an essential role, giving rise to well-known phenomena such as enhanced backscattering, Anderson localization and universal conductance fluctuations [2–7]. Recently, another striking interference effect has caught much attention, that is, the existence of highly transmitting channels, terms "open channel" in a random system [8–15]. These open channels, which enable an optimally prepared coherent input beam to transmit through a strong scattering medium with order unity efficiency, were predicted initially for electrons [16–19]. However, they have not been directly observed in mesoscopic electronics due to the extreme difficulty of controlling the input electron states. In contrast, it is much easier to prepare the input states of classical waves, such as electromagnetic waves or acoustic waves. Recent developments of adaptive wavefront shaping and phase recording techniques in optics have enabled experimental studies of open channels [20–23]. The

1. This chapter is primarily based on the work published in ref. [1].

open channels greatly enhance light penetration into scattering media, that will have a profound impact in a wide range of applications from biomedical imaging and laser surgery to photovoltaics and energy-efficient ambient lighting [23–25].

The transmission channels are eigenvectors of the matrix $t^\dagger t$, where t is the field transmission matrix of the system. The eigenvalues τ are the transmittance of the corresponding eigenchannels. In the lossless diffusion regime, the density of eigenvalues τ has a bimodal distribution, with one peak at $\tau \simeq 0$ that corresponds to closed channels, and a peak at $\tau \simeq 1$ that corresponds to open channels [16–19]. The diffusion process is dominated by the open channels, and the average transmittance is proportional to the ratio of the number of open channels by the total number of propagating channels [16, 17]. At the transition to localization, the number of open channels is reduced to one, and the open channels disappear in the localization regime. The conductance of a localized system is dominated by the single highest transmitting channel. In the past few years, wavefront shaping has been utilized to increase the coupling of the incident light to the open channels of random media [8, 12, 13, 15, 26, 27]. Numerical simulations reveal that the open channels enhance the energy stored inside the disordered medium [10]. In the diffusion regime, the field energy of an open channel is spread over the entire transverse extent of a sample, while in the localization regime the maximal transmission channel becomes confined in the transverse direction normal to the transmission direction [11].

In addition to the transmission channels, the transport can also be interpreted in terms of resonances, which are referred to as "levels" for electrons and "modes" for classical waves [28, 29]. For an open system, one can define quasi-normal mode. These are eigenfunctions of the Maxwell equations with complex frequency that satisfy the boundary conditions of the outgoing wave. They describe states that have stationary normalized spatial profiles and amplitudes decaying in time due to radiative losses. These quasi-normal modes play an important role in transport, e.g., in

the localization regime energy is transported either by tunneling through a localized mode in the middle of the sample or by hopping over a necklace state that is formed via coupling of several localized modes [30–35]. If the input beam is coupled to multiple modes, the interference of these modes at the output end determines the total transmission [28]. The two approaches to describe transport phenomena, transmission channels and resonant modes, complement each other [29]. At any frequency, the transmission eigenchannels can be expressed as a frequency-dependent superposition of resonant modes with specific resonance frequencies and widths. In the localization regime, the maximal transmission channel can typically be identified with a single resonant mode [29].

Absorption of radiation is usually assumed to suppress interference effects such as the occurrence of open channels. Most studies on transmission eigenchannels have considered lossless random media where absorption is negligible. In reality absorption exists in any material system, and could have a significant impact on diffusion and localization [36, 37]. In the microwave regime for instance, absorption is particularly difficult to avoid and leads to a significant reduction of the transmission through disordered waveguides [12, 38]. Absorption does not destroy the phase coherence of scattered waves, but it attenuates the longer scattering paths more than the shorter paths, thus modifying the interference patterns. Since the open channels penetrate deeper into the random medium than the closed channels, they would experience more absorption. In other words, absorption should have a stronger effect on the open channels than on the closed channels. However, it is not clear how absorption would modify the open channels. Moreover, it has been shown lately that light absorption in strongly scattering media can be greatly enhanced or inhibited by coherent effects [39–41]. Thus the interplay between absorption and interference determines not only the amount of energy being transmitted, but also the amount of energy being deposited in the random media. The investigation of strongly scattering

systems with absorption is therefore not only important to the fundamental study of mesoscopic transport, but also relevant for applications in imaging, light harvesting, and lighting technology [23–25, 42, 43].

In this chapter, we address the following questions: how does absorption modify the open channels? How does the channel bandwidth vary with absorption? What is the correlation between a transmission and a reflection channel in the presence of absorption? In weak absorption, when the ballistic absorption length l_a is much larger than the average path length $l_p = 2L^2/l_t$ (l_t is the transport mean free path), most scattering paths are not affected by absorption. However, when ballistic absorption length becomes smaller than the average path length $l_a < l_p$, attenuation of long scattering paths significantly affects the transport through the system. To study the change of light transport, we compute the spatial field distribution inside the random medium. The spectral width of the maximal transmission channel is important to many of the aforementioned applications, for instance, a broad spectral width is desired for light harvesting. To address this question, we calculate the frequency bandwidth of input wavefront corresponding to the maximal transmission channel and its scaling with absorption. Experimental studies of the transmission channels rely on the access to both sides of the scattering media. It is, however, often more convenient and less invasive to work in a reflection configuration, where all measurements are on the input side of the sample. For example, without absorption, the total transmission is maximized by finding the minimal reflection channel [44]. In presence of absorption, the relation between the maximal transmission channels and the minimal reflection channels is not known. Therefore, we investigate the correlation between these two channels as a function of absorption.

6.2 Numerical model

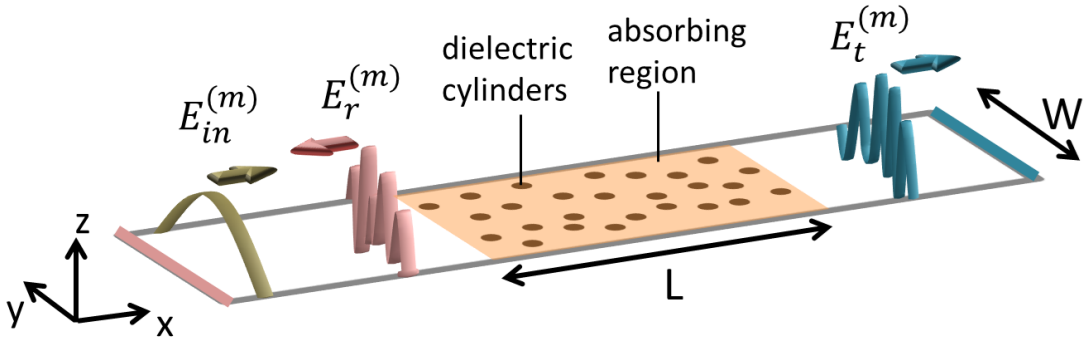

Figure 6.1: Schematic of the 2D disordered waveguide used in our numerical simulation. Dielectric cylinders are placed randomly in a waveguide with perfect-reflecting sidewalls. The waveguide width is W, and the length of the disordered region is L. A light field $E_{in}^{(m)}$ is launched from the left end of the waveguide, and scattered by the cylinders. The transmitted light field $E_t^{(m)}$ is probed at the right end, and the reflected light field $E_r^{(m)}$ at the left end. Perfectly-matched-layers are placed at both open ends to absorb the transmitted and reflected waves.

We consider a two-dimensional (2D) disordered waveguide, shown schematically in Fig. 6.1. Dielectric cylinders with refractive index $n = 2.5$ and radius $r_c = 0.098\lambda$ are randomly positioned inside the waveguide with perfectly reflecting sidewalls. The dielectric cylinders occupy an area fraction of 0.04 corresponding to an average distance between cylinders of $a = 0.87\lambda$. We select to work at the wavelength of input light that avoids the Mie resonances of individual dielectric cylinders. This frequency is in photonic regime above the first band gap of a triangular lattice with the same area fraction [45]. Light enters the waveguide from the left open end and is scattered by the cylinders. Light transmitted through or reflected from the random array is absorbed by the perfectly-matched-layers placed at both ends of the waveguide. We consider transverse-magnetic (TM) polarized light, whose electric field is parallel to the cylinder axis (z-axis). The width of the waveguide is $W = 10.3\lambda$, the number of guided modes in the empty waveguide is $N = 2W/\lambda = 20$. The length of the random array of cylinders is $L = 20.2\lambda$.

To calculate the electromagnetic field inside the random waveguide, we solve Maxwell's equations using the finite-difference frequency-domain method [46]. The intensity is averaged over a cross-section of the waveguide to obtain the evolution $I(x)$ along the waveguide in the x direction. The ensemble-averaged $I(x)$ exhibits the well known linear decay, from which we extract the transport mean free path $l_t = 0.073L$ [47]. Since $l_t \ll L$, light experiences multiple scattering. The localization length is $\xi = (\pi/2)Nl_t = 2.3L$. The system is in the diffusion regime, as confirmed from the linear decay of intensity but it is close to the localization regime. The reason we chose this regime is as follows. In the localization regime, the maximal transmission eigenchannel is composed of only one or two quasi-normal modes [29]. In the diffusion regime ($\xi \gg L$), many overlapping modes contribute to the maximal transmission channel, making the analysis complicated. Since our system is in the diffusive regime, close to the localization transition, the maximal transmission channel consists of a few quasi-normal modes. In this regime the transport displays a large fluctuation from one realization to another. Within the same statistical ensemble there are random realizations that are closer to or further away from the localization transition. We can therefore study a wide range of behavior in the same ensemble.

Usually, absorption exists either inside the scattering particles, in the waveguide wall or in the background material that hosts the particles. The concomitant contrast in the imaginary part of the refractive index causes additional scattering, which modifies the resonant modes [48]. We prefer to avoid this additional scattering effect by introducing a spatially homogeneous imaginary refractive index γ to both scatterers and background, so that mode wavefunctions do not change and we can focus on the effects of absorption and energy loss. The ballistic absorption length is $l_a = 1/(2k\gamma)$, where the wavevector is $k = 2\pi/\lambda$. When the ballistic absorption length l_a reaches the average path length of light in a 2D diffusive system $l_p = 2L^2/l_t$, the diffusive absorption length $\xi_a = \sqrt{l_t l_a/2}$ becomes equal to the system length $\xi_a = L$.

To construct the transmission matrix t of the disordered waveguide, we use the guided modes or propagation channels in the empty waveguide as the basis. We launch a guided mode $E_{in}^{(m)}$ from the input end, calculate the transmitted wave and decompose it by the empty waveguide modes at the output end, $E_t^{(m)} = \sum_{n=1}^{N} t_{nm} E_{in}^{(m)}$. The coefficient t_{nm} relates the field transmission from an input channel m to an output channel n. After repeating this procedure for $m = 1, 2, ...N$, we obtain all the elements t_{nm} for the transmission matrix t. Similarly, the reflection matrix is constructed by computing the reflected waves $E_r^{(m)}$ at the input end.

6.3 Maximal transmission channel

A singular value decomposition of the transmission matrix t gives

$$t = U\ \Sigma\ V^{\dagger}\ , \tag{6.1}$$

where Σ is a diagonal matrix with non-negative real numbers, $\sigma_n = \sqrt{\tau_n}$, τ_n is the eigenvalue of $t^{\dagger}t$, $\tau_1 > \tau_2 > \tau_3 ... > \tau_N$. U and V are $N \times N$ unitary matrix, V maps input channels of the empty waveguide to eigenchannels of the disordered waveguide, and U maps eigenchannels to output channels. The column vectors in V (U) are orthonormal and are called input (output) singular vectors. The value τ_n represents the transmittance of the n^{th} transmission channel. The input singular vector corresponding to the highest transmission eigenvalue τ_1 gives the maximal transmission eigenchannel, its elements represent the complex coefficients of the waveguide modes that combine to achieve maximum transmission through the random medium.

6.3.1 Effects of absorption on spatial field distribution and energy flow of the maximal transmission channel

We inject light into the maximal transmission channel and investigate the field profile inside the random medium. In Fig. 6.2(a) we plot the spatial distribution of the electric field amplitude $|E_z|$ inside the disordered waveguide with increasing L/ξ_a. To map the energy flow inside the disordered medium, we compute the Poynting vector $\vec{S}(x,y) = \frac{1}{2}\mathrm{Re}[\vec{E}(x,y) \times \vec{H}^*(x,y)]$. Its projection onto the propagation direction (x-axis) is $S_x(x,y) = \vec{S}(x,y) \cdot \vec{e}_x$, where $\vec{e}_x$ is the unit vector along the x-axis. The net flow over a cross section of the disordered waveguide is $F(x) = \int_0^W S_x(x,y)dy$. Without absorption, the net flow is a constant, $F(x) = F(0)$. In the presence of absorption, $F(x)$ decays exponentially along x. For a clear visualization of the energy flow deep inside the random structure, we normalize the Poynting vector $\vec{S}(x,y)$ by $F(x)$ to compensate the energy decay such that $\vec{S}'(x,y) = \vec{S}(x,y)/F(x)$. Figure 6.2(b) plots the magnitude of normalized Poynting vector $|\vec{S}'(x,y)|$. For a quantitative analysis of the light propagation direction, we compute the angle of the Poynting vector $\vec{S}(x,y)$ with respect to the x-axis, $\theta_s(x,y) = \tan^{-1}[(\vec{S}(x,y) \cdot \vec{e}_y)/(\vec{S}(x,y) \cdot \vec{e}_x)]$ where $\vec{e}_y$ is the unit vector along the y-axis. In Fig. 6.2(c), we plot the histogram of θ_s weighted by the relative amplitude of the Poynting vector, $P(\theta_s) = \int |\vec{S}'(x,y)|\delta(\theta_s - \theta_s(x,y))dxdy$.

Let us now discuss the results in Fig. 6.2(a-c). When absorption is weak ($L/\xi_a < 1$), the maximal transmission channel has nearly the same field pattern as the channel without absorption. The energy flow inside the random structure resembles meandering random paths that are intertwined, and many "loops" are seen. The multiply scattered light propagates in many directions, and the distribution of Poynting vector's angle $P(\theta_s)$ is broad and has a large variance. Once L/ξ_a exceeds 1, the spatial profile evolves. At $L/\xi_a = 4$, a noticeable change of the field pattern is observed: the loops gradually disappear, and the creeks become straighter. This behavior occurs because the longer scattering paths that involve more windings are strongly attenu-

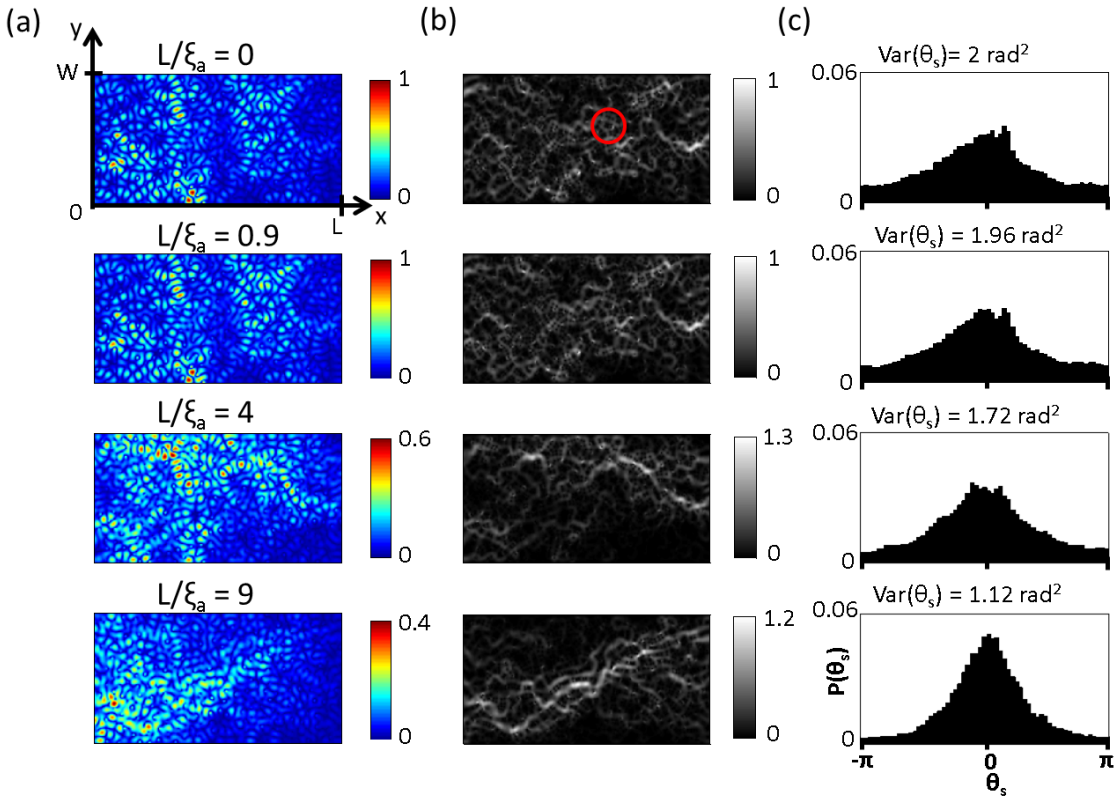

Figure 6.2: Evolution of maximal transmission channel with absorption. Calculated electric field amplitude $|E_z|$ [column (a)], normalized Poynting vector amplitude $|\vec{S}'(x,y)|$ in gray scale [column (b)], and histogram of weighted Poynting vector direction $P(\theta_s)$ [column (c)] of the maximal transmission channel inside the disordered waveguide as absorption L/ξ_a increases from top to bottom. In (a), the maximal transmission channel remains robust against absorption with nearly identical field pattern up to $L = \xi_a$ and changes significantly beyond that point. In (b) the winding paths of light are illustrated inside the random structure in the weak absorption regime $L/\xi_a < 1$, and more straight "snake-like" paths in the strong absorption regime $L/\xi_a > 1$. A "loop" in the energy flow is circled in red. In (c), the angle θ_s from the Poynting vector to the x-axis is widely spread between $-\pi$ and π when $L/\xi_a < 1$, but concentrates close to 0 when $L/\xi_a > 1$. The variance of θ_s, indicated above each panel, decreases with increasing L/ξ_a

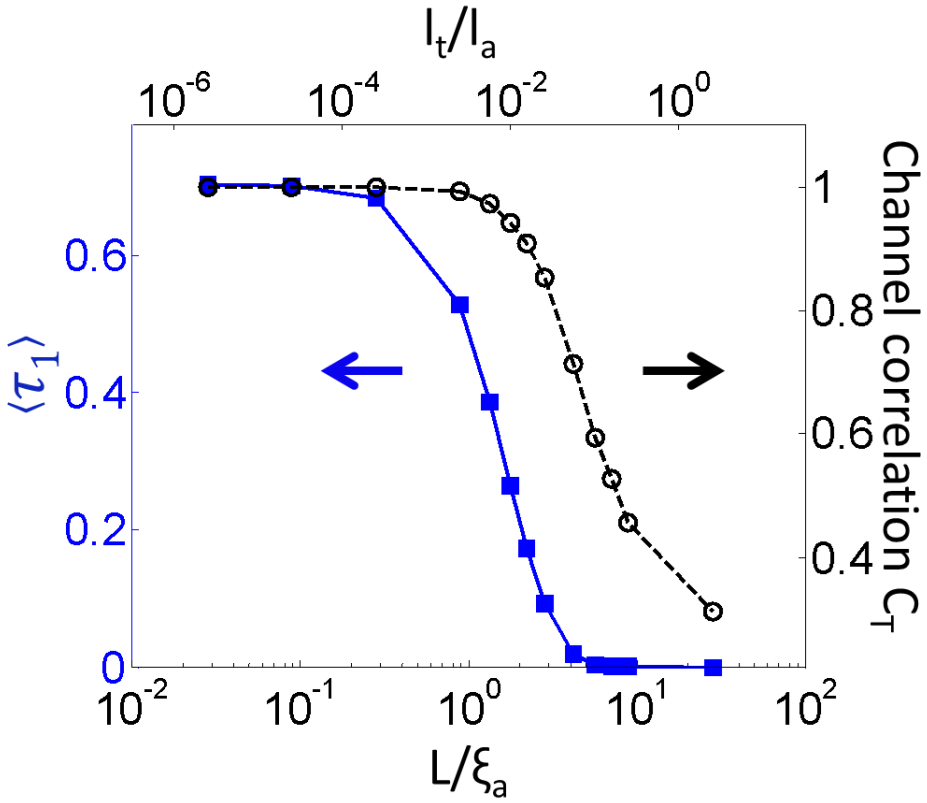

Figure 6.3: Maximal transmission eigenvalue and eigenvector versus absorption. Filled squares connected by solid line represent the ensemble-averaged highest transmission eigenvalue $\langle \tau_1 \rangle$ as a function of absorption (bottom axis L/ξ_a, top axis l_t/l_a). Open circles connected by dashed line represent the correlation of the input singular vector with absorption to the one without absorption C_T. The maximal transmission eigenchannel changes at higher absorption level compared to its eigenvalue.

ated by absorption. To maximize the transmission through the random system, light takes a shorter and more straight path to minimize absorption. As a result, the distribution of Poynting vector's angle $P(\theta_s)$ becomes narrow and its variance decreases. When absorption becomes very strong ($L/\xi_a = 9$), the maximal transmission channel bears no resemblance to the one with weak absorption. All meandering creeks eventually merge into a single stream with few windings and light propagates mostly in the forward direction.

For a quantitative characterization of the change of the maximal transmission channel by absorption, we compute the correlation of its input singular vector $\mathbf{v_1}$ with

the one without absorption $\mathbf{v_0}$:

$$C_T = |(\mathbf{v_0}, \mathbf{v_1})|, \tag{6.2}$$

where $(\mathbf{v_0}, \mathbf{v_1}) = \mathbf{v_0}^\dagger \mathbf{v_1}$ is the inner product of the normalized singular vectors $\mathbf{v_1}$ and $\mathbf{v_0}$. Figure 6.3 plots the channel's correlation C_T, averaged over 40 random realizations, as a function of L/ξ_a. Its value stays close to 1 when system length is smaller than the diffusive absorption length $L < \xi_a$, and it drops abruptly as $L > \xi_a$. In the same figure, we also plot the ensemble-averaged highest transmission eigenvalue $\langle \tau_1 \rangle$ versus L/ξ_a. Due to the small number of input channels ($N = 20$) in the waveguide, the highest transmission eigenvalue $\langle \tau_1 \rangle$ does not reach 1 even without absorption ($L/\xi_a = 0$). As the absorption L/ξ_a increases, the highest transmission eigenvalue $\langle \tau_1 \rangle$ decreases much earlier than the channel's correlation C_T. For example, at $L/\xi_a = 2.2$, the highest transmission eigenvalue $\langle \tau_1 \rangle$ is already reduced by a factor of 4, while the correlation C_T remains more than 0.9. Thus in the weak absorption regime, the maximal transmission eigenvalue decreases while the eigenvector remains almost the same. This means that interference remains strong, and absorption merely reduces the amount of energy reaching the output end, but does not change the interference pattern. However, in the strong absorption regime, the number of significant scattering paths is greatly reduced, and the interference effects are weakened. Consequently, the maximal transmission channel starts to change dramatically and becomes "ballistic-like" as we have seen in Fig. 6.2.

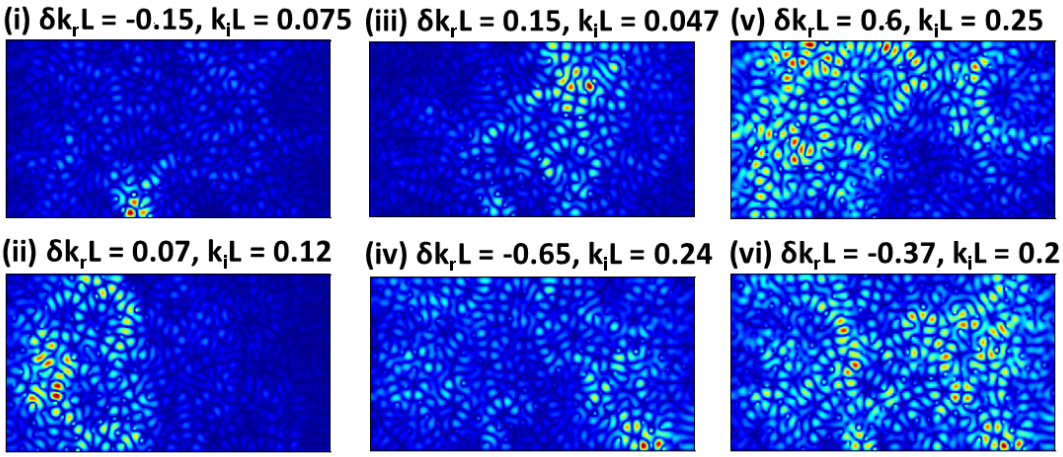

Figure 6.4: Quasi-normal modes contributing to the maximal transmission channel. (a) Spatial distribution of electric field amplitude ($|E_z|$) for the six quasi-normal modes with the highest degree of correlation with the maximal transmission channel in Fig. 6.2. The normalized center frequency $\delta k_r L = (k_r - k_o)L$ and linewidth $k_i L$ of each mode are given on top of each panel within parentheses ($\delta k_r L$, $k_i L$), where $(k_r + ik_i)c = \omega_r + i\omega_i$ is the complex frequency of the quasimode at zero absorption.

6.3.2 Correlation of the maximal transmission channel with quasi-normal modes

To understand how the maximal transmission channel is formed and how it is modified by absorption, we investigate the related quasi-normal modes. Unlike the input or output singular vectors of the transmission matrix, the quasi-normal modes of an open random system are not orthogonal [49–51], thus it is difficult to decompose the 2D field pattern of a transmission eigenchannel by the quasi-normal modes. Alternatively, we compute the degree of correlation between each quasimode and the eigenchannel to identify the modes that contribute significantly to the transmission channel. We used the commercial program Comsol to compute the complex frequency ($\omega = \omega_r + i\omega_i$) and field pattern of each quasi-normal mode in the disordered waveguide. The imaginary part ω_i of the complex frequency gives the decay rate or spectral width of the resonance, and the ratio of ω_r to ω_i is proportional to the quality factor. The contribution of a mode to the maximal transmission channel is reflected in

the correlation of their spatial field profiles, $C_M = |\int E_q^*(x,y)E_c(x,y)dxdy|$, where $E_q(x,y)$ and $E_c(x,y)$ represent the normalized spatial distribution of the electric field E_z for the mode and the channel, respectively.

For the maximal transmission channel in Fig. 6.2, we identify six quasimodes

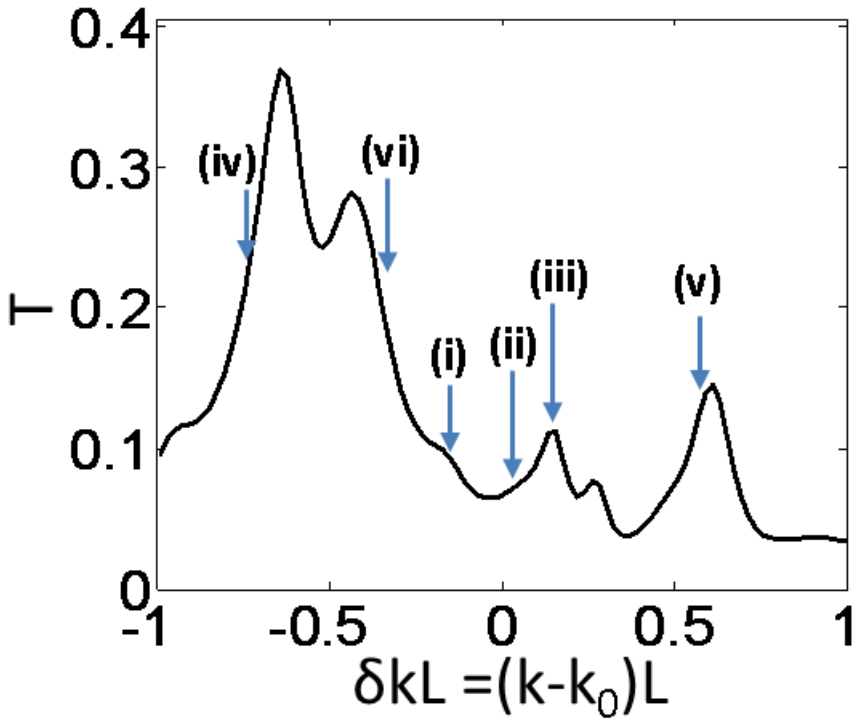

Figure 6.5: (a) A typical transmission spectrum for a random input field. The arrows mark the center frequency of the modes (i)-(vi).

with the highest degrees of correlation, and present their field patterns in Fig. 6.4. The first three modes, labeled (i) - (iii), have the dominant contributions to the maximal transmission channel at zero absorption. Mode (i) is a tightly confined mode, which is visible in the field profile of the eigenchannel [Fig. 6.2(a)]. Modes (ii) and (iii) are more extended, but they are not spread over the entire system, instead mode (ii) concentrates in the left-half of the disordered waveguide, and mode (iii) in the right-half. Their field patterns can be recognized in that of the eigenchannel. In contrast, modes (iv)-(vi) are spatially extended over entire disordered waveguide, and

their linewidths (decay rates) are larger than those of modes (i)-(iii). Figure 6.5 plots a typical transmission spectrum for a random input field. Modes (i)-(iii) are closest to the probe frequency and they have the largest contributions to the maximal transmission channel. Since these modes have little spatial overlap, optimum transport of energy is facilitated by hopping through them. Hence, the maximal transmission channel can be regarded as a necklace of resonances strung from one side of the system to the other. It is similar to the necklace state that dominates the transport in the localization regime [31], except that it is not a single state (quasi-normal mode) but an eigenchannel of the transmission matrix. Although the total transmission at the center frequency of mode (ii) is lower than that of mode (v), mode (v) is spectrally further away from the probe frequency than modes (ii), and its contribution to the maximal transmission channel is much smaller. We note that if the probe frequency shifts to the vicinity of the center frequency of mode (v), this mode will dominate the highest transmission channel, and the maximal energy transport occurs via an extended mode. Thus the necklace-like channels of maximal transmission exist only at certain probe frequencies.

Figure 6.6 shows how the correlation between the maximal transmission channel and the quasi-normal modes change with absorption. In the regime of weak absorption ($L < \xi_a$), the correlation with each mode remains nearly constant, thus the field pattern of the transmission channel hardly changes. Note that the absorption is uniform and does not modify the spatial profile of individual quasimodes. When the absorption is strong ($L > \xi_a$), the correlations with modes (i)-(iii) decreases while the correlations with modes (v)-(vi) increases. These modes, unlike modes (i)-(iii), are extended over the entire system, and their contributions to the maximal transmission channel increase with absorption. With a further increase of absorption to $L/\xi_a = 9$, the maximal transmission channel has contributions from all the quasimodes that have spectral overlap with the channel. The interference of these modes leads to the

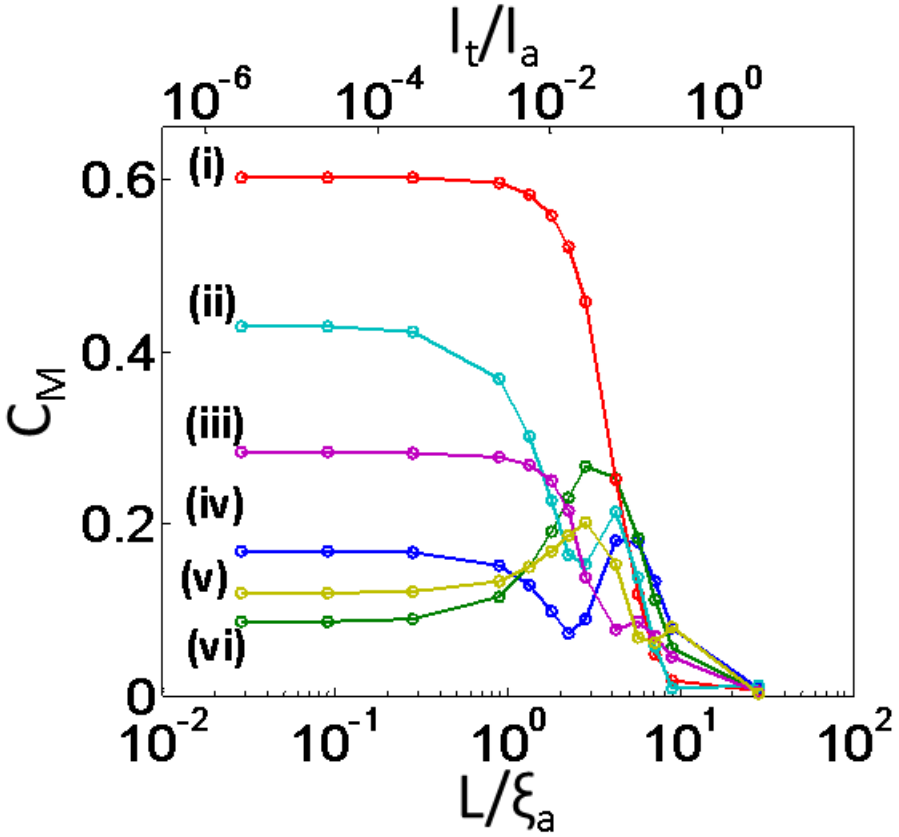

Figure 6.6: Correlation of the six quasimodes, labeled (i) - (vi) in Fig. 6.5, with the maximal transmission channel C_M as a function of L/ξ_a. Modes that contribute the most at low absorption are closest to the channel frequency but spatially confined in the random structure so maximal transmission is facilitated through resonances hopping. However, when absorption is strong, more modes contribute to the maximal transmission channel and form less winding light paths to reduce the total absorption.

formation of the ballistic-like channel with maximal transmission.

6.3.3 Scaling of spectral width of maximal transmission channel with absorption

The profile of the maximal transmission channel changes with frequency. Its spectral width gives the frequency interval over which a fixed input wavefront, optimized at a single frequency, still leads to strongly enhanced transmission. A previous study on light focusing through lossless turbid media shows that the frequency bandwidth of a wavefront optimized for a single focus is equal to the width of speckle correlation function D/L^2, where D is the diffusion coefficient [52]. In this section, we investigate how absorption modifies the frequency bandwidth of the maximal transmission channel.

To compute the bandwidth, we first input monochromatic light at frequency k_0 with the wavefront corresponding to the input singular vector of the maximal transmission channel, and calculate the total transmission $T(k_0)$ at the output end. Then, we scan the input light frequency k while keeping the same wavefront and calculate the new transmission value $T(k)$. As the frequency k is detuned from k_0, the total transmission T decreases. The bandwidth of the transmission channel is defined by the full-width-at-half-maximum (FWHM) as $\Delta k = k_2 - k_1$, where $T(k_1) = T(k_2) = T(k_0)/2$, $k_1 < k_0 < k_2$. With the introduction of absorption, Δk increases.

We observe varying scaling of Δk with l_t/l_a for various disorder configurations. Figure 6.7(a) shows three types of behavior where the bandwidth increases linearly for realization A (blue dashed line), sub-linearly for realization B (green solid line), and super-linearly for realization C (red dotted line) with l_t/l_a. In contrast, all the quasi-normal modes exhibit the same linear increase of their spectral width with absorption. The average spectral width of quasimodes is shown by the black dash-dotted

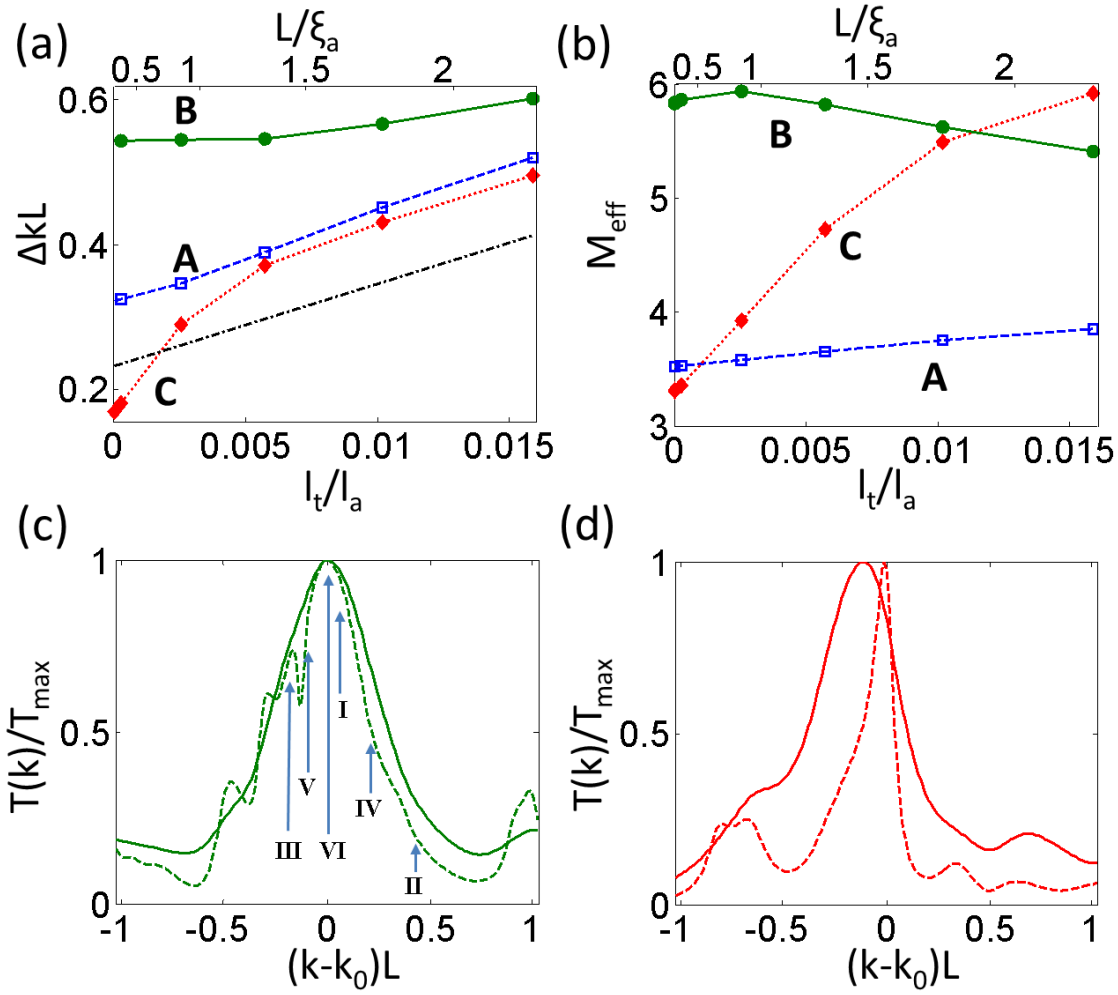

Figure 6.7: Dependence of the spectral width of the maximal transmission channel on absorption. (a) Spectral width of the maximal transmission channel Δk with absorption (bottom axis l_t/l_a, top axis L/ξ_a) for three waveguide realizations A, B, C. The increase is linear for realization A (open squares connected by blue dashed line), sub-linear for B (filled circles connected by green solid line), and super-linear for C (filled diamonds with red dotted line). Black dash-dotted line represents the average linewidth for the quasimodes. (b) Mode participation number M_{eff} vs. absorption, it increases slightly for A, decreases for B and increases dramatically for C. (c,d) Total transmission for the input vector that gives the maximal transmission at k_0 as a function of frequency detuning of input light $k - k_0$ at $l_t/l_a = 0$ (dashed line) and 0.016 (solid line) for realizations B and C.

line in Fig. 6.7(a).

To interpret these results, we again consider the quasi-normal modes underlying the transmission eigenchannel. We calculate the mode participation number defined as $M_{\text{eff}} \equiv (\sum C_M)^2/(\sum C_M^2)$. The summation includes modes within a fixed frequency range of $|k - k_0|L < 0.62$. Modes with a frequency beyond this range have a negligible contribution as they are spectrally located far outside the bandwidth of the maximal transmission channel. Figure 6.7 (b) plots the mode participation number versus absorption for the three realizations A, B, C. For A (linear scaling of Δk with l_t/l_a), M_{eff} increases slightly with l_t/l_a, whereas for B (sublinear scaling of Δk with l_t/l_a), M_{eff} decreases. In contrast, C, which features a superlinear scaling of Δk with l_t/l_a, exhibits a rapid increase in M_{eff} as absorption increases. These results indicate that the bandwidth of the maximal transmission channel is related to the number of quasimodes contributing to the transmission. Figure 6.7 (c) and (d) show the total transmission for the input vector that gives the maximal transmission at k_0 versus the frequency detuning of input light $k - k_0$ at $l_t/l_a = 0$ and 0.016 for realizations B and C, respectively. We note that without absorption, the transmission of B that possesses a higher mode participation number, has a broader bandwidth than C. This is explained by the fact that more modes at different frequencies contribute to the total transmission. The dramatic increase in the mode participation number for C adds to the absorption-induced broadening, leading to a super-linear increase of the channel bandwidth. Conversely, for B the broadening due to the increase of absorption is partially compensated by the reduction in the number of modes participating in the transmission, resulting in a sub-linear behavior.

We have calculated many realizations, and found the behavior of A and C to be more common. To explain the trend of B in Fig. 6.7(b), we plot in Fig. 6.8(a) the correlations of the maximal transmission channel with six quasimodes, labeled (i)-(vi), in the disordered waveguide B. These modes have the highest correlations

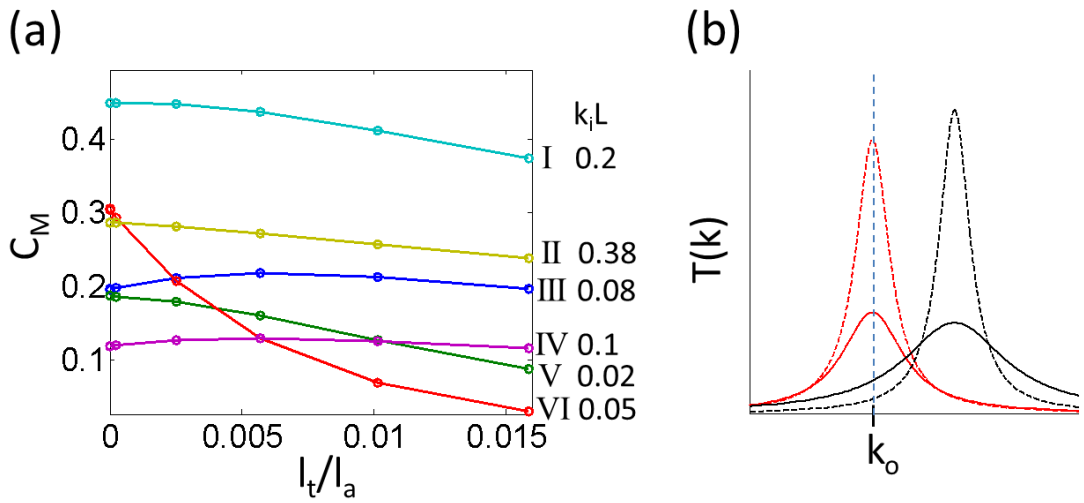

Figure 6.8: Effect of modes' contribution in the change of linewidth. (a) Correlation of six quasimodes, labeled (i)-(vi), with the maximal transmission channel as a function of l_t/l_a. The normalized center frequency of each mode is marked by an arrow in (c), and the normalized linewidth k_iL at zero absorption is given next to the panel. (b) Schematic of the transmission spectrum having two quasimodes in the absence of absorption (dashed line) and with absorption (solid line). It shows how the spectral broadening by absorption modifies the contributions of these two modes to the transmission channel at k_0. For the mode centered at k_0, its contribution to the channel decreases rapidly. For the mode farther way from the probe frequency, its contribution increases when absorption becomes strong.

with the maximal transmission channel at zero absorption. The center frequencies of these modes are marked by arrows in Fig. 6.7(c), and their linewidths are given in Fig. 6.8(a). With increasing absorption, mode (vi) quickly de-correlates with the maximal transmission channel, indicating its contribution to the channel decreases rapidly. This mode is located close to the probe frequency and its linewidth is small without absorption. As shown schematically in Fig. 6.8(b), absorption spectrally broadens this mode, and its spectral overlap with the channel decreases, leading to a reduction in its contribution to the maximal transmission channel. Another mode (v) which has narrower linewidth than mode (vi) is detuned from the probe frequency, and its spectral overlap with the channel is lower. Consequently its contribution only decreases slightly with absorption. All other modes have broader linewidth at zero absorption, and the absorption-induced broadening is relatively weak. Thus their contributions to the maximal transmission channel change more slowly with absorption. Therefore, the decrease of mode participation number with absorption is due to rapid reduction in contributions from the long-lived modes that are almost in resonance with the channel. With a further increase of absorption, the modes, initially having little overlap with the probe frequency, are spectrally broadened enough to contribute to the maximal transmission channel at the probe frequency, leading to an increase of the mode participation number.

Even though there appears to be different scaling behavior from one disorder realization to another, the ensemble-averaged bandwidth of the maximal transmission channel increases linearly with absorption. This result echoes the finding reported in Ref. [41] where the linewidth of perfect absorption channel exhibits a linear scaling with absorption.

6.4 Minimal reflection channel

In lossless random media, the maximal transmission channel is equivalent to the minimal reflection channel; the only way of reducing reflection is to enhance transmission. In an absorbing medium, this is no longer true: reflection may be reduced by enhancing absorption instead of transmission. In this section, we study the relations between the maximal transmission channel, the minimal reflection channel and the maximal absorption channel in absorbing random media.

The reflection eigenchannels are obtained by singular value decomposition of

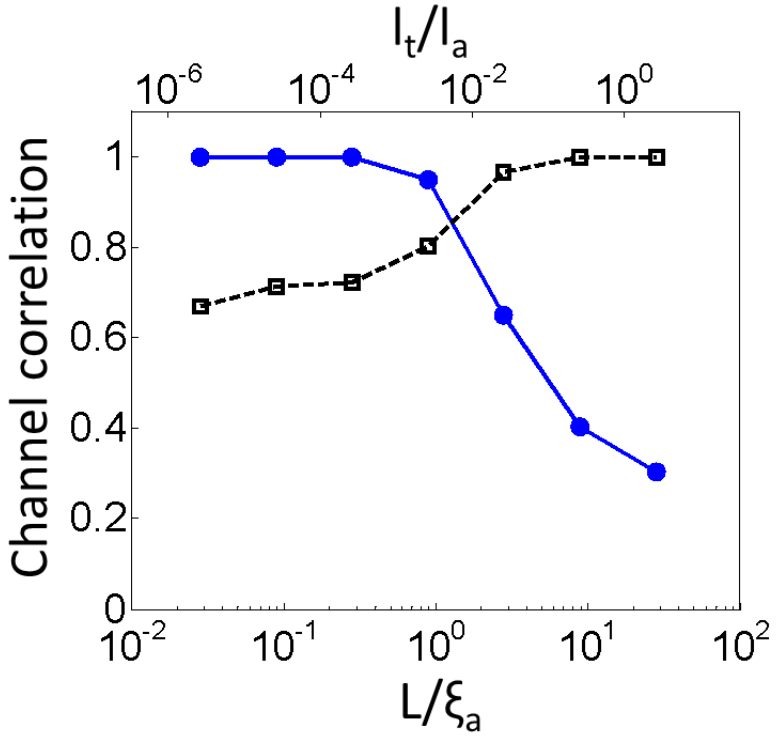

Figure 6.9: Absorption-induced change of minimal reflection channel. Filled circles connected by solid line represent the correlation between the minimal reflection channel and the maximal transmission channel. Open squares connected by dashed line represent the correlation between the minimal reflection channel and the maximal absorption channel. The minimal reflection channel is the same as the maximal transmission channel when absorption is weak $L < \xi_a$, but it approaches the maximal absorption channel as absorption is strong $L > \xi_a$.

the field reflection matrix r. The input singular vector corresponding to the lowest

singular value gives the minimal reflectance. We compute the correlation between the input singular vector for maximal transmission and that for minimal reflection using the same definition as in Eq.(6.2) and present the result in Fig. 6.9 (blue solid line). The correlation is almost one in the weak absorption regime ($L < \xi_a$), but drops quickly once in the strong absorption regime ($L > \xi_a$). When the absorption is weak, the lowest reflection is still achieved by maximizing transmission. With strong absorption, light that is not reflected can be either transmitted or absorbed. Hence, reflection is reduced by enhancing both transmission and absorption.

To find the maximal absorption channel, we introduce the matrix h that links

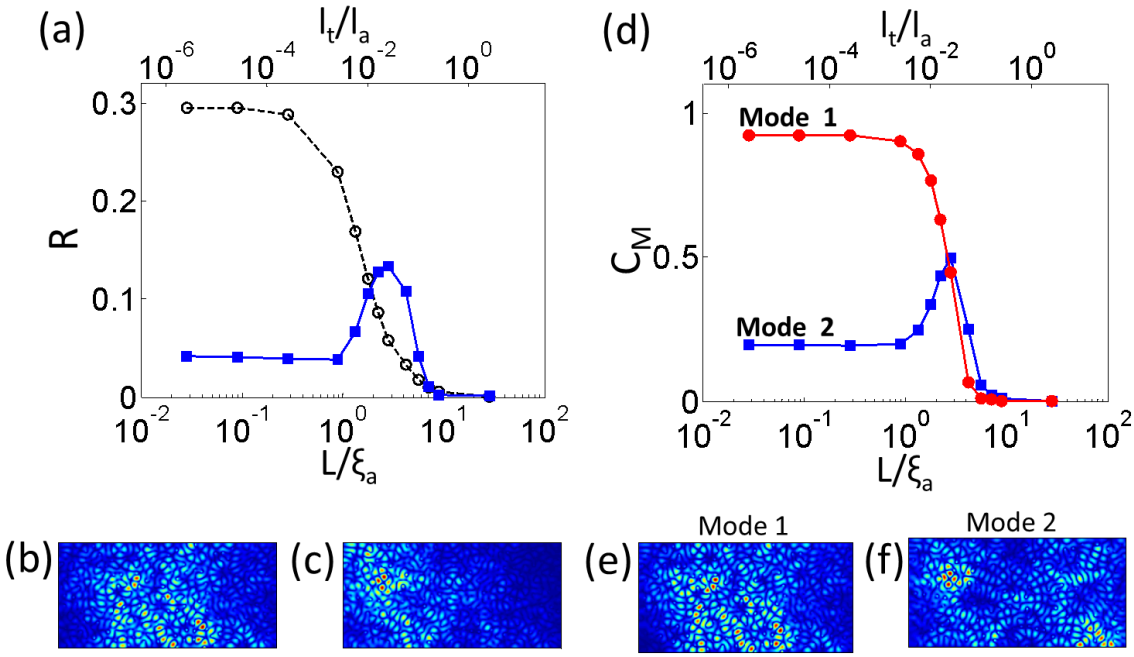

Figure 6.10: Example of increasing minimal reflectance with absorption. (a) Open circles connected by dashed line represent the ensemble-averaged lowest reflection eigenvalue as a function of absorption. Filled squares connected by solid line represent the lowest reflection eigenvalue of a selected realization that increases with absorption. (b-g) are for the selected realization. (b, c) Spatial distribution of the electric field amplitude $|E_z(x, y)|$ inside the random waveguide at $L/\xi_a = 0$ and 3, respectively. The lowest reflection eigenvalue reaches a local maximum at $L/\xi = 3$. (d) Correlation of the minimal reflection channel with quasimodes 1 and 2. (e, f) Electric field patterns of mode 1 and 2.

light incident from one end of the waveguide to the transmitted and reflected fields:

$$h = \begin{pmatrix} r \\ t \end{pmatrix} \tag{6.3}$$

where r and t are the field reflection and transmission matrices. An eigenvalue of $h^\dagger h$ represents the sum of the reflectance and the transmittance of its associated input singular vector. The singular vector of h with the smallest singular value corresponds to the maximal absorption channel. The correlation coefficient between the minimal reflection and maximal absorption channels is plotted as a function of the absorption in Fig. 6.9 (black dashed line). As the correlation between the minimal reflection channel and the maximal transmission channel decreases, the correlation between the minimal reflection channel and the maximal absorption channel increases. Eventually, in the strong absorption regime, the minimal reflection channel becomes identical to the maximal absorption channel, indicating that the minimal reflection is achieved by maximizing absorption instead of transmission.

Intuitively one expects all reflection eigenvalues to decrease with increasing absorption. Indeed, we show in Fig. 6.10(a), the ensemble-averaged minimal reflection eigenvalue decreases with absorption. Strikingly, in a significant number of realizations we have observed the opposite behavior, a counter-intuitive increase of reflection caused by absorption. In Fig. 6.10(a) we show the minimal reflectance of a selected realization. The minimal reflectance (eigenvalue of $r^\dagger r$) first decreases slightly as L/ξ_a increases from 0 to 1, then rises rapidly by a factor of 3 before dropping again at larger absorption. In Fig. 6.10(b) and (c) we show the electric field patterns inside the random waveguide corresponding to the minimal reflectance without absorption and at $L/\xi_a = 3$ where the lowest reflection eigenvalule reaches a local maximum. In the absence of absorption, light penetrates deep into the random medium with the

field maxima close to the center of the sample. However, at $L/\xi_a = 3$, the penetration depth is greatly reduced and the field maxima shift to the input end of the random system. The field pattern close to the input surface of the same is also strongly modified.

To understand this counter-intuitive behavior, we investigate the quasi-modes that contribute to the minimal reflection channel. Fig. 6.10(d) plots the degree of correlation between the minimal reflection channel and two quasi-modes (labeled 1, 2) that have the highest contributions, and in Fig. 6.10(e) and (f) show their field patterns. Without absorption, the least reflection channel is dominated by mode 1 that is located near the center of the sample. Destructive interference of various scattering paths of light in the disordered waveguide minimizes the reflectance. This explains the low minimal reflectance value of the selected realization compared to the ensemble-averaged one. With the introduction of absorption to the system, relative amplitudes of these paths are changed, the longer paths are attenuated more than the shorter paths, thus the destructive interference is weakened, leading to an increase of the reflectance as shown in Fig. 6.10(a). When the minimal reflectance has a maximum at $L/\xi_a = 3$, the field pattern of the minimal reflection channel shown in Fig. 6.10(c), resembles that of mode 2 in the left half of the waveguide. At this strong absorption level, the contribution of mode 1 to the minimal reflection channel is negligible, whereas mode 2 becomes dominant, which is a mode with a larger overlap with the input light into the disordered waveguide. Therefore, the interference in the bulk of the sample - that is the cause of open transmission channels - is suppressed, which leads to an increased reflectance.

Let us now consider the input wavefront E_1, which corresponds to the minimal reflection channel (or maximal transmission channel) without absorption. E_1 couples most of the input energy into mode 1. Figure 6.11 shows the reflectance associated with input wavefront E_1 as a function of absorption L/ξ_a. When absorption be-

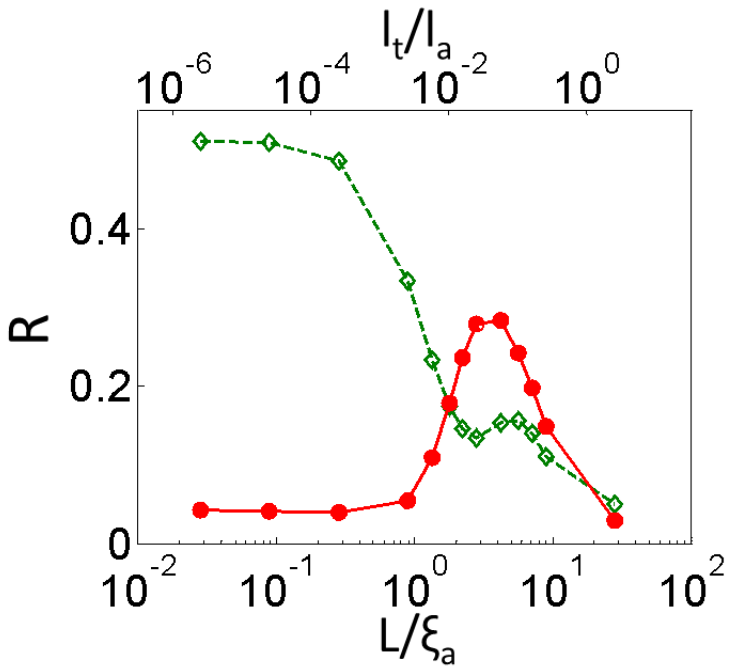

Figure 6.11: Reflection with different input wavefronts. Filled circles connected by solid line (open diamonds connected by dashed line) represent the reflectance of a fixed input wavefront $E_1(E_2)$ that corresponds to the input singular vector of the minimal reflection channel at $L/\xi_a = 0$ $(L/\xi_a = 3)$.

comes significant ($L > \xi_a$), the reflectance increases rapidly, up to 5 times its value at $L/\xi_a = 0$. Another input wavefront E_2, corresponding to the minimal reflection channel at $L/\xi_a = 3$, couples most of the energy into mode 2. In Fig. 6.11, we show the evolution of the reflection value associated to this wavefront with absorption. As expected, the reflectance decreases with increasing absorption. Once the reflectance with input wavefront E_2 becomes lower than that associated with E_1, mode 2 becomes dominant in the minimal reflection channel. This illustrates that with increasing absorption, the mechanism that produces the minimal reflection channel changes from transmission to bulk absorption. Moreover, it shows the significant role played by interference of scattered waves up to the point where the absorption becomes dominant.

6.5 Discussion

It has been suggested that the change in transport behavior of the maximal transmission channel with increasing absorption bears similarity to the change found recently in the dynamic transport of localized samples [53]. There ballistic transport was observed at early times after a pulsed excitation, which involved all excited quasimodes. At later times, the modes with shorter lifetimes dissipate, and only the modes with longer lifetimes survive and dominate transmission. In the case of strong absorption, long optical paths are eliminated and only short paths survive, making the transport ballistic-like. The maximal transmission channel consists of both long-lived and short-lived modes, similar to the dynamic transport at early times. In the long time limit, the transmission of a localized sample is dominated by a single quasi-mode with the longest lifetime, however, the maximal transmission channel in a diffusive sample with weak or no absorption consists of multiple long-lived modes as shown in section III.

It is worth to note that such necklace-like transport due to hopping of several spatially confined modes is unlikely to exist if the width of the disordered waveguide is increased significantly. This is because the localization length, which increases linearly with the waveguide width, will become much larger than the system length. Hence the system moves further away from the localization regime, most quasimodes are spatially extended over the random media. Also the mode density increases with the system size. No matter what the probe frequency is, there are always extended modes nearby which contribute significantly to the transmission channel. Thus the maximal transmission channel is expected to consist of many extended modes whose interference leads to highest transmission. Only in the diffusive system close to localization transition, some of the quasi-modes become spatially confined, and the maximal transmission channel can be necklace-like.

The ballistic-like maximal transmission channel, found here in the presence of strong absorption, may enable new modes of imaging that are specific to absorbing media. To check whether such ballistic-like transmission channels also exist without absorption, we examine all transmission channels in the non-absorbing disordered waveguides. We compute the histogram of Poynting vector direction $P(\theta_s)$ for every transmission eigenchannel in three random realizations. The variance of $P(\theta_s)$ remains large for all transmission eigenchannels, including those with low transmission eigenvalues. Hence, ballistic-like transmission channel does not seem to exist in our systems without absorption. Nevertheless, it is important to introduce a physical quantitative that measures how "ballistic" a transmission channel is. One possibility is the average transmission time [54], which merits further study.

6.6 Conclusion

We have performed a detailed numerical study to understand how absorption modifies transport in a 2D disordered waveguide, with emphasis on the maximum transmission channel. The maximal transmission channel is relatively robust against absorption compared to the transmittance. Its input wavefront remains nearly unchanged up to $L \approx \xi_a$, but changes rapidly beyond that point. In the maximal transmission channel, light propagates through the random structure along winding paths when absorption is weak ($L < \xi_a$), and takes more straight routes once absorption is significant ($L > \xi_a$). We investigate the correlations between the quasi-normal modes and the maximal transmission channel to illustrate the mechanism of enhanced transmission in both weak and strong absorption regimes. Maximal transmission is facilitated by hopping through localized modes when absorption is weak, and is dominated by more extended modes when absorption is strong. We observe distinct scaling behavior for the spectral width of maximal transmission channel in different random configurations. Such differences result from the absorption-induced change in the number of quasimodes that participate in the maximal transmission channel. The channel spectral width increases linearly with absorption, if the mode participation number M_{eff} remains almost constant; the width increases sublinearly if M_{eff} decreases, and superlinearly if M_{eff} increases.

In the absence of absorption, minimal reflection corresponds to maximal transmission, but this correspondence no longer holds in the regime of strong absorption ($L > \xi_a$), where minimal reflection corresponds to enhanced absorption. In some instances, we have observed the surprising feature that the minimal reflection eigenvalue increases with absorption, which can be explained by the reduction of destructive interference. The numerical study presented here provides a physical understanding of the effects of absorption on transmission and reflection eigenchannels at the relevant mesoscopic scale, which will hopefully serve in the interpretation of experimental

work, and in the design of practical applications.

Bibliography

[1] S. F. Liew, S. M. Popoff, A. P. Mosk, W. L. Vos, and H. Cao, Phys. Rev. B **89**, 224202 (2014).

[2] M. P. Van Albada and A. Lagendijk, Phys. Rev. Lett. **55**, 2692 (1985).

[3] P.-E. Wolf and G. Maret, Phys. Rev. Lett. **55**, 2696 (1985).

[4] B. L. Altshuler, A. P. Lee, and R. A. Webb, Mesoscopic phenomena in solids (North Holland, Amsterdam, 1991).

[5] F. Scheffold and G. Maret, Phys. Rev. Lett. **81**, 5800 (1998).

[6] E. Akkermans and G. Montambaux, Mesoscopic physics of electrons and photons (Cambridge University Press, Cambridge, 2007).

[7] A. Lagendijk, B. van Tiggelen, and D. S. Wiersma, Phys. Today **62**, 24 (2009).

[8] I. M. Vellekoop and A. P. Mosk, Phys. Rev. Lett. **101**, 120601 (2008).

[9] J. B. Pendry, Physics **1**, 20 (2008).

[10] W. Choi, A. P. Mosk, Q. H. Park, and W. Choi, Phys. Rev. B **83**, 134207 (2011).

[11] W. Choi, Q. H. Park, and W. Choi, Opt. Express **20**, 20721 (2012).

[12] Z. Shi and A. Z. Genack, Phys. Rev. Lett. **108**, 043901 (2012).

[13] M. Kim, Y. Choi, C. Yoon, W. Choi, J. Kim, Q. Park, and W. Choi, Nat. Photon. **6**, 581 (2012).

[14] M. Davy, Z. Shi, J. Wang, and A. Z. Genack, Opt. Express **21**, 10367 (2013).

[15] S. M. Popoff, A. Goetschy, S. F. Liew, A. D. Stone, and H. Cao, Phys. Rev. Lett. **112**, 133903 (2014).

[16] O. N. Dorokhov, Solid State Commun. **44**, 915 (1982).

[17] O. N. Dorokhov, Solid State Commun. **51**, 381 (1984).

[18] P. A. Mello, P. Pereyra, and N. Kumar, Annals of Physics **181**, 290 (1988).

[19] Y. V. Nazarov, Phys. Rev. Lett. **73**, 134 (1994).

[20] I. M. Vellekoop and A. P. Mosk, Opt. Lett. **32**, 2309 (2007).

[21] Z. Yaqoob, D. Psaltis, M. S. Feld, and C. Yang, Nat. Photon. **2**, 110 (2008).

[22] S. M. Popoff, G. Lerosey, R. Carminati, M. Fink, A. C. Boccara, and S. Gigan, Phys. Rev. Lett. **104**, 100601 (2010).

[23] I. M. Vellekoop, A. Lagendijk, and A. P. Mosk, Nat. Photon. **4**, 320 (2010).

[24] S. Popoff, G. Lerosey, M. Fink, A. C. Boccara, and S. Gigan , Nat. Commun. **1**, 81 (2010).

[25] W. L. Vos, T. W. Tukker, A. P. Mosk, A. Lagendijk, and W. L. IJzerman, Appl. Opt. **52**, 2602 (2013).

[26] M. Kim, W. Choi, C. Yoon, G. H. Kim, and W. Choi , Opt. Lett. **38**, 2994 (2013).

[27] W. Choi, M. Kim, D. Kim, C. Yoon, C. Fang-Yen, Q. Park, and W. Choi, arXiv:1308.6558 (2013).

[28] J. Wang and A. Z. Genack, Nature **471**, 345 (2011).

[29] J. Wang, Z. Shi, M. Davy, and A. Z. Genack, Intern. J. Mod. Phys. **11**, 1 (2012).

[30] J. B. Pendry, J. Phys. C **20**, 733 (1987).

[31] J. B. Pendry, Adv. Phys. **43**, 461 (1994).

[32] J. Bertolotti, S. Gottardo, D. S. Wiersma, M. Ghulinyan and L. Pavesi, Phys. Rev. Lett. **94**, 113903 (2005).

[33] P. Sebbah, B. Hu, J. M. Klosner, and A. Z. Genack, Phys. Rev. Lett. **96**, 183902 (2006).

[34] K. Y. Bliokh, Y. P. Bliokh, V. Freilikher, A. Z. Genack, B. Hu, and P. Sebbah, Phys. Rev. Lett. **97**, 243904 (2006).

[35] K. Y. Bliokh, Y. P. Bliokh, V. Freilikher, A. Z. Genack, and P. Sebbah, Phys. Rev. Lett. **101**, 133901 (2008).

[36] P. W. Brouwer, Phys. Rev. B **57**, 10526 (1998).

[37] A. G. Yamilov and B. Payne, Opt. Express **21**, 11688 (2013).

[38] A. A. Chabanov, M. Stoytchev, and A. Z. Genack, Nature **404**, 850 (2000).

[39] Y. D. Chong, L. Ge, H. Cao, and A. D. Stone, Phys. Rev. Lett. **105**, 053901 (2010).

[40] W. Wan, Y. D. Chong, L. Ge, H. Noh, A. D. Stone, and H. Cao, Science **331**, 889 (2011).

[41] Y. D. Chong and A. D. Stone, Phys. Rev. Lett. **107**, 163901 (2011).

[42] M. Grätzel, J. Photochem. Photobiol. C., **2**, 145 (2003).

[43] A. Hagfeldt, G. Boschloo, L. Sun, L. Kloo, and H. Pettersson, Chem. Rev. **11**, 6595 (2010).

[44] M. Kim, W. Choi, C. Yoon, G. H. Kim, S. Kim, G. Yi, Q. Park, and W. Choi, arXiv:1308.6553 (2013)

[45] J. D. Joannopoulos, S. Johnson, J. Winn, and R. Meade, Photonic Crystals: Molding the Flow of Light (Princeton University Press, Princeton, NJ, 2008)

[46] http://www.comsol.com

[47] M. C. W. van Rossum and T. M. Nieuwenhuizen, Rev. Mod. Phys. **71**, 313 (1999).

[48] X. Wu, J. Andreasen, H. Cao, and A. Yamilov, J. Opt. Soc. Am. B **24**, A26 (2007).

[49] P. T. Leung, S. S. Tong, and K. Young, J. Phys. A **30**, 2139 (1997).

[50] P. T. Leung, S. S. Tong, and K. Young, J. Phys. A **30**, 2153 (1997).

[51] E. S. C. Ching, P. T. Leung, A. Maassen van den Brink, W. M. Suen, S. S. Tong, and K. Young, Rev. Mod. Phys. **70**, 1545 (1998).

[52] F. van Beijnum, E. G. van Putten, A. Lagendijk, and A. P. Mosk, Opt. Lett. **36**, 373 (2011).

[53] J. Wang, A. A. Chabanov, D. Y. Lu, Z. Q. Zhang, and A. Z. Genack, Phys. Rev. B **81**, 241101(R) (2010).

[54] S. Rotter, P. Ambichl, and F. Libisch, Phys. Rev. Lett. **106**, 120602 (2011).

Chapter 7

Control of microcavity lasers by selective pumping

7.1 Introduction

[1] Semiconductor microdisk lasers have simple geometry, small footprint, and low lasing threshold, making them excellent candidates for on-chip light sources for integrated photonics applications [2, 3]. Due to high refractive index contrast at the disk boundary, light is strongly confined by total internal reflection, forming the whispering-gallery modes (WGMs) with high-quality (Q) factor. A circular microdisk much larger than the optical wavelength support densely packed WGMs, and lasing usually occurs in multiple modes of different frequencies. For many applications, lasing at a single frequency is desired. However, it is difficult to have only one mode lasing when many WGMs of similar Q exist within the gain spectrum. It is even more challenging to switch the lasing mode from one to another, after the laser is fabricated.

In addition to the lack of control on the lasing frequency, the isotropic emission

1. The first half of this chapter is primarily based on the journal article published in ref. [1].

from circular microdisks seriously limits the application because directional output is usually required. One way to generate directional emission is deforming the cavity shape to break the circular symmetry [4–6]. Directional coupling of light output from whispering-gallery mode microdisk lasers has been realized using patterned asymmetries in the shape of microdisk resonators, which enabled control of both direction and intensity of light output without dramatically increasing laser thresholds [7, 8]. With large deformation, refractive escape is dominant, and all the whispering-gallery-like modes have similar output directionality which is dictated by the ray dynamics [9–11]. Such universality hinders switching of emission directionality even if one can select different mode to lase. For a weakly deformed cavity, evanescent tunneling dominates over refractive escape. Although the intracavity mode patterns remain nearly unaltered by slight shape deformation, the external emission can be much more sensitive [12–16]. Even a tiny boundary variation may lead to wildly varying external fields, producing large intensity contrast between the directions of maximal and minimal emission. The emission patterns differ significantly for the high-Q modes, offering the capability of switching the output directionality by selecting different mode to lase.

Pump engineering is an efficient way to control the lasing frequency and output direction of a semiconductor laser. To select a particular mode to lase, one may reduce its lasing threshold by enhancing the spatial overlap between the pump and the mode [17–21]. For instance, a ring-shaped optical pump has been used to lower the lasing threshold of WGMs in circular micropillars [22] or to produce directional emission from spiral-shaped microdisk lasers [23]. The same method has been adopted for electrically pumped semiconductor lasers by patterning the electrodes to match the targeted mode profiles [24–26]. Switching of emission directions was realized by injecting currents to separate electrodes that had maximal overlap with individual modes [27]. This technique requires *a priori* knowledge of the mode profiles and

demands little spatial overlap between the selected modes. Hence, it limits the switching capability to a few modes, and becomes practically unviable once the modes have strong spatial overlap.

Lately active control of pump profile was demonstrated for random lasers using the spatial light modulator (SLM) [28]. Even for strongly overlapped modes, adaptive shaping of the spatial profile of the optical pump enabled selection of any desired lasing frequency without prior knowledge of the mode profiles [29,30]. Numerical studies also demonstrated pump-controlled directional emission from two-dimensional (2D) random lasers [31].

In this chapter, we apply the active control of pump profile to the semiconductor microdisk lasers. The disks are slightly deformed due to fabrication imperfection. Since the Q spoiling is weak, the lasing threshold remains low. The high-Q modes, whose emission is determined by evanescent tunneling, exhibit distinct emission patterns. Optical gain is provided by optical pumping of the semiconductor quantum dots (QDs) embedded in the disk. The broad gain spectrum allows lasing in multiple high-Q modes. These modes have strong spatial overlap near the disk boundary, which adds complexity to the mode selection process, and makes finding the best solution a nontrivial operation. By adaptive control of the pump profile, we are able to select different modes to be the dominant lasing mode and suppress all other lasing modes. Consequently, the laser emission pattern is changed. Our results demonstrate an effective and flexible method to exploit the multimode characteristic of nearly circular microdisk lasers for switching of lasing frequency and emission direction.

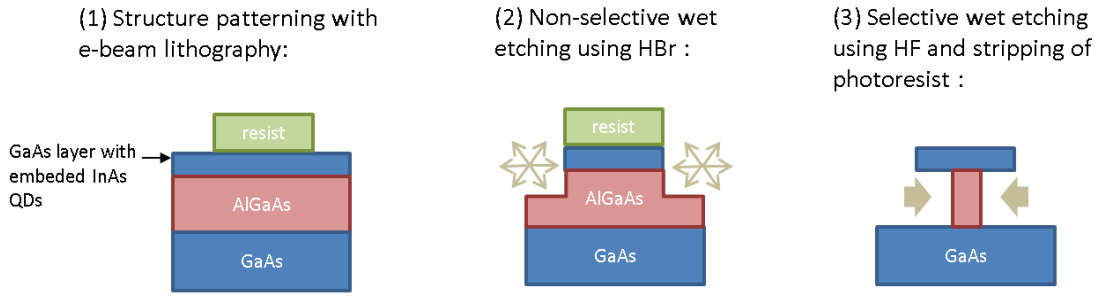

Figure 7.1: Fabrication of microdisk. The structure was first patterned using e-beam lithography on a GaAs substrate with embedded layers of InAs QDs. The pattern was then transfered to the GaAs by non-selective wet etching process using HBr. Due to anisotropic etching rate, the disk can be easily distorted. Additional selective etching step using HF undercut the AlGaAs layer below the microdisk and form a thin pedestal to support the disk.

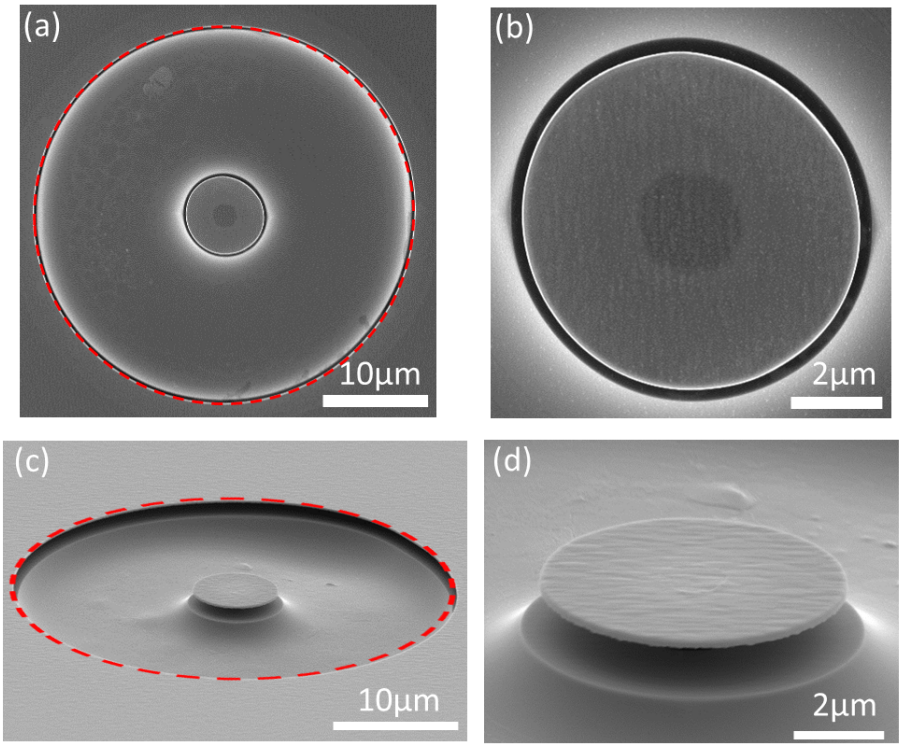

Figure 7.2: (a) Low magnification top-view scanning electron micrograph (SEM) of the microdisk. Red circle denotes the outer edge of an annular air gap, which is used to measure emission pattern. (b) The microdisk shows slight deformation from circular shape. Center dark area is on top of the AlGaAs pedestal. (c) Tilt-view of the microdisk in (a). (d) Surface roughness exists at the edge of the disk.

7.2 Microdisk fabrication and characterization

The sample is grown on a GaAs substrate by molecular beam epitaxy. It consists of a 1μm-thick $Al_{0.68}Ga_{0.32}As$ layer and a 200nm-thick GaAs layer with three embedded layers of InAs QDs. Each QD layer contains 2.5 monolayers of InAs. As shown in Fig. 7.1, the microdisks are fabricated by electron beam lithography and two steps of wet etching [32]. The first is non-selective etching of the GaAs and $Al_{0.68}Ga_{0.32}As$ layers with HBr, forming microcylinders. The second step is a HF-based selective etch to undercut the $Al_{0.68}Ga_{0.32}As$ and create a pedestal to isolate the GaAs disk from the substrate. Figure 7.2(a) shows the top-view scanning electron micrograph (SEM) of a fabricated disk. The disk at the center is surrounded by an annular air gap that separates the disk from the unetched GaAs layer. The outer circle (red dashed line), with a radius of 18μm, is used to measure the emission pattern. The non-selective etching process is not perfectly isotropic, thus the disk shape deviates from the original design of a circle, as can be seen in Fig. 7.2(b). In addition, the etching also creates surface roughness at the disk boundary [Fig. 7.2(d)]. From the high-resolution SEM, we extract the disk boundary and fit it in the polar coordinates as $\rho(\theta) = R\,[1 + a\cos(2\theta + \alpha) + b\cos(3\theta + \beta)]$, where $R = 3.71\mu$m, $a = 0.024$, $b = 0.0089$, and $\alpha = 1.38$, $\beta = 0.13$. The dominant deformation originates from the $\cos(2\theta)$ modulation, but the contribution from the $\cos(3\theta)$ is non-negligible. Note that both modulations have very small magnitudes, $a, b \ll 1$, confirming the cavity is nearly circular and the output is dominated by evanescent tunneling.

7.3 Adaptive shaping of spatial pump profile

The fabricated samples are tested in a liquid helium cryostat at temperature $\sim$ 10K. Optical excitation is provided by a mode-locked Ti:Sapphire laser (λ = 790nm) op-

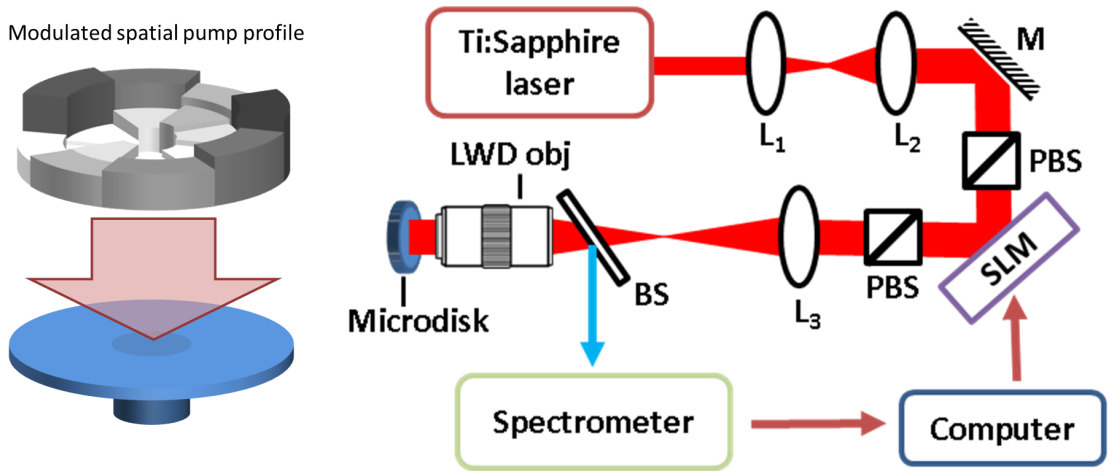

Figure 7.3: Schematic of optical setup: L_1, L_2, L_3: lens. PBS: polarizing beam splitter. SLM: spatial light modulator. BS: non-polarizing beam splitter. LWD obj: long-working distance objective lens.

erating at 76MHz with 200fs pulses. As shown schematically in Fig. 7.3, the pump beam is first expanded by a telescope to cover the entire surface of the SLM (Hamamatsu X10468-02). The SLM is positioned between a pair of polarizers to introduce intensity modulation on the pump beam. The spatially modulated pump pattern is then projected onto the top surface of a microdisk. Since the AlGaAs pedestal causes light leakage from the GaAs disk to the substrate, the high-Q modes avoid the central region of the disk. Thus the pump region is set as a ring. It is divided into two subrings, each is further divided into eight sections in the azimuthal direction. Optical power within each section can be modulated separately using the SLM while the total power is kept constant.

In order to select one mode to lase while suppressing all other modes, we adopt the genetic algorithm in MATLAB to search for the optimum spatial pump profile. The cost function is defined as $G = I_m/I_o$, where I_m is the intensity of the targeted mode, and I_o is the highest intensity among all other modes in the spectra. The algorithm starts with an initial population of ten pump patterns where one of them is a homogeneous ring and the rest are random. The emission spectrum for each

pump pattern is recorded, and the cost function is evaluated. The pump patterns are ranked by their cost function, and the ones with higher ranking have a larger chance of being chosen as "parents" to generate ten "children". The first two are the pump patterns with the highest ranking among the parents, which are copied to the next generation without changes. The next six childrens are generated through crossover by randomly selecting different parts of the pump patterns from a pair of parents and combine them. The last two are created through mutation by making random changes to a single parent. The mutation rate decreases with generation and is set to zero after ten generations. After ten generations, we reset the initial population to include the highest ranked pump pattern from the previous trial and nine randomly generated patterns, and repeat the genetic algorithm to search unexplored parameter space for a better solution. During the optimization process, the total pump power is kept constant, the pump energy is merely re-distributed to different regions of the disk. Between successive pump patterns test, the microdisk is pumped with a homogeneous ring to eliminate any residual thermal effect from the previous pump profile.

7.4 Spectral and emission pattern control of microdisk laser

Figure 7.4 presents the results for adaptive pumping of the microdisk shown in Fig. 7.2. When the pump intensity is uniform across the annular pump region, the emission spectrum contains three major peaks at the pump power of 2.2 mW [Fig. 7.4(a)]. No additional lasing peak is found beyond the spectral range of Fig. 7.4(a). We are able to make any one of the three to be the dominant lasing mode after optimizing the pump pattern in 30 generations. Figure 7.4(b-d) are the emission spectra after optimizing modes (i)-(iii) respectively, and the insets are the optimized pump patterns. The

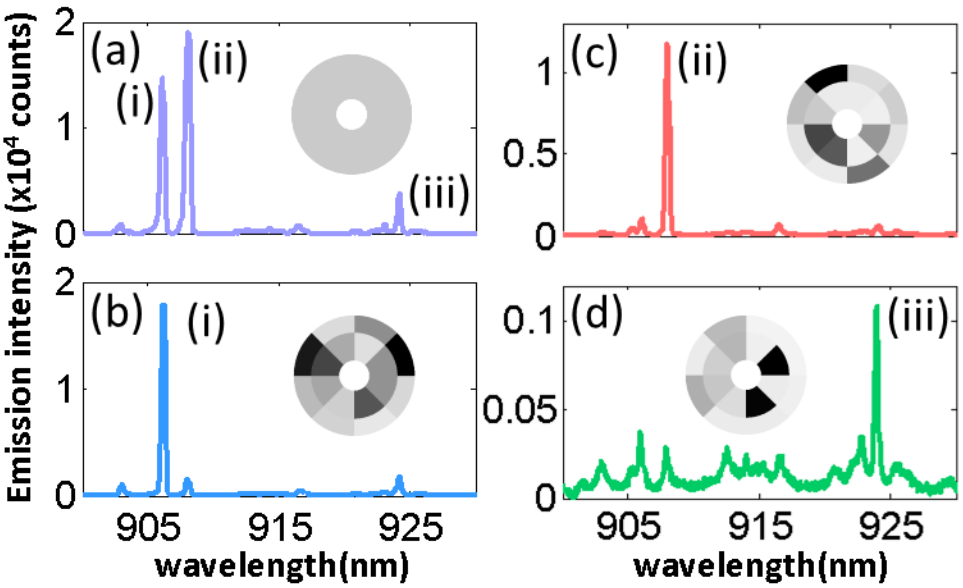

Figure 7.4: Emission spectra of the microdisk shown in Fig. 7.2(a) when pumped with different spatial patterns. The total pump power is kept at 2.2mW. Three modes lase with a homogeneous ring pump (a). Each of the three modes, (i-iii), becomes the dominant lasing mode (b-d) after the optimal pump profile is found by the genetic algorithm. The inset in each panel is the final pump pattern. Darker color corresponds to higher pump intensity.

emission intensity of the selected mode changes slightly but the intensities of non-selected modes are greatly reduced. For example, when mode (iii) is chosen to be the dominant lasing mode [Fig. 7.4(d)], the intensities of mode (i) and (ii) are an order of magnitude lower than under the homogeneous pumping [Fig. 7.4(a)].

Next, we investigate the output directionality of the lasing modes. The in-plane emission from the disk boundary propagates to the outer edge of the air gap [red circle in Fig. 7.2(a)] and is scattered out of the plane. The scattered light is imaged from the top of the disk by an objective lens onto a CCD camera, and its intensity distribution reflects the emission pattern. When three modes lase simultaneously with homogeneous pumping [Fig. 7.4(a)], the total laser emission is bidirectional as shown in Fig. 7.5(b). It is attributed to the dominant $\cos(2\theta)$ modulation of the cavity boundary and light is emitted tangentially from the two places of the highest curvature on the cavity boundary. Next we place a narrow-bandpass filter

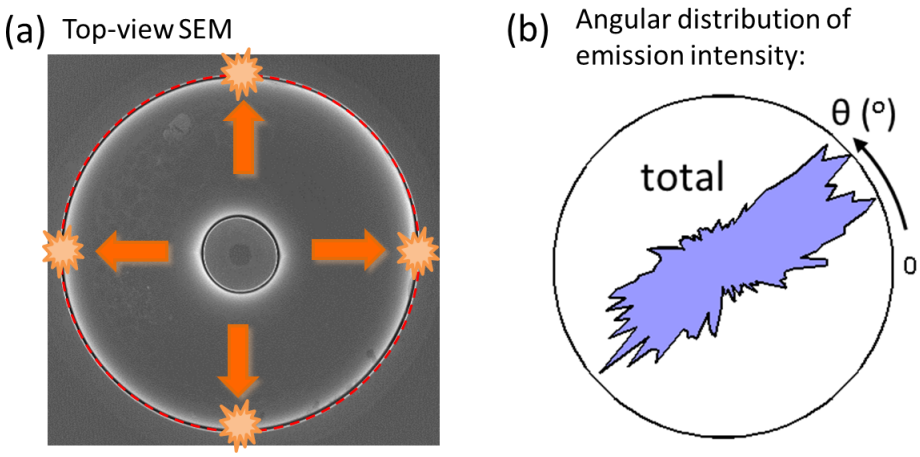

Figure 7.5: (a) Schematic showing that the emission pattern was inferred from the out-of-plane scattering of the light escaping from the boundary of the disk. (b) Angular distribution of emission intensity measured for the microdisk in Fig. 7.2 when pumped with a homogeneous ring. The corresponding emission spectra are shown in Fig. 7.4(a). The total emission from all three lasing modes is bi-directional.

in front of the camera to select a single lasing mode. Figure 7.6 show the angular distribution of emission intensity for each of the three lasing modes. It is evident that the three modes have distinct emission patterns. When one of them becomes the dominant lasing mode by selective pumping, we remeasure its emission pattern and find it remains the same. Hence, the modes themselves are barely modified by the redistribution of pump energy. This result differs from the weakly scattering random lasers [29, 30], because in our case the modes are strongly confined due to high index contrast at the disk boundary.

7.5 Numerical simulation

To understand the modal dependent output directionality, we extract the cavity shape from the SEM and perform numerical simulation. The lasing modes usually correspond to the high-Q modes in the passive cavity, whose frequencies are within the

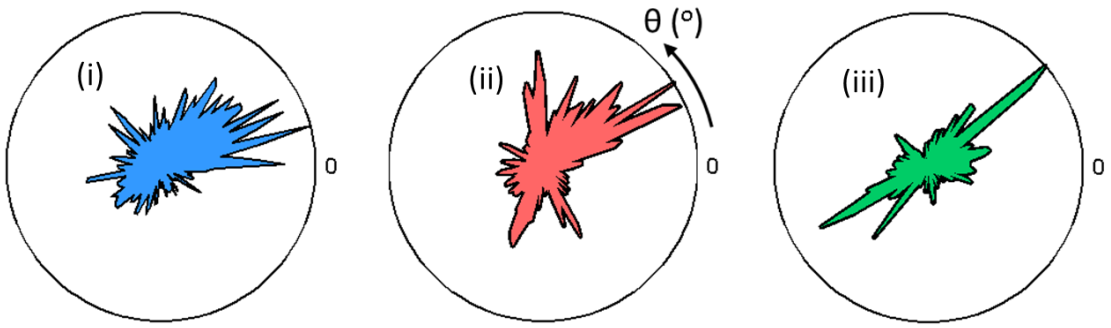

Figure 7.6: Angular distribution of emission intensity measured for individual lasing mode. Each of the lasing mode, (i-iii), exhibits distinct emission pattern. The mode labeling is the same as that in Fig. 7.6.

gain spectrum. Thus we numerically calculate the high-Q modes in the passive disk using the finite element method (COMSOL). Since the disk radius is much larger than the disk thickness, a microdisk can be treated as a 2D cavity with an effective index of refraction $n = 3.13$ [32]. To simulate the open boundary condition, the disk is placed in air, which is surrounded by a perfectly matched layer (PML) to absorb all outgoing waves. Since we do not know the exact temperature of the GaAs disks when optically pumped inside the liquid-Helium cryostat, we cannot get the accurate value of the refractive index n to match the numerically calculated modes with the experimentally measured lasing peaks. Instead of a quantitative comparison, our numerical simulation aims to provide a qualitative understanding of the characteristic of the lasing modes.

Figure 7.7 presents the results of two high-Q modes in the wavelength range of InAs QD gain spectrum. Their quality factors $Q = \omega_r/2\omega_i$ are 67000 and 69000 respectively, where $\omega_r - i\omega_i$ is the complex frequency of the cavity mode, and the imaginary part ω_i is inversely proportional to the mode lifetime in the open cavity. As shown in Fig. 7.7(a,b), both modes are spatially localized near the cavity boundary, similar to the WGMs. However, their intensities are not uniformly distributed in the azimuthal direction, because of boundary roughness. Outside the cavity, the azimuthal variation of the field intensity becomes much stronger as seen in Fig. 7.7(c,d).

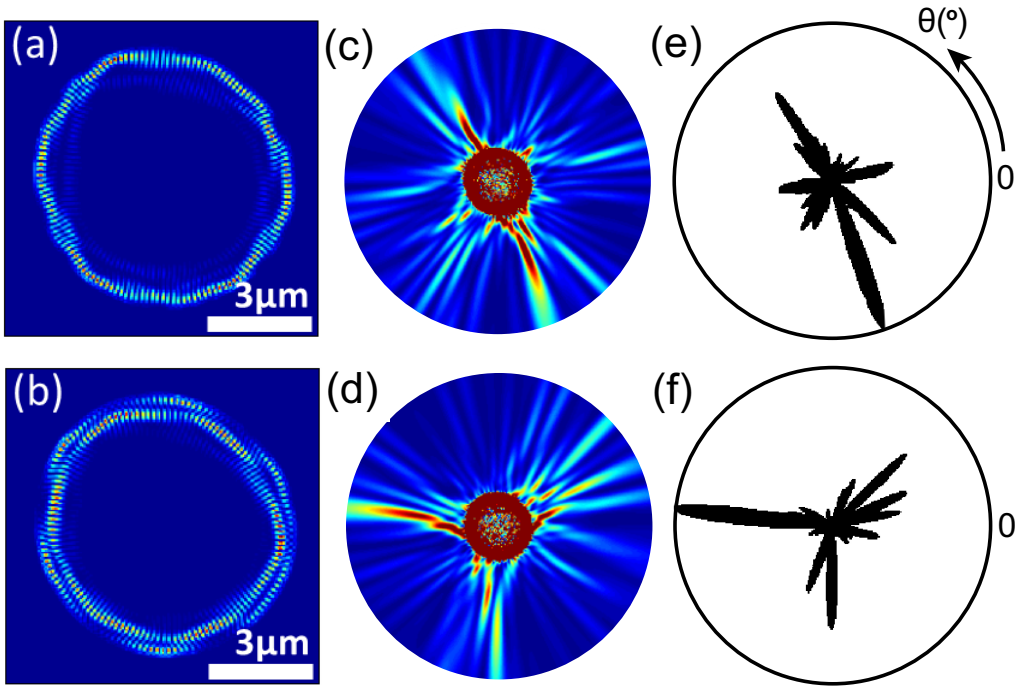

Figure 7.7: Numerical simulation of two high-Q modes, one at $\lambda = 913.4$nm (a,c,e), the other at $\lambda = 927.7$nm (b,d,f), in the microdisk shown in Fig. 7.2. (a,b) Spatial distribution of electric field intensity, resembling the WGM but distorted due to boundary roughness. (c,d) Electric field intensity distribution outside the disk, highlighted by saturating the intensity inside the disk, showing the two modes have distinct outputs. (e,f) Angular distribution of emission intensity, convolved with the experimental resolution, at a distance of 18μm from the disk center.

The two modes exhibit distinct intensity distributions outside the cavity, indicating that light output via evanescent tunneling is dramatically different. Figure 7.7(e) and (f) are the angular distributions of emission intensity at a distance of $18\mu m$ from disk center, similar to the experimental measurement. The calculated intensity distribution is convolved with the experimental resolution of ~ 0.9 μm. We have simulated other high-Q modes and observed similar phenomena. Finally, we checked that without boundary roughness, the microdisk defined by the fitted boundary curve $\rho(\theta)$, contains only high-Q modes with similar emission patterns. This result confirms that boundary roughness is responsible for the distinct emission directionality of individual high-Q modes. The sidewall roughness not only modifies the local evanescent tunneling, but also induces mode coupling which affects the far-field pattern [15, 16]. The diversity in the output directionality among the high-Q modes enables the switching of emission direction by selecting different modes to lase with adaptive pumping.

In conclusion, we demonstrate selection of lasing modes with directional emission in weakly deformed semiconductor microdisks by adaptive pumping. Despite strong spatial overlap of the lasing modes, we are able to select any one of them to be the dominant lasing mode by suppressing all other modes. Slight shape deformation and sidewall roughness due to fabrication imperfection creates directional emissions that are mode dependent. Combining these features, both lasing frequency and emission pattern can be switched by external pump, after the laser is fabricated. This method may be extended to electrically pumped microdisks by using multiple eletrodes to modulate the spatial profile of current injection.

7.6 Pump controlled lasing dynamics

We measured the lasing thresholds and power slopes of each lasing modes to understand the underlying physical mechanisms for mode selection. However, the lasing

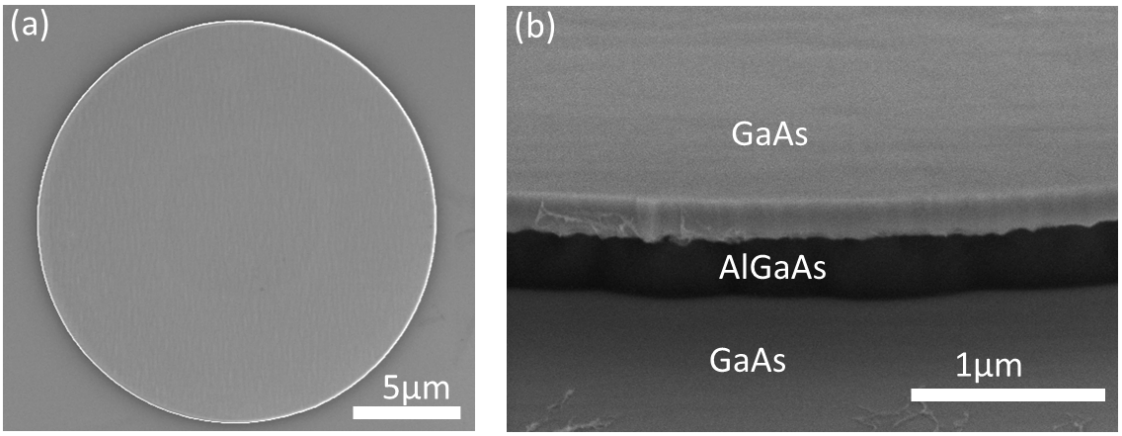

Figure 7.8: SEM of microdisk. (a) Top-view SEM of the big microdisk. (b) Tilt-view SEM of the microdisk showing surface roughness at the boundary.

threshold for the weakly deformed microdisk cavity is very high and thus it is difficult to measure the power slope. Hence, we switch to another disk with a larger radius and less deformation, where lasing thresholds are low and allow us to obtain the power slope. The new microdisk had a radius of 9.2 μm and fabricated with slightly different process than the previous disk. Instead of non-selective wet-etching process, the disk was fabricated by selective etching process (reactive-ion etching) where the etching rate is more isotropic across the disk. Fig. 7.8(a) shows that the fabricated disk has very little deformation compared to the smaller disk in Fig. 7.2. However, from the tilt-view SEM in Fig. 7.8(b), surface roughness still exists at the edge of the disk.

By using the same experimental setup, we test the fabricated device at cryo-temperature about 10K. With a uniform ring pump pattern, the lasing spectrum contains more than ten modes within a wavelength range of 28 nm [Fig. 7.9(a)]. The free spectral range (FSR) of the disk is estimated to be $\Delta\lambda\ \lambda/nkR = 4.7nm$. The small FSR indicates the lasing spectrum in Fig. 7.9(a) contains higher-order radial WGMs as well. Then, we select each of the modes labeled (i-v) to become the dominant lasing mode using the Genetic algorithm with same cost function as defined in the previous section. The final lasing spectra and optimized pump profile for each

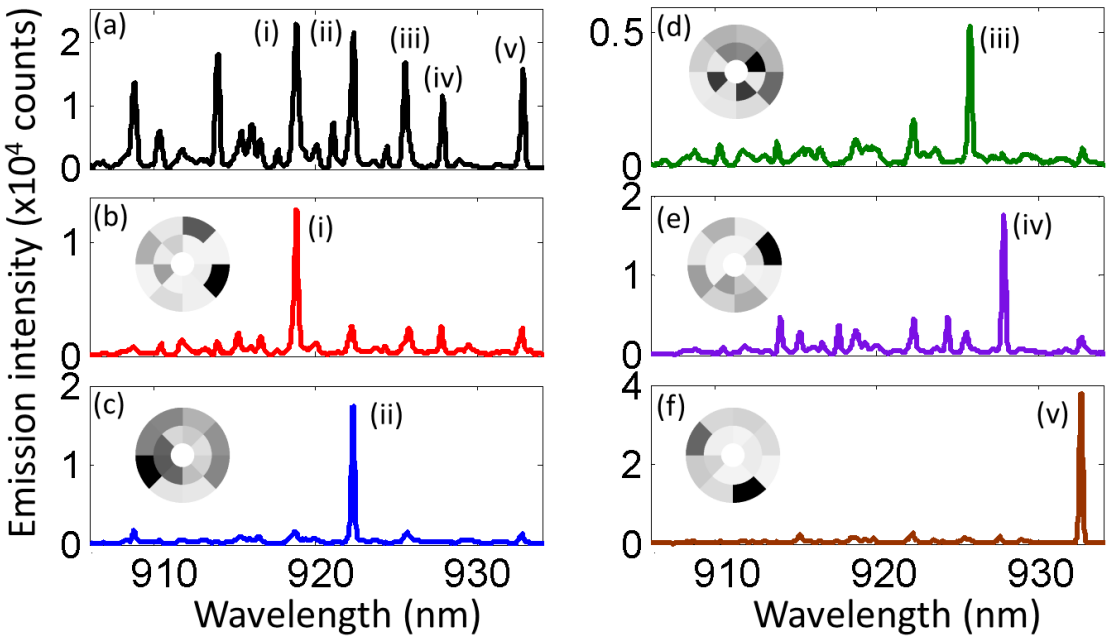

Figure 7.9: Lasing spectra of the microdisk shown in Fig. 7.8 with different spatial pump patterns. The total pump power is kept at 4 mW. More than ten modes lase with a homogeneous ring pump in (a). Each of the five dominant modes, labeled (i-v) becomes the dominant lasing mode (b-f) after the optimal pump profile is found by the genetic algorithm. The inset in each panel is the final pump pattern. Darker color corresponds to higher pump intensity.

mode are shown in Fig. 7.9(b-f). The total pump power is kept constant at 4 mW during the optimization process. We observe that for modes (iv) and (v), their final lasing intensity becomes higher with selective pumping but for the other modes, their lasing intensity either decrease (i, iii) or remain similar (ii).

To investigate the lasing dynamics of different modes, we measured their lasing thresholds and power slopes (differential quantum efficiency). In Fig. 7.10(a), we show the change of lasing intensity as a function of pump power for mode (i-v) with uniform ring pump profile. All L-I curves show threshold behavior and the lasing modes turn on at similar pump power of 3 mW. The lasing thresholds are estimated by the intersection point of the two linear regression lines, each fitting the data points before and after a lasing mode turns on. Fig. 7.10(b) plots the lasing thresholds of

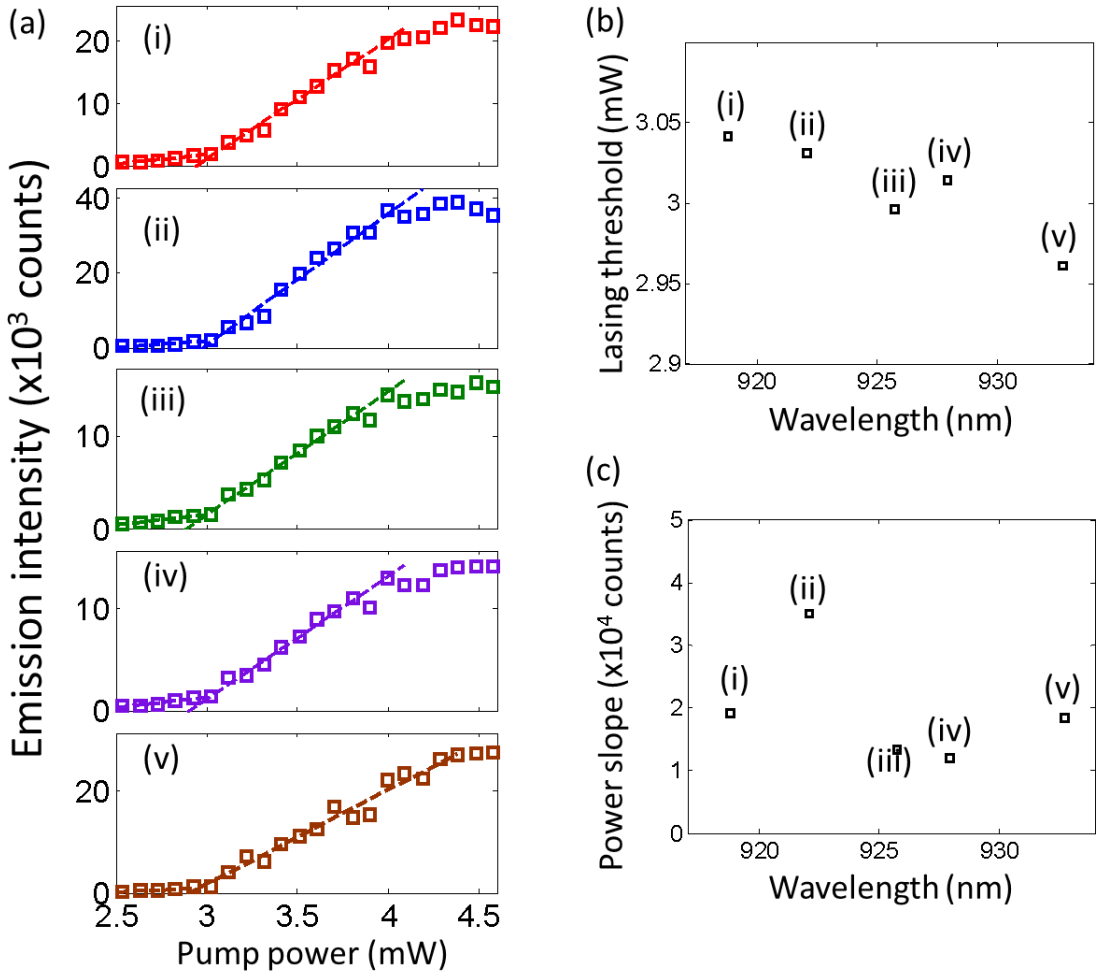

Figure 7.10: Lasing thresholds and power slopes of lasing modes with uniform ring pump pattern. (a) Emission intensity of different lasing modes as a function of pump power. From (a), we extract the (b) lasing thresholds and (c) power slopes of each modes (i-v).

different modes with uniform pumping. The power slope of each lasing mode is the slope of the second linear line fitting the data points for pump power higher than the threshold. Power slopes of mode (i-v) are presented in Fig. 7.10(c) which show a larger fluctuation than the lasing mode thresholds. For example, power slope of mode (ii) is about three times of mode (iii) and (iv) while their lasing thresholds only differ less than 2 %.

We measured the lasing thresholds and power slopes again after optimizing each mode to become the dominant lasing mode. Fig. 7.11(a-e) show the results after

optimizing for each mode (i-v) and their corresponding lasing spectra are plotted in Fig. 7.9(b-f). In general, selective pumping increases the lasing thresholds of all modes including the targeted mode compared to uniform pumping. In Fig. 7.11(a), (c) and (e), Mode (i), (iii) and (v) have the lowest thresholds with selective pumping to make them the dominant lasing modes. Power slopes of these two modes reduce compared to uniform pumping but remain the highest among the non-selected modes. As a result, we can attribute the selection of mode (i), (iii) and (v) to their lowest lasing threshold and highest power slope. However, this is not a necessary condition for a lasing mode to be selected as the dominant one. In Fig. 7.11(b) and (d), mode (ii) and (iv) were selected as the dominant lasing mode but their thresholds were not the lowest among all other modes. Nevertheless, after lasing mode (ii) and (iv) turns on, they lases with the highest power slope and surpass the intensity of earlier lasing modes. From these results, we observe that the selective pumping not only suppresses the non-selected modes by increasing their lasing threshold but also decreasing their power slopes. The suppression of power slopes indicates that the selective pumping not only changes the spatial overlap between the mode and pump but also affects the lasing modes interaction/competition.

7.7 Numerical simulation of microdisk with surface roughness

To understand the effect of selective pumping on the microdisk laser, we simulated a circular microdisk with artificially introduced boundary roughness. Surface roughness is added to the boundary of the disk by introducing some high order harmonic perturbations, $\rho(\theta) = r_o + \sum_{20}^{80} a_m \cos(m\theta + \phi_m)$ where r_o =3 μm, $|a_m| \leq$0.5 nm and $|\phi_m| \leq \pi$. Values of a_m and ϕ_m were randomly selected for each azimuthal number m. Using COMSOL, we compute the eigenfrequencies and the magnetic spatial field pro-

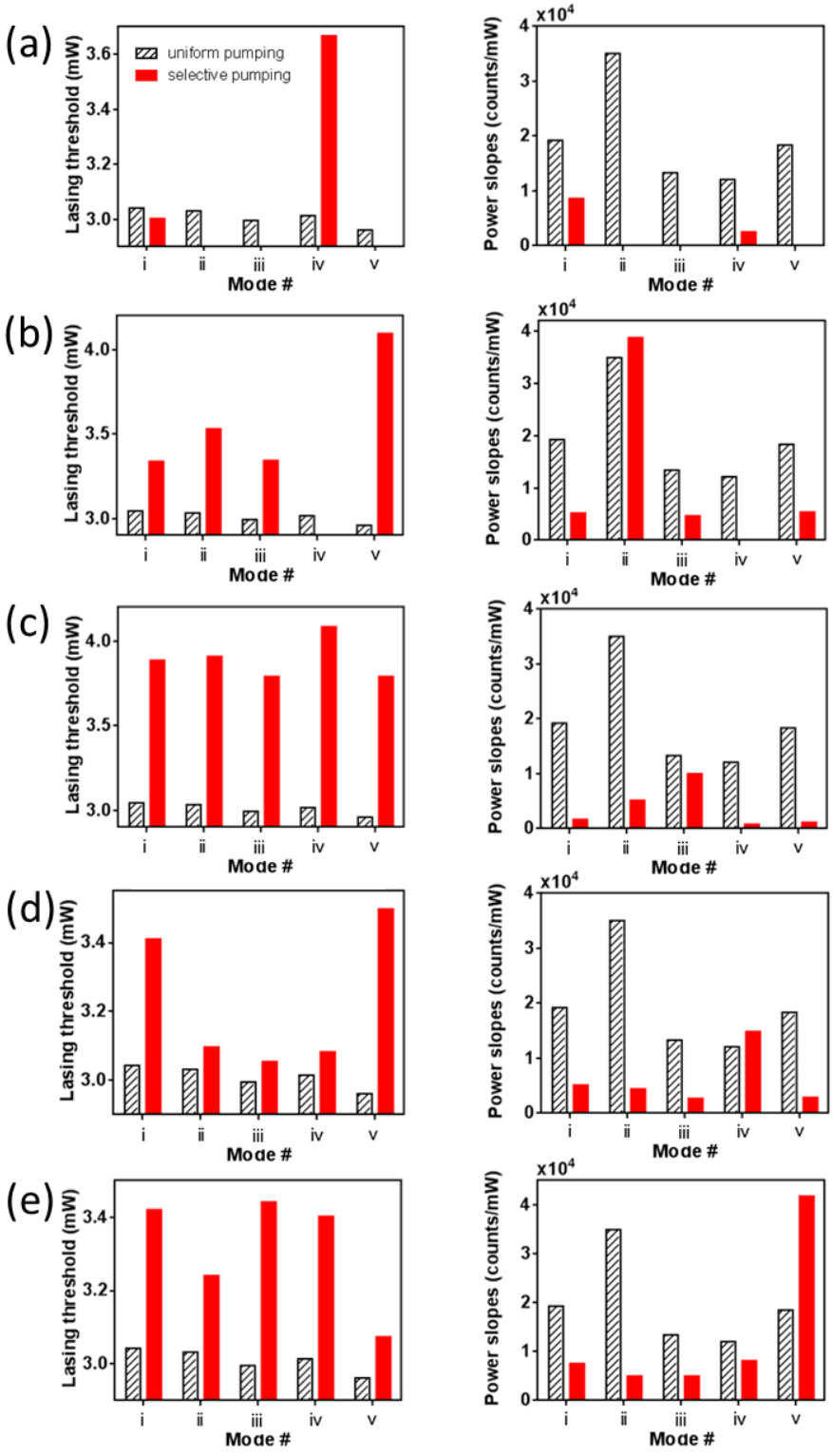

Figure 7.11: Lasing thresholds and power slopes of lasing modes for different optimized pump profiles. (a-e) Lasing thresholds (left column) and power slopes (right column) for lasing modes (i-v) with lasing spectra correspond to Fig. 7.9(b-f). Some of the modes stop lasing with selective pumping and we omit those data points in the plots.

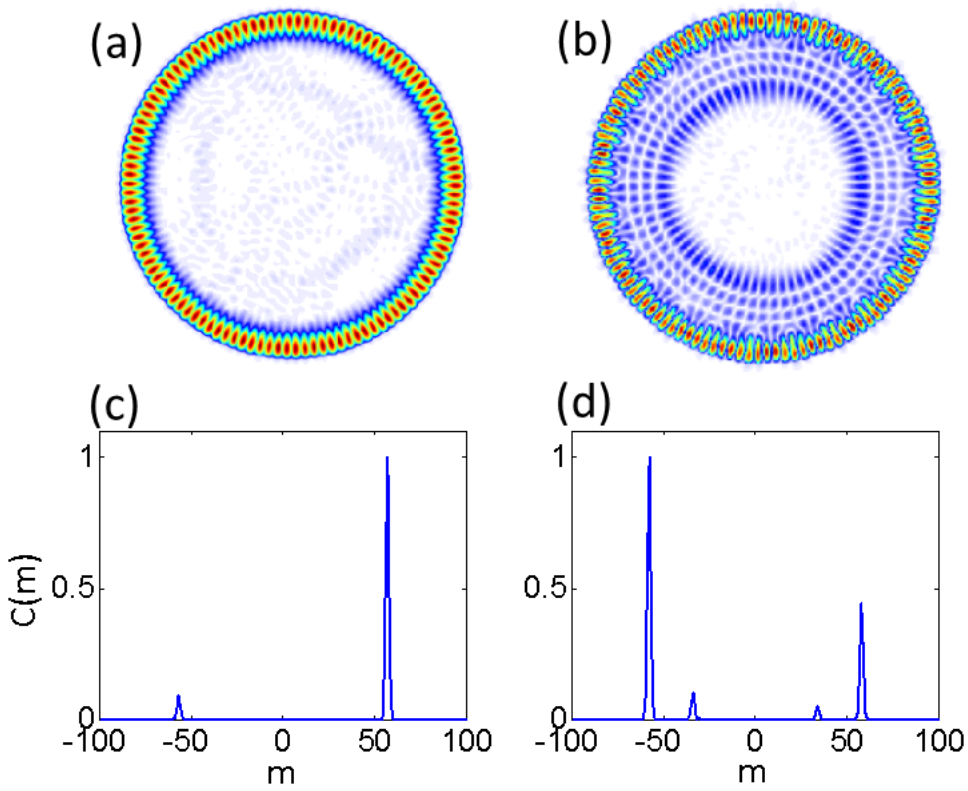

Figure 7.12: Spatial distribution of magnetic field $|H_z(x, y)|$ and chirality of the simulated modes. (a,b) The spatial magnetic field profile for two high-Q modes are shown in the top row. The Q for the modes are (a)Q = 119500, (b)Q = 108900 respectively. (c,d) Bessel functions decomposition of field profiles for mode (a,b). Mode (a) with orbital angular momentum $m = 57$ has very high chirality of 0.9 and mode (b) with $m = 58$ mixed with another low-Q mode with $m = 34$.

file ($|H_z|$) of two successive first order radial WGM with TE polarization (in-plane electric fields) [Fig 7.12(a-b)]. Mode (a) and (b) have very similar Q, their Q are 119500 and 108900 respectively. Mode (a) is more radially confined at the edge of the disk compared to mode (b) which has additional field components closer to the center of the disk. Mode (a) looks more like a propagating wave than stationary wave pattern because the node points have disappeared. This propagating wave pattern indicates that mode (a) has very high chirality.

To investigate the chirality of mode (a) and additional field components in mode (b), we decompose the field profile using Bessel functions $J_m(nkr)$ as the basis,

$H_z(r,\theta) = \sum_{-\infty}^{\infty} a_m J_m(nkr)\exp(-im\theta)$. At the bottom row of Fig. 7.12, we plot the square of the decomposition coefficients $C(m) = |a_m|^2$. For both modes, the CW and CCW waves have unequal weight. This imbalance of CW and CCW waves can be attributed to the random ϕ_m term in the harmonic perturbations, which breaks the chiral symmetry of the disk boundary. As a result, the scattering of CW and CCW waves at the boundary is not symmetry and the final mode profile contains unequal portions of CW and CCW waves. The spatial chirality of a mode is defined as $\alpha = 1 - min[\sum_{-\infty}^{1} C(m), \sum_{1}^{\infty} C(m)]/max[\sum_{-\infty}^{1} C(m), \sum_{1}^{\infty} C(m)]$ [33]. Surprisingly, even though the surface roughness is added randomly, chirality of the modes are quite significant where $\alpha = 0.9$ and 0.55 for mode (a) and (b) respectively. Since mode (a) is dominated by the positive orbital angular momentum component, the field profile resembles a propagating wave pattern instead of the conventional standing wave pattern.

In addition to the large chirality, mode (b) also contains field components that correspond to a higher order radial WGM. Ref. [15] shows that coupling of multiple resonances can occur by boundary wave scattering. For this coupling mechanism to occur, the resonances have to be spectrally close to one another. More importantly, the cavity must have harmonic boundary deformation that enables scattering of waves from one resonance to another with different angular momentum. These conditions are satisfied for the two modes, one is a high-Q mode with $m = 58$ and another is a low-Q higher order radial mode with $m = 34$. The random harmonic perturbations that were artificially introduced to the disk boundary provide the scattering path that couple the CW or CCW waves of these two resonances with different angular momentum. As a result, the mode profile of $m = 58$ contains the field components from the adjacent $m = 34$ mode due to the boundary wave scattering.

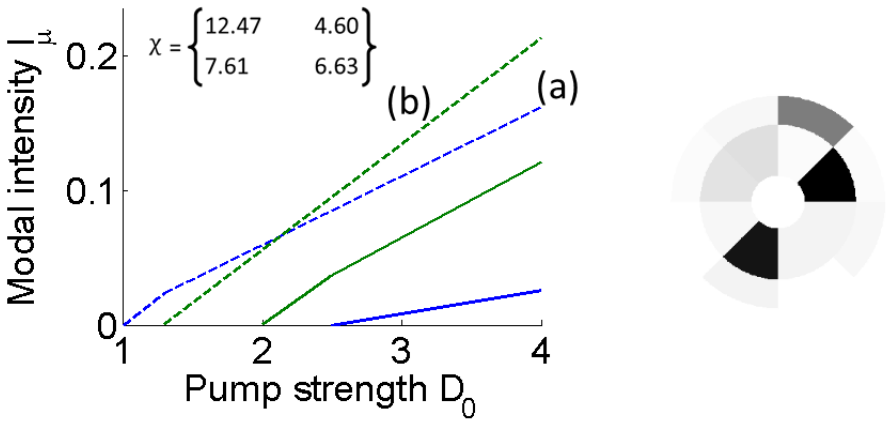

Figure 7.13: Modal intensity of two lasing modes [mode(a) and (b) in Fig. 7.12] with uniform pumping (dashed lines). Their lasing order exchanged with selective pumping (solid lines). Lasing threshold and power slope of mode (a) increase more compared to mode (b). Inset shows the interaction coefficients and the optimized pump pattern is shown on the right.

7.8 Numerical analysis using SPASALT

To understand how selective pumping might affect the lasing behaviors of mode (a) and (b) in Fig. 7.12, we compute the lasing intensity by using the Steady-state *ab initio* laser theory [34]. For qualitative understanding, we use the single-pole approximation and solve a set of linear equations to obtain their lasing intensity. The lasing dynamics depends greatly on the mode interaction and the interaction coefficients are defined as

$$\chi_{ij} = \frac{1}{A}\left|\int_{cavity} d\vec{r}\psi_i^2(\vec{r})|\psi_j(\vec{r})|^2\right| \tag{7.1}$$

where $\psi(\vec{r})$ is the normalized magnetic field profile inside the cavity. As the modes are strongly localized at the disk boundary with very high Q, we assume the wave functions remain the same as the passive cavity and not affected by selective pumping. In Fig. 7.13, we show the lasing intensity of mode (a) and mode (b) with uniform pumping (dashed lines) and selective pumping (solid lines). Their interaction coeffi-

cients are given in the inset of Fig. 7.13. Mode (a) with higher Q is the first mode to lase. Then, we adopt the same genetic algorithm to find the pump pattern which makes mode (b) becomes the first lasing mode and increases the threshold of mode (a). Figure 7.13 shows that with selective pumping, mode (b) becomes the first lasing mode and lasing threshold of mode (a) increases by more than factor of 2. The final pump pattern in Fig. 7.13 indicates more pump energy is being deposited in the inner ring compared to outer ring. Since mode (b) has additional field components closer to the center of the disk, the final pump patten will favor the lasing of mode (b) and greatly suppress mode (a). To be more quantitative, we can compute a pump overlap factor to determine the spatial overlap between the pump pattern and the mode field intensity. The overlap factor is defined as

$$f_i = \frac{1}{A}\int_{cavity} d\vec{r} P(\vec{r})|\psi_i(\vec{r})|^2 \tag{7.2}$$

where $P(\vec{r})$ is the distribution of pump power. $f = 1$ with the uniform ring pump pattern. The final overlap factors for mode (a) and (b) are $f_a = 0.4699$ and $f_b = 0.5487$. The lasing thresholds of both modes increase by selective pumping because of overlap factor less than 1. However, the pump pattern overlaps better with mode (b) than mode (a), and switches the lasing order. This switching is only possible because both mode (a) and (b) have different field profile due to surface roughness. If the boundary is smooth, both of these modes will have almost identical field profiles in the radial direction, and selective pumping will not work.

We have shown that selective pumping can switch the lasing order of the two high-Q modes. Now, we will consider another case where the lasing order remains the same but the power slope of the first lasing mode is suppressed significantly. For this purpose, we choose another pair of high-Q mode with different ratio of χ_{11}/χ_{21} and χ_{22}/χ_{12}. Figure 7.14 shows the field profile of the two second radial order WGMs.

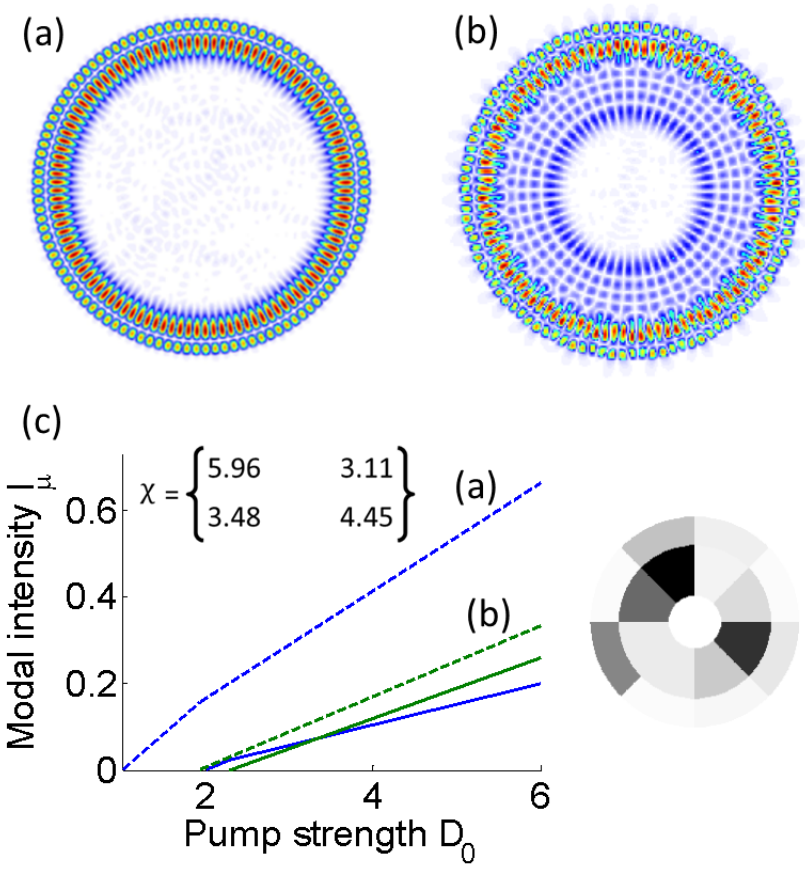

Figure 7.14: (a,b) Spatial field profile of two high-Q modes with $Q = 130800$ and $Q = 104560$ respectively. (c) Modal intensity of the two lasing modes with uniform pumping (dashed lines). Their lasing order remain the same but power slope of mode (a) is suppressed significantly with selective pumping (solid lines). Inset shows the interaction coefficients and the optimized pump pattern is shown on the right.

Again, mode (b) contains extra field components close to the center of the disk and mode (a) is dominantly confined at the boundary. Mode (a) has $Q = 130800$ which is higher than mode (b) with $Q = 104560$, so mode (a) is the first one to lase. Then, we use the genetic algorithm to maximize the ratio of power slopes of mode (b) to (a). In Fig. 7.14(c), the lasing order remains the same with selective pumping but the power slope of mode (a) is greatly suppressed. In this case, selection of mode (b) is due to higher power slope and not lower lasing threshold. This results match with the experimental observations in Fig. 7.11(b) and (d), where the targeted mode does not has the lowest lasing threshold but highest power slope. In summary, our numerical simulation here serves as a qualitative explanation of the lasing dynamics we observed in experiment. Exact matching between experiment and simulation is difficult because of the inaccuracy in measuring the refractive index and surface roughness of the microdisk cavity in experiment. Nevertheless, we have shown that by using selective pumping, not only is the lasing order can be switch by changing the pump and mode overlap but the mode interaction (power slope) can be controlled as well.

Bibliography

[1] S. F. Liew, B. Redding, L. Ge, G. S. Solomon, and H. Cao, Appl. Phys. Lett. **104**, 231108 (2014).

[2] S. L. McCall, A. F. J. Levi, R. E. Slusher, S. J. Pearton, and R. A. Logan, Appl. Phys. Lett. **60**, 289 (1992).

[3] M. Fujita, A. Sakai, and T. Baba, IEEE J. Sel. Top. Quantum Electron. **5**, 673 (1999).

[4] A. D. Stone, Phys. Scr. T **90**, 248 (2001).

[5] Y.-F. Xiao, C.-L. Zou, Y. Li, C.-H. Dong, Z.-F. Han, and Q. Gong, Front. Optoelectron. China **3**, 109 (2010).

[6] T. Harayama and S. Shinohara, Laser Photonics Rev. **5**, 247 (2011).

[7] A. F. J. Levi, R. E. Slusher, S. L. McCall, J. L. Glass, S. J. Pearton, and R. A. Logan, Appl. Phys. Lett. **62**, 561 (1993).

[8] J. U. Nöckel and A. D. Stone, Nature **385**, 45 (1997).

[9] H. G. L. Schwefel, N. B. Rex, H. E. Tureci, R. K. Chang, A. D. Stone, T. Ben-Messaoud, and J. Zyss, J. Opt. Soc. Am. B **21**, 923 (2004).

[10] S.-B. Lee, J. Yang, S. Moon, J.-H. Lee, K. An, J.-B. Shim, H.-W. Lee, and S. W. Kim, Phys. Rev. A **75**, 011802(R) (2007).

[11] J. Wiersig and M. Hentschel, Phys. Rev. Lett. **100**, 033901 (2008).

[12] S. Lacey, H. Wang, D. H. Foster, and J. U. Nöckel, Phys. Rev. Lett. **91**, 033902 (2003).

[13] S. C. Creagh, Phys. Rev. Lett. **98**, 153901 (2007).

[14] S. C. Creagh and M. M. White, Phys. Rev. E **85**, 015201 (2012).

[15] L. Ge, Q. Song, B. Redding, A. Eberspächer, J. Wiersig, and H. Cao, Phys. Rev. A **88**, 043801 (2013).

[16] L. Ge, Q. Song, B. Redding, and H. Cao, Phys. Rev. A **87**, 023833 (2013).

[17] S. F. Pereira, M. B. Willemsen, M. P. van Exter, and J. P. Woerdman, Appl. Phys. Lett. **73**, 2239 (1998).

[18] Y. F. Chen and Y. P. Lan, J. Opt. B **3**, 146 (2001)

[19] Y. F. Chen, Y. P. Lan, and S. C. Wang, Appl. Phys. B **72**, 167 (2001).

[20] J.-F. Bisson, A. Shirakawa, Y. Sato, Y. Senatsky, and K.-I. Ueda, Opt. Rev. **11**, 353 (2004).

[21] D. Naidoo, T. Godin, M. Fromager, E. Cagniot, N. Passilly, A. Forbes, and K. At-Ameur, Opt. Commun. **284**, 5475 (2011).

[22] N. B. Rex, R. K. Chang, and L. J. Guido, IEEE Photon. Technol. Lett. **13**, 1 (2001).

[23] G. D. Chern, H. E. Tureci, A. D. Stone, R. K. Chang, M. Kneissl, and N. M. Johnson, Appl. Phys. Lett. **83**, 1710 (2003).

[24] T. Fukushima, T. Harayama, P. Davis, P. O. Vaccaro, T. Nishimura, and T. Aida, Opt. Lett. **27**, 1430 (2002).

[25] M. Kneissl, M. Teepe, N. Miyashita, N. M. Johnson, G. D. Chern, and R. K. Chang, Appl. Phys. Lett. **84**, 2485 (2004).

[26] S. Shinohara, T. Harayama, T. Fukushima, M. Hentschel, T. Sasaki, and E. E. Narimanov, Phys. Rev. Lett. **104**, 163902 (2010).

[27] T. Fukushima and T. Harayama, IEEE J. Sel. Top. Quantum Electron. **10**, 1039 (2004).

[28] M. Leonetti and C. Lpez, Appl. Phys. Lett. **102**, 071105 (2013).

[29] N. Bachelard, J. Andreasen, S. Gigan, and P. Sebbah, Phys. Rev. Lett. **109**, 033903 (2012).

[30] N. Bachelard, S. Gigan, X. Noblin, and P. Sebbah, Nat. Phys. Advance online publication, doi:10.1038/nphys2939 (2014).

[31] T. Hisch, M. Liertzer, D. Pogany, F. Mintert, and S. Rotter, Phys. Rev. Lett. **111**, 023902 (2013).

[32] Q. H. Song, L. Ge, J. Wiersig, J.-B. Shim, J. Unterhinninghofen, A. Eberspächer, W. Fang, G. S. Solomon, and H. Cao, Phys. Rev. A, **84**, 063843 (2011).

[33] J. Wiersig, A. Eberspächer, J.-B Shim, J.-W Ryu, S. Shinohara, M. Hentschel, and H. Schomerus, Phys. Rev. A **84**, 023845 (2011)

[34] L. Ge, Y. D. Chong, and A. D. Stone, Phys. Rev. A **82**, 063824 (2010)

Chapter 8

Conclusions and future prospects

In this thesis, we have investigated numerically the effect of disorder on photonic band gap, localization length and decay rates of modes on 1D PhC in chapter 2. In particular, we studied two types of disorders, one is uncorrelated disorder and another is correlated disorder. For structures with uncorrelated disorder, the PBG remains robust and is only affected when the magnitude of disorder becomes comparable to the lattice constant. The long-range order in the PhC is preserved under independent perturbation from their center position/size. However, in the case of correlated disorder, the PBG diminishes very quickly due to accumulation of disorder with each successive layer in the structure and causes the loss of long-range order just after a few periods. In top-down fabrication process such as lithography, the structural disorder is likely to be uncorrelated, where the size of the scatterers or their center position is slightly perturbed from its designed values. On the other hand, structures fabricated using the self-assembly or deposition method is likely to accumulate errors during the growth process, and thus it corresponds to correlated disorder.

In chapter 3, we studied numerically the PBG effect in 3D photonic amorphous structures (PASs) which only have short-range order. In the first part, we compared the PBG in two types of topologies, the cermet topology which consists of

closely-packed dielectric spheres or its inversed counterpart, and the network topology which each vertex is connected by four bonds (tetrahedral bonding). The tetrahedral network structures which contain uniform interconnected dielectric cylinders support better PBG. Counter-intuitively, we observed that a more ordered network has smaller PBG compared to a partially ordered network. In other words, between totally disordered (random) and completely ordered (periodic) networks, there exists an optimum degree of order to generate the largest PBG. The largest PBG is generated when the network has the most uniform distribution of bond angles. Higher refractive index contrast and lower fraction of high-index material are also important for PBG formation. From this study, we have identified several parameters that can be tuned to create broad isotropic PBG in photonic amorphous structures in the absence of long-range structural order.

Another class of non-periodic structures which supports complete PBG is the deterministic aperiodic structures (DASs). In this thesis, we focus on the golden-angle (GA) spiral lattice that has full circular symmetry in its Fourier spectrum. In the absence of translational and rotational symmetries, the GA spiral supports a wide PBG similar to the one in a triangular lattice. More interestingly, the optical resonances display unexpected features compared to the conventional band edge modes in a PhC. The band edge modes in a GA spiral are all extended azimuthally but radially confined, exhibiting ring patterns with different radius. In addition, due to the underlying structural symmetry, each mode contains discrete orbital angular momenta which correspond to the numbers in Fibonacci sequence. These optical resonances can be promising candidates for free-space optical communication where information is encoded using the orbital angular momentum of light instead of modulation in intensity or frequency [1,2]. In this way, it can improve the security and also increase the capacity of the communication link by multiplexing different orbital angular momentum beams that are in principle orthogonal to each other. The GA spiral can be

used as cavity for generating laser beams which carry certain orbital angular momentum, similar to the photonic crystal surface emitting laser (PCSEL) [3].

Instead of non-periodic structure factor, a DAS can also be created by spatially varying anisotropic scatterers (form factor). This structure was inspired by the topological defects in liquid crystal systems, which shows interesting optical properties. Here, we studied the optical resonances in photonic structures with topological defects, where the system consists of wavelength scale ellipses. Due to continuously rotating ellipses in the system, the spatial profile of the extended band edge mode is twisted compared to those in a PhC. Moreover, the presence of a singular point at the center of the structure generates modes which display circular energy flow. By artificially removing some scattering units, we created a high-Q defect state that contains non-zero net orbital angular momentum and potentially be used to generate optical vortex beam.

In nature, photonic amorphous structures (PASs) have been widely used to generate non-iridescent colors. The color is being generated by single or double scattering instead of PBG effect because the refractive index of the biological materials is too low to open up a band gap. Inspired by these findings, a biomimetic PAS was fabricated to generate angle-independent structural colors. The work in chapter 4 characterizes the scattering lengths of the biomimetic PAS to provides a better fundamental understanding and also to determine the critical system size for the PAS to operate in single scattering regime. We observed that the transport mean free path extracted from the coherent backscattering experiment is much longer than the simple estimation using independent scattering approximation. Further modeling shows that both the short-range order and near-field effect have to be taken into account to match the experimental results. These results also demonstrate a counter-intuitive phenomena, where higher packing density reduces scatterings. Nevertheless, the near-field effect can be accounted by the reduced index contrast between the particles and its sur-

rounding due to close packing.

Studies of structural colors in nature usually involve random sampling of animals with interesting nanostructures and recreating it artificially in the lab. The evolution of the colors and the nanostructures have been overlooked in most of the studies. In a collaborative work with the evolutionary biologists, we investigate how these colors and nanostructures evolved within a group of closely related butterflies from the genus Bicyclus. We also artificially evolve violet color from a lab model butterfly which originally has UV-brown color. From detailed nanostructure characterizations and numerical analysis, we identified the color producing mechanism, which is the thin-film interference effect from the lamina layer at the bottom of the scale. The artificial evolution of color is due to the change of the lamina thickness. We further analyze two butterfly species that have evolved their blue/violet colors in nature separately and found that their coloration mechanisms are the same. This result implies that the natural evolution of colors in different species of Bicyclus butterflies is likely to be the same, which is through the change of the lamina thickness. In this work, we only show the artificial color evolution from UV to violet, but the color can potentially be extended to longer wavelengths.

In chapter 6 of this thesis, we turn our attention to light transport in random media especially on the transmission channels with the highest transmission eigenvalues. We show that with strong absorption where system length L is larger than the diffusive absorption length ξ_a, light transport in the maximal transmission channel changes from diffusive to quasi-ballistic. This behavior implies that with absorption, we are able to increase the ratio of the ballistic photons to the diffusive one and could potentially find applications in the field of imaging by making the samples slightly more absorbing. When absorption is weak ($L < \xi_a$), we can use the minimum reflection channel to infer the maximum transmission channel because they are the same. However, this relation breaks down when absorption becomes strong, where

the minimum reflection channel converges to the maximum absorption channel. Experimentally, minimizing reflection to achieve maximum transmission will not work when the sample is absorbing.

Finally, in the last chapter, we show that by optimizing the spatial profile of the pump beam, a multimode lasing microdisk can be turned into a single mode laser. Due to slight deformation and surface roughness on the microdisk, each of the lasing modes has different emission directionality, which provides us the knob to tune the final laser emission pattern as well. From the measurements of the lasing thresholds and power slopes, we observe that selection of a lasing mode can be achieved by either increasing the lasing thresholds of the competitive modes or reducing their power slopes. From numerical simulations, we show that selective pumping not only can change the lasing threshold through the overlapping between mode and pump but also affect the lasing mode interactions. As a result, selective pumping can be used as a powerful method to create a tunable on-chip light source. Instead of manipulating the pump beam, we are investigating the change of lasing dynamics in a microdisk cavity by introducing another probe laser beam that will change the real part of the refractive index through photothermal effect [4]. Preliminary experimental result shows that by focusing the probe beam at different locations on the disk, some lasing modes can be greatly suppressed while the others can be enhanced. Consequently, we hope this probe beam can offer another degree of control to manipulate the lasing spectrum and also for fundamental understanding of the complex lasing dynamics.

Bibliography

[1] G. Gibson, J. Courtial, M. J. Padgett, M. Vasnetsov, V. Pas'Ko, S. M. Barnett, and S. Franke-Arnold, Opt. Express **12**, 5448 (2004).

[2] N. Bozinovic, Y. Yue, Y. Ren, M. Tur, P. Kristensen, H. Huang, A. E. Willner, and S. Ramachandran1, Science **340**, 1545 (2013).

[3] M. Imada, S. Noda, A. Chutinan, T. Tokuda, M. Murata, and G. Sasaki, Appl. Phys. Lett. **75**, 316 (1999).

[4] M. A. Dündar, J. A. M. Voorbraak, R. Nötzel, A. Fiore, and R. W. van der Heijden, Appl. Phys. Lett. **100**, 081107 (2012).